DEVELOPMENT OF MAGNETIC FIELD-BASED MULTISENSOR SYSTEM FOR MULTI-DOF ACTUATORS

A Dissertation
Presented to
The Academic Faculty

by

Shaohui Foong

In Partial Fulfillment
of the Requirements for the Degree
Doctor of Philosophy in the
School of Mechanical Engineering

Georgia Institute of Technology
December 2010

DEVELOPMENT OF MAGNETIC FIELD-BASED MULTISENSOR SYSTEM FOR MULTI-DOF ACTUATORS

Approved by:

Dr. Kok-Meng Lee, Advisor
School of Mechanical Engineering
Georgia Institute of Technology

Dr. Yang Wang
School of Civil & Environmental Engineering
Georgia Institute of Technology

Dr. Nader Sadegh
School of Mechanical Engineering
Georgia Institute of Technology

Dr. Fumin Zhang
School of Electrical & Computer Engineering
Georgia Institute of Technology

Dr. William Singhose
School of Mechanical Engieering
Georgia Institute of Technology

Date Approved: [July 28, 2010]

ACKNOWLEDGEMENTS

This thesis would not been possible without the numerous people who have supported and shaped my academic development at Georgia Tech. First and foremost, I would like to extend my sincere gratitude to my advisor, Dr Kok-Meng Lee for his insightful guidance and wise counsel. To me, he is more than just an advisor but also a caring mentor who has contributed immensely to my academic and professional maturity. I am also deeply grateful and appreciative to the members of my reading committee: Dr Nader Sadegh, Dr William Singhose, Dr Yang Wang and Dr Fumin Zhang who have provided invaluable advice and suggestions.

I would like to take this opportunity to thank former and present fellow students who have one way or another played a role in making this thesis a reality. To Dr Qiang Li, Dr Hungsun Son, Mati Chessin, Daxue Wang and Yang Xie: Thank you all for your collaboration on the Live Transfer project. To Kun Bai: Thank you for your time and effort in the sensor data collection of the spherical motor. To Jiajie Guo, Chih-Hsing Liu and Jungyoul Lim: I appreciate and cherish your valuable inputs and comments during our numerous lab meetings. To Adam Cardi and Aaron Enes: I will always remember the exhausting sessions we had together while preparing for the qualifying exams.

Last but not least, I am especially indebted to my family who despite being thousands of miles away, has provided unwavering support and encouragement throughout my time as an undergraduate and graduate student at Georgia Tech. There is just not enough space to fully describe what they have done for me.

The financial support of the US Poultry and Eggs Association, the Georgia Agriculture Technological Research Program (ATRP), Georgia FoodPAC and the Korean Institute of Machinery & Materials (KIMM) is gratefully acknowledged.

TABLE OF CONTENTS

LIST OF TABLES

LIST OF FIGURES

LIST OF SYMBOLS

Upper Case	Description
A	Unit *z*-axis vector projection onto *XY* plane
B	Magnetic flux density
C	Circular path of radius R_s which sensors lie in
D	Electric induction
E	Electric field
H	Magnetic field intensity
H_s	Vertical displacement distance of sensor plane
O	Rotational center of system
R_{PM}	Distance between **O** and each PM
R_s	Distance between **O** and each sensor
$X_sY_sZ_s$	s^{th} sensor fixed local frame
XYZ	Stator fixed reference frame

Lower Case	Description
a,b,c,d	Affine transformation factors for segment and sensor field calibration
g	Number of hidden layers in ANN
h	Number of hidden nodes per hidden layer in ANN
k	Time step integer
m	Field sector index
m_T	Total number of sectors
n	Field segment index
n_T	Total number of segments
p	Sensor pair index
q	Rotor orientation vector in Euler angles
$\mathbf{q}_{TB}$	Rotor orientation vector in Tait-Bryan angles
s	Sensor index

s_T	Total number of sensor pairs
t	time
u	Control input vector
v	Artificial neural network training set index
xyz	Rotor moving frame

Greek	**Description**
α, β, γ	Bryan-Tait angles (xyz body fixed motion)
ψ, θ, ϕ	Euler angles (zyz body fixed motion)
ψ_s	Angular spacing of sensors
μ_o	Magnetic permeability
ε_o	Permittivity of free space
ρ	Aspect ratio
$\mathbf{\Sigma}$	Set of all possible orientation coordinates
$\mathbf{\Lambda}$	Set of all possible field measurements

LIST OF ABBREVIATIONS

Abbreviation	Description
3-D	Three dimensional
ADC	Analog to digital converter
ANN	Artificial neural network
ANOVA	Analysis of variance
AT	Affine transformation
DAC	Digital to analog converter
DOF	Degrees of freedom
DMP	Distributed Multi-Pole
EM	Electromagnet
LS	Least squares
LUT	Look-up table
MSE	Mean Squared Error
SWM	Spherical Wheel Motor
PM	Permanent magnet

SUMMARY

Growing needs for precise manipulation in medical surgery, manufacturing automation and structural health monitoring have motivated development of high accuracy, bandwidth and cost-effective sensing systems. Among these is a class of multi-axis electromagnetic devices where embedded magnetic fields can be capitalized for compact position estimation eliminating unwanted friction, stiction and inertia arising from dedicated and separate sensing mechanisms. Using fields for position measurements, however, is a challenging 'inverse problem' since they are often modeled in the 'forward' sense and their inverse solutions are often highly non-linear and non-unique.

A general method to design a multisensor system that capitalizes on the existing magnetic field in permanent magnet (PM) actuators is presented. This method takes advantage of the structural field symmetry and meticulous placement of sensors to discretize the motion range of a PM-based device into smaller magnetic field segments, thereby reducing the required characterization domain. Within these localized segments, unique field-position correspondence is induced using field measurements from a network of multiple-axis sensors. A direct mapping approach utilizing trained artificial neural networks to attain multi-DOF positional information from distributed field measurements is employed as an alternative to existing computationally intensive model-based methods which are unsuitable for real-time control implementation. Validation and evaluation of this technique are performed through field simulations and experimental investigation on an electromagnetic spherical actuator. An inclinometer was used as a

performance comparison and experimental results have corroborated the superior tracking ability of the field-based sensing system.

While the immediate application is field-based orientation determination of an electromagnetic actuator, it is expected that the design method can be extended to develop other sensing systems that harnesses other scalar, vector and tensor fields.

CHAPTER 1

INTRODUCTION

1.1 MOTIVATION

Magnetic sensors are commonly utilized to locate the orientation and position of solitary high-coercive rare-earth permanent magnets (PM) by detecting the variation of their unique magnetic fields. Sensing systems that operate on this principle are able to function in harsh conditions as magnetic fields are invariant to temperature, pressure, radiation and other environmental factors. In addition, these systems are non-contact and permit sensing across multiple non-ferromagnetic mediums. Harnessing magnetic fields for orientation/position sensing is not new as evident by Raab's et al. [1] magnetic tracking system introduced three decades ago. Despite major advancement in miniaturization and magnetic sensing technology where modern sensors possess small physical footprints and high sensitivity [2][3], the use of magnetic sensors for real-time feedback control of actuators and devices is under exploited. The main obstacle preventing widespread adoption of such magnetic field-based non-contact sensors is the complexity involved and non-uniqueness encountered in determining the orientation/position of the PM with field measurements from the sensors. Inspired by developments in sensor fusion and sensing networks, an unorthodox multi-sensing approach is pursued.

Other than magnetic sensors, a spectrum of sensing solutions is available for real time closed loop control of multi-degree-of-freedom (DOF) dexterous devices. The

capability of high-speed and precise control of these actuators, such as those described in [4]-[8], enables a multitude of potential medical, automation, manufacturing and robotics applications. The premise of non-contact sensing solutions, unlike conventional single axis encoders which introduce friction, stiction, and inertia caused by constraining mechanisms, has motivated the adaptation of optical [9] and vision [10] sensors for measuring the 3-DOF orientation of a spherical body. The main issue with utilizing optical sensors is the staunch requirement of a consistent 'patterned' surface for reliable positional sensing. Vision (cameras) and ultrasonic sensors are limited by their precision and require 'a line of sight'. Although high end sensors employing eddy current, capacitive and triangulation technologies are able to provide measurements with high precision, they only work with metallic surfaces, in clean environments and reflective exteriors respectively. Laser interferometers, which uses reflected laser light to measure displacements to resolutions in the order of nanometers, are bulky/clumsy and costly which makes implementation exorbitant and unpractical. Inclinometers, accelerometers and other inertia/gyroscopic sensors offer an alternative means to measure the orientation and position through direct attachment to the moving body. However, unless these sensors are powered autonomously and transmit measurements wirelessly, constrictive bridging connections are required.

In an era of efficiency, a sensing system that requires minimal additions or modifications to the actuator to provide feedback is highly acclaimed. This notion provides the impetus for the development of a multisensor system for electromagnetic devices that uses the existing assembly of PMs to concurrently provide both actuation and sensing feedback. While the focus articulated here is vector field-based sensing

(specifically the magnetic field), this approach can be extended and adapted to develop other sensing systems that capitalize on scalar (temperature), other vector (electrostatic, gravitational) and even tensor (stress) fields.

1.2 Background and Impetus for Multi-sensor Approach

Rapid advances in low-cost computing technologies and low-power wireless communications within the last ten years have spawned a flurry of research and development on large scale sensor networks for a multitude of applications such as home, healthcare, military ISR, environment protection, water management, and livestock and endanger monitoring [11][12][13][14]. In the meso-scale, growing interest and stringent requirements for high precision smooth manipulation for a diverse application in medical surgery, manufacturing automation and structural health monitoring systems has motivated research aiming at capitalizing on the collaborative, complementary and competitive characteristics of sensor networks to synergistically fuse information.

Simultaneous processing and interpretation of sensory information is a seamless and almost effortless process for humans. An example of such advantageous integration of information is stereopsis (stereo vision) which is the sensation of depth resulting from the difference of spatial perception from two or more visual senses. In numerous engineering applications, physical sensors are used to observe and measure the system states for subsequent feedback control and automation. With the advent and proliferation of affordable vision systems along with maturity of image processing algorithms, many of these control and automated processes have been achieved using vision sensors. A common issue encountered is the tradeoff between responsiveness and the operating range of the sensor that often limits the accuracy of the controlled system. For example,

images with higher resolutions are required in order to achieve more precise control, thereby increasing the computation overheads with additional pixels to be processed. In addition, vision sensors often exhibit measurement errors which could further degrade the controlled system performance. An effective alternative to overcome the above problems is to employ an organized sensor network with multi-sensor fusion.

Measurement errors of physical sensors can be classified as systematic and random errors. Unlike the former, random errors are stochastic in nature and although they cannot be predicted, they can be adequately modeled using stochastic models. Since these measurements occur in discrete intervals, the Discrete Kalman Filter (DKF) has been extensively and effectively used to estimate the true measurement from raw observations and prior knowledge of system dynamics [15][16][17].

To address the inherent latency and improve performance in vision based control, different sensor network architectures were investigated in [18]. In these studies, it was found that by sequentially activating vision sensors in a network, the maximum velocity that can be tracked was increased. Direct comparison between sequential and parallel architectures of sensor networks has been investigated in recent decades [16][17], and marginally favors sequential processing. However, there is a lack of a unified approach to amalgamate these two architectures in a complementary fashion. A network of sensors having elements of both architectures can improve the sensing performance two fold through reduction in overall sampling time and suppression of measurement noise.

Inspired by developments in dynamic sensor networks, where an energy efficient sensor network is achieved through adaptively adjusting network density and coverage quality [19], the performance of the sensor network can be adjusted and regulated just

like a normal feedback controller. Such active management of the network reduces overall utilization of the entire sensor network while retaining the potential and capabilities of a fully operational sensor network.

While multisensor data fusion (pertaining to synthesizing raw data from multiple sensors in a coherent, systematic and comprehensible manner/format) has dominated contemporary literature, the notion and critical role of multisensor planning (the physical structure and operational schemes/architecture of the sensor network) is becoming increasingly evident. The characterization of an organized sensor network that is fundamentally based on the temporal measurement model for a sensor is explicitly developed in Appendix A. This temporal model allows the subsequent derivation of optimal weighting scheme between concurrent sensor measurements. The throttling controller which actively manages the network configuration is introduced as well. To compare and evaluate control performance of various sensor configurations and effectiveness of network throttling, simulations of DKF assisted state feedback control of an inverted pendulum system in perfect (no noise) and practical (with noise) environments are used.

Using the inverted pendulum as a system platform, the feasibility of an organized sensor network to improve command tracking under feedback control was investigated. In simulations, it was found that while the system controlled by a DKF state feedback benefitted from additional sensors in the steady state case, the effect on the transient response of the system due to a unit step was statistically undetectable. Using this result, a throttling sensor network that uses a reduced set of sensors in the transient response and a full complement of sensors at steady state was simulated. It was found that the

transition between configurations affects the performance of the system and the system under throttling sensor network outperformed the same system with static network while maintaining lower sensor utilization.

The investigation and results drawn from the *temporal* optimization of sensor networks facilitated improved performance in control processes and automation. Motivated by these promising findings, sensing performance can similarly be enhanced by the corresponding *spatial* analysis of sensor networks. Such investigation pertains to the positional installation of sensors for optimal sensing coverage for complementary, cooperative sensing parameters, and competitive fusion. For multi-DOF electromagnetic actuators with PM assemblies, a networked circular array of discrete magnetic sensors as will be presented is capable of unobtrusive orientation/position detection.

The last decade has seen a monumental shift in microprocessor development with the focus now on improving processor performance through multi-core applications rather than increasing the raw clock speed of the processor. In the last 5 years, multi-core technologies have been the driving force in the performance advancement in processors. The bottom-line is clear: improvements in sensing technologies in the future should not rely solely on the pursuit of superior individual sensors but assisted in a collective and broad approach in sensor network design and implementation.

1.3 PRIOR AND RELATED WORK IN MULTI-DOF SENSING

The major challenge encountered in multi-DOF systems, especially those relating to rotational motion, is the achievement of simultaneous measurement for each degree of freedom. Developing a sensing system for 3-DOF spherical actuator has proved to be especially demanding and have been approached using a variety of methods and

techniques. Early designs utilize connecting linkages to decouple motion into 3 separate Euler rotations which can be subsequently measured by single axis rotary encoders [20][21]. These connections are undesirable as they are susceptible to mechanical wear and introduce undesirable inertia and friction. Non-contact solutions using vision and optical sensors were proposed by Lee at el [9][10]. In this vision-based system, the orientation of the rotor is obtained through a grid pattern recognition algorithm applied on collected image frames. The accuracy and sampling rate of such a sampling system will depend enormously on the resolution of the camera and processing capability of the sensing system. But the main concern is the requirement of a specially treated patterned surface for sensing. Optical sensors on the other hand generate electrical signals that are a linear function of its relative motion on the surface and while they do not require any specific pattern, the surface needs to be continuous and suitable for use with optical sensors. Another technique to detect motion in multi-DOF systems is to mount the inertia/gyroscopic sensors (such as inclinometers) onto the moving body as it is done in aircrafts and Unmanned Aerial Vehicles (UAVs) [22]. However the installation of these sensors not only introduce dynamical imbalance to the system, their measurements must be transmitted off the moving body which entails an additional wireless communication system.

As magnetic sensors been used to localize the orientation and position of individual PMs, Son and Lee used the distributed multipole (DMP) model [23] to characterize the magnetic field of a single PM and design a magnetic field-based 2-DOF orientation sensor using methodically placed sensors [24]. One method involved extraction of the PM orientation by estimating and expressing the measured nonlinear

magnetic field density as a polynomial function and solving the inverse problem. In an effort to extend this technique to 3-DOF, a novel sensing methodology using Anisotropic Magneto-Resistive (AMR) sensors is described in [25] to detect directional changes of the magnetic field generated by the rotor that contains cylindrical PMs (used for actuation) and an auxiliary ring PM. As the magnetic field radiating from the ring PM is invariant to the rotor spin, it is used exclusively by 2 orthogonal AMR sensors to extract the rotor 2-DOF orientation. The third DOF, the spin of the rotor, is perceived through relative motion of the cylindrical PMs and because of the inability of the AMR sensor to distinguish between PMs, the spin determination appears to be only local. A decoupled 3-DOF translational flux density based sensing system designed for active servoing is articulated in [26] and it uses a single hall probe to detect its relative position to a PM through measurement of the magnetic field. Compared to 3-DOF rotational motion, the expressions for the magnetic flux density as a function of translational position is less involved. A problem that the paper identifies is the presence of multiple solutions due to the symmetry in the magnetic field and tackles it by restricting the possible locations of the sensor probe.

The remote nature of magnetic sensing techniques and ability to measure multiple DOFs at once has attracted considerable interest in the biomedical industry. This scheme is adapted to monitor the integrity of artificial medical valves [27] and real-time tracking of capsule endoscopy [28][29] through attachment of miniature but high coercive PMs. Sensors placed outside the body are able to track the relative position of the valves and capsules because the human body has a magnetic permeability similar to that of air and like other non-ferromagnetic materials, do not influence the magnetic field. It has also

been used to create a rotation sensing feedback to improve the control of prosthetic arm rotation in amputees by inserting a PM into the distal end of residual bone of the subjects with an upper limb amputation [30]. In endovascular catheterization, a PM attached to the probe is used to aid the navigation of the catheter in the body and elimination of repetitive and unnecessary X-Ray scans [31].

The same principle is also adapted in the navigation of autonomously guided vehicles (AGVs). By installing PMs in the ground, a set path can be created for AGVs to pursue using sensors mounted on the vehicle [32][33]. For enhanced performance, an array of single-axis magnetic sensors specially designed to isolate the linear region of the magnetic field can be installed for greater precision [34]. Using a 32 sensor 1-D array of sensors, the magnetic field of a bar magnet was used to compute its position [35].

In separate setups and approaches described in [36][37], [38][39] and [40], 2-D sensor arrays were successfully used to track a PM's 5-DOF (3 translation, 2 rotation) position by exploiting the unique magnetic field of the PM as measured simultaneously by all sensors at various orientation and position. In [40], it is particularly distinguished for operating a heterogeneous array of magnetic sensors containing a mixed combination of single and multi axis Hall-effect sensors. Inverse computation of the PM's position is achieved using a nonlinear optimization algorithm to minimize the deviation between measured and calculated magnetic field (using a single dipole analytical model). This approach is relatively slow, high in complexity and requires a good initial guess of the parameters. A viable and quicker alternative is to employ trained Artificial Neural Networks to map orientation estimates to measured fields [41]. It is noted that contemporary research is heavily polarized on the tracking and tracing of the motion of

solitary PMs using numerous sensors concurrently (in 1-D and 2-D sensor arrays), with sparse literature on the corresponding issue with an assembly of PMs. While the shift to network sensing is encouraging, there is a noticeable lack of an organized scheme to proficiently manage the individual measurements in these sensor arrays.

The concurrent use of sinusoidally magnetized ring shaped PMs with low cost Hall-effect sensors have been utilized as an absolute single DOF rotary position [42][43]. Both approaches involve measuring the amplitude and direction of the magnetic field in the radial direction to infer the angular position of the PM. The knowledge of just the direction of a magnetic field in a pair of two-axis sensors can be used to robustly infer translational position of a cylindrical magnet [44]. The magnetic tracking approach discussed here is not limited to PMs and easily extended to EMs as an array of 64 EM coils has been successfully used to compute the position of a receiving coil [45][46].

1.4 PHILOSOPHY OF DISTRIBUTED FIELD SENSING

The notion of distributed embedded field sensing is two-fold: Capitalize on the incidence of existing fields in dynamic systems for efficient and unobtrusive position sensing and given a set of instantaneous field measurements, provide positional estimates accurately and swiftly (low computational lag) as feedback for closed loop control. In general, a field is a physical quantity associated to every point in space (or time). Quantities at each point may be a scalar, vector or matrix generating scalar, vector and tensor fields respectively. In classical field theory, fields exist due to presence of field sources such as mass for gravitational fields and heat for temperature gradients. Whichever the field, the measurement of the quantities at multiple points in space can be used to infer location and orientation of the field sources. As many dynamic systems

contain fields that are embedded and inherent in the system, the detection of these moving fields permit direct correspondence to the system's position and/or orientation. Furthermore, this eliminates the need for auxiliary sensor-delegated mechanisms that would have a detrimental effect on the dynamic performance on the system.

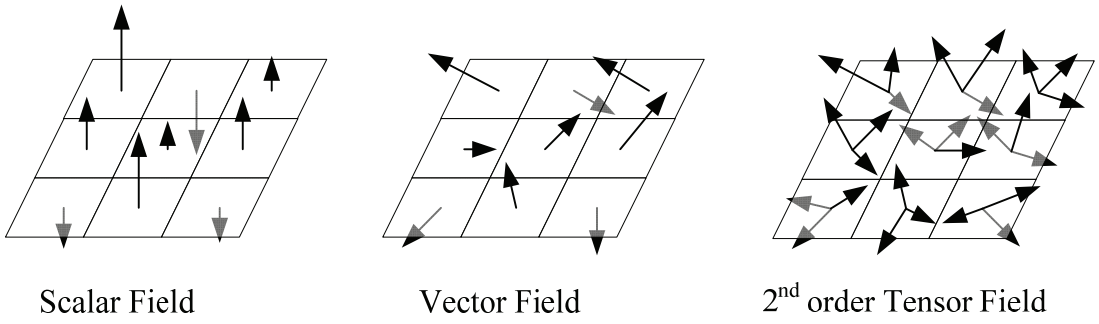

Figure 1-1 Scalar, vector and tensor fields in space

The notion of using measured fields for positional sensing can be visually presented using a simplistic diagram of various fields as shown in Figure 1-1 where each field occupies a 3×3 spatial space. For the scalar field, the field quantity within each space is a scalar and represented by the magnitude of the arrow. Similarly, in a vector field, the field quantity is represented by the direction and magnitude of an arrow while a 2^{nd} order tensor field can be represented by a collection of three arrows within each space. If each space presents a unique position/orientation of a dynamic system and field measurements in each space are also unique, the field measurement at any time can be used to directly infer the coordinates within the field space and hence the corresponding dynamic system's position/orientation.

The main difficulties in cultivating position-field correspondence are the complexities of analytical field models and absence of bijectivity (both injective and surjective or encompassing one-to-one and onto correspondence) between field

measurements and position/orientation. Also known as the magnetic "inverse problem", contemporary literature has labeled this class of quandary being 'highly non-linear and without formulations to follow' [47], as well as 'not solvable uniquely, even with complete knowledge of … magnetic field everywhere' [48].

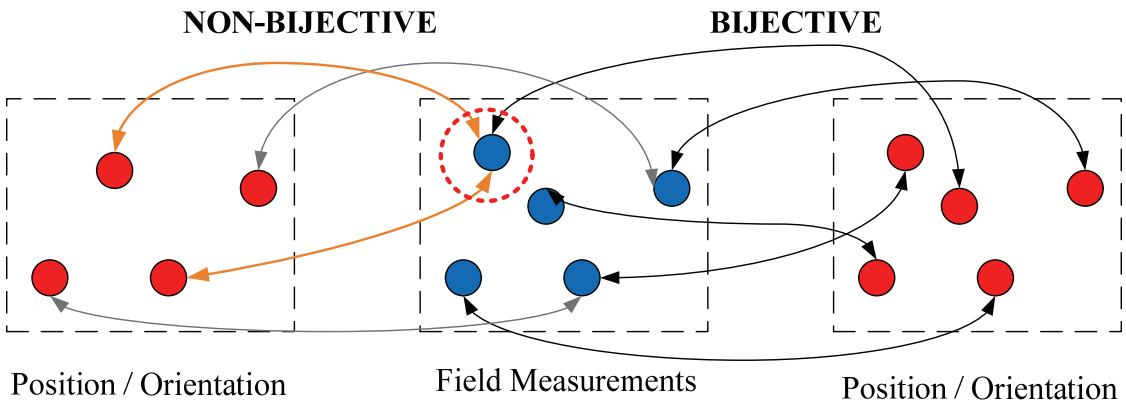

Figure 1-2 Comparison between a non-bijective and bijective transformation

The differences between a bijective and non-bijective relationship is visually shown in Figure 1-2. In a non-bijective relationship, multiple positions/orientations share a common field measurement value. However, in a bijective relationship each field measurement is associated to only one position or orientation. It is clear that without a bijectivity, associating an arbitrary field measurement with a unique position is difficult. While theoretical field models for the prediction of fields in space are available, they are often highly complex and not in a tractable form for direct inverse computation operations. Moreover, model predictions and actual field measurements can differ and these discrepancies can significantly hamper the consequential sensing accuracy. However, even if these models are highly accurate and computation speed is not an issue, the symmetry inherent in all fields impedes bijectivity between measurements and position. This concern is exacerbated in systems with multiple field sources.

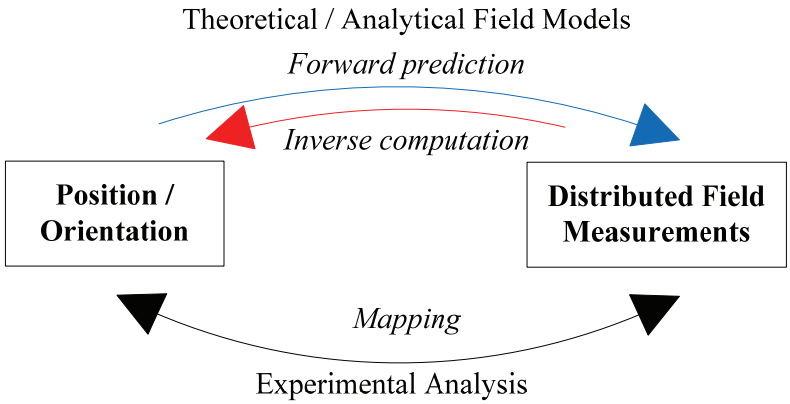

Figure 1-3 Relating between field measurements and position/orientation

An evident alternative to theoretical models is through actual experimental analysis as shown in Figure 1-3. Direct experimentation allows the actual field to be analyzed and correspondence between position and distributed field measurements can be artificially and accurately constructed using function fitting methods. These methods are akin to performing sensor calibration, like relating the expansion length of the fluid in a thermometer to temperature. However unlike conventional calibration where the mapping is from a scalar to a scalar, field mapping involves vector to vector correspondence: relating multiple field measurements to multi-DOF positions. The most popular function fitting approach is least squares (LS) where the optimal fit between modeled and observed data is the instance where the sum of squared residuals (difference between an observed value and the value provided by the model) is at its minimal. Although LS mapping is computational swift, it is not intended to associate a large number of field measurements to position/orientation as the high order models required to adequately provide fitting become extremely complex. For such cases, artificial neural networks (ANN) are better suited due to their ease in relating multi-input-multi-output (MIMO) systems. Another simpler alternative is to employ lookup tables (LUT) to associate field

measurements with position (similar to multiplication tables). One shortcoming is the discrete nature of the relationship, though interpolation and spline functions allow construction of data between known value sets. However the amount of memory required for pre-caching grows exponentially with higher number of inputs (field measurements). With experimental data which is usually corrupted with sensing noise, the nature of LUTs inhibits discernment between signal and noise which reduces mapping accuracy.

The predicament in field-position uniqueness can be counteracted by using multiple sensors to concurrently measure the field at various points in space. In addition, the field map relating position and measurements can be characterized critically to obtain a field map with a reduced localized domain where bijectivity holds. This would allow unique and absolute mapping within these localized segments and an incremental approach can be used to track mappings between segments.

Although experimental data is used to construct the map, analytical field models offer valuable insight on the composition of the field to provide an outlet for design purposes to select or position/orient field sensors such that their measuring range is maximized and no saturation occurs.

1.5 RESEARCH OBJECTIVES

This research aims to develop a sensing system that uses distributed field-based measurements for non-contact orientation determination. Accomplishment of this goal comprises of the following objectives:

The first is the development of a novel embedded field sensing system which capitalizes on the capacity of a network of field sensors to detect moving periodic fields for direct position/orientation correspondence.

This methodology utilizes inherent or embedded fields which are already present in the system for efficient and unobtrusive sensing. Only installations of static field sensors are required and the system's dynamics are unchanged as no additional mechanisms are attached. This approach takes into consideration the intrinsic symmetry of fields in 3-D space and occurrence of periodicity in fields with multiple sources through characterization and classification of measured fields into segments. Through field analysis, swift direct mapping techniques can be implemented to uniquely relate field measurements to position/orientation within field segments.

A general framework for vector (magnetic, gravitational, electrostatic) field sensing is presented though it is expected that the design method can be extended to develop other sensing systems that harnesses scalar (temperature, pressure, light) and tensor (stress, strain) fields.

The second objective is the evaluation of the theoretical and operational performance of the sensing system in a magnetic field environment using analytical models and experimental investigation.

Using analytical magnetic field models such as the DMP model [23][24], the predicted/projected magnetic fields of two distinct multi-PM configurations are used to determine the theoretical sensing accuracy limit of the field-based system. The first PM assembly consists of 24 PMs positioned in a circular path on a single-DOF rotating disk shaped rotor while the second assembly is based on an actual multi-DOF electromagnetic spherical actuator prototype being developed at Georgia Institute of Technology [4]. With a matching configuration of 24 static magnetic sensors, the first setup allows statistical insight and examination of the experimental field variation between identically

graded and geometrically sized magnets as well as field measurement disparities between similar sensors. These propagating effects on sensing performance are consequentially scrutinized. The prototype actuator offers a platform to illustrate the sensing system for a multi-DOF system using multi-axis magnetic sensors.

The third and final objective is demonstrating this sensing system for non-contact open and closed loop control of an electromagnetic actuator.

Lastly, the sensing system is implemented on a multi-DOF electromagnetic actuator using a network of magnetic sensors. As actuation is provided by the interactions between stationary EMs and a moving PM on the rotor, the field contributions by these EMs on measured magnetic fields must be actively compensated. Through isolation of the moving rotor field, the sensing system can be employed for accurate system identification and determination of the rotor orientation and provide real-time feedback for closed-loop control.

1.6 Outline and Organization of Thesis

The remainder of the dissertation is outlined as follows.

Chapter 2 commences with the development of the embedded field sensing system for a dynamic system with up to three degrees of independent motion. This system consists of the forward and inverse model whereby the forward model is reserved for offline analysis for characterization and calibration, the inverse model is used in real-time orientation determination. During field analysis, the entire field map is divided into segments to coincide with the inherent periodicity in the embedded field and symmetry of the field allows further classification into sectors. Within these segments/sectors, the field

measurements and instantaneous position exhibit bijectivity (one-to-one correspondence) which permit accurate mapping between the two.

In Chapter 3, a single-DOF system with embedded magnetic field constructed using an assembly of 24 identical PMs is used as an illustrative example to validate the sensing methodology. Matched with an equal number of field sensors, statistical analysis on the field variation between segments and measurement disparity between sensors can be performed. These natural variations are arrested by optimally calibrating field measurements in segments and by sensors to a reference segment and sensor using affine transformation. These effects on the corresponding experimental sensing accuracy of the system are quantified and evaluated against the theoretical limit using analytical field models.

The experimental investigation continues into Chapter 4 where the feasibility of the sensing system for multi-DOF sensing is examined on a spherical electromagnetic actuator. As such systems utilize existing embedded magnetic fields for actuation via EM PM electromagnetic interactions, the sensing system must compensate for the field contributions by these stationary EMs. Building on the previous chapter where a single-DOF sensing system was implemented, the extension to multi-DOF is presented and investigated experimentally using multi-axis magnetic sensors.

Chapter 5 presents an application of the sensing system that takes advantage of its swift and direct nature for closed loop control of an electromagnetic actuator. Exploiting the high bandwidth of magnetic sensors, the sensing system is able to perform online parameter identification to determine the system model and provide real-time positional

information for feedback control. Open and closed loop controllers were implemented and evaluated.

Finally Chapter 6 summarizes the conclusions and findings of this dissertation and offer recommendations for future research in distributed field-based sensing.

CHAPTER 2

CAPITALIZING EMBEDDED MAGNETIC FIELDS FOR SENSING

2.1 OVERVIEW

Developing a sensing system to track a moving body with an attached magnetic field requires three considerations. The first is to understand the physics of the field in the medium and its behavior in motion. The second is to use parametric spaces to characterize and classify the field into smaller spatial segments where bijective relationship holds. With these segments, the third and final consideration is associating a set of distributed field measurements to a set of positional/orientation coordinates swiftly and efficiently without using time-consuming mathematical tools. Finally, as this approach assumes perfect symmetry of fields and multiple sensors, statistical based calibration methods are proposed to overcome real world implementation issues.

2.2 QUASI-STATIC MODEL FOR FIELD SENSING

In Figure 2-1, a physical body containing magnetic sources in a system can be described by the coordinates **O** of the origin. Using the Euler notation, the orientation of the moving *xyz* frame is described by a sequence of body-fixed rotations about *x*, *y* and finally *z* axis by the corresponding angles of α, β and γ respectively. The closed boundary **Ω** represents the free space containing the magnetic field. It is desired to use field measurements in **Ω** to extract the position and orientation of the moving field and body.

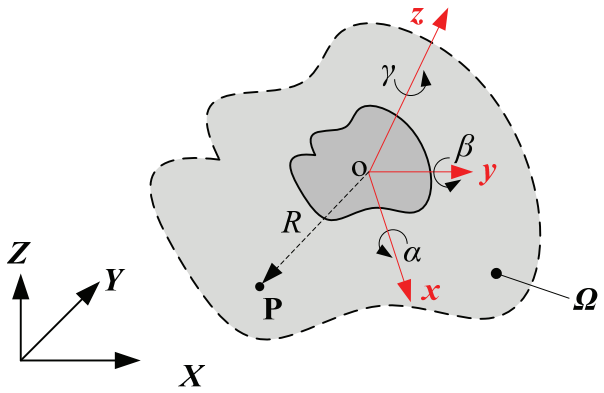

Figure 2-1 Describing a moving body with an attached field

In this source-free and current-free space **Ω**, the conservative magnetic field satisfies Maxwell's equations given by

$$\nabla \times \mathbf{H} = \frac{\partial \mathbf{D}}{\partial t} \tag{2.1}$$

$$\nabla \cdot \mathbf{B} = 0 \tag{2.2}$$

$$\nabla \times \mathbf{E} = -\frac{\partial \mathbf{B}}{\partial t} \tag{2.3}$$

$$\nabla \cdot \mathbf{D} = 0 \tag{2.4}$$

where **H** and **B** are the magnetic field intensity and flux density respectively; and **E** and **D** are the electric field and induction respectively. These quantities are related through

$$\mathbf{B} = \mu_o \mathbf{H} \tag{2.5}$$

$$\mathbf{D} = \varepsilon_o \mathbf{E} \tag{2.6}$$

where μ_o is the magnetic permeability and ε_o is the permittivity in free space respectively. Taking the curl of Equation (2.1),

$$\nabla \times \left(\nabla \times \mathbf{H} \right) = \frac{\partial \left(\nabla \times \mathbf{D} \right)}{\partial t} \tag{2.7}$$

and using the vector identity

$$\nabla \times \left(\nabla \times \mathbf{B} \right) = \nabla \left(\nabla \cdot \mathbf{B} \right) - \nabla^2 \mathbf{B} \tag{2.8}$$

the propagation of the moving magnetic field can be derived from combining Maxwell's equations which leads to a homogeneous vector wave equation of the form:

$$\nabla^2 \mathbf{B} - \frac{1}{c_o^{\,2}} \frac{\partial^2 \mathbf{B}}{\partial t^2} = 0 \tag{2.9}$$

where $c_o = 1/\sqrt{\mu_o \varepsilon_o}$ which represents the speed of magnetic wave propagation in free space (speed of light). From the general theory of relativity, in other mediums, this value will always be lower than that in free space.

Taking into account the observation distance R, propagation speed of the magnetic field c_o and following the derivation in [49] for propagation of EM waves, the magnetic flux density as measured at a stationary point **P** in **Ω** can be expressed by

$$\mathbf{B}_\mathbf{P}(t) = \lim_{R/c_o \to 0} \left[\mathbf{B}_\mathbf{P}(t - R/c_o) + \frac{R}{c_o} \frac{\partial \mathbf{B}_\mathbf{P}(t - R/c_o)}{\partial t} \right] \tag{2.10}$$

The first term in Equation (2.10) follows directly from propagation delay and the second component accounts for the delayed change in field due to spatial rotation. Some intuitive insights can be drawn from the value of the time-scale quantity R/c_o and the angular velocities:

- For R/c_o <1 μsec, where **P** is close to the radiating body, the contribution of the second term is minimal and the time delay effects of both terms are insignificant. Physically, the magnetic wave propagation effects can be suitably neglected. This allows the expression in Equation (2.10) to be invariant to time and only dependent on the spatial angles

$$\mathbf{B}_\mathbf{P} = \mathbf{B}\left(\mathbf{R}, \alpha, \beta, \gamma \right) \tag{2.11}$$

- For appreciable distances of R such that R/c_o is significant, the propagation delays are more apparent. Using chain rule, the second term in Equation (2.10) can be explicitly expanded to obtain

$$\frac{\partial \mathbf{B_P}(t-R/c_o)}{\partial t} = \frac{\partial \mathbf{B_P}(t-R/c_o)}{\partial \alpha}\frac{d\alpha}{dt} + \frac{\partial \mathbf{B_P}(t-R/c_o)}{\partial \beta}\frac{d\beta}{dt} + \frac{\partial \mathbf{B_P}(t-R/c_o)}{\partial \gamma}\frac{d\gamma}{dt} \quad (2.12)$$

  This expression reveals that the second term in Equation (2.10) can be neglected if the angular speed of the moving field is low (with respect to the speed of light).

The above implies that for most electromechanical systems considered here, the time-scale R/c_o is in the order of nanoseconds and motion of the system is non-relativistic, validating the quasi-static assumption of the magnetic field in **Ω**. Such static magnetic fields are curl-free vector fields and hence **H** can be expressed by

$$\mathbf{H} = -\nabla\varphi \quad (2.13)$$

and φ is the scalar magnetic potential. In an isotropic and homogenous medium **Ω**, the magnetic flux density at any point in this **Ω** space is obtained through the solution of Laplace's equation

$$\nabla^2\varphi = 0 \quad (2.14)$$

With proper boundary conditions for Equation (2.14), the **B** field in the space **Ω** is well defined and independent of time. Solutions to the Laplace's equation are explicit functions of the spatial coordinates; as a result, the field measurements at **P** are only a function of the spatial angles of α, β and γ.

For field based sensing where consideration of the field propagation speed can be neglected, it is essential to uniquely relate a set of position/orientation coordinates of a system **Σ** to a corresponding set of stationary sensor measurements **Λ**. There are two ways to relate and visualize these two sets:

Forward Model: $\mathbf{\Sigma} \rightarrow \mathbf{\Lambda}$

- This model can be visually illustrated with the aid of Figure 2-2 where the space within the forward model cuboid is the set of all possible orientation coordinates of a system $\mathbf{\Sigma}$. For any α, β and γ, which corresponds to a point in the cuboid, the value at that coordinate is $\boldsymbol{\lambda}=[B_{PX}\ B_{PY}\ B_{PZ}]^{T}$ the magnetic flux density measurement at $\mathbf{P}$. For bijection, for all $\mathbf{q} \in \lambda$ there is exactly one unique element $\boldsymbol{\lambda} \in \mathbf{\Lambda}$ such that no unmapped element exists in either $\mathbf{\Sigma}$ or $\mathbf{\Lambda}$ or multiple mapping to a single element. In other words, every position/orientation $\mathbf{q}$ of the field should have a unique corresponding measurement $\boldsymbol{\lambda}$ that no other position/orientation would exhibit. As it will be shown, analysis of the field measurements in this parametric space is critical for field-based sensing.

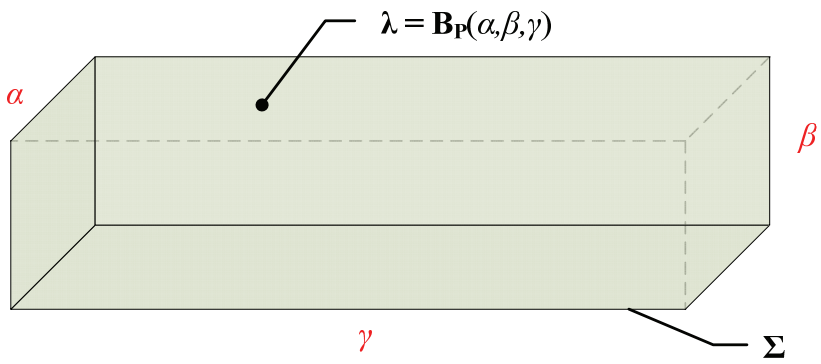

Figure 2-2 Forward model parametric space

Inverse Model: $\mathbf{\Lambda} \rightarrow \mathbf{\Sigma}$

- Mathematically, if the forward model is bijective, the inverse model $\mathbf{\Lambda} \rightarrow \mathbf{\Sigma}$ exists and is bijective as well. This property allows sensor measurements to be mapped uniquely to position/orientation coordinates, which is the fundamental mechanics of a sensing system. As with the forward model, a visual representation of the inverse model can be constructed and illustrated in Figure 2-3. The cuboid

represents each of the three independent magnetic flux density measurements at **P** and the entire space within the cuboid is the set of field measurements $\mathbf{\Lambda}$. For any $\mathbf{B_P}$, which corresponds to a point in the inverse model cuboid, the value at that coordinate is $\mathbf{q}=[\alpha\ \beta\ \gamma]^T$ the spatial orientation of the field.

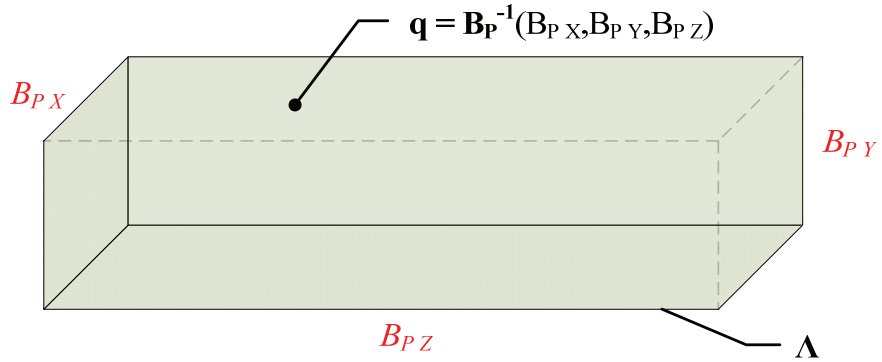

Figure 2-3 Inverse model parametric space

Illustrative example:

Consider a moving body (moving *xyz* frame) containing a single magnetic source modeled using a single dipole model [50] as shown in Figure 2-4. Both poles have equal but opposite field strength *m* and fixed onto the *z*-axis. The dipoles are centered about **O** and the distance between the negative to positive pole is *L*. By the principle of superposition, the magnetic flux density at point **P** is with respect to the fixed *XYZ* frame is the additive effect due to both dipoles

$$\mathbf{B}_{\mathrm{p}} = \frac{m\mu_o}{4\pi}\left\{\frac{\mathbf{R}-\mathbf{L}/2}{\left|\mathbf{R}-\mathbf{L}/2\right|^3}-\frac{\mathbf{R}+\mathbf{L}/2}{\left|\mathbf{R}+\mathbf{L}/2\right|^3}\right\} \tag{2.15}$$

where $\mathbf{R}=[R_X\ R_Y\ R_Z]^T$ is the directional vector in the *XYZ* frame between the origin $\mathbf{O}=[O_X\ O_Y\ O_Z]^T$ and $\mathbf{P}=[P_X\ P_Y\ P_Z]^T$ defined by

$$\mathbf{R}=\mathbf{P}-\mathbf{O} \tag{2.16}$$

Through coordinate transformation of the unit vector in the z-axis, the expression for $\mathbf{L}$ is

$$\mathbf{L} = L\left[\sin\beta \quad \sin\alpha\cos\beta \quad \cos\alpha\cos\beta\right]^{\mathrm{T}} \tag{2.17}$$

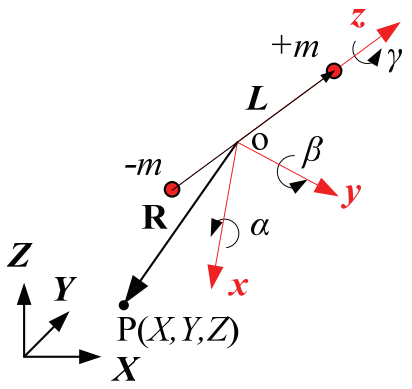

Figure 2-4 Magnetic field generated by a single dipole model

The absence of γ in Equation (2.15) is due to the placement of the magnetic dipoles on the z-axis, causing $\mathbf{B_P}$ to be invariant to γ. Equation (2.15) can be converted into a non-dimensional form as shown by

$$\mathbf{B}_{\mathrm{p}} \Big/ \frac{m\mu_o}{4\pi L^2} = \tilde{\mathbf{B}}_{\mathrm{p}} = \left\{ \frac{L^2\left(\mathbf{R}-\mathbf{L}/2\right)}{\left|\mathbf{R}-\mathbf{L}/2\right|^3} - \frac{L^2\left(\mathbf{R}+\mathbf{L}/2\right)}{\left|\mathbf{R}+\mathbf{L}/2\right|^3} \right\} \tag{2.18}$$

By defining the aspect ratio $\rho=R/L$, and through variable manipulations in Equation (2.18), the following expression for the non-dimensional field measurement $\tilde{\mathbf{B}}_{\mathrm{p}}$ is obtained

$$\tilde{\mathbf{B}}_{\mathrm{p}} = \frac{\rho\vec{\mathbf{R}}-\vec{\mathbf{L}}/2}{\left|\rho\vec{\mathbf{R}}-\vec{\mathbf{L}}/2\right|^3} - \frac{\rho\vec{\mathbf{R}}+\vec{\mathbf{L}}/2}{\left|\rho\vec{\mathbf{R}}+\vec{\mathbf{L}}/2\right|^3} \tag{2.19}$$

where $\vec{\mathbf{R}}$ and $\vec{\mathbf{L}}$ are unit vectors. An observation to note is for a given $\vec{\mathbf{R}}$, the expression for $\tilde{\mathbf{B}}_{\mathrm{p}}$ satisfies the following constraint:

$$\tilde{\mathbf{B}}_{\mathrm{p}_1}\left(\vec{\mathbf{R}}\right) = \tilde{\mathbf{B}}_{\mathrm{p}_2}\left(-\vec{\mathbf{R}}\right) \tag{2.20}$$

This property suggests that in the space **Ω**, there are at two points, $\mathbf{P_1}$ and $\mathbf{P_2}$ such that the field measurements are not independent.

For $\rho \to 0$, where the distance between **P** and **O** are orders less than the separation distance between the dipoles, Equation (2.18) can be approximated by

$$\tilde{\mathbf{B}}_{\mathrm{p}} \approx -8\vec{\mathbf{L}} = -8\begin{bmatrix}\sin\beta & \sin\alpha\cos\beta & \cos\alpha\cos\beta\end{bmatrix}^{\mathrm{T}} \tag{2.21}$$

For $\rho \to \infty$, where the distance between **P** and **O** are orders more than the separation distance between the dipoles, the expression for $\tilde{\mathbf{B}}_{\mathrm{p}}$ is

$$\tilde{\mathbf{B}}_{\mathrm{p}} \approx \frac{-\vec{\mathbf{L}}}{\rho^3} = -\frac{1}{\rho^3}\begin{bmatrix}\sin\beta & \sin\alpha\cos\beta & \cos\alpha\cos\beta\end{bmatrix}^{\mathrm{T}} \tag{2.22}$$

both extreme cases, the magnetic flux density is invariant to $\vec{\mathbf{R}}$ and only a direct function of the direction of **L**; a closed form expression to obtain α, β for a given flux density measurement exists by simultaneously solving any 2 of the 3 component equations in Equations (2.21) or (2.22).

Of interest in quasi-static field sensing for multi-DOF actuators is when the aspect ratio is unity (where *R* and *L* are in the same order). The corresponding equation for $\tilde{\mathbf{B}}_{\mathrm{p}}$ is

$$\tilde{\mathbf{B}}_{\mathrm{p}}\left(\rho = 1, \vec{\mathbf{R}}, \alpha, \beta\right) = \frac{\vec{\mathbf{R}} - \vec{\mathbf{L}}/2}{\left|\vec{\mathbf{R}} - \vec{\mathbf{L}}/2\right|^3} - \frac{\vec{\mathbf{R}} + \vec{\mathbf{L}}/2}{\left|\vec{\mathbf{R}} + \vec{\mathbf{L}}/2\right|^3} \tag{2.23}$$

Clearly this expression is now a function of the direction of the unit vector $\vec{\mathbf{R}}$, and the rotation angles α,β.

With orthogonality in mind, one possible choice for the unit vector of **R** is $\vec{\mathbf{R}} = \begin{bmatrix}1 & 0 & 0\end{bmatrix}^{\mathrm{T}}$. With this $\vec{\mathbf{R}}$ the distance between **P** and the magnetic dipoles are equal when α and β are zero. Using the expression in Equation (2.23), the dimensionless magnetic flux density measurement at **P** can be presented in forward model parametric

space $\boldsymbol{\Sigma}$ using 3 distinct plots as shown in an illustrative example in Figure 2-5 for $\vec{\mathbf{R}} = \begin{bmatrix} 1 & 0 & 0 \end{bmatrix}^{\mathrm{T}}$. The axes of this Cartesian parametric space are the individual components of $\mathbf{q}$; and the value at each point in space is a singular component of the vector $\boldsymbol{\lambda}$. This parametric space is also the visual representation of the set $\boldsymbol{\Sigma}$ and analysis of this space permits field characterization with respect to the individual components of $\mathbf{q}$. Points with positive magnetic flux densities are shaded lightly and vice versa.

Alternatively, the relationship between measured magnetic flux $\tilde{\mathbf{B}}_{\mathrm{p}}$ and $\mathbf{q}$ can be characterized and presented in the inverse model parametric space $\boldsymbol{\Lambda}$. In this space, the axes of this Cartesian parametric space are the individual components of $\tilde{\mathbf{B}}_{\mathrm{p}}$; and the value at each point in space is a singular component of the vector $\mathbf{q}$. To facilitate illustration and avoid constructing visually confusing volumetric plots, two of the three measuring axes (such as (B_X, B_Y), (B_X, B_Z) and (B_Y, B_Z) are chosen and the numerical value of α and β computed to create surface plots as shown in Figure 2-6. In this 3 by 2 grid of surface plots, the left and right columns depict the possible values of α and β respectively for a given combination of the measuring axes. For unique sensing, it is desired to associate a unique α and β for a set of field measurements. Clearly, from the surfaces plots in Figure 2-6, for the same set of measurement, multiple values of α and β exists.

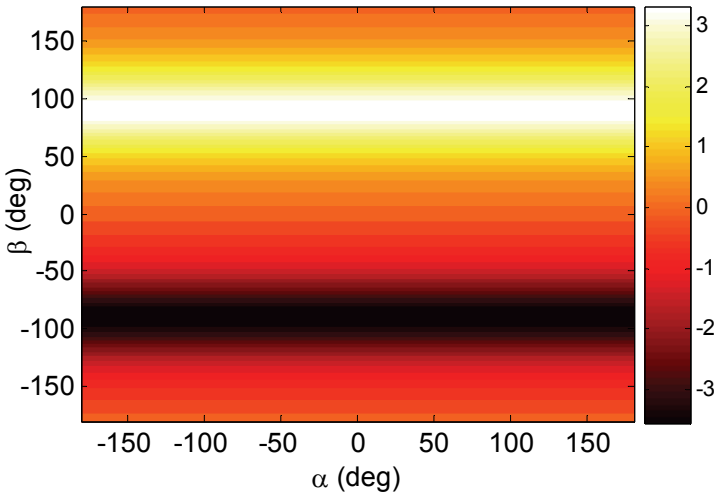

(a) *X*-component of **B** as measured from **P**

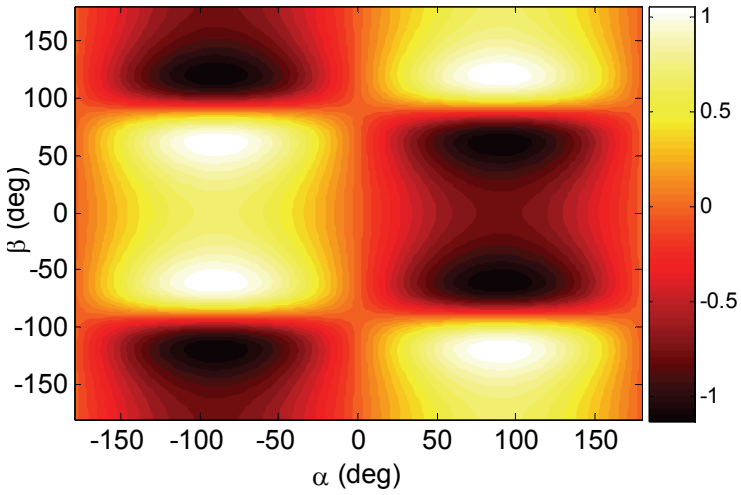

(b) *Y*-component of **B** as measured from **P**

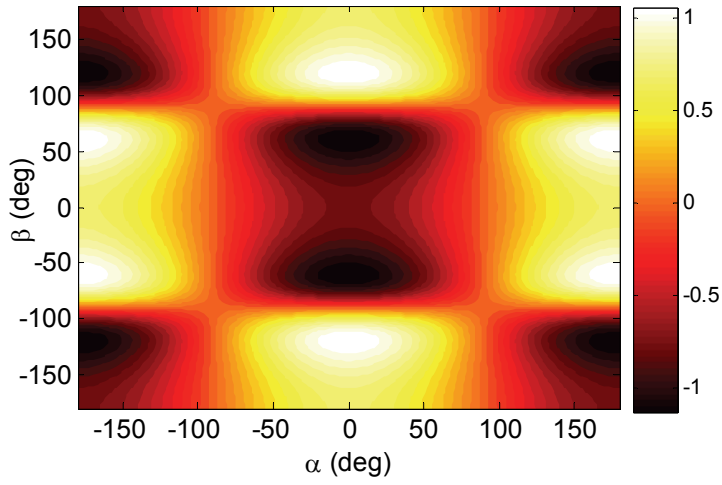

(c) *Z*-component of **B** as measured from **P**

Figure 2-5 Field measurements in forward model parametric space **Σ**

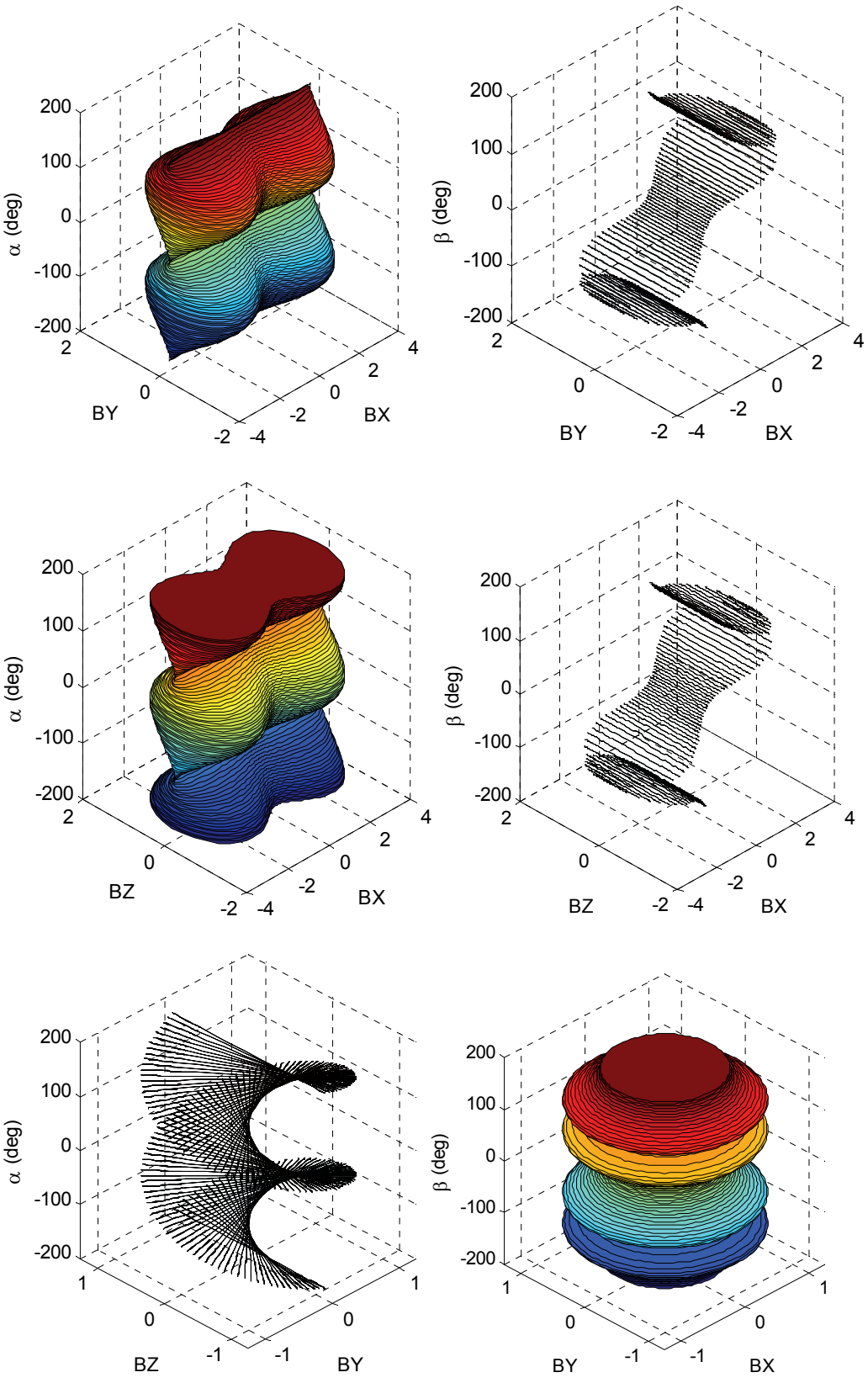

Figure 2-6 Surface plots in inverse parametric space **Λ**

Unlike the forward parametric space, the domain of the inverse parametric space is not well defined. As both spaces are equivalent, analysis and examination of the forward parametric space is used to draw insights and conclusions in the inverse parametric space. Through observation of the field distribution in the forward parametric space and noting well defined segmentation, the parametric space in Figure 2-5 can be segregated in 4×4 grid with 16 *equal* sectors as shown in Figure 2-7 with each sector referenced by the sign of the magnetic field in each component of **λ**. To facilitate identification, each sector is referenced using the column and row index. As there are three sensing axis at **P**, only up to 2^3 sectors can be uniquely described. Hence the entire parametric space is not bijective; $\mathbf{B}^{-1}$ does not exist for the entire space. For example, the field map in sector (1,1) and sector (2,3) are identical; It is not possible to uniquely distinguish between the two sectors.

However, subsets of the parametric space are bijective and determining such spaces is achieved directly from the classified space in Figure 2-7. Using all three sensing axes, one possible bijective subdomain is defined by $\alpha \in (-\pi, \pi)$ and $\beta \in (-\pi/2, \pi/2)$ where all 8 sectors are uniquely referenced by the sign of **λ**. With two sensing axes, it is easily deduced that only up to 2^2 sectors can be uniquely described. One possible subdomain that is bijective to B_X and B_Y is $\alpha \in (-\pi/2, \pi/2)$ and $\beta \in (-\pi/2, \pi/2)$. In summary, bijection depends on both the function **B** and the domain space of **Σ**.

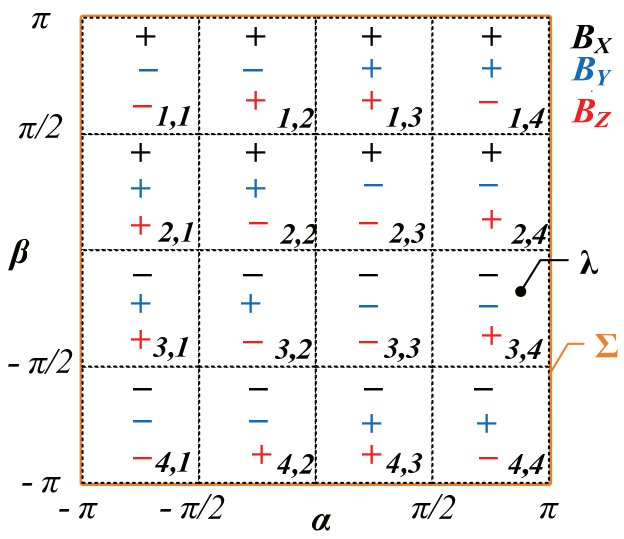

Figure 2-7 Field classification in forward model parametric space **Σ**

2.3 MULTI-SENSOR APPROACH FOR DISTRIBUTED FIELD SENSING

The preceding section and accompanying example investigated the use of field measurements at a point to determine the orientation of a rotating field. Relaxing the restriction of utilizing only single point measurements, this portion generalizes the field sensing approach for a spatial network of sensors in the free space **Ω**. In this generalized case, the function $\boldsymbol{f}$ relates simultaneous position/orientation coordinates $\mathbf{q}$ to corresponding distributed field measurements $\boldsymbol{\lambda}$ in the space **Ω**. To facilitate illustration, only rotary motion of the field is considered. For a network of $2s_T$ sensors, the measurement $\boldsymbol{\lambda}$ is a matrix whose columns are the field measurements by independent sensors and each row denotes the sensing axes. Mathematically, it is defined by

$$\boldsymbol{\lambda} = \begin{bmatrix} f_{X,1}(\mathbf{q}) & f_{X,2}(\mathbf{q}) & \cdots & f_{X,2s_T}(\mathbf{q}) \\ f_{Y,1}(\mathbf{q}) & f_{Y,2}(\mathbf{q}) & \cdots & f_{Y,2s_T}(\mathbf{q}) \\ f_{Z,1}(\mathbf{q}) & f_{Z,2}(\mathbf{q}) & \cdots & f_{Z,2s_T}(\mathbf{q}) \end{bmatrix} = \boldsymbol{f}(\mathbf{q}) \tag{2.24}$$

where $\mathbf{q} = [\alpha, \beta, \gamma]^T$. As observed in the preceding section, the domain of $\mathbf{q}$ plays a significant role in unique correspondence between measurements and orientation. For physical systems such a domain are usually finite continuous interval and can described by $\mathbf{q} \in [\mathbf{q}_l, \mathbf{q}_u]$ where $\mathbf{q}_l$ and $\mathbf{q}_u$ denote the lower and upper limits. To determine if the domain of $\mathbf{q}$ (or subset of $\boldsymbol{\Sigma}$) is bijective in $\boldsymbol{f}$, requires the analysis of the parametric space. Unlike in the singular sensor case the value of $\boldsymbol{\lambda}$ at any arbitrary orientation is a vector, the value of $\boldsymbol{\lambda}$ is a matrix in the forward model parametric space.

As presented using the illustrative example, visual analysis of parametric spaces allows characterization of the space and the field which it represents and offers a means of performing bijection analysis. In this space, the effects of field periodicity in multi source fields, and sensing equivalence in multiple points in physical space $\boldsymbol{\Omega}$ can be more readily illustrated and observed. This facilitates demarcation of the largest domain in the parametric space defined as a segment, where bijection exists. This procedure is highlighted as summarized in Figure 2-8.

With this segment specified in the parametric space, $\boldsymbol{f}^{-1}$ exists and localized mapping can be performed using the inverse model parametric space. Even if a closed form expression for $\boldsymbol{f}^{-1}$ may not be available or conveniently evaluated, artificial mapping tools such as the ANNs and least squares models can be used. Hence the accuracy of segment mapping is sensitive to the mapping tool used, the combination of the inputs, as well as mapping resolution.

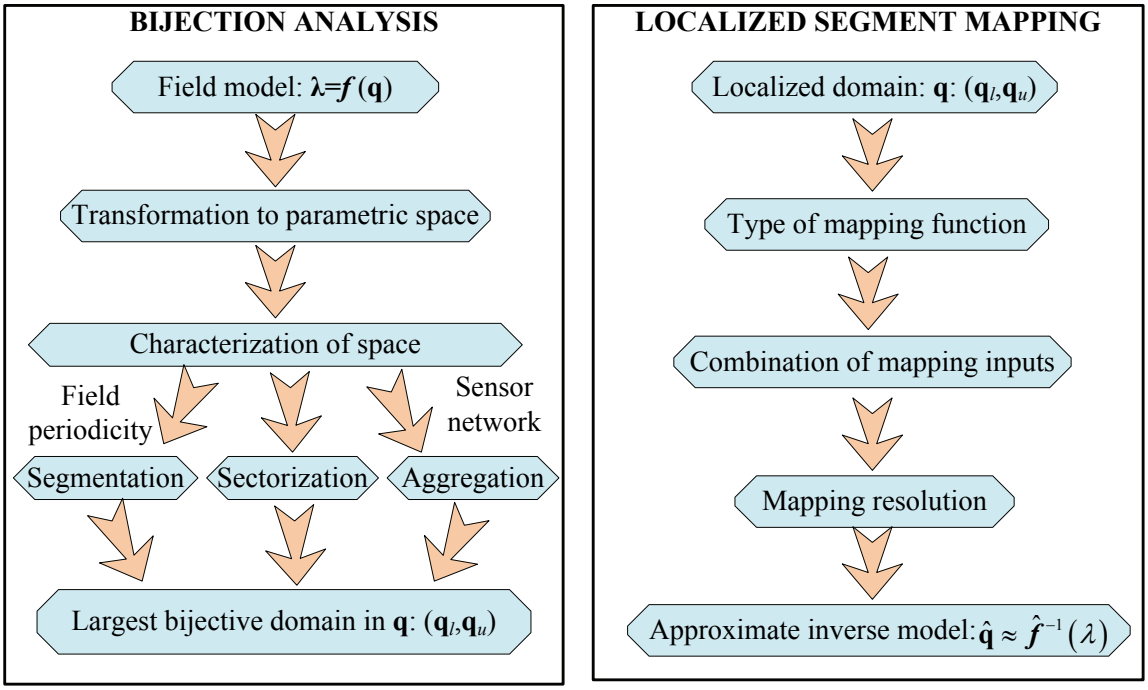

Figure 2-8 Flowchart of bijective field mapping

Due to symmetry of fields, segments can be divided into smaller sectors. By observing the sign of the individual components of $\boldsymbol{\lambda}$, the specific sector which the measurement $\boldsymbol{\lambda}$ is associated with is immediately known. With the approximate inverse model $\hat{\mathbf{q}} = \hat{f}^{-1}(\lambda)$ for that particular sector, the specific spatial location within that sector can be determined. Using both information, sector transformation can be performed to obtain the localized coordinate with the segment and hence the estimated orientation. If the entire parametric space is composed of multiple segments, an indexer is required to keep track of the incremental count of the current segment index. The diagram visually describing this process is shown in Figure 2-9.

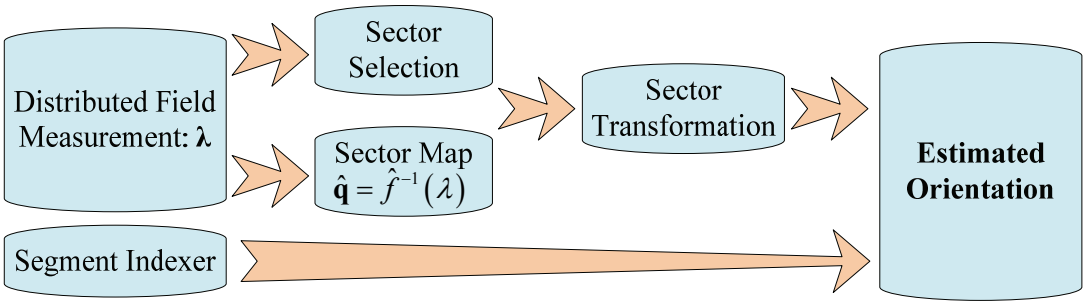

Figure 2-9 Flowchart of online field based sensing

2.3.1 Characterization in Forward Model Parametric Space

Few physical systems contain isolated single magnetic sources and multi-DOF electromagnetic actuators [4][5][6], similar to the one presented in Figure 2-10 feature an assembly of multiple PMs in a concentric pattern on the moving body. As such assemblies have the magnetic sources positioned off the *z*-axis, the spinning motion or change in γ can be detected by sensors in $\mathbf{\Omega}$. However an undesirable effect of such multi-PM configurations is the presence of multiple magnetic sources which introduces periodic nature of the resultant field along the γ spin axis. The approach to tracking moving magnetic fields due to multi-PM assemblies is similar to that of single source fields: Characterization of the forward model parametric space is required. This characterization allows the determination of bijective space. To induce a greater degree of bijection within this space, the dimension of $\boldsymbol{\lambda}$ can be increased by installing more sensors to simultaneously measure multiple locations in $\mathbf{\Omega}$.

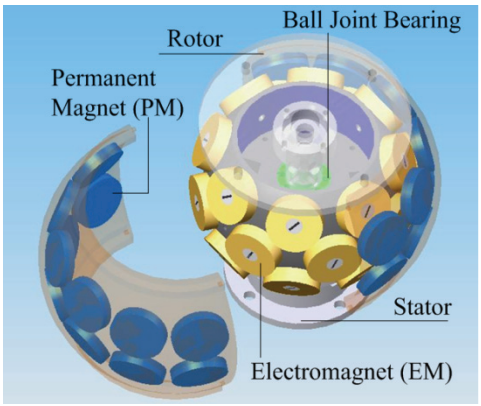

Figure 2-10 Multi-DOF actuator with symmetric assembly of PMs [4]

The following conditions are assumed during field characterization and segregation:

- Motion of the embedded field is rotary in nature. Characterization is presented for up to 3-DOF rotary motion.
- The inherent field sources are in a symmetric configuration which produces a periodic field about the *z*-axis of system. The spatial period is denoted as Φ.
- This field is perfectly periodic and the performance of each sensor is identical. As this is not realizable in actual systems, field calibration is used to compensate for such effects.

To maintain a consistent terminology, the 'rotor' is defined as the moving entity with an assembly of multiple field sources. The 'stator' is the stationary reference frame where field sensors are fixed to and defined from. While the analysis is presented in the context of three degrees of rotational motion, it can be adapted for systems with three degrees of translational motion or even systems with mixed rotational and translational motions. The orientation of the rotor with respect to the reference coordinate system *XYZ*

can be described in Euclidean 3-D space using two conventions: *Euler* angles and *Tait-Bryan* angles. The differences between the two conventions are shown in Figure 2-11 in red and blue respectively. Both notations, however, use one angle to describe the spin of the rotor about the *z*-axis and differ in describing the direction of the *z*-axis.

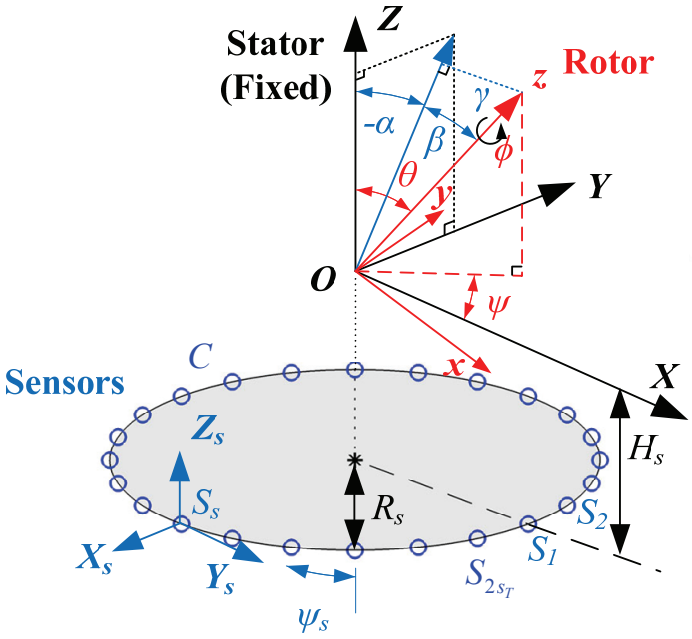

Figure 2-11 Defining the orientation of rotor using two conventions

The stator contains $2s_T$ sensors or s_T sensor pairs (blue circles) spaced equally along a circular path C of radius R_s in a plane parallel to the XY plane as shown in Figure 2-11. This sensor plane is displaced by $-H_s$ along the Z-axis. The s^{th} sensor position in the XYZ plane is

$$\mathbf{S}_s = R_s\left[\cos\left((s-1)\psi_s\right) \quad \sin\left((s-1)\psi_s\right) \quad -H_s\right]^T \tag{2.25}$$

where s=1,2,…, $2s_T$; s_T is a positive integer and $\psi_s = \pi / s_T$ is the angular spacing between adjacent sensors. In addition, there are $2s_T$ sensors to guarantee that each sensor

has an opposite pair on C. The sensors are orientated such that the sensing X_s and Y_s axis of each sensor are normal and tangential to C.

To account for physical constraints pertaining to rotor inclination, the total range of motion of the rotor in terms of Euler and Tait-Bryan angles are

$$0 \le \psi \le \pi \ , \ -\theta_{\max} \le \theta \le \theta_{\max} \ , \ 0 \le \phi \le 2\pi \tag{2.26}$$

$$-\alpha_{\max} \le \alpha \le \alpha_{\max} \ , \ -\beta_{\max} \le \beta \le \beta_{\max} \ , \ 0 \le \gamma \le 2\pi \tag{2.27}$$

where ψ, θ and ϕ specifies location of inclination axis (or y-axis when ϕ=0), the degree of inclination, and spin position of the rotor about the z-axis respectively. In Tait-Bryan notation, α, β and γ denotes the degree of inclination about the x and y axis and spin position of the rotor about the z-axis respectively. The forward parametric space for both notions is visually presented in Figure 2-12. The differences in describing the z-axis by both notations in Figure 2-11 can be more clearly understood by viewing the projection of a unit vector on a z-axis (denoted by **A**) onto the XY plane as shown in Figure 2-13. Hence **A** represents a unique inclination of the rotor. In terms of the Euler angles, **A** is described in fashion similar to polar coordinates where ψ and θ represents the polar angle and 'distance' from origin. Similarly, the Tait-Bryan angles are analogous to Cartesian coordinates.

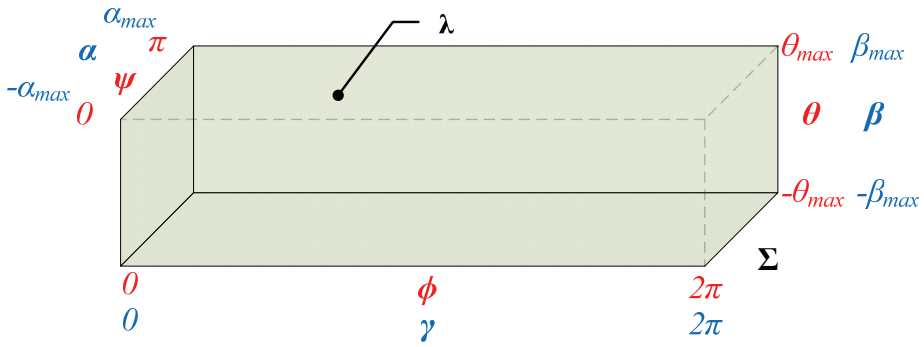

Figure 2-12 Forward parametric space in Euler (red) and Tait-Bryan (blue) angles

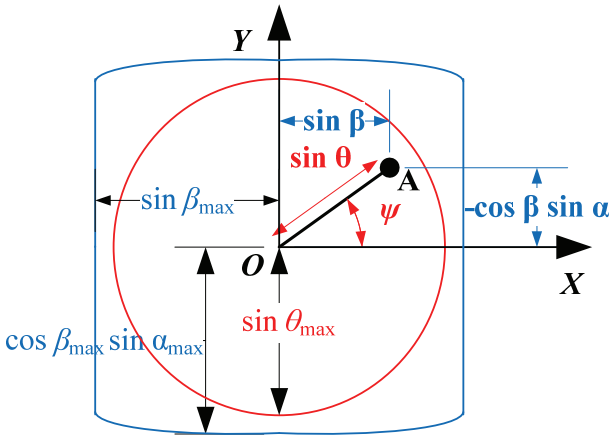

Figure 2-13 Differences in describing the *z*-axis using Euler and Tait-Bryan angles.

For a rotor exhibiting symmetric inclination, which is the case for most actuators, the red circle centered about the origin in Figure 2-13 depicts the allowable range of **A**. In Euler angles, the radius of this circle is sin θ_{max}. The advantage of describing the motion in Tait-Bryan angles is the ability to characterize asymmetrical inclination $\left(\alpha_{max} \neq \beta_{max}\right)$ which is not possible in Euler angles. For limits of α_{max} and β_{max}, the allowable asymmetrical range is illustrated by the blue perimeter. To describe symmetrical inclination in Tait-Bryan angles and relate it to the corresponding expression in Euler angles, the following inequality must hold:

$$\sin^2\beta + \cos^2\beta \sin^2\alpha \leq \sin^2\theta_{max} \tag{2.28}$$

2.3.1.1 Field Segmentation and Sectorization

The presence of field periodicity Φ, which is assumed to exist about the *z*-axis or spin-axis, allows discretization of the 3-D map of the parametric space into equal segments as shown in Figure 2-14. The determination of Φ can be obtained analytically through examination of the configuration of the field sources or experimentally by applying a Fourier Transform to the parametric map. These segments represent the field

periodicity and reduce the uniqueness of the parametric space to a single segment (in this case, the n^{th} segment) whose domain $\boldsymbol{\Sigma}_n$ is demarcated by:

$$0 \le \psi \le \pi, \quad -\theta_{\max} \le \theta \le \theta_{\max}, \quad (n-1)\Phi \le \phi_n' \le n\Phi \tag{2.29}$$

$$-\alpha_{\max} \le \alpha \le \alpha_{\max}, \quad -\beta_{\max} \le \beta \le \beta_{\max}, \quad (n-1)\Phi \le \gamma_n' \le n\Phi \tag{2.30}$$

in Euler and Tait-Bryan angles respectively. The variable n represents the segment index and primes denote the localized coordinate. There are a total of $n_T=2\pi/\Phi$ segments and each segment is indistinguishable from one another. The relationship between field measurements in different segments is defined as

$$\boldsymbol{\lambda}_n(\psi,\theta,\phi) = \boldsymbol{\lambda}_{n+n_1}(\psi,\theta,\phi - n_1\Phi) \tag{2.31}$$

$$\boldsymbol{\lambda}_n(\alpha,\beta,\gamma) = \boldsymbol{\lambda}_{n+n_1}(\alpha,\beta,\gamma - n_1\Phi) \tag{2.32}$$

in Euler and Tait-Bryan angles respectively and n_1 is an integer.

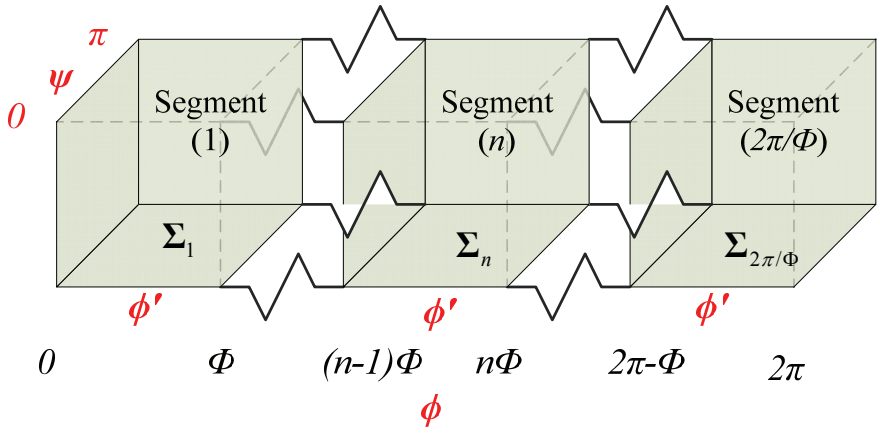

Figure 2-14 Field Segmentation due to periodicity

With a uniform circular distribution of $2s_T$ sensors around the stator and using Euler angles to describe rotor orientation, each segment in Figure 2-14 can be

alternatively and complementary characterized by s_T smaller sub-segments; each with the reduced domain of $\boldsymbol{\Sigma}_{(n,s_T)}$ defined by:

$$(p-1)\pi / s_T \le \psi'_p \le p\pi / s_T \ , \ -\theta_{\max} \le \theta \le \theta_{\max} \ , \ (n-1)\Phi \le \phi'_n \le n\Phi \tag{2.33}$$

where p is a positive integer that represents a reduced sensor pair indexer (p=1,2,…, s_T). This is achieved by exploiting the distribution of the sensors and prior knowledge of the orientation of the z-axis projected onto the XY plane. This is best illustrated by viewing the projection of the unit z-axis vector **A** and sensors onto the XY plane. All possible locations of **A** for a specified segment is demarcated by the red circle of radius sin ($\theta_{\max}$) in Figure 2-15 and denoted by $\boldsymbol{\lambda}_n$. This circle can be divided into $2s_T$ equal wedges whose boundaries coincide with the location of the sensors. Wedges opposite one another constitute one single sub-segment. Comparing two arbitrary locations of the z-axis projection defined by $\mathbf{A_1}(\psi, \sin\theta)$ and $\mathbf{A_2}(\psi+p_1\pi/s_T, \sin\theta)$, which are located in the p^{th} and $(p+p_1)^{\text{th}}$ wedge, with respect to S_p and S_{p+p_1}, both locations are identical. Hence, for any arbitrary θ and ϕ, measurements by multiple sensors for any segment (in this case, the n^{th} segment and between the p^{th} and $(p+p_1)^{\text{th}}$ sensors) are related through

$$\boldsymbol{f}_{(n,p)}(\psi,\theta,\phi) = \boldsymbol{f}_{(n,p+p_1)}(\psi - p_1\pi / s_T,\theta,\phi) \tag{2.34}$$

where p_1 is an integer.

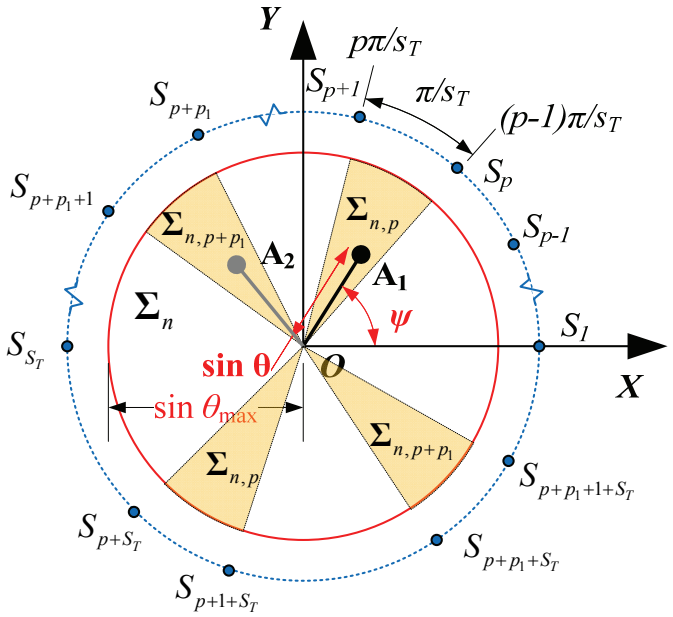

Figure 2-15 Aggregate sensing using multiple sensors

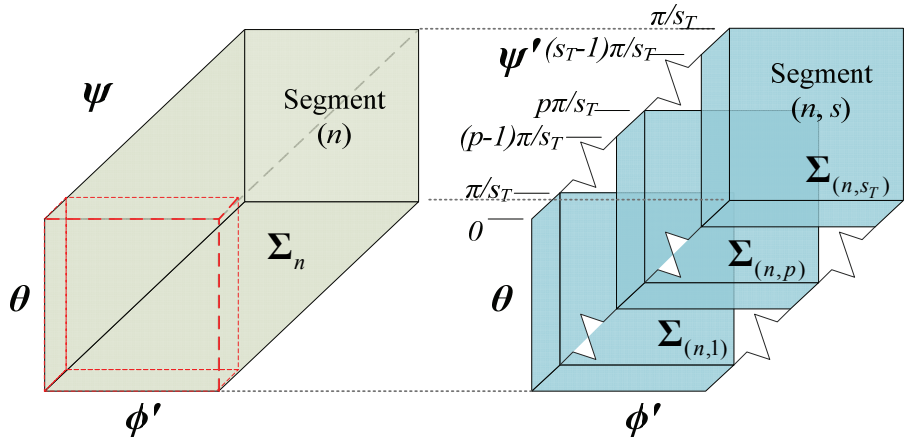

Figure 2-16 Aggregate segmentation due to sensing network

The significance of Equation (2.34) is that $\mathbf{\Sigma}_n$ can be completely characterized alternatively with only one of the wedges $\mathbf{\Sigma}_{(n,p)}$ provided the approximate location of **A** is known. The aggregated characterization of s wedges would produce the entire map as shown in Figure 2-16. The relationship between field measurements between wedges (or the $(n, p)^{th}$ and $(n, p+p_1)^{th}$ segment) can be generalized to the entire sensing assembly as

$$\boldsymbol{\lambda}_{(n,p)}\left(\psi,\theta,\phi\right)=\boldsymbol{\lambda}_{(n,p+p_1)}\left(\psi-p_1\,\pi/s_T,\theta,\phi\right) \tag{2.35}$$

where the composition of $\boldsymbol{\lambda}_{(n,p)}$ is a function of p to ensure Equation (2.35) holds and it is defined as follows:

$$\boldsymbol{\lambda}_{(n,p)}=\begin{bmatrix}\boldsymbol{f}_{(n,p)} & \cdots & \boldsymbol{f}_{(n,2s_T)} & \boldsymbol{f}_{(n,1)} & \cdots & \boldsymbol{f}_{(n,p-1)}\end{bmatrix} \tag{2.36}$$

and for completeness,

$$\boldsymbol{\lambda}_{n}=\boldsymbol{\lambda}_{(n,1)}=\begin{bmatrix}\boldsymbol{f}_{(n,1)} & \cdots & \boldsymbol{f}_{(n,p)} & \cdots & \boldsymbol{f}_{(n,2s_T)}\end{bmatrix} \tag{2.37}$$

As Equations (2.31) and (2.35) are independent, they can be succinctly combined to produce

$$\boldsymbol{\lambda}_{(n,p)}\left(\psi,\theta,\phi\right)=\boldsymbol{\lambda}_{(n+n_1,p+p_1)}\left(\psi-p_1\pi/s_T,\theta,\phi-n_1\Phi\right) \tag{2.38}$$

which relate field measurements between the $(n,\ p)^{\text{th}}$ and $(n+n_1,\ p+p_1)^{\text{th}}$ segment. In summary, the correspondence between the global and localized coordinates of the (n^{th}, p^{th}) segment can be summarized by

$$\begin{aligned}\phi&=\phi_n'+(n-1)\Phi\\ \psi&=\psi_p'+(p-1)\pi/s_T\end{aligned} \tag{2.39}$$

The property in (2.38) greatly simplifies the global 3-D parametric map of the sensing network (in Figure 2-12) to just a single segment (in Figure 2-16). When describing the rotor orientation using Euler angles, there are a total of $n_T \times s_T$ segments compared to n_T segments when using Tait-Bryan notation. It is noted that for all 3-D volumetric parametric maps discussed earlier, the value at any arbitrary $\mathbf{q}$ or $\mathbf{q}_{\text{TB}}$ is a *matrix* containing multisensor multi-axis field components.

Within each segment, the localized map can be demarcated further into smaller sectors by considering only the *magnitude* of $\boldsymbol{\lambda}_n$ or $\boldsymbol{\lambda}_{(n,p)}$ and using the *direction* of $\boldsymbol{\lambda}_n$ or

$\boldsymbol{\lambda}_{(n,p)}$ for sector selection and identification. Again because of the spatial periodicity of the field from a homogenous PM assembly and equivalence of North and South poles of a magnet (magnitude wise), only half of the volumetric segment is unique when considering $\left|\boldsymbol{\lambda}_n\right|$ or $\left|\boldsymbol{\lambda}_{(n,p)}\right|$. A single sector is defined by

$$\begin{aligned} &(p-1)\pi / s_T \le \psi'_p \le p\,\pi / s_T, -\theta_{\max} \le \theta \le \theta_{\max}, \\ &[n-1+(m-1)/2]\Phi \le \phi'_{n,m} \le [n-1+m/2]\Phi \end{aligned} \tag{2.40}$$

where m=1,2,…,m_{T} is the sector referencing index. The collective field measurement matrix for a specific sector is consequently $\boldsymbol{\lambda}_{(n,p),m}$ or $\boldsymbol{\lambda}_{n,m}$ for segments with double and single indices. A visual illustration showing the composition of segments and sectors in the volumetric map as seen from the $\psi\phi$ plane is shown in Figure 2-17. Hence, for a 3-D volumetric matrix map that is complementary characterized using multiple sensors and existence of field periodicity, characterization of any single volumetric segment is sufficient to obtain a localized rotor position (within a segment) and knowledge of the segment indexes (p and n) allows direct correspondence to the global rotor position.

To facilitate segment selection, a kinematic predictor is proposed. This predictor uses the present and past position to estimate the future position in the 3-D volume map of Figure 2-12

$$\mathbf{q}_{(k+1)T} = \mathbf{q}_{kT} + \dot{\mathbf{q}}_{kT}T + \ddot{\mathbf{q}}_{kT}T^2/2 \tag{2.41}$$

where $\mathbf{q}_{kT}$ is the rotor orientation at time=kT and T is the sampling time of the sensors. Using the backward difference equation to numerically estimate $\dot{\mathbf{q}}_{kT}$ and $\ddot{\mathbf{q}}_{kT}$ the kinematic predictor can be simplified to

$$\hat{\mathbf{q}}_{(k+1)T} = 3\mathbf{q}_{kT} - 3\mathbf{q}_{(k-1)T} + \mathbf{q}_{(k-2)T} \tag{2.42}$$

An arbitrary rotor position **q** at time kT can be uniquely associated with a point in a single indexed segment as shown in Figure 2-17. The specific segment can be identified by computing the indexes p and n:

$$n_{kT} = \text{int}\left(\begin{bmatrix}0 & 0 & 1\end{bmatrix}\mathbf{q}_{kT} / 2\pi\right) \tag{2.43}$$

$$p_{kT} = \text{int}\left(\begin{bmatrix}1 & 0 & 0\end{bmatrix}\mathbf{q}_{kT} / \pi\right) \tag{2.44}$$

where int(∗) denotes integer operand on ∗. Combining Equations (2.42) with (2.43) and (2.44) allows for the prediction of the segment indexes at a future time of $t=(k+1)T$.

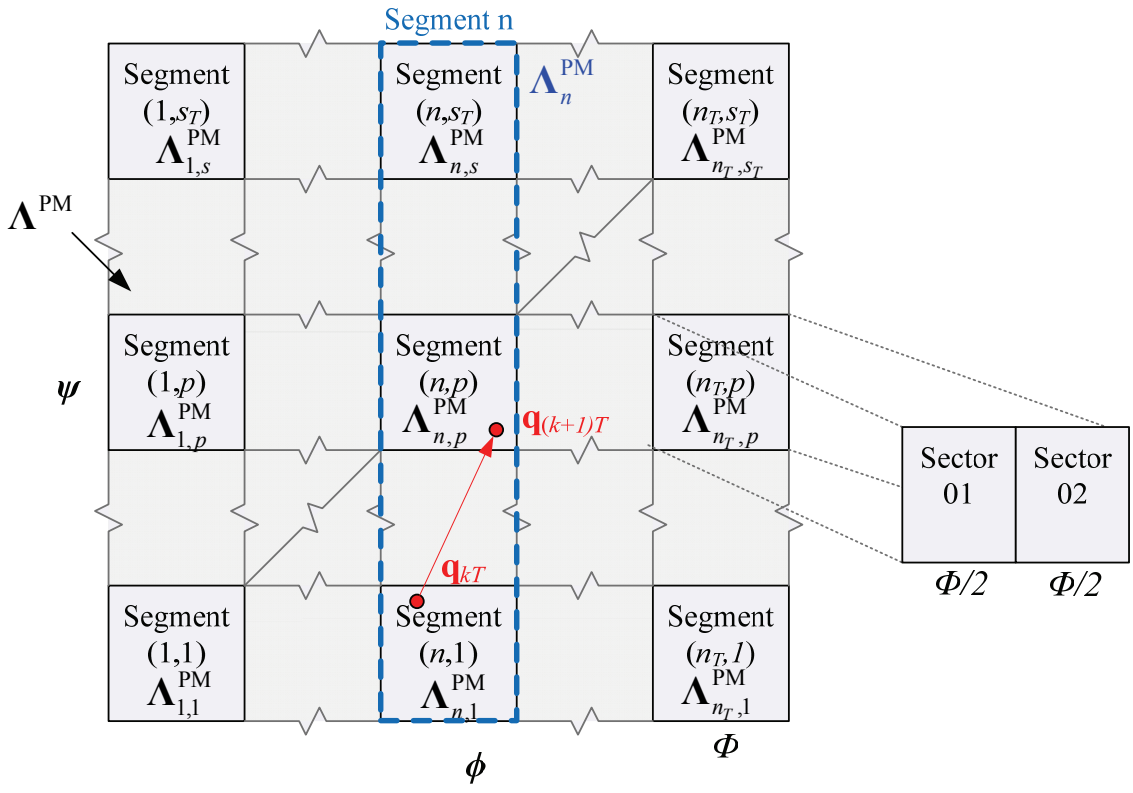

Figure 2-17 Spatial distribution of segments and sectors as seen from $\psi\phi$ plane

2.3.2 Mapping in Inverse Model Parametric Space

As analytical inverse computation of orientation from field measurements using analytical models is not tractable, computationally intensive and unsuitable for real-time

feedback, a function fitting approach is adopted. Such methods include straightforward Look-Up Table (LUT) methods, conventional least squares (LS) using basis functions of polynomials, sinusodials, etc and artificial neural networks (ANN). Both the LUT and LS approaches are more extensively used due to their simplicity, but ANNs are more adaptable when mapping multiple inputs and outputs. In addition, adding hidden layers or nodes has minimal effect on computation time as only arithmetic operations are required during real-time operation of ANN. The main drawback of ANNs is the offline initial training phase which can be time consuming.

Look up tables:

A LUT is a structured data where the location within this data structure contains pre-computed value of the desired output. These locations (known as lattice points) are discrete in nature and computation of the output for non-lattice points are obtained using interpolation methods. Consider a 3-D LUT whose axes represent the independent field measurements (λ_1, λ_2, λ_3) as shown in Figure 2-18. Each point in space is the value of the input field measurements and the numerical value at that location is the corresponding orientation **q**. However, only the value at lattice points (in red) are explicitly known. If λ_1, λ_2 and λ_3 coincides with the lattice point, the orientation is immediately known from the LUT. If not, trilinear interpolation is required to extract the value of **q** using the closest 8 lattice points.

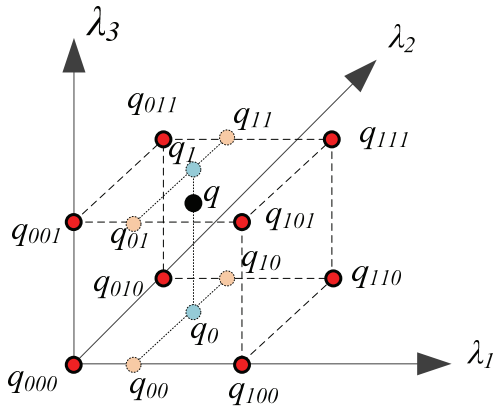

Figure 2-18 Mapping using 3-D LUT and trilinear interpolation

Trilinear interpolation operation can be visualized by locating the 8 corner lattices that surround the point of interest q in parametric space. these corner lattices are q_{000}, q_{100}, q_{010}, q_{110}, q_{001}, q_{101}, q_{011} and q_{111}). Linear interpolation is performed between the following 4 sets of points: (q_{000} and q_{100}), (q_{001} and q_{101}), (q_{011} and q_{111}) and (q_{010} and q_{110}) to obtain the points q_{00}, q_{01}, q_{11} and q_{10} respectively. Executing interpolation on q_{00} and q_{10} as well as q_{01} and q_{11} allows computation of q_0 and q_1. The desired value of q is achieved from a final linear interpolation between q_0 and q_1.

An issue with using LUT with interpolation is the significant increase in complexity in constructing the LUT and performing successive interpolation as the number of independent field measurements increases. For mappings requiring more than 3 axes of independent field measurement, this method becomes memory intensive due to the large array of pre-computed data and requirement of numerous interpolating operations.

Least Squares Models

Another commonly used method in data fitting is least squares. The best fit in the least-squares sense minimizes the sum of squared residuals. A residual is defined as the

difference between a desired observed value and the value provided by a model. A model can be linear or nonlinear and for the single input case, some of the well known models are polynomials and sinusoidals (Fourier series). Like LUT, it is not easily scalable with increased inputs and higher order models. For a system with 3 independent measuring axes (3 inputs) and single output, the number of coefficients required for a linear model (highest power is 1) is 3 (for each of the terms: λ_1, λ_2 and λ_3). For a quadratic model, the number of coefficients increases to 9 (for each of the terms: λ_1^2, λ_2^2, λ_3^2, $\lambda_1\lambda_2$, $\lambda_1\lambda_3$, $\lambda_2\lambda_3$, λ_1, λ_2 and λ_3) and for a cubic model, the total number of coefficients totals to 19 (for each of the terms: λ_1^3, λ_2^3, λ_3^3, $\lambda_1^2\lambda_2$, $\lambda_1^2\lambda_3$, $\lambda_2^2\lambda_1$, $\lambda_2^2\lambda_3$, $\lambda_3^2\lambda_1$, $\lambda_3^2\lambda_2$, $\lambda_1\lambda_2\,\lambda_3$, λ_1^2, λ_2^2, λ_3^2, $\lambda_1\lambda_2$, $\lambda_1\lambda_3$, $\lambda_2\lambda_3$, λ_1, λ_2 and λ_3). Hence, scalability of LS models is an issue. Moreover, these models are limited to a single output. For multiple outputs, independent multiple models must be used.

Artificial Neural Networks

An artificial neural network is a mathematical model that tries to mimic the structure and functional aspects of biological neural networks. Paired with supervised learning, back propagation ANNs can be trained to fit a desired set of inputs to a corresponding set of outputs by iteratively adjusting the weighting coefficients in the network. A commonly used cost function is the mean-squared error which tries to minimize the average squared error between the network's output desired target values over all data pairs. There are two approaches in obtaining the minimum: Gauss-Newton algorithm and the gradient descent method. However, the Levenberg-Marquardt algorithm, which interpolates between both methods, is usually employed. Neural networks are scalable as the general training algorithm is not dependent on the number of

inputs and outputs. The order of the network is easily controlled by the number of hidden layers g and number of hidden nodes within each layer h. A single hidden layer back propagation neural network architecture is shown in Figure 2-19. For any given fully connected back propagation network, the total number of weights in the network W is given by

$$W = \left(m_{in} + m_{out}\right)h + \left(g-1\right)h^2 \tag{2.45}$$

where m_{in} and m_{out} are the number of inputs and outputs of the ANN.

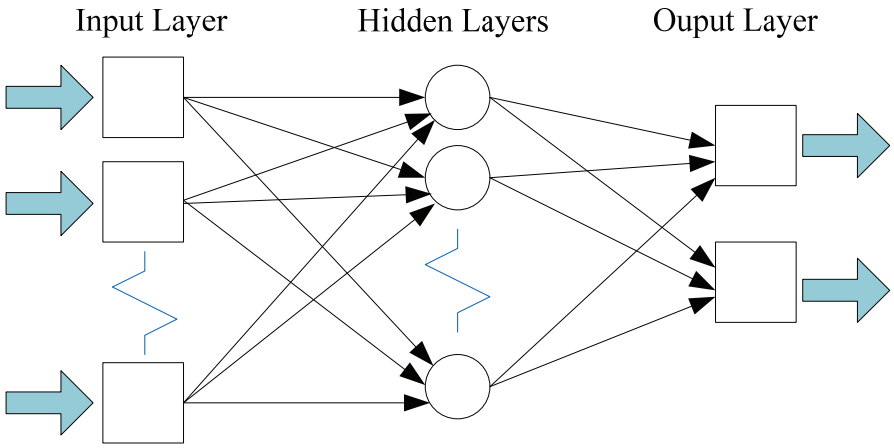

Figure 2-19 Back propagation artificial neural network

In order to map field measurements $\boldsymbol{\lambda}$ to the angular positions of $\mathbf{q}$ or $\mathbf{q}_{TB}$, the entire and sectionalized segments or sectors volume map is discretized into a $N_1 \times N_2 \times N_3$ spatial grid, resulting to total of $N_1\ N_2\ N_3$ training-target sets. These sets are then used to construct LUTs, design LS models or train ANNs. Clearly, the resolution of this map has a direct impact on the mapping accuracy. For field mapping using the ANN, 80% of the sets will be used for training, 15% for validation and 5% for testing. For this application, the inputs of the neural network (g hidden layers, h hidden nodes per hidden layer) are

field measurements by all sensors and the outputs are the target position. This can be mathematically represented in Equation (2.46)

$$\hat{\mathbf{q}}_v = \mathbf{NN}_{g,h}\left(\lambda_{(n,p),m}(v)\right) \tag{2.46}$$

where v is an integer representing the training set index ($1 \le v \le N_1 N_2 N_3$), and $\hat{\mathbf{q}}_v$ is the angular estimates of the neural network. The mean squared error (MSE) is used to evaluate of the performance of a neural network and is expressed as:

$$\text{MSE} = \frac{1}{N_1 N_2 N_3} \sum_{v=1}^{N_1 N_2 N_3} \left(\psi_v - \hat{\psi}_v\right)^2 + \left(\theta_v - \hat{\theta}_v\right)^2 + \left(\phi_v - \hat{\phi}_v\right)^2 \tag{2.47}$$

The domain of the mapping depends on the field characteristics of the rotor assembly. If no periodicity is assumed or present, the domain of the ANN mapping will be the entire volume in Figure 2-12. With periodicity and/or multisensor aggregation, field segmentation reduces the required domain to just a segment or a sector if field symmetry is considered. The number of segments and mapping domains for these cases are compiled in Table 2-1.

Table 2-1 Differences in mapping domain from types of field characteristics

Field characteristics	None	Segmentation	Aggregation	Segmentation & Aggregation
No. of segments	1	$2\pi/\Phi$	s_T	$2\pi s_T/\Phi$
Mapping domain	$0 \le \psi \le \pi$ $-\theta_{\max} \le \theta \le \theta_{\max}$ $0 \le \phi \le 2\pi$	$0 \le \psi \le \pi$ $-\theta_{\max} \le \theta \le \theta_{\max}$ $0 \le \phi \le \Phi$	$0 \le \psi \le \pi / s_T$ $-\theta_{\max} \le \theta \le \theta_{\max}$ $0 \le \phi \le 2\pi$	$0 \le \psi \le \pi / s_T$ $-\theta_{\max} \le \theta \le \theta_{\max}$ $0 \le \phi \le \Phi$
Mapping domain (with sectors)		$0 \le \psi \le \pi$ $-\theta_{\max} \le \theta \le \theta_{\max}$ $0 \le \phi \le \Phi / 2$	$0 \le \psi \le \pi / s_T$ $-\theta_{\max} \le \theta \le \theta_{\max}$ $0 \le \phi \le \pi$	$0 \le \psi \le \pi / s_T$ $-\theta_{\max} \le \theta \le \theta_{\max}$ $0 \le \phi \le \Phi / 2$

While the discussion in the prior sections has been focused on a system with 3-DOFs, the direct field sensing methodology is extensible to other DOFs. For the 2-DOF case, there are two possible types of motion: dual inclinations and single inclination with spinning motion. In both cases, the field map is no longer a volume (3-DOF) but now a surface as there are only 2 independent DOFs. As with the 2-DOF case, there are two possible types of motion for 1-DOF case: only spin or only inclination. The field map is reduced further a single dimension lines. A summary of the differences between 1, 2 and 3-DOF parameters is shown in Table 2-2.

Table 2-2 Differences in parameters for 1, 2 and 3-DOF sensing systems.

	1-DOF		**2-DOF**		**3-DOF**
Motion	Spin	Inclination	Inclination & spin	Dual inclination	Unrestricted inclination & spin
$\mathbf{q}$ =	ϕ or ψ	θ	$[\theta, \phi]^T$	$[\psi, \theta]^T$	$[\psi, \theta, \phi]^T$
$\mathbf{q}_{TB}$ =	γ	α or β	$[\alpha, \gamma]^T$ or $[\beta, \gamma]^T$	$[\alpha, \beta]^T$	$[\alpha, \beta, \gamma]^T$
Range of Motion	$0 \le \phi \le 2\pi$	$-\theta_{max} \le \theta \le \theta_{max}$	$-\theta_{max} \le \theta \le \theta_{max}$ $0 \le \phi \le 2\pi$	$0 \le \psi \le \pi$ $-\theta_{max} \le \theta \le \theta_{max}$	$0 \le \psi \le \pi$ $-\theta_{max} \le \theta \le \theta_{max}$ $0 \le \phi \le 2\pi$
	Line		Surface		Volume
Field Map			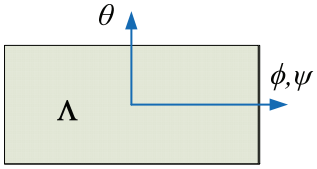		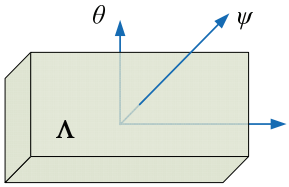

2.3.3 Relationship between Sensor Maps

In 2-DOF motion, field measurements of the moving rotor by a stationary sensor to create a map in forward parametric space can be alternatively perceived as the map obtained if the rotor was stationary and the sensor was in motion. Either way, this map represents a unique measurement which relates the position of the sensor with respect to the rotor PM surface. As all sensors are arranged in a systematic manner around the rotor,

the field maps by multiple sensors are geometrically related. In addition, it is worth nothing that the normal component (X-component) of the field measurement of any sensor is independent of the rotation of the field about the sensor. This equivalence allows construction of the normal component of multiple sensor maps with only one sensor map. The extension of this equivalence is that from this 2-D field map (of 2-DOF motion), the corresponding 3-D field map (of 3-DOF motion) can be constructed. As a result, this relationship permits real time diagnosis of sensors to determine faulty sensors as well as allowing the construction of 3-D field maps from experimentally obtained 2-D field maps.

Consider a complete field map of the normal component of the field measurements at S_1 has been obtained. For a given inclination θ and spin position ϕ of the rotor, the field measurement by S_1 can be obtained using the field map and using the values of θ and ϕ as Cartesian coordinates in the 2-D field map. As the field map of S_1 uses spherical coordinates, the map can be visualized as a sectionalized part of a sphere. For an arbitrary rotor inclination and spin as shown in Figure 2-20, the instantaneous normal component of the field measurements of S_1 and S_2 are different due to the spatial positional differences between sensors. However, the measurement by S_2 at this rotor orientation is present in the field map of S_1 albeit at a different spatial location on the map. Hence, it is possible to estimate the field measurement at S_2 using only known measurements of S_1.

Denoting the primes as coordinates of the respective sensors on the field map when the inclination is zero for any angular spin position, it can be seen geometrically that the instantaneous measurement of S_2 is spatially related to the corresponding

measurement of S_1 through the spatial shifts of $\phi_{2,1}$ and $\theta_{2,1}$ on the field map of S_1. The blue path designates the relative position of S_2 as the degree of inclination is increased. As seen in Figure 2-20, this path is not straight in the field map of S_1. Computation of these spatial shifts can be obtained by locating S_2 with respect to the moving *xyz* axis and computing the equivalent spherical coordinates representation to obtain the spatial shifts.

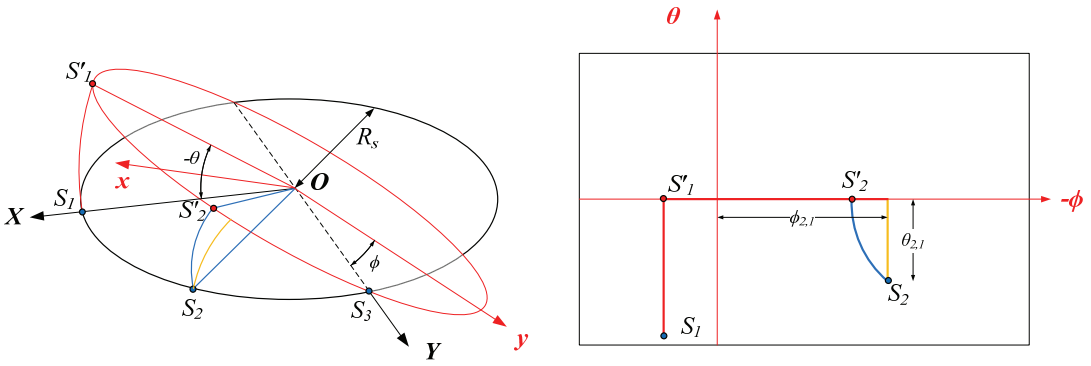

Figure 2-20 Left: spatial relationship between sensors, Right: Field map of S1.

The coordinates of S_2 with respect to the moving *xyz* system are

$$\begin{bmatrix} x \\ y \\ z \end{bmatrix}_{S_2} = \begin{bmatrix} \cos\phi & \sin\phi & 0 \\ -\sin\phi & \cos\phi & 0 \\ 0 & 0 & 1 \end{bmatrix} \begin{bmatrix} \cos\theta & 0 & -\sin\theta \\ 0 & 1 & 0 \\ \sin\theta & 0 & \cos\theta \end{bmatrix} \begin{bmatrix} X \\ Y \\ Z \end{bmatrix}_{S_2} \tag{1.48}$$

Transforming these coordinates into equivalent spherical coordinates with respect to the Cartesian *xyz* coordinates allows the determination of the coordinate of S_2 in the field map of S_1.

$$\theta_{2,1} = \cos^{-1}\left(z_{S_2} / R_s\right) - \pi/2 \tag{1.49}$$

$$\phi_{2,1} = \tan^{-1}\left(y_{S_2} / x_{S_2}\right) \tag{1.50}$$

Using the above relationship, the field map of S_2 can be reconstructed using a complete field map of S_1. For every set of θ and ϕ in the field map of S_1, the corresponding

measurement of S_2 is directly obtained by the spatial shifts $\phi_{2,1}$ and $\theta_{2,1}$ in the field map of S_1. Since the field map may be discrete in nature (such as those obtained experimentally), the computed values of S_2 using the field map of S_1 and the spatial shifts require 2-D interpolation. As this relationship is one-to-one, the inverse of this procedure allows the reconstruction of the field map of S_1 from the complete field map of S_2. However, due to the position of S_2, the entire map of S_1 is not reconstructable solely from the field map of S_2. This is due to the position of S_2, which covers a smaller surface area of the rotor as compared to S_1 for a pre-defined range of θ. The ratio of $\theta_{2,1}$ / θ characterizes the amount of the map that can be reconstructed and is a function of the angular spacing between sensors. This relationship is graphed in Figure 2-21. At an angular spacing of 45°, the ratio is 0.71 and monotonously decreases with larger angular spacing where it is zero at 90°.

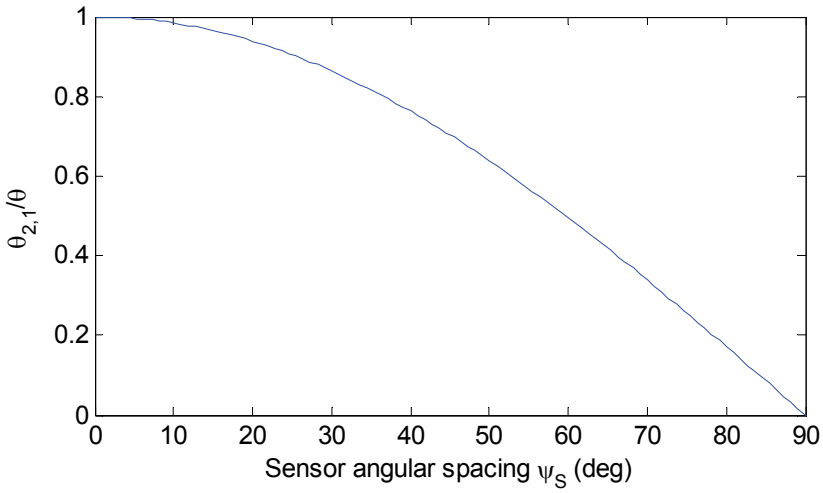

Figure 2-21 Reconstruction ratio as a function of sensor angular spacing.

The approach used can also be used to construct the entire 3-D map from a single 2-D map of the sensor. The coordinates of S_1 with respect to a moving xyz system in 3-DOF are

$$\begin{bmatrix} x \\ y \\ z \end{bmatrix}_{S_1} = \begin{bmatrix} \cos\phi & \sin\phi & 0 \\ -\sin\phi & \cos\phi & 0 \\ 0 & 0 & 1 \end{bmatrix} \begin{bmatrix} \cos\theta & 0 & -\sin\theta \\ 0 & 1 & 0 \\ \sin\theta & 0 & \cos\theta \end{bmatrix} \begin{bmatrix} \cos\psi & \sin\psi & 0 \\ -\sin\psi & \cos\psi & 0 \\ 0 & 0 & 1 \end{bmatrix} \begin{bmatrix} X \\ Y \\ Z \end{bmatrix}_{S_1} \quad (1.51)$$

Transforming these coordinates into equivalent spherical coordinates with respect to the Cartesian *xyz* coordinates using Equations (1.49) and (1.50) allows the determination of the coordinate of S_1 in the field map of S_I. Using this relationship, the 3-D field map of S_1 can be reconstructed using a complete 2-D field map of S_I. The set of ψ,θ,ϕ in the required 3-D field map of S_I is directly obtained by the spatial shifts in the existing 2-D field map of S_I.

2.4 PHYSICAL SENSING CONSIDERATIONS

Field segmentation and aggregation reduces the required characterization to any single segment. Within this segment, the field must be proficiently measured by sensors which possess sensing limitations as well as maintain a high signal to noise ratio (SNR) to minimize unsolicited noise effects which compromises mapping performance. Table 2-3 evaluates a handful of magnetic sensors available in the industry today used for magnetic flux density measurements. The operating principles employed by majority of the sensors are Hall-effect, Giant magnetoresistance (GMR) and Anisotropic magnetoresistance (AMR). These sensors are available in single and multi-axis editions and most importantly of all, exhibit different sensing sensitivities and ranges.

Armed with these sensing specifications, for a pre-defined location and orientation of sensors, analytical magnetic field models (such as the DMP model) can be used to simulate and generate the predicted fields at these desired sensing locations. The field range encountered at these areas can be used to meticulously select the sensors that

would fully utilize its entire sensing range without saturation. Alternatively, the sensors can be carefully preselected to meet cost or bandwidth stipulations and instead regulate the position and orientation of the sensors to ensure the entire sensing range is exploited. In such cases, low field sensors such as the Honeywell HMC1043 sensor need to be placed further away from PMs to avoid saturation while strong field sensors such as the Asahi HG-362A can be positioned close to PMs with no saturation effects. While low field sensors are more susceptible to stray background field effects, their high sensitivity is invaluable in micro/nano-scale PM configurations and assemblies where the magnetic fields are weaker and not detectable in strong field sensors.

Table 2-3 Specifications of various types of industrial magnetic sensors

Manufacturer	Model	Type	Polarity	Sensing Axes	Sensitivity (mV/mT)	Range (mT)	Bandwidth (kHz)	Price
Allegro	A1301	Hall	Bipolar	one	25	± 100	20	$1.14
Asahi	HG-362A	Hall	Bipolar	one	2.5	± 2000	100	$1.58
Ametes	MFS-3A	Hall	Bipolar	three	280	± 7.3	100	$24
NVE	AA003-02E	GMR	Unipolar	one	320	1.4	1000	$7.85
Honeywell	HMC1043	AMR	Bipolar	three	100	± 0.6	5000	$40

2.4.1 Field Calibration

As noted earlier, the premise of field segmentation relies on the indistinguishable measured fields among segments. A direct method to compensate for the inevitable experimental field variation between segments is to implement affine transformation (AT) on field measurements of all segments with respect to a chosen ‘reference’ segment. For single axis sensors, the AT consists of scaling and translation factors. These factors will be chosen through optimization such that the field measurements in transformed segments will resemble the reference segments in the least squares sense.

The segment AT of the n^{th} segment of the s^{th} sensor can be expressed by

$$\widehat{\mathbf{B}}_{(n,s)} = \mathbf{a}_{n,s}\mathbf{B}_{(n,s)} + \mathbf{b}_{n,s} \tag{2.52}$$

where $\mathbf{a}_{n,s}$ and $\mathbf{b}_{n,s}$ are the linear transformation and translational factors of the AT for n^{th} segment of the s^{th} sensor. These factors are optimally chosen such that the following error function is minimized

$$\left\| \widehat{\mathbf{B}}_{(n,s)} - \overline{\mathbf{B}}_{(r,s)} \right\|_2^2 \tag{2.53}$$

where $\overline{\mathbf{B}}_{r,s}$ is the least squares or ANN fitted model of the r^{th} segment of the s^{th} sensor.

In aggregate multi-sensing, the sensing similarity among sensors permitted the reduction of the domain required for segment mapping. However, sensing variation can occur between seemingly identical sensors which can be attributed to sensor mis-positioning, misalignment or inherent manufacturing related differences between sensors. As with field variation between segments, the approach of using affine transformation to calibrate and 'standardize' measurements across sensors is adopted.

Similarly, the sensor AT of the s^{th} sensor with respect to a reference sensor for any segments in that sensor can be expressed by

$$\tilde{\mathbf{B}}_{(n,s)} = \mathbf{c}_s\widehat{\mathbf{B}}_{(n,s)} + \mathbf{d}_s \tag{2.54}$$

where $\mathbf{c}_s$ and $\mathbf{d}_s$ are the linear transformation and translational factors for the s^{th} sensor. These factors are optimally chosen such that the following error function is minimized

$$\left\| \tilde{\mathbf{B}}_{(r,s)} - \overline{\mathbf{B}}_{(r,r)} \right\|_2^2 \tag{2.55}$$

where $\overline{\mathbf{B}}_{r,r}$ are the least squares or ANN fitted model of the reference segment in the reference r^{th} sensor.

2.5 SUMMARY

Employing pre-existing embedded fields for sensing has numerous advantages and a method to use distributed field measurements for orientation sensing has been presented. This methodology addresses the difficulties encountered in magnetic inverse problems of high non-linearity and non-uniqueness through analysis and characterization of the forward parametric space. For an assembly of identical PMs, due to field symmetry and periodicity and meticulous placement of sensors, only a fraction of the mappable parametric space is unique and suitable for defining unique correspondence between measurements and orientation. In addition, this approach is model-independent and uses a computationally swift function fitting approach to directly map measurements to orientation of the system which permits lag-free positional determination for real-time feedback control. Since perfect symmetry and periodicity do not exist in actual implementation, a statistical calibration approach is employed to compensate for field variation between PM sources and sensors. An in-depth analysis of using a network of sensors to detect a multi-source field is experimentally investigated in the next chapter.

CHAPTER 3

EXPERIMENTAL ANALYSIS OF MULTI-SOURCE MAGNETIC FIELDS FOR POSITIONAL SENSING

3.1 OVERVIEW

Physical fields exhibit symmetry and in systems with multiple magnetic field sources, field periodicity occurs. While analytical and theoretical models predict perfect symmetry and periodicity, in actual implementation and experimentation, due to physical imperfections and sensing noise, these occurrences usually do not materialize. From the previous chapter, the field sensing methodology relies on the field periodicity inherent from an assembly of field sources and equivalence of measurements from multiple sensors. This chapter seeks to experimentally investigate these assertions and their corresponding effects on mapping accuracy using magnetic fields. This investigation is done on a platform which contains a symmetric arrangement of permanent magnets which is present in many single-DOF rotary systems such as DC and stepper motors.

Of particular interest is the statistical variation in field measurement due to different field sources (PMs) and sensors. The approach of statistical standardization using affine transformation is used as a practical means to compensate for these variations. This investigation is divided into two parts: the first part focusing on field variation from measuring multiple PM sources from the same sensor and the second studies the corresponding field variation of measuring the same sources between sensors.

3.2 FIELD PERIODICITY FROM MULTIPLE SOURCES AND SENSORS

Using 24 similarly graded (N35) neodymium rare-earth cylindrical PMs (axially magnetized) and 24 large range Galium Arsenide (GaAs) single axis Hall-Effect magnetic sensors (Asahi HG-362A), the field measurements of multiple PMs by multiple sensors were collected and statistically analyzed. These measurements are used to relate position to produce field-position correspondence and mapping for a magnetic field-based sensing for a single-DOF system with multiple field sources.

3.2.1 Experimental Setup

As shown in Figure 3-1, the 24 PMs are arranged in a circular fashion onto a movable rotor with a single DOF (spinning motion). The *xyz* and *XYZ* axes represent the moving (rotor) and fixed (sensors) reference frames. The angular spacing between PMs is ϕ_R and every PM is R_R from the axis of rotation (*Z*-axis). The PMs are numerically indexed in a counterclockwise manner with the midpoint between PM_1 and PM_{24} coincident with the rotor *x*-axis (and the midpoint between PM_{18} and PM_{19} coincident with the *y*-axis) and they are orientated such that their magnetization vector is parallel to the negative *Z*-axis (Red surfaces denote south poles of the PMs). As a result, the spatial periodicity Φ of this assembly is 15°. The sensors (denoted by circles) are distributed around a circular path as discussed in the previous chapter. These single-axis sensors are orientated such that the measuring axes are coincident with the *Z*-axis. The rotor containing the PM assembly is rotated about a fixed shaft using a DC stepper motor (Motor: PMI Motion Technologies USS75B SynchroStep DC step motor, Stepper Drive: PMI Motion Technologies BSD-40 bipolar chopper drive) via a pinion and gear

assembly. The stepper motor and drive setup are rated at 400 steps/rev during half-step mode (200 steps/rev during full-step mode) and the gear ratio between the pinion and gear is 4:1; hence, a complete revolution of the rotor would require 1600 steps (0.225° effective step resolution). A ball screw provides accurate adjustment between the separation H_s between the PMs and sensors. This adjustment allows the investigation of the field variation where the aspect ratio ρ is close to unity. The complete setup is illustrated in Figure 3-2. The physical dimensions and magnetization strength of the PMs are compiled in Table 3-1 along with the corresponding DMP model used to analytically model the field of each PM. The setup's physical parameters are tabulated in Table 3-2.

Table 3-1 PM and corresponding DMP parameters

PM			DMP			
Radius (mm)	Length (mm)	Magnetization (T)	Characteristic length (mm)	No of dipoles	No of loops	Dipole strength (A/m)
4.7625	12.7	1.1	9.1021	6	1	-1.340×10^{-6} 2.030×10^{-5}

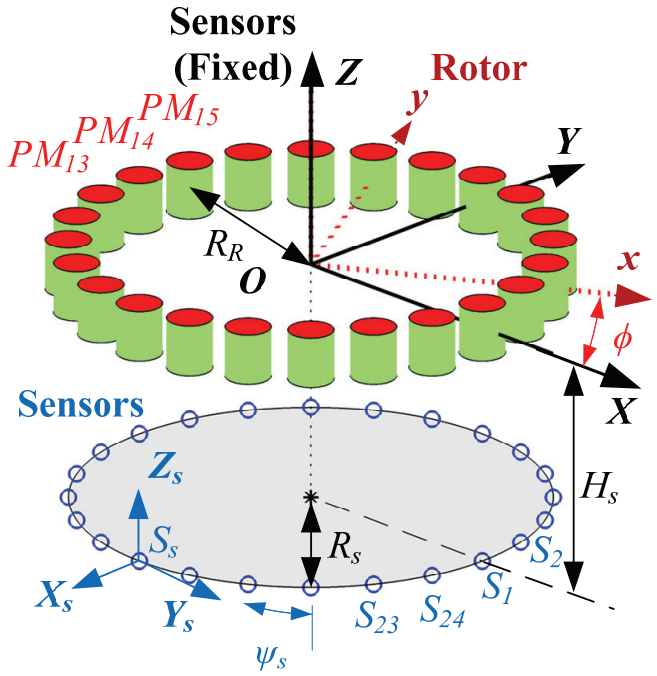

Figure 3-1 Rotating multi-PM assembly and stationary sensor placements

Table 3-2 Experimental physical dimensions and parameters

Rotor PMs			**Sensors**			
No. of PMs	R_R (mm)	ϕ_R (deg)	$2S_T$	R_S (mm)	ψ_s (deg)	H_s (mm)
24	49.53	15	24	49.53	15	9.517

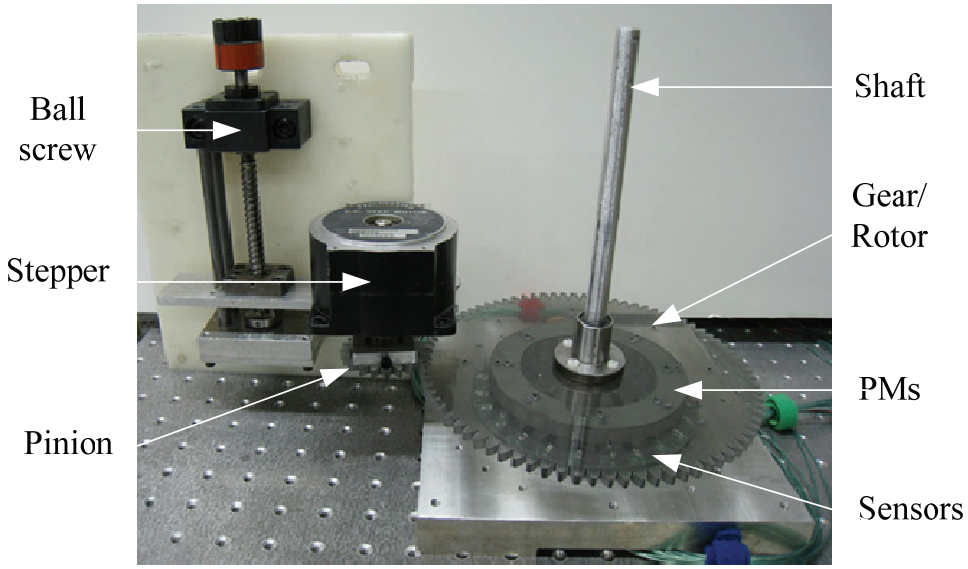

Figure 3-2 Experimental setup used for investigation of field characteristics

The electrical and communication schematics of the setup are presented in Figure 3-3. The outputs of the magnetic sensors, which are powered by a 8V DC power supply (HP 6236B triple output power supply), are transmitted in analog format as voltages and digitally acquired using 24 independent and dedicated 16-bit (15-bit signed format) Delta Sigma analog to digital converter (ADC) banks (aggregated using four Turck Inc. BL20-4AI-U/I and two Turck Inc. BL20-2AI-U). A sensing/actuation gateway (SAG) (Turck Inc. BL20-PG-EN) comprising of a 32-bit Reduced Instruction Set Computer (RISC) and 100BASE-TX Ethernet connectivity is attached to the ADCs and digital to analog converter (DAC) banks (aggregated using two Turck Inc. BL20-2AO). Field measurements by the sensors are communicated to a Human Machine Interface (HMI) (Turck Inc. Turckeye) and a PC over Ethernet connection to provide instantaneous

display and data logging capabilities. A custom C program running on the PC can collect measurements and automatically increment the stepper motor by transmitting transistor–transistor logic (TTL) signals to the stepper drive, which is powered by a 20 V DC power supply (Kepco BOP 50-4M bipolar operational power supply) via the DAC.

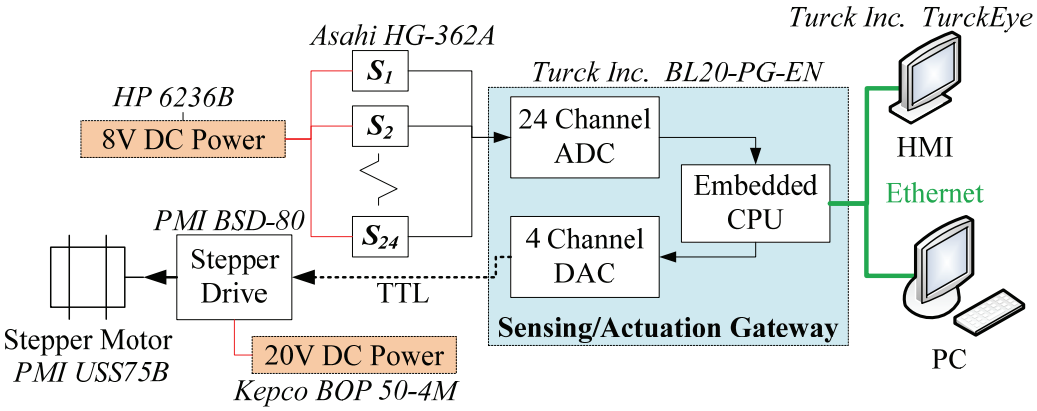

Figure 3-3 Electrical and communication schematics

3.3 Field Characterization of Multiple PMs

By using the stepper drive to increment the angular position of the entire PM assembly (ϕ), the field measurements by all 24 sensors can be recorded at every spatial increment step. Figure 3-4 shows the field measurements in the Z-direction of all 24 PMs by sensor S_1 along with the predicted field measurements using the DMP model. As this a single-DOF system, Figure 3-4 also represents the forward parametric space of the system. The first trough at ϕ=7.5°, corresponds to the proximity of PM_1's magnetization axis while the adjacent trough at ϕ=22.5°, is due to the proximity of PM_2 and so forth. A number of critical observations can be drawn by comparing the DMP field model and experimental field,

- The actual strength of the magnetic fields near the PM's magnetization axes are weaker, and
- More importantly, while the DMP model assumes indistinguishability between the magnetic fields of PMs, in actual experimentation, there exists variation between the magnetic fields of the PMs which can be attributed to physical imperfections. These imperfections result in field variation among segments.

A total of 24 troughs are present and each trough corresponds to a specific PM or segment index as discussed in the preceding chapter. With this knowledge, the measurements by S_1 in different segments (or due to the proximity of specific PMs) can be isolated. Figure 3-5 depicts the field measurements by four consecutive segments as collected from S_1. Each segment (demarcated by $(n-1)\Phi \le \phi \le n\Phi$) can be further segregated into 2 equally sized sectors as observed in Figure 3-5. The variation in the field measurements in all segments is compared in Figure 3-6 by using the localized spin coordinate. Visual inspection suggests that the measurement variation is more significant at the troughs (at center of PMs, middle of segments) than the peaks (in between PMs, boundaries of segments) and this is reflected in all sensors. The reason is primarily due to natural variation of the magnetization strength in different PMs (despite being identically graded) which is accentuated at the troughs where the sensors are closest to each PM. As the magnetic fields in between the magnets are substantially weaker, the variations at the peaks are less noticeable.

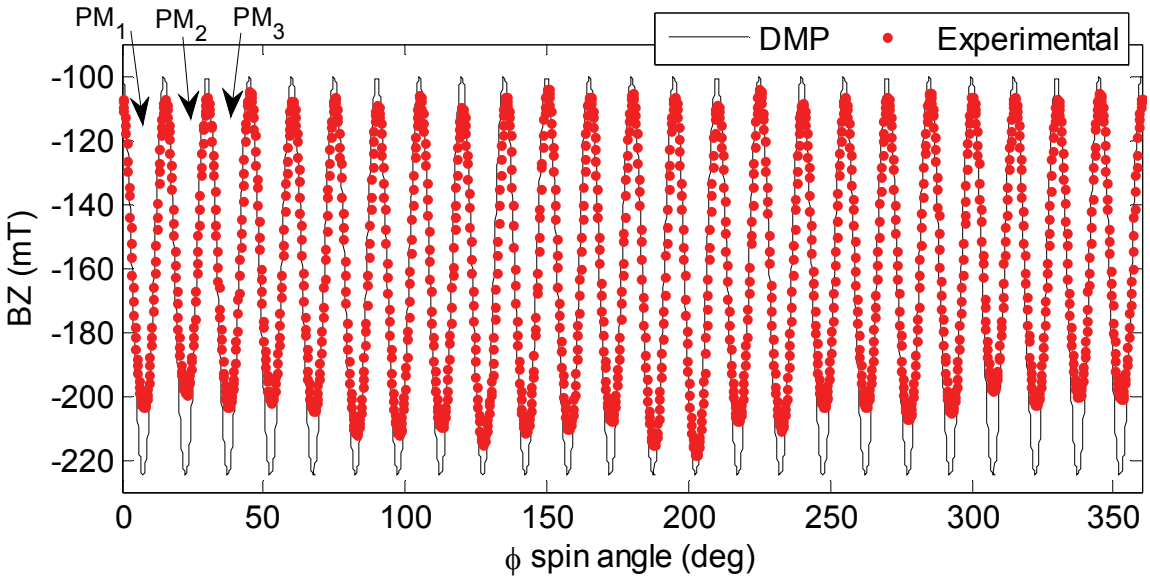

Figure 3-4 Measured and DMP predicted field as a function of rotor rotation by S_1

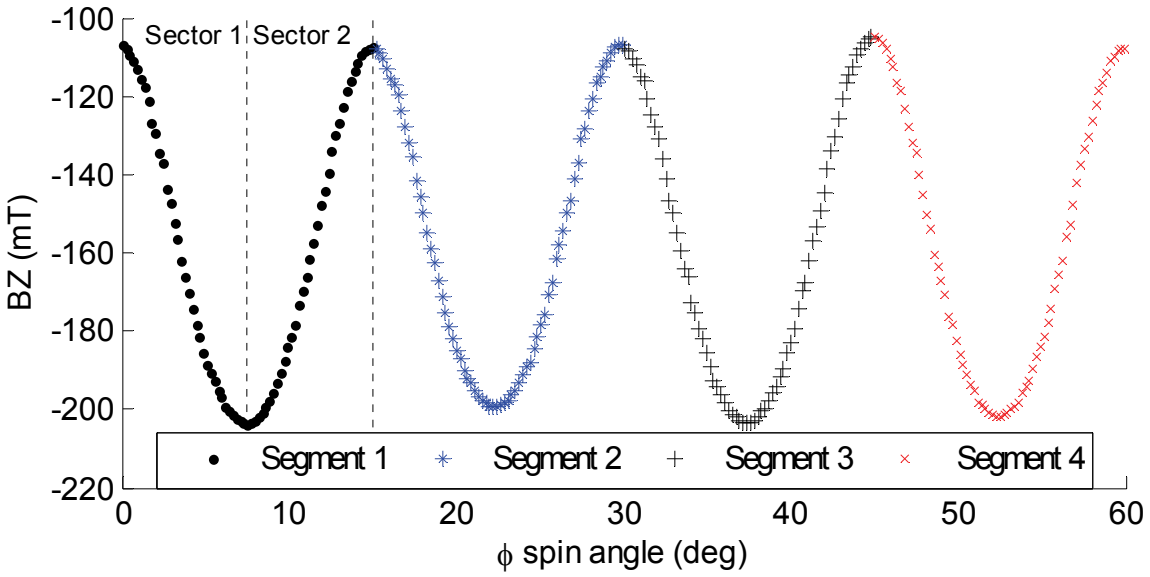

Figure 3-5 Variation in measured field from four different segments by S_1

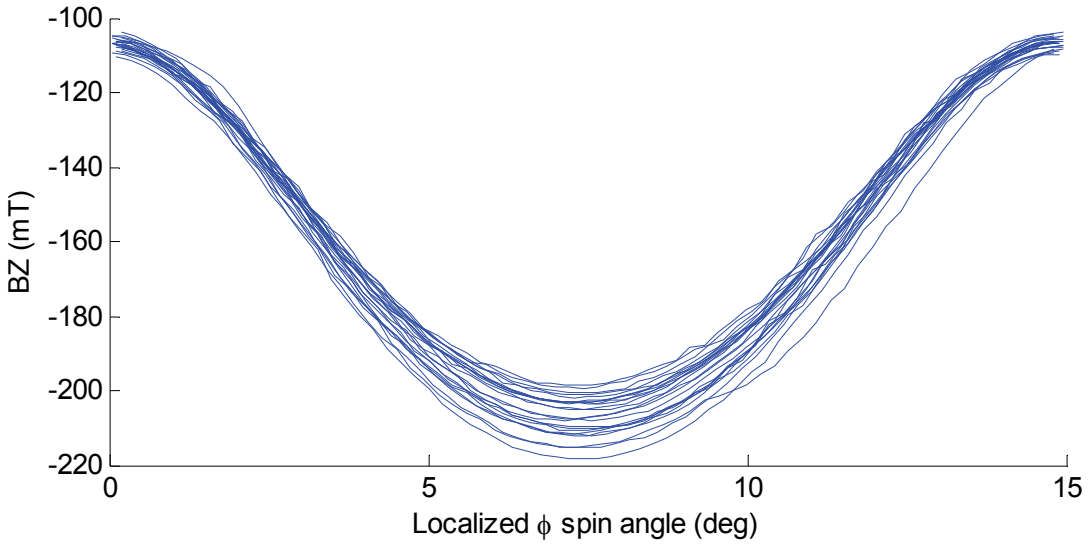

Figure 3-6 Variation in measured field from all segments by S_1

3.3.1 Segment Field Calibration

As noted earlier, the premise of field segmentation relies on the indistinguishable measured magnetic fields among segments. A direct method to compensate for the inevitable experimental field variation between PMs (or segments) is to implement affine transformation (AT) on field measurements of all segments with respect to a chosen 'reference' segment. For a single-DOF case, the AT consists of scaling and translation factors. These factors will be chosen through optimization such that the field measurements in transformed segments will resemble the reference segments in the least squares sense.

As the measurements in all segments contain experimental sensing noise, a model of the field for the reference segment (r^{th} segment) should be constructed using the least squares method to avoid transference of such noise to other segments during affine transformation. Using segment 1 (demarcated by $0 \le \phi \le \Phi = 15°$) as the baseline segment, polynomial models of various orders are constructed in the reduced domain of

the first sector ($0 \le \phi \le \Phi/2$) to fit all field measurements in segment 1 (both sectors). The goodness of the fit statistics of these models, as well as their corresponding coefficients are produced in Table 3-3. The 7th order polynomial fit of S_1's segment 1 is displayed in Figure 3-7.

Table 3-3 Goodness of fit and coefficients of polynomial models used to fit segment 1

Poly model order		Cubic	4th	5th	6th	7th
Sum squared error		167.8	119.9	118.8	117	116.9
R^2		0.9979	0.9985	0.9985	0.9986	0.9986
coefficients	c_0	-105.9	-107.9	-107.6	-107.2	-107.1
	c_1	-3.456	2.5	1.037	-1.569	-2.52
	c_2	-5.003	-8.722	-7.277	-3.527	-1.641
	c_3	0.5031	1.29	0.7618	-1.312	-2.773
	c_4		-0.0531	0.02746	0.557	1.107
	c_5			-0.00434	-0.0673	-0.1746
	c_6				0.00282	0.01328
	c_7					-0.000401

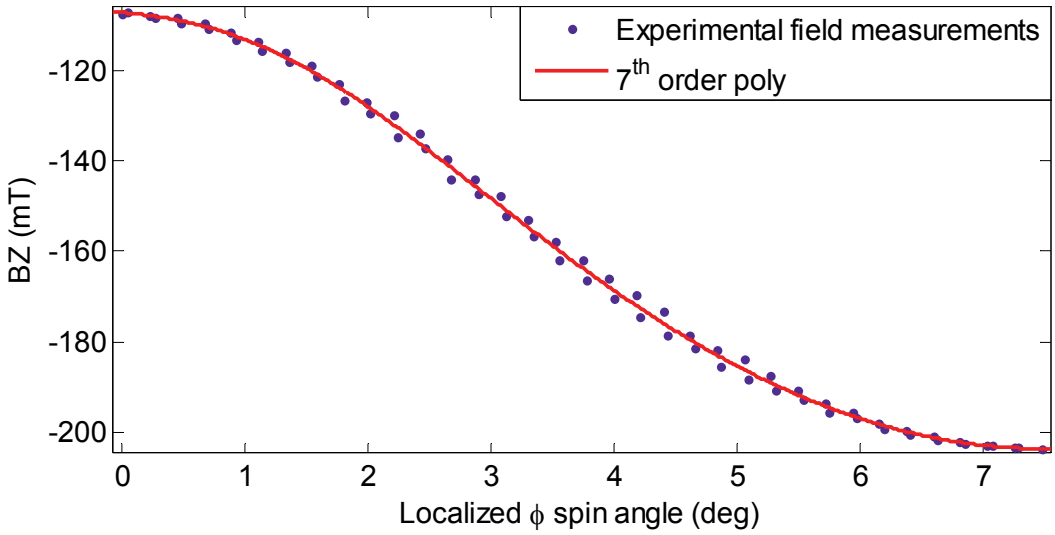

Figure 3-7 Polynomial model fitting of field measurements in segment 1 of S_1

The affine transformed segments of S_1 are illustrated in the global and localized spin position in Figure 3-8 and Figure 3-9 respectively. The computed optimal AT coefficients are appended in Table 3-4.

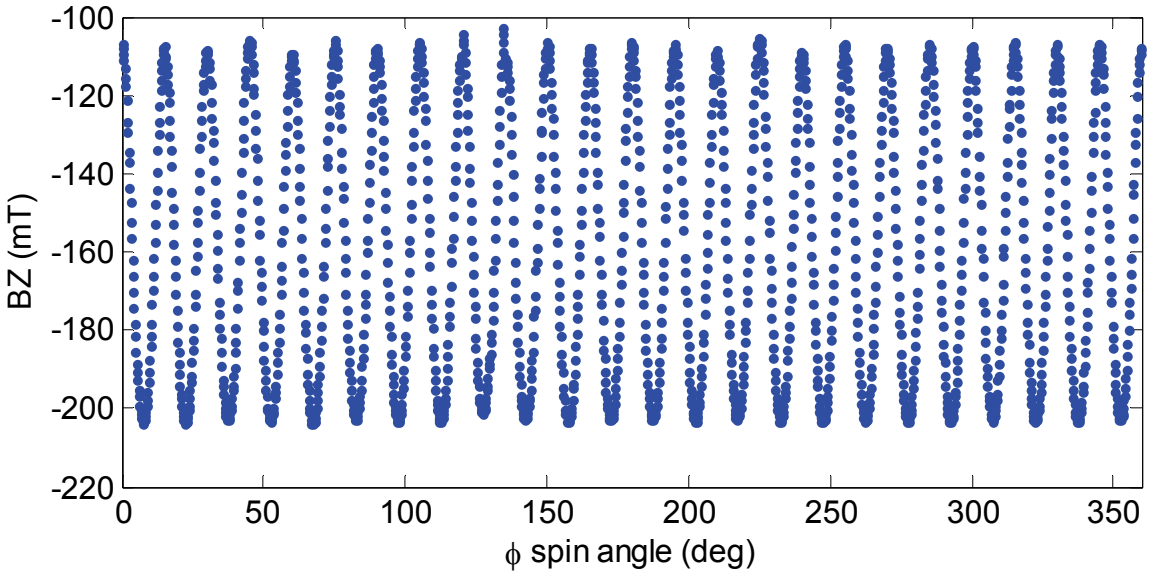

Figure 3-8 Field measurements by S_1 across segments after affine transformation

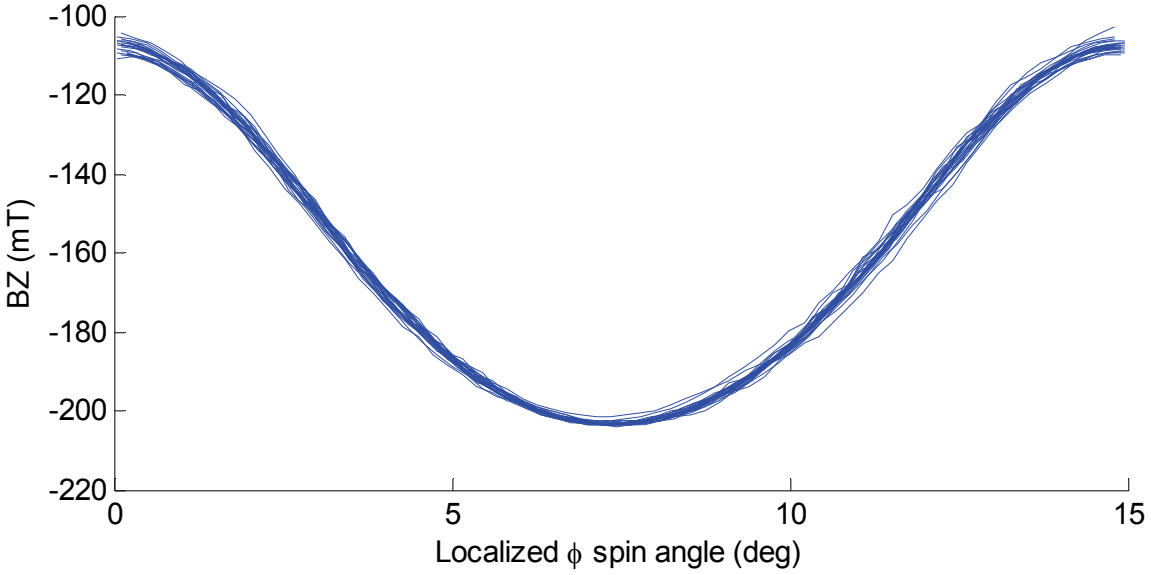

Figure 3-9 Variation in measured field from all segments by S_1 after affine transformation

Table 3-4 Affine transformation coefficients for the segments in S_1

Seg	1(ref)	2	3	4	5	6	7	8	9	10	11	12
a	1	1.02	0.98	1.00	0.97	0.92	0.91	0.93	0.92	0.88	0.91	0.93
b	0	1.306	-2.65	-0.88	-3.80	-6.41	-8.92	-6.78	-2.85	-16.16	-11.62	-7.70
Seg	13	14	15	16	17	18	19	20	21	22	23	24
a	0.87	0.86	0.93	0.92	0.99	0.99	0.94	0.96	1.04	1.00	1.01	1.00
b	-15.54	-13.72	-7.32	-8.55	-1.08	-1.65	-7.50	-4.79	3.37	0.87	-0.28	0.15

With the data in Figure 3-6 and Figure 3-9, a one-way analysis of variance (ANOVA) is used to determine if the variation in different segments by a single sensor before and after AT are statistically significant. In this case, the ANOVA tests the null hypothesis that field measurements of all 24 segments by S_1 are drawn from the same population. Statistical visualization of the variation in field measurements in segments without AT and with AT are reproduced in Figure 3-10 and Figure 3-11 respectively. On each box, the central mark is the median, the bottom and top edges of the box are the 25th and 75th percentiles and the whiskers extend to the most extreme data points. The results of the ANOVA are summarized in Table 3-5 and the high *p*-value implies that the null hypothesis for both cases cannot be rejected. The higher *p*-value for the segments with AT (value of 1) suggest a higher confidence that that the transformed measurements in segments are statistically indistinguishable.

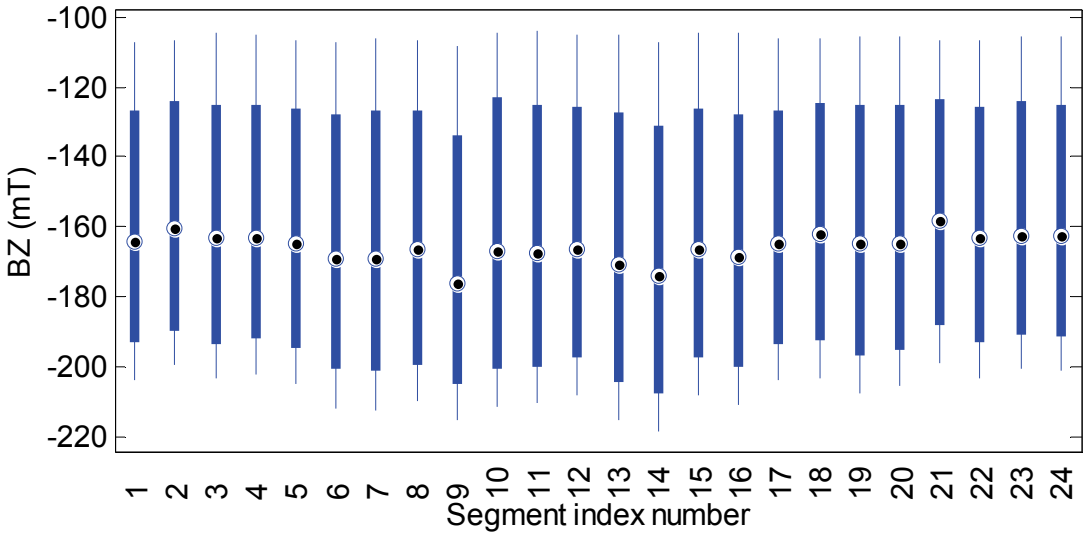

Figure 3-10 Statistical box plot of field measurement in all segments by S_1

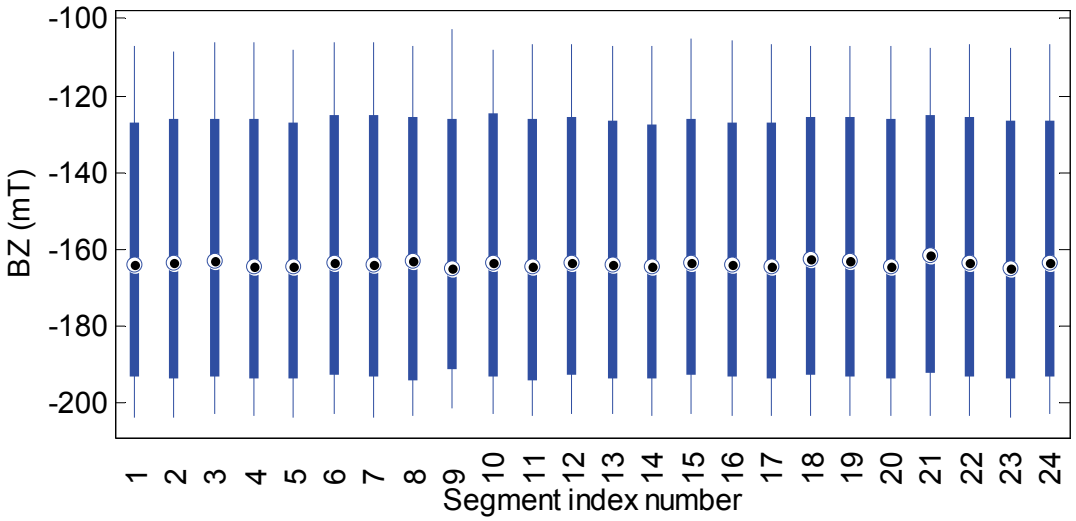

Figure 3-11 Statistical box plot of field measurement after affine transformation by S_1

Table 3-5 ANOVA results from field measurements in all segments by S_1

	Source	Sum of squares	Degrees of freedom	Mean squares	*F*-statistic	*p*-value
No AT	Segments	18856	23	819.83	0.64	**0.9009**
	Error	2049740.	1608	1274.71		
	Total	2068596	1631			
With AT	Segments	243.316	23	10.58	0.01	**1.0000**
	Error	1868899	1608	1162.25		
	Total	1869142	1631			

Table 3-6 Effects of affine transformation on *p*-values across all sensors

Sensor		S_1	S_2	S_3	S_4	S_5	S_6
No AT	*p*-value	0.9009	0.8581	0.8620	0.8628	0.7808	0.7486
With AT		1.0000					
Sensor		S_7	S_8	S_9	S_{10}	S_{11}	S_{12}
No AT	*p*-value	0.7538	0.8077	0.8073	0.9422	0.8581	0.8135
With AT		1.0000					
Sensor		S_{13}	S_{14}	S_{15}	S_{16}	S_{17}	S_{18}
No AT	*p*-value	0.8247	0.7833	0.8586	0.8926	0.8801	0.9008
With AT		1.0000					
Sensor		S_{19}	S_{20}	S_{21}	S_{22}	S_{23}	S_{24}
No AT	*p*-value	0.9141	0.9546	0.9659	0.9328	0.8870	0.8583
With AT		1.0000					

By extending this statistical analysis to all 24 sensors, the *p*-values before and after AT for each sensor can be computed and are contrasted in Table 3-6. Across all sensors, the *p*-value increases to 1 after affine transformation, denoting high statistically similarity between segments in all sensors.

3.3.2 Field – Position Mapping Across Segments

Observation of Figure 3-4 reveals that for the entire rotor rotation, the association between field measurement and position is not bijective and indiscriminate mapping of the entire field map ($0 \le \phi \le 360°$) will cause in erroneous results. To numerically verify this issue, all 24 sensor inputs can be used to associate simultaneous field measurements with spin position (over entire range) via training of the ANN (24 input and single output network). The MSE of the resulting ANN as a function of *h* is shown in Figure 3-12. At high *h*, the MSE stabilizes around 10 deg^2. To spatially visualize the error, the absolute error resulting from the ANN trained global map as a function of spin location is presented in Figure 3-13. As shown, the error can be as high as 20° and more importantly noticeably periodic, which correlates with the periodic nature of the field.

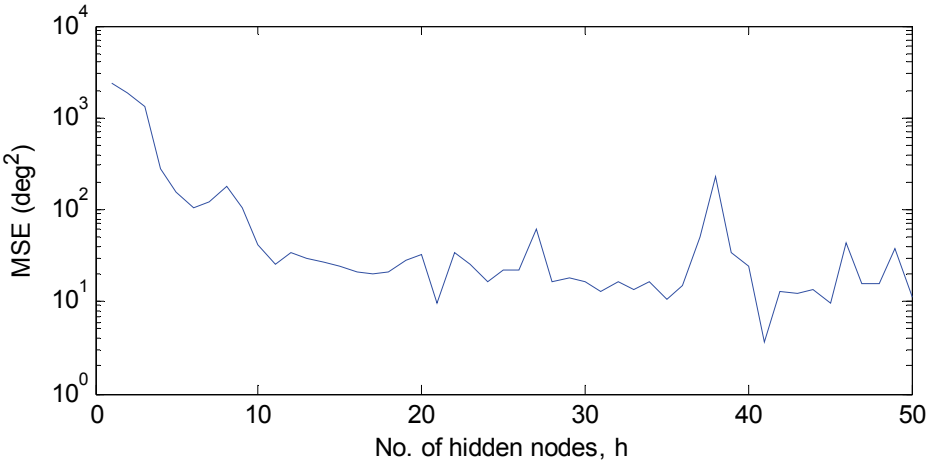

Figure 3-12 MSE as a function of hidden nodes for global mapping

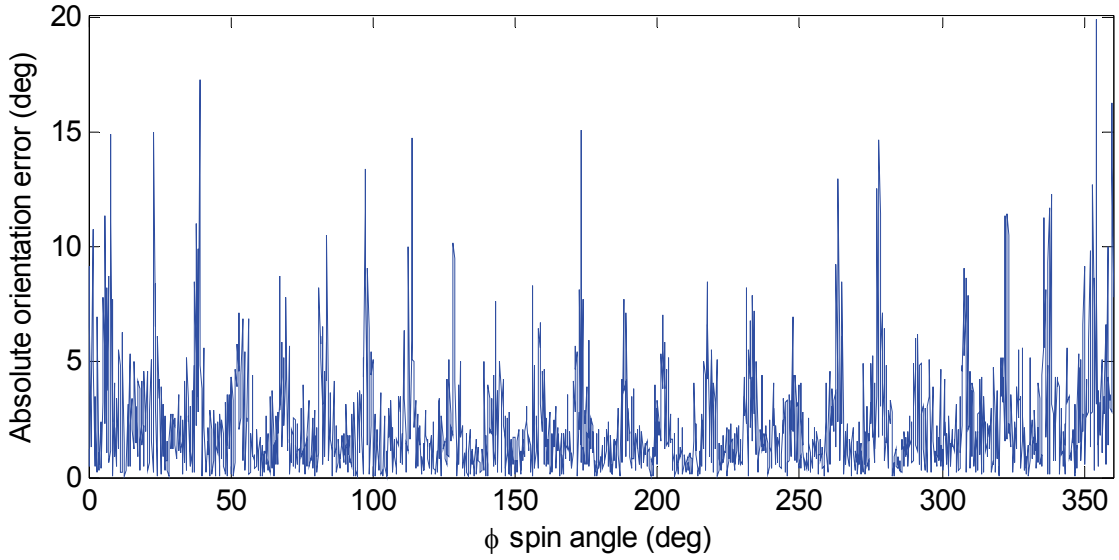

Figure 3-13 Estimation error resulting from using indiscriminate global map, h=50

Hence, to generate accurate correspondence between field measurements and position estimate for direct field sensing, segment or sector mapping is required. Using AT, the field measurements of all segments can be statistically 'standardized' with respect to the reference segment. Hence a mapping constructed using the reference segment can be used on other transformed segments. This section seeks to characterize and quantify the positional error resulting from this technique. For a single DOF case, this map can be constructed using polynomial models or using an ANN, though for multi-DOF or multi-input cases (such as using multiple independent field measurements), the ANN is better suited.

Using segment 1 ($0 \le \phi \le 15°$) as the baseline segment and observing that sector 1 and 2 are symmetric, mapping models of various orders are constructed in the reduced domain of the first sector to fit positional measurements in both sectors of segment 1. A mapping model (7^{th} order polynomial) created using experimental data from segment 1 of

S_1 is shown in Figure 3-14. With knowledge of the sector index m, the coordinate transformation between sectors and segment is described by

$$\phi' = \begin{cases} \phi_1' & \text{if } m = 1 \\ \Phi - \phi_1' & \text{if } m = 2 \end{cases} \tag{1.1}$$

where ϕ_1' is the localized position within sector 1 and ϕ' is the localized position within the segment. It is observed visually that the resulting map exhibits bijectivity resulting in low mapping error. The Mean Squared Error (MSE) of these sector mappings of S_1 using polynomials and ANNs as a function of model order and hidden nodes are shown in Table 3-7.

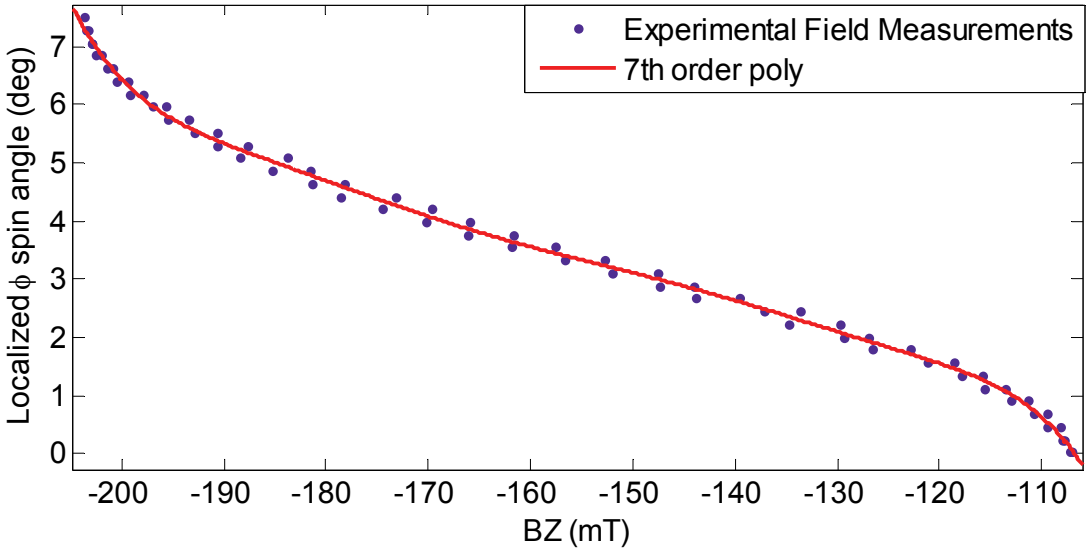

Figure 3-14 Segment 1 mapping using experimental measurements of S_1

Table 3-7 Error analysis of various mapping functions for S_1

Mean Squared Error (deg^2)									
Polynomial order					ANN hidden nodes (h)				
Cubic	4^{th}	5^{th}	6^{th}	7^{th}	3	4	5	6	7
0.02111	0.02081	0.01125	0.01126	0.00804	0.00787	0.00693	0.00684	0.00656	0.00635

As there are multiple sensors, it is possible to utilize the ANN to efficiently and concurrently map all 24 sensor measurements in segment 1 to a specific orientation (sector map has 24 inputs (one for each sensor) and 1 output (ϕ angle)); an advantage not effortlessly realizable with polynomial models. Table 3-8 summarizes the effects on the number of network inputs on the MSE for ANN based mapping. Clearly, the inclusion of more sensors for field-position mapping results in lower MSE. The ANN which uses all 24 sensor measurements resulted in an MSE of 0.00087 deg^2, which about two orders of magnitude better than the ANN which uses only S_1 as its input.

Table 3-8 MSE for using multiple sensors during ANN mapping

	Number of inputs to ANN (h=2)					
	1	2	4	8	16	24
Sensors involved	S_1	S_1, S_2	S_1, S_2, S_3, S_4	S_1, ...,S_8	S_1, ...,S_{16}	S_1, ...,S_{24}
MSE (deg^2)	0.01688	0.01320	0.00984	0.00461	0.00384	0.00087

Using the sector mapping model, the errors resulting from applying this model (based on a 7th order polynomial) on non-reference segments of S_1 are computed and spatially illustrated in Figure 3-15. The constructed map (of 1 segment) required only characterization of 1/24 of the total global map (or slightly less than 5%). Due to field variations between segments, the estimation error ($\left|\hat{\phi}-\phi\right|$) varies across segments and can be positively correlated with each segments' deviation from the box plot of segment 1 in Figure 3-10. These errors can be arrested using segment AT and the resulting estimation from using transformed field measurements are provided for comparison in Figure 3-16. After segment AT, the absolute estimation errors do not exceed 0.7° as compared to exceeding 7° at multiple locations without segment AT. It is worth noting

that even without segment AT, the error in Figure 3-15 is significantly lower than the indiscriminate global map in Figure 3-13.

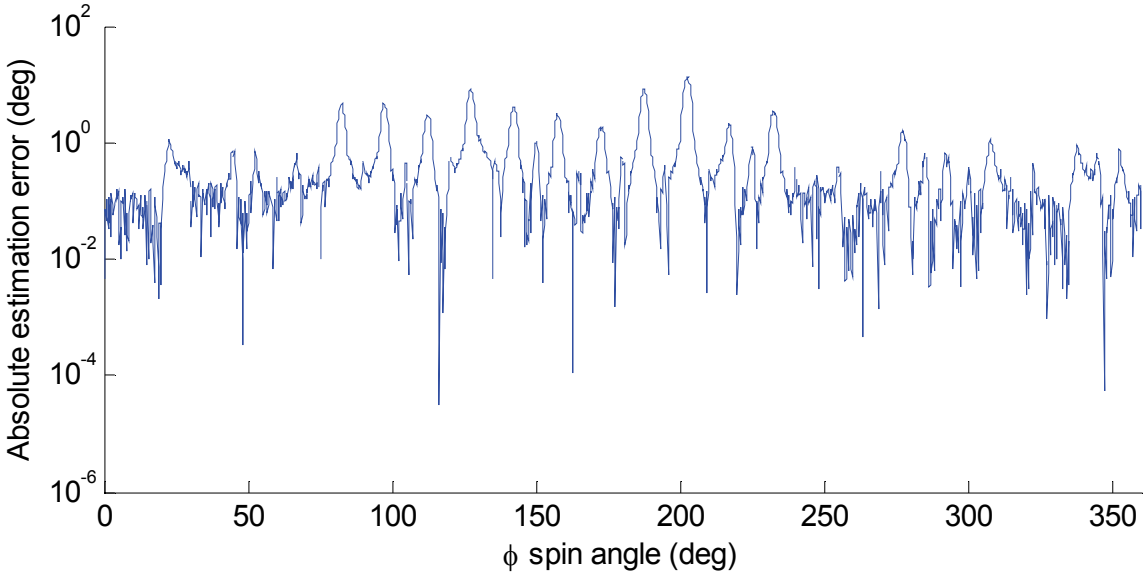

Figure 3-15 Estimation error resulting from using reference map on other segments in S_1

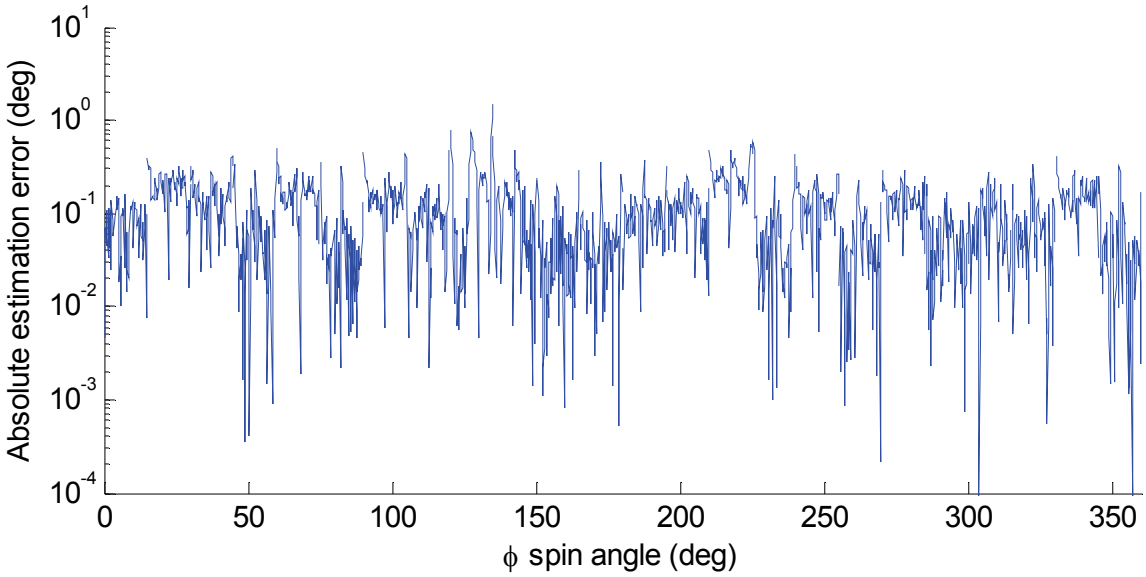

Figure 3-16 Estimation error resulting from using reference map on segments with AT

To attain better accuracy across segments, each segment can be individually mapped. The drawback, however, is the requirement of 24 distinct mapping

functions/models for each segment. The estimation error resulting from using independent segment maps are spatially illustrated in Figure 3-17. The theoretical sensing limit is provided for comparison and uses DMP analytical field model to compute the errors resulting from only the mapping model (in this case a 7^{th} order LS polynomial). As shown in the figure, the theoretical estimation error resulting from using a mapping approach is approximately an order less than the experimentally obtained corresponding errors.

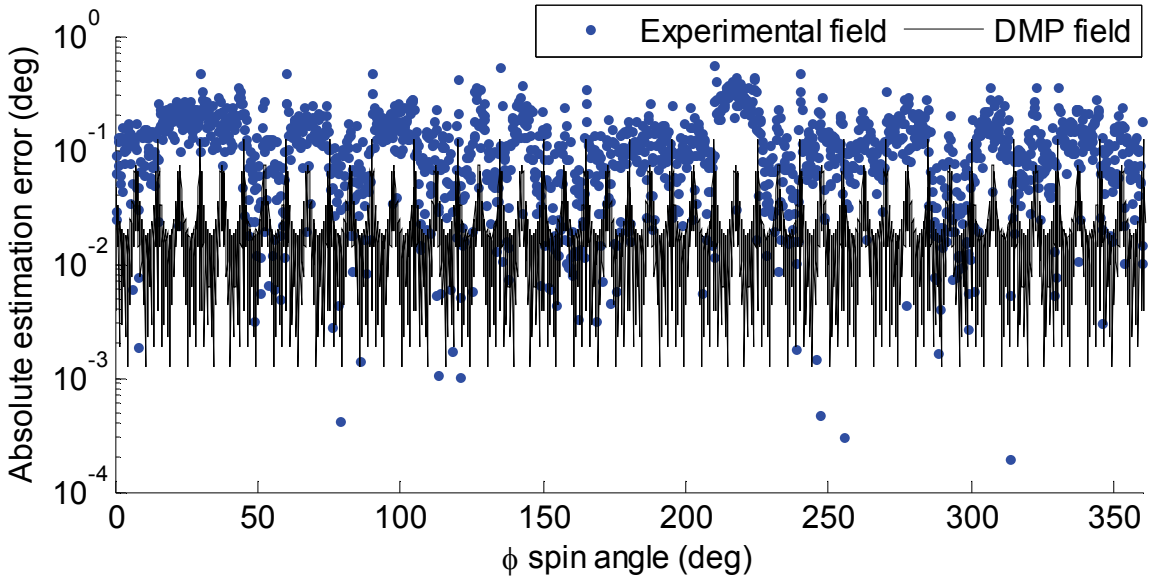

Figure 3-17 Estimation errors resulting from individual segment maps and analytical field

For a more in-depth analysis, the estimation errors in Figure 3-15 and Figure 3-16 are categorized with respect to their segment origin and the MSE of the estimation error computed and aggregated. The breakdown of the MSE in each segment with and without AT for sector mappings using both polynomial and ANN is organized in Table 3-9. In all cases, affine transformation has a significant impact on the overall MSE; lowering each segment's MSE and reducing the entire MSE for the polynomial and ANN mappings by two and three orders of magnitude respectively. For the ANN map, without affine

transformation, the substantial field variation in segment 14 instigated an MSE of more than 400 deg^2. However, with AT, the MSE is radically reduced to under 0.02 deg^2. With AT, the average MSE for all segments using the polynomial and ANN mappings are 0.02569 deg^2 and 0.02449 deg^2 respectively, which are an order higher than the reference's (segment 1) mapping MSE.

Table 3-9 Comparison of MSE across different types of mapping models and segments

Segment	Mean Squared Error (deg^2)			
	Polynomial (only S_1) (7^{th} order)		ANN (only S_1) $g=1,h=3$	
	No AT	With AT	No AT	With AT
1 (Ref)	0.00804		0.00787	
2	0.19469	0.04690	0.19850	0.04636
3	0.04636	0.03158	0.04099	0.03031
4	0.05617	0.01426	0.05605	0.01306
5	0.05447	0.03151	0.06576	0.03187
6	2.78599	0.00906	10.87799	0.00912
7	2.70748	0.03477	10.88868	0.03321
8	1.18999	0.01395	3.23464	0.01260
9	9.34537	0.13190	74.19064	0.11632
10	2.21750	0.03199	7.67895	0.03156
11	1.36853	0.00790	3.88583	0.00666
12	0.49778	0.00777	0.96656	0.00767
13	9.15840	0.01270	77.32280	0.01302
14	23.10532	0.01525	417.42707	0.01539
15	0.55836	0.08025	0.99547	0.07807
16	1.62198	0.02116	5.03296	0.01822
17	0.02484	0.02251	0.02355	0.02166
18	0.01101	0.00509	0.01050	0.00538
19	0.32426	0.02462	0.56312	0.02413
20	0.05814	0.00463	0.07807	0.00454
21	0.17007	0.01194	0.17262	0.01218
22	0.00938	0.01105	0.01142	0.00911
23	0.13607	0.03260	0.13891	0.03214
24	0.05397	0.00671	0.05786	0.00705
Max	23.10532	0.13190	417.42707	0.11632
Min	0.00938	0.00509	0.02355	0.00454
Mean	**2.32108**	**0.02569**	**25.58044**	**0.02449**

In an effort to investigate the effects of mapping model orders (degree of polynomials or number of hidden nodes) on the overall MSE of the position estimation, the aggregate MSE obtained by applying sector map to all segments are computed for a variety of sector map models and shown in Table 3-10. Without AT, the MSE for the polynomial models increases monotonously with higher model orders, the relationships between hidden nodes and MSE for the ANN models appear haphazard. However, in both types of models, the AT has an effect of stabilizing the MSE for all mapping orders. This is most likely due to the stronger fitting nature of higher order models to the reference sector and as a result higher MSE when the map is applied onto non-reference sectors.

Table 3-10 Effects of model order/hidden nodes on MSE of estimation error

Poly Model Order	Mean Squared Error (deg^2)		ANN hidden nodes	Mean Squared Error (deg^2)	
	No AT	With AT		No AT	With AT
Cubic	0.32052	0.02923	2	0.50339	0.02603
4^{th}	0.36150	0.02803	3	25.58044	0.02449
5^{th}	0.78941	0.02419	4	9468.57	0.03008
6^{th}	0.92622	0.02346	5	194.593	0.02388
7^{th}	2.32108	0.02569	6	2.04026	0.02484
8^{th}	3.16563	0.02451	7	4712.50	0.02379

3.4 CHARACTERIZATION OF MULTIPLE SENSORS

In aggregate multi-sensing, the sensing similarity among sensors permitted the reduction of the domain required for segment mapping. The field measurements collected for a complete rotor rotation by all sensors is presented in a box plot format in Figure 3-18. Visually, it can be seen that the variation in field measurements between sensors are not comparable. The results of a one-way ANOVA applied on the data in Figure 3-18 is consolidated in and confirms this issue. As shown in Table 3-11, the *p*-value is so close to

zero that there is sufficient statistical evidence to confidently reject the null hypothesis (that measurements by all sensors are statistically similar). Using a field map generated using measurements of S_1 will cause large positional estimation errors if field measurements of another sensor is used. This phenomenon occurs despite the fact that all sensors were of the same make and model and common supply voltage was supplied to all sensors. However, the disparities can be attributed to sensor mis-positioning, misalignment or inherent manufacturing related differences between sensors. As with field variation between segments, the approach of using affine transformation to calibrate and 'standardize' measurements across sensors is adopted.

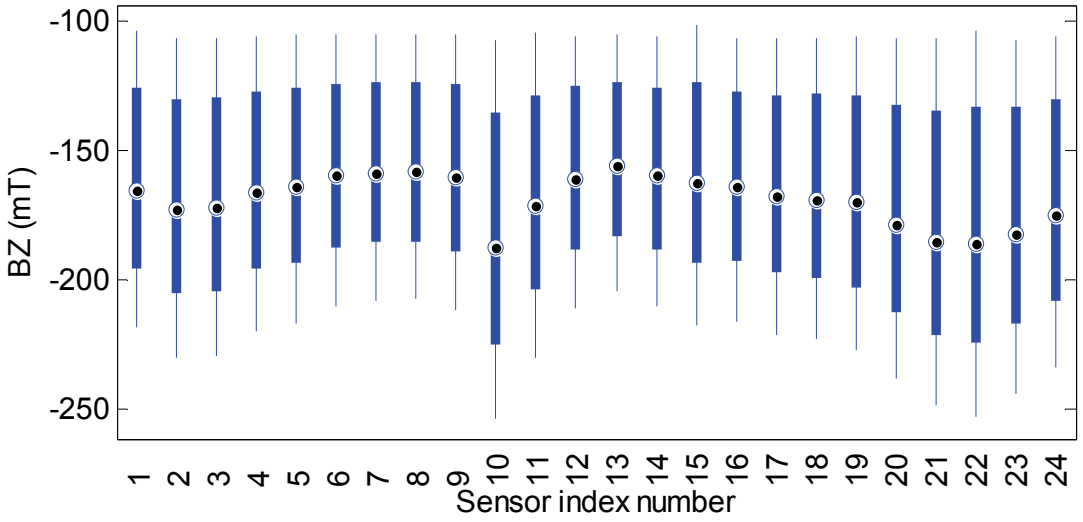

Figure 3-18 Statistical variation in the measurements of the PM assembly by all sensors

Table 3-11 ANOVA results from field measurements by multiple sensors

	Source	Sum of squares	Degrees of freedom	Mean squares	*F*-statistic	*p*-value
No AT	Sensors	2553760	23	111033	80.79	**0.000**
	Error	54094400	39360	1374.4		
	Total	56648200	39383			
With AT	Sensors	93.2132	23	4.05	0	**1.000**
	Error	1887384	1608	1173.75		
	Total	1887477	1631			

3.4.1 Sensor Field Calibration

With segment field calibration where measurements in all segments are calibrated to a designated reference segment (in this case segment 1), calibration between the reference segments of all sensors will ensure every segment in every sensor are statistically standardized. Using S_1 as the designated reference sensor, the affine transformed field measurements of all remaining sensors can be computed by minimizing the function defined in Equation (2.53). The computed optimal coefficients for sensor AT are appended in Table 3-12. After AT, the statistical variation in field measurements between sensors are illustrated statistically using a box plot in Figure 3-19. The results of a one-way ANOVA applied on the data in Figure 3-19 is provided in Table 3-11 for comparison with the pre AT data. The high p-value denotes that there is insufficient statistical evidence to confidently reject the null hypothesis.

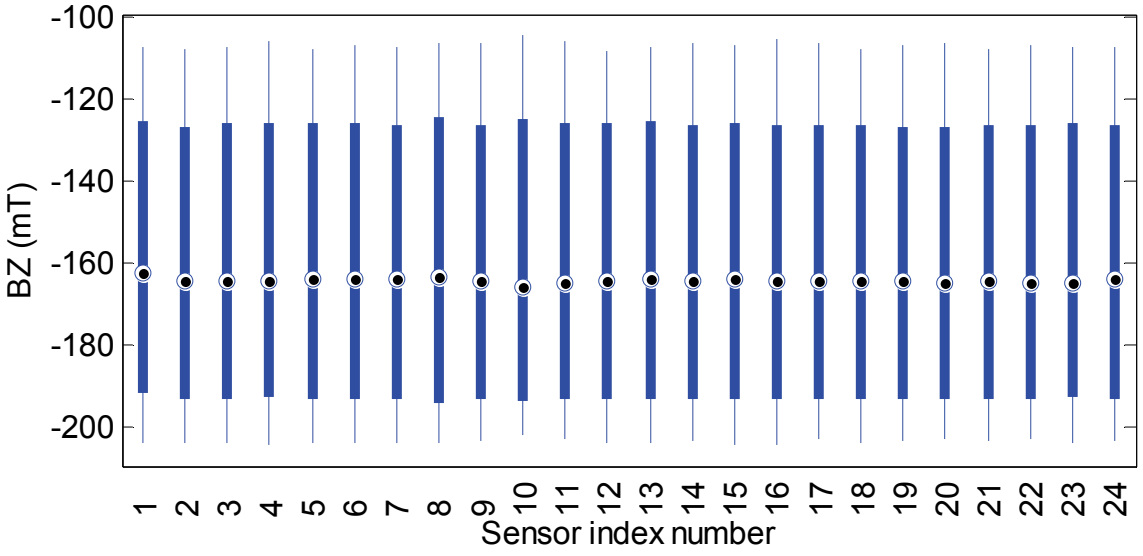

Figure 3-19 Statistical variation in the measurements of the PMs by all sensors with AT

Table 3-12 Affine transformation coefficients for individual sensors (S_1 is reference)

sensor	1(ref)	2	3	4	5	6	7	8	9	10	11	12
c	1	0.970	0.927	1.023	1.025	1.029	1.044	1.090	0.976	0.716	0.843	1.041
d	0	-1.441	-7.343	2.425	3.364	4.832	6.006	11.858	-0.296	-27.00	-16.75	5.294
sensor	13	14	15	16	17	18	19	20	21	22	23	24
c	1.017	0.964	0.938	0.985	1.010	0.976	0.900	0.840	0.830	0.772	0.860	0.907
d	1.744	-0.345	-9.294	1.739	4.141	-1.336	-10.12	-15.43	-16.48	-23.47	-12.34	-9.301

3.4.2 Field – Position Mapping Across Sensors

As was seen earlier, a sector map constructed using the measurements in the reference segment was used to determine position estimates in non-reference segments with minimal estimation error through segment affine transformation. By optimally 'standardizing' field measurements across segments as well as sensors, a single sector map of a reference sensor can be used across its own segments as well as across other sensors. The MSE of using the sector map of the reference sensor (S_1) on the remaining 23 sensors on the first 3 segments are shown in Table 3-13. Just as segment AT has reduced the MSE across segments, sensor AT has the comparable effect on lowering the MSE across sensors as well. Without AT, using the sector map of S1 on segment 1 across all sensors yielded an MSE average of 371 deg^2 and with a peak of 7553 deg^2. However, with sensor AT, the average MSE reduces to 0.0589 deg^2 (which is less than one order of magnitude higher than the reference map MSE of 0.00804 deg^2) and does not exceed 0.3101 deg^2. This trend is replicated for segment 2 and 3 as shown in Table 3-13.

The above results are significant because now not only 24 segments can be mapped accurately using only 1 sector map; all 24 sensors can use the same map with comparable accuracy. Any designated sector map can be used on any of the 576 (24

segments × 24 sensors) segment of all sensors, which represents less than 0.1% of the total mappable domain.

Table 3-13 MSE distribution across segments and sensors from reference sector map

Sensor	Mean Squared Error (deg^2)					
	Segment 1 (Ref)		Segment 2		Segment 3	
	No AT	With AT	No AT	With AT	No AT	With AT
1 (Ref)	0.00804		0.19469	0.04690	0.04636	0.03158
2	0.52215	0.00640	3.54069	0.03205	1.94265	0.01238
3	2.61876	0.04147	1.71383	0.09094	5.70980	0.03395
4	0.15763	0.13027	0.08654	0.02600	2.66036	0.07396
5	0.07241	0.04674	0.70266	0.03076	0.79964	0.07862
6	0.06362	0.04675	0.11294	0.11397	0.10450	0.04505
7	0.08430	0.01295	0.19729	0.04270	0.04436	0.00525
8	0.33952	0.19366	0.38129	0.37028	0.51382	0.43671
9	0.52540	0.03864	0.11026	0.06978	0.01032	0.00957
10	7553.90	0.31013	6456.45	0.12486	3503.05	0.22467
11	46.0183	0.08787	20.1790	0.03273	185.808	0.06735
12	0.13526	0.07753	0.46154	0.07807	2.14421	0.11433
13	0.07239	0.04973	0.07872	0.04820	0.57691	0.22768
14	1.60990	0.01684	0.25710	0.18481	0.05494	0.03721
15	0.34063	0.03421	1.16279	0.09119	0.06212	0.05161
16	0.65134	0.03165	0.12092	0.07544	0.10760	0.05589
17	0.12348	0.03481	0.12237	0.05965	0.89286	0.06420
18	0.32400	0.02504	2.08002	0.00728	1.00446	0.05775
19	7.18257	0.01656	3.22575	0.00860	0.08260	0.01802
20	78.5096	0.01325	10.0850	0.03854	39.9080	0.02408
21	122.585	0.03629	387.141	0.07071	216.468	0.08976
22	650.855	0.01718	350.185	0.02565	435.681	0.01914
23	66.5801	0.07555	89.4305	0.09453	134.044	0.13587
24	5.47079	0.01088	11.1602	0.01873	2.23369	0.01815
Max	7553.90	0.31013	6456.45	0.37028	3503.05	0.43671
Min	0.06362	0.00640	0.07872	0.00728	0.04636	0.00525
Mean	371.249	0.05890	305.799	0.07430	188.914	0.08050

3.5 SUMMARY

In this chapter, the experimental field variation due to 24 similarly graded and geometrically sized PMs was investigated using 24 single-axis magnetic sensors. As

expected, the variation between PMs has a detrimental effect on the performance in field-position mapping. However, with affine transformation which compensates for individual field variation among PMs, the MSE of the field-position map is reduced by two orders of magnitude and is only an order of magnitude higher than the MSE of the reference segment map. Using the same approach, the field variation due to manufacturing effects and misalignment of multiple sensors, which is significantly higher than the variation due to different PM sources, can be compensated as well. The corresponding reduction in MSE is more pronounced when applying sensor AT where the MSE has been reduced by four orders of magnitude across sensors. Combining both segment and sensor AT, only one sector/segment map of any one sensor is required which can be applied to the remaining segments of all sensors. This represents less than 0.1% of the total mappable domain.

CHAPTER 4

SENSING SYSTEM FOR MULTI-DOF EM DEVICE

4.1 OVERVIEW

This chapter describes the development of a field based sensing system for an electromagnetic actuator which comprises of an embedded assembly of PMs. As such devices utilize EMs for actuation, magnetic fields generated by these EMs need to be actively compensated to isolate the rotor magnetic field for accurate field-based sensing. Even with isolated rotor field measurements, the measured fields are spatially nonlinear and contain periodicity due to the arrangement of PMs. As a result, even with closed form magnetic field models, the correspondence between orientation and field measurements are not unique. A mapping approach using ANNs is used to provide direct correspondence between field measurements and orientation of the system.

Using a prototype multi-DOF electromagnetic actuator currently being developed at Georgia Tech [4] as a platform for experimental analysis, the remainder of this chapter is organized as follows:

1. The embedded rotor magnetic field is isolated and extracted using active and passive methods.
2. Bijective correspondence between orientation and field measurements for direct field based sensing is generated through segmentation and sectorization of the forward parametric space. With this bijective domain, ANN mapping

methods are used to associate distributed field measurements to orientation of the rotor.

3. The effects of number and type of field measurements on the mapping accuracy are experimentally investigated using high and low field sensors.

4.2 Embedded Magnetic Field Sensing for Multi-DOF Actuator

Multi-axis dexterous actuators such as electromechanical spherical motors utilize the intrinsic electromagnetic interaction between PMs and EMs on the rotor and stator respectively for rapid and agile actuation. These embedded PM assemblies already present on the rotor can be harnessed for sensing purposes and subsequently feedback control at low cost. Unlike conventional sensing feedback mechanisms which extract the positional information of the rotor from the physical motion of the rotor, the approach presented here uses the inherent magnetic field of the rotor PMs as measured by a network of magnetic sensors on the stator for embedded field-based sensing as conveyed in the block diagram in Figure 4-1.

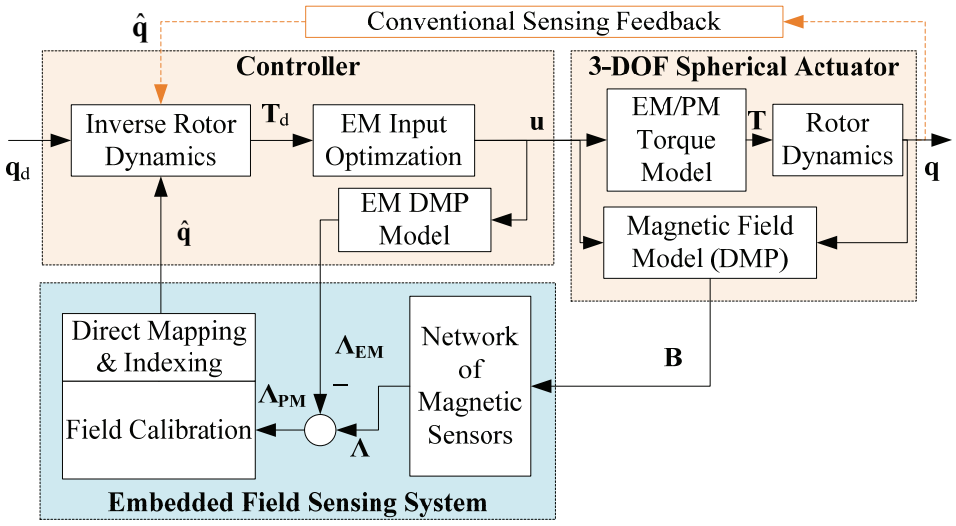

Figure 4-1 Block diagram of control multi-DOF electromagnetic actuator

As articulated in [4], the controller determines the desired torque $\mathbf{T}_d$ using rotor orientation **q** and prior knowledge of the actuator dynamics. Since the actuator has more controllable inputs than mechanical DOF, an optimized controlling current input vector **u** is required and obtained through minimization of total input energy. By Lorentz force law, currents flowing in the energized EMs under the influence of the magnetic field due to the PMs induce a torque **T** on the rotor which translates into rotational motion of the rotor. Due to the rotor multi-PM assembly, an inherent magnetic field **B** moving in tandem with the rotor can be detected and measured coherently and complimentary by magnetic sensors on the stator. With knowledge of **u** and position of all EMs and sensors the magnetic field originating from the EMs, $\mathbf{\Lambda}_{EM}$ can be computed. Using the principle of superposition, the magnetic field due to the moving rotor $\mathbf{\Lambda}_{PM}$ can be isolated from direct field measurements $\mathbf{\Lambda}$. Through methodical analysis and meticulous characterization of $\mathbf{\Lambda}_{PM}$, an estimate for the rotor position $\hat{\mathbf{q}}$ can be computed in real-time for active feedback control of the system.

Hence positional sensing of a multi-DOF electromagnetic actuator can be broken down into two main components:

- Isolation and extraction of rotor magnetic flux density
- Position and rotor magnetic field correspondence using the field-based sensing system.

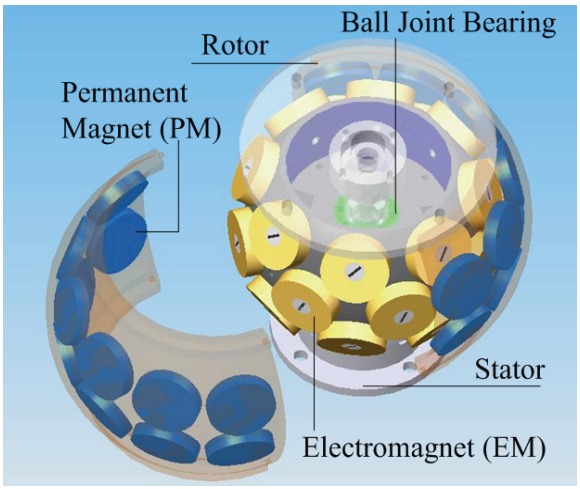

Figure 4-2 CAD model of spherical actuator with PMs and EMs [4]

4.2.1 EM/PM Configuration and Sensing Network

Multi-DOF electromagnetic actuators consist of a stationary stator and a moving rotor. The rotor is attached to the stator by means of a passive mechanical mechanism, such as spherical/ball bearing joints. Both the rotor and stator are composed of multiple layers of cylindrical PMs and EMs respectively. Figure 4-2 shows a CAD model of a prototype actuator currently being developed at Georgia Tech [4] with an internal stator (with 3 layers of EMs, each layer with 8 EMs) and external rotor (with 2 layers of PMs, each layer with 12 PMs). As these actuators are both dynamically and magnetically balanced, the PMs and EMs are designed such that their magnetization axes pass radially through the motor center. In addition, as part of the actuating principle of electromagnetic actuators, the magnetization axes of adjacent PMs are intentionally alternating by design. As a consequence, a spatial pattern of the PMs is inadvertently generated. This also results in the corresponding magnetic field periodicity of the entire PM assembly.

To minimize current input to the EM during actuation and improve energy efficiency and heat management, the EMs are installed close to the PMs to maximize

force/torque generation. A direct consequence of the close proximity between the EMs and PMs is that the EM and PM magnetic fields are undistinguishable from one another and a sensor in the vicinity will measure the aggregate magnetic field of all EMs and PMs. Figure 4-3 defines the coordinate systems of the stator, rotor and measurement field sensors, which are denoted as *XYZ* (fixed reference), *xyz* (moving), and $X_sY_sZ_s$ (fixed local to each sensor) respectively. The center of the spherical bearing is defined at **O** and it coincides with the origin of all coordinate systems.

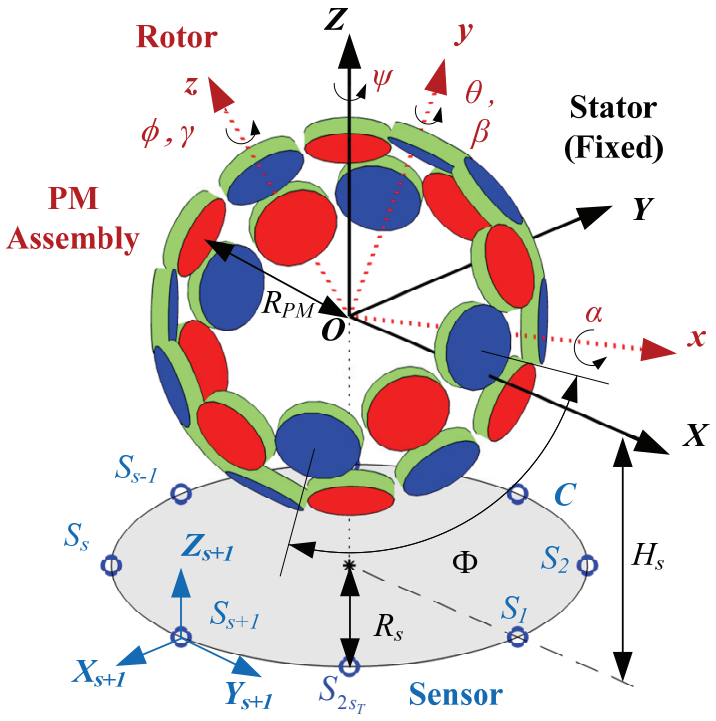

Figure 4-3 Coordinate systems for rotor, stator and sensors

The centroid location of the e^{th} PM on the ± layer (each containing 12 PMs) on the rotor expressed in the *xyz* frame using spherical angles as depicted in Figure 4-3 is

$$\mathbf{PM}_{e\pm} = R_{PM}\left[\cos\phi_e\cos\theta_\pm \quad \sin\phi_e\cos\theta_\pm \quad \sin\theta_\pm\right]^T \tag{4.1}$$

$$\phi_e = \left(e-1/2\right)\phi_{PM}, \quad \phi_{PM} = 2\pi/12 \tag{4.2}$$

$$\theta_{\pm} = \pm\theta_L / 2 \tag{4.3}$$

where e = 1,2,3 … 12, ϕ_{PM} is the azimuth spacing between adjacent PMs in each layer, θ_L is the zenith spacing between PM layers, R_{PM} is the radial distance of each PM from **O**. In rotor coordinates, the magnetization vector of each PM (axially magnetized with radius a and length l) is given by

$$\mathbf{r}_{e\pm} = \pm(-1)^e \left[\cos\phi_e \cos\theta_{\pm} \quad \sin\phi_e \cos\theta_{\pm} \quad \sin\theta_{\pm}\right]^T \tag{4.4}$$

In Figure 4-3, the blue and red surfaces represent the north and south poles of the PMs respectively. The PM configuration on both layers can be visually illustrated in spherical coordinates in Figure 4-4.This configuration possesses a distinct geometric pattern about the z-axis of the rotor which can be characterized by the azimuth spatial pitch (or periodicity) of the rotor, Φ and is equal to $2\phi_{PM}$. Visually it can be verified that the entire PM configuration of the rotor is composed of 6 identical segments (each containing 4 PMs) demarcated by Φ. The consequence of the physical occurrence of Φ is the analogous symmetry of the magnetic field radiating from the assembly of PMs on the rotor.

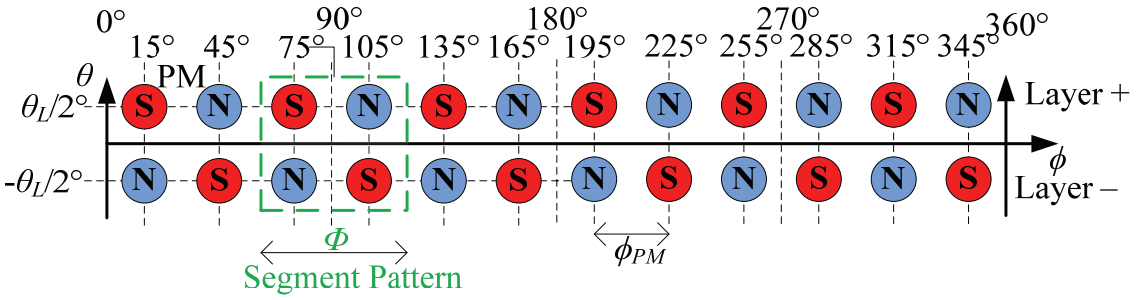

Figure 4-4 PM positioning and orientation in spherical coordinates when **q**=0

4.2.2 Rotor Magnetic Field Isolation

In order to isolate the magnetic field of the rotor PMs, the magnetic field generated by the EMs must be actively negated. This can be achieved using one and/or both of the following approaches:

- Exploiting the center of each of the EMs where the magnetic field generated by each EM in the direction orthogonal to the magnetization axis is zero. Sensors placed in these locations benefit from this occurrence and measure only the magnetic field of the PMs on the rotor.
- Compensating the magnetic field from EMs at each sensor location. This can be analytically achieved by modeling it as an equivalent PM and using the DMP model [23][24]. As the EMs and sensors are stationary and of known distance and orientation from each other, this analytical closed form model is only a function of the input currents and will facilitate forward computation of the magnetic flux density originating from the EMs in real-time. Alternatively, such a model can be experimentally obtained using the measurements of the field sensors.

The combined field measurements from all sensors can be consolidated column by column into matrix defined by:

$$\mathbf{\Lambda}(\mathbf{q},\mathbf{u}) = \left[\mathbf{B}_1 \cdots \mathbf{B}_s \cdots \mathbf{B}_{2s_T}\right] \tag{4.5}$$

where s is the referencing index of the sensor; and $\mathbf{B}_s$ is the magnetic flux density as measured by the s^{th} sensor which has w sensing axes. $\mathbf{\Lambda}$ contain field measurements of both the EM and PM and hence is a function of both the input and orientation of the

rotor. As the EMs are fixed on the stator, magnetic flux density contribution by the EMs is not a function of **q** and is simply

$$\mathbf{\Lambda}^{\mathrm{EM}}\left(\mathbf{u}\right)=\left[\mathbf{B}_1^{\mathrm{EM}}\left(\mathbf{u}\right)\cdots\mathbf{B}_s^{\mathrm{EM}}\left(\mathbf{u}\right)\cdots\mathbf{B}_{2s_T}^{\mathrm{EM}}\left(\mathbf{u}\right)\right] \tag{4.6}$$

where $\mathbf{B}_s^{\mathrm{EM}}\left(\mathbf{u}\right)$ is the aggregate magnetic field as measured by the s^{th} sensor from the entire EM assembly when the input is **u**. Due to applicability of superposition, the aggregate magnetic field is the summation of field effects from each individual EM as described by

$$\mathbf{B}_s^{\mathrm{EM}}\left(\mathbf{u}\right)=\sum_{f=1}^{24}\mathbf{B}_s^{\mathrm{EM}_f}\left(\mathbf{u}\right) \tag{4.7}$$

where $\mathbf{B}_s^{\mathrm{EM}_f}$ is the magnetic field as measured by the s^{th} sensor by the f^{th} EM in the assembly. Using this result, the magnetic flux density (as measured by the sensor network resulting from only the PM assembly on the rotor) can be isolated using the following:

$$\mathbf{\Lambda}^{\mathrm{PM}}\left(\mathbf{q}\right)=\mathbf{\Lambda}\left(\mathbf{q},\mathbf{u}\right)-\mathbf{\Lambda}^{\mathrm{PM}}\left(\mathbf{u}\right)=\left[\mathbf{B}_1^{\mathrm{PM}}\left(\mathbf{q}\right)\cdots\mathbf{B}_s^{\mathrm{PM}}\left(\mathbf{q}\right)\cdots\mathbf{B}_{2s_T}^{\mathrm{PM}}\left(\mathbf{q}\right)\right] \tag{4.8}$$

where $\mathbf{B}_s^{PM}$ is aggregate magnetic field of all rotor PMs as measured by the s^{th} sensor. Hence, obtaining a model for $\mathbf{\Lambda}^{\mathrm{EM}}\left(\mathbf{u}\right)$ which potentially requires characterization (analytical or experimental) of up to $24\times2s_T$ individual models of $\mathbf{B}_s^{\mathrm{EM}_f}$. In addition, as the EMs do not contribute to the measured magnetic field when the current into the EMs are zero and this allows the spherical actuator to function as a spherical encoder in an absence of **u**.

4.3 NUMERICAL ANALYSIS AND INVESTIGATION

The computation of the magnetic flux density of the PM assembly as measured by the sensors is achieved using the distributed multipole (DMP) model [23][24]. The use of the DMP model is preferred because of its ability to accurately characterize magnetic fields at close proximity to PMs and EMs and are extendable to objects of other geometry. By superposition, the resultant field at a point due to an assembly of PMs is the summation of the fields due to each individual PM. Each cylindrical PM has a radius of 1.59 cm and is 0.635 cm long. They are modeled using a 4 loop and 10 dipoles DMP model as summarized in Table 4-1. The parameters of the 24 PM rotor and 8 sensor network defining the configuration are compiled in Table 4-2. Eight magnetic sensors are installed in the center of each of the 8 EMs on the *XY* plane ($H_s = 0$) to create an actuator-sensor pair.

Table 4-1 PM and DMP model parameters

PM:	**DMP:** (k=4,n=10);
$\boldsymbol{M}$=1.31T,	$\bar{\ell}$ = 0.191 cm
a = 1.59 cm,	m_o = 33.5 x 10^{-6} A/m, m_{1i} = 24.5 x 10^{-6} A/m
l = 0.635 cm	m_{2i} = 57.6 x 10^{-6} A/m, m_{3i} = 52.0 x 10^{-6} A/m
	m_{4i} = 276 x 10^{-6} A/m

Table 4-2 Rotor and sensor network parameters

Sensor Network	$2s_T = 8, R_s$ = 6.16 cm, $\psi_s = 45°$, $H_s = 0$
Rotor PMs	R_{PM}=6.80 cm, $\phi_{PM} = 30°$, $\Phi = 60°$

4.3.1 2 DOF Characterization

The total range of motion in the 2-DOF case is the unrestricted spin of the rotor about the z-axis ($-\infty \le \phi \le \infty$) and inclination of the rotor about the y-axis ($-15° = -\theta_{\max} \le \theta \le \theta_{\max} = 15°$). Assuming that ψ is an integer multiple of ψ_s, at least one sensor group will be coincident with the x-axis of the rotor when θ=ϕ=0. The

simultaneous measurement of all three sensing axis of these sensors as a function of the two independent orientation angles (θ, ϕ) allow construction of a 2-D surface field map in forward parametric space for each sensing axis. Due to the spatial periodicity of the rotor PM configuration, there will be a total of 6 segments. These segments are identical so only the analysis of one segment is sufficient. Noting the field symmetry of the magnetic dipoles, for the 2 DOF case these segments can be further partitioned into smaller sectors. The geometric relationship between the global surface map and local segment and sector maps is shown in Figure 4-5. The sectors are referenced using a two-digit number with the most and least significant digit representing the row and column index respectively.

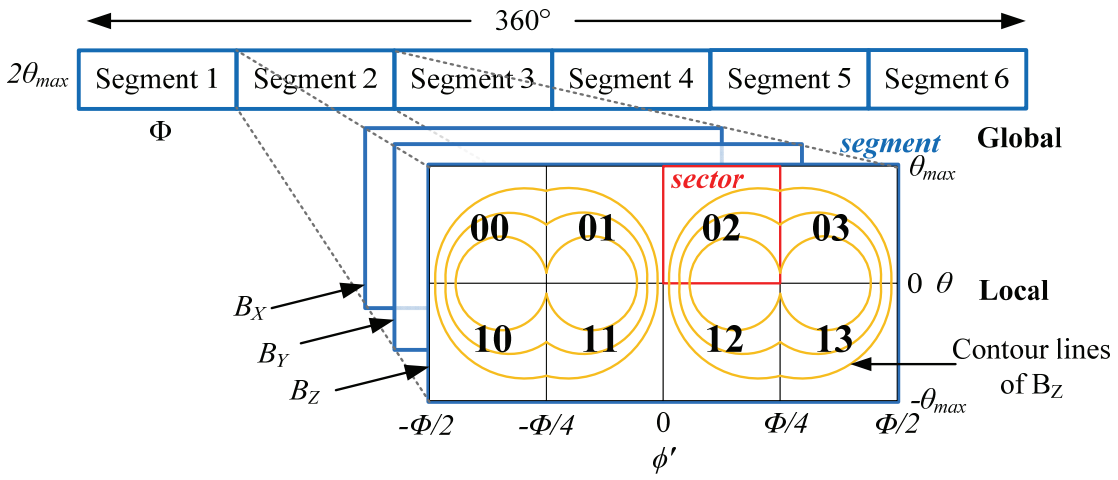

Figure 4-5 Segmentation and sectorization of 2-D surface map

As a consequence of magnetic dipole symmetry, the *magnitude* of the surface map within each sector is related to the $\theta\phi'$ axes of the surface map segment through the following coordinate sector transformation:

$$\begin{bmatrix}\theta\\ \phi'\end{bmatrix}=\begin{bmatrix}(-1)^i & 0\\ 0 & (-1)^j\end{bmatrix}\begin{bmatrix}\theta_{ij}\\ \phi'_{ij}\end{bmatrix}+\begin{bmatrix}0\\ \delta_j\end{bmatrix}\frac{\Phi}{2} \text{ where } \delta_j=\begin{cases}-1 & \text{if } j=0\\ 1 & \text{if } j=3\\ 0 & \text{otherwise}\end{cases} \quad (4.9)$$

and θ_{ij} and ϕ'_{ij} are the coordinate axes of the ij^{th} sector for $0 \le i \le 1$ and $0 \le j \le 3$ as visually shown in Figure 4-6. The conclusion from Figure 4-5 and Figure 4-6 is that the magnetic field mapping of only any *one* of the eight sectors is required to completely describe the entire segment and hence the global surface. The ratio of the area of any single sector map to the area of the global surface is $\Phi/(16\pi)$. For simplicity, the sector whose coordinate axis coincides with the axes of the segment (highlighted in red).

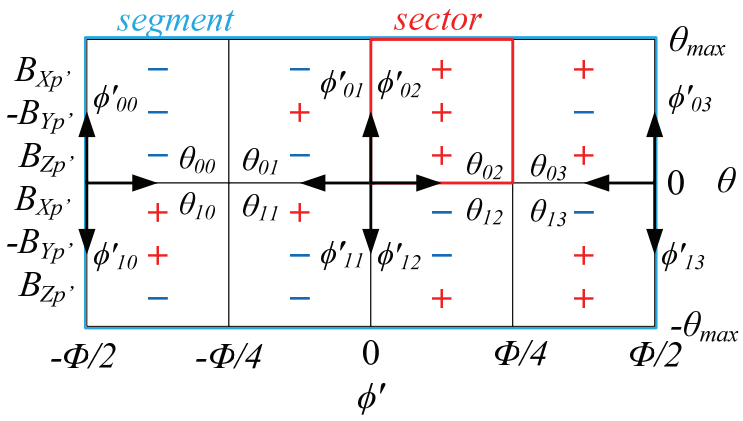

Figure 4-6 Coordinate axes and sign distribution across the sectors in a segment

Assuming ψ=0, the localized 2-D contour surface map of the magnetic flux density for all 3 axis as a function of θ and ϕ' as measured by S_1 is reproduced in Figure 4-7. For completeness, the corresponding surface maps for S_2, S_3 and S_4 are shown in Figure 4-8, Figure 4-9 and Figure 4-10 respectively. The lighter and darker regions represent areas of positive and negative values as annotated by the colorbar. It can be visually verified that the three surface maps of S_1 adhere to the segregation in Figure 4-5. The smaller segment and sector maps are shown in greater detail in the reduced parametric space in Figure 4-11. Analysis of this segment parametric space verifies that only 1/8 of the surface is unique and the remaining surface can be obtained by applying the transformation in Equation (4.9). In fact, only 2% of the global surface map is required for characterization.

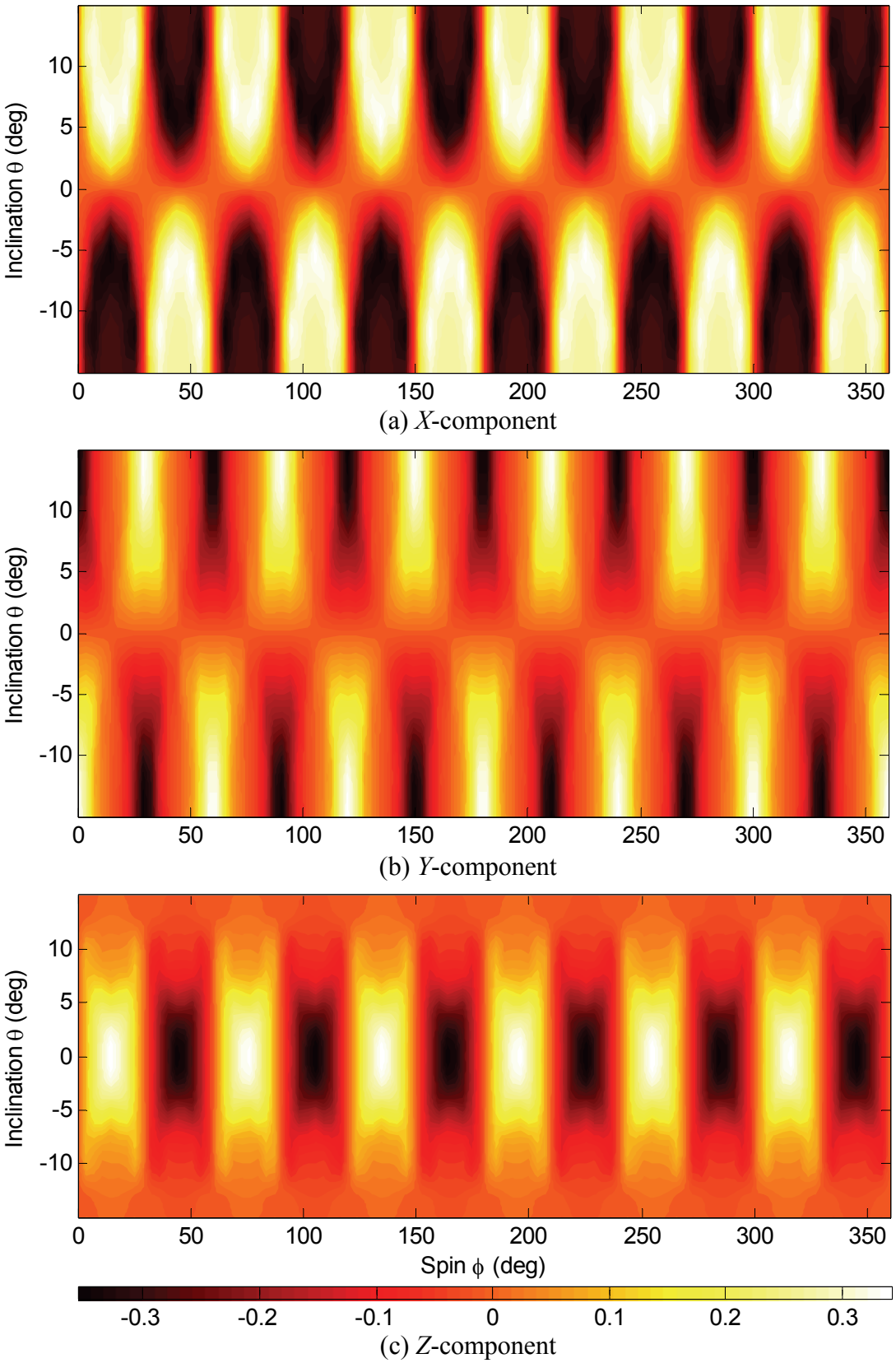

Figure 4-7 Contour field map of measurements by S_1 in parametric space (Units: Tesla)

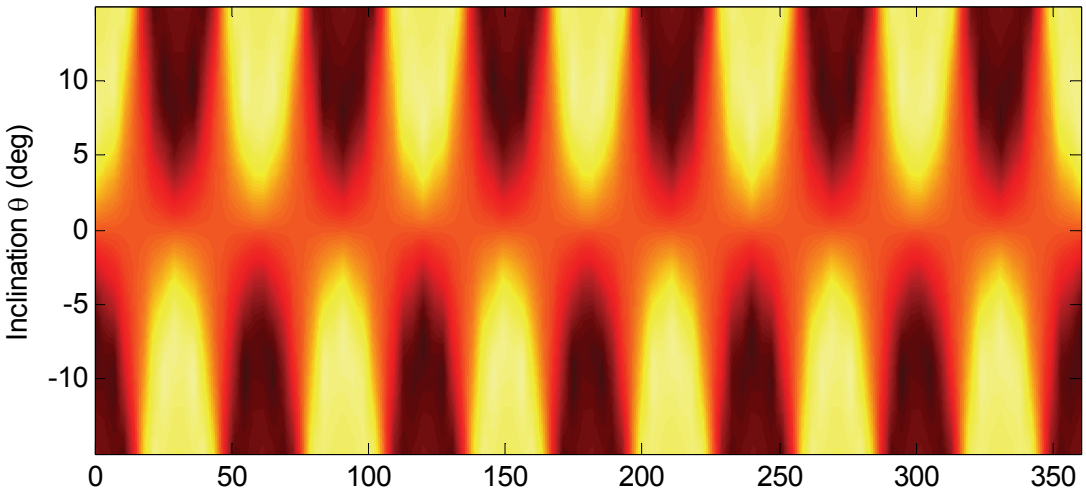

(a) *X*-component

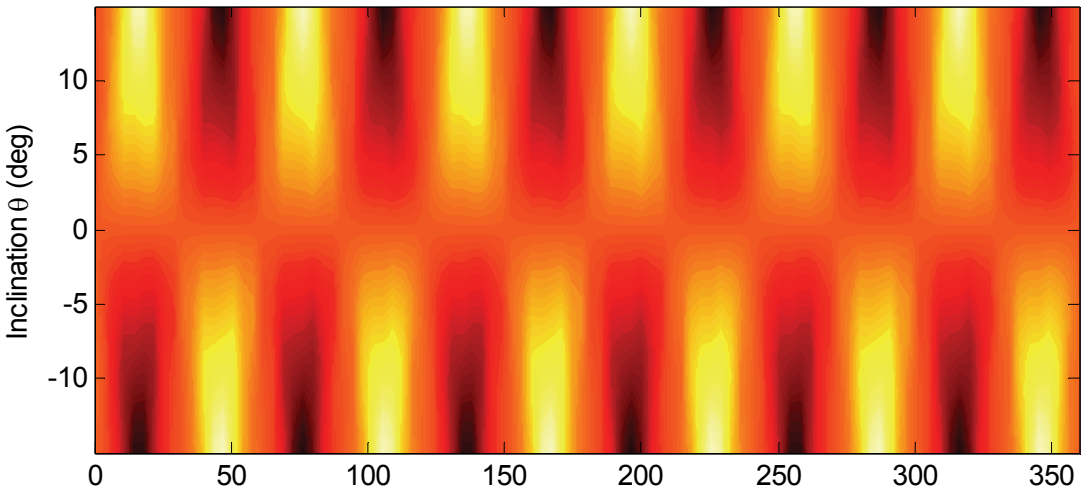

(b) *Y*-component

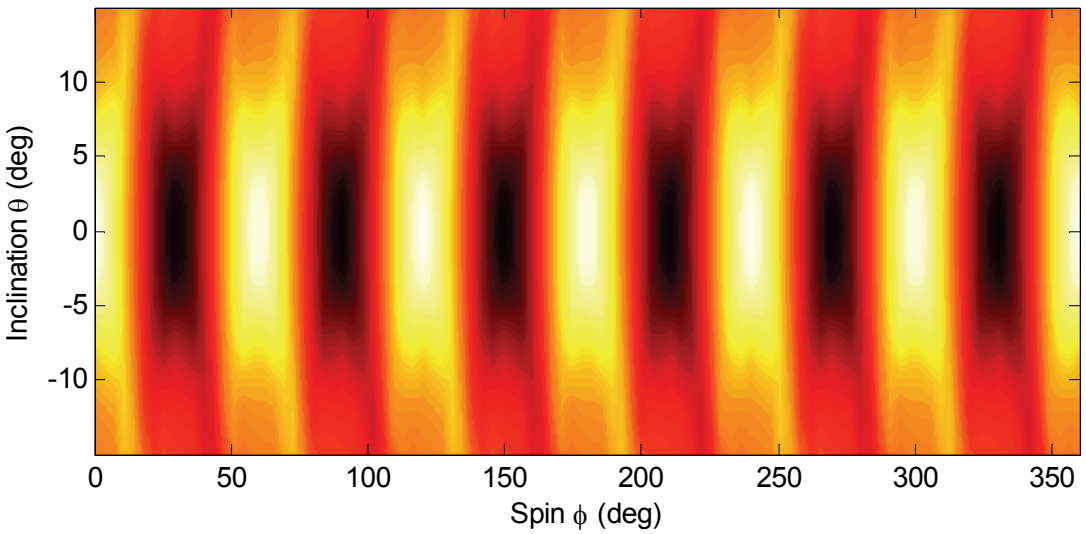

(c) *Z*-component

Figure 4-8 Contour field map of measurements by S_2 in parametric space (Units: Tesla)

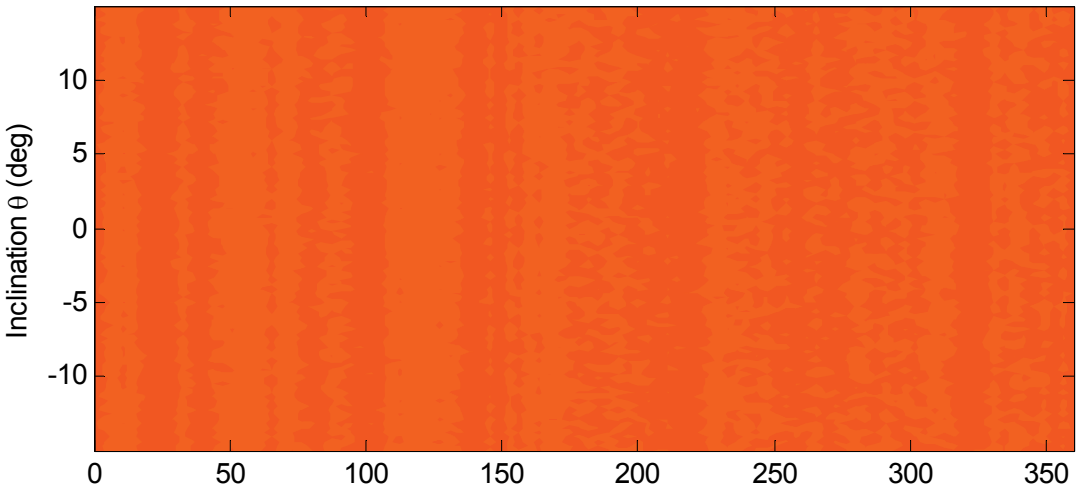

(a) *X*-component

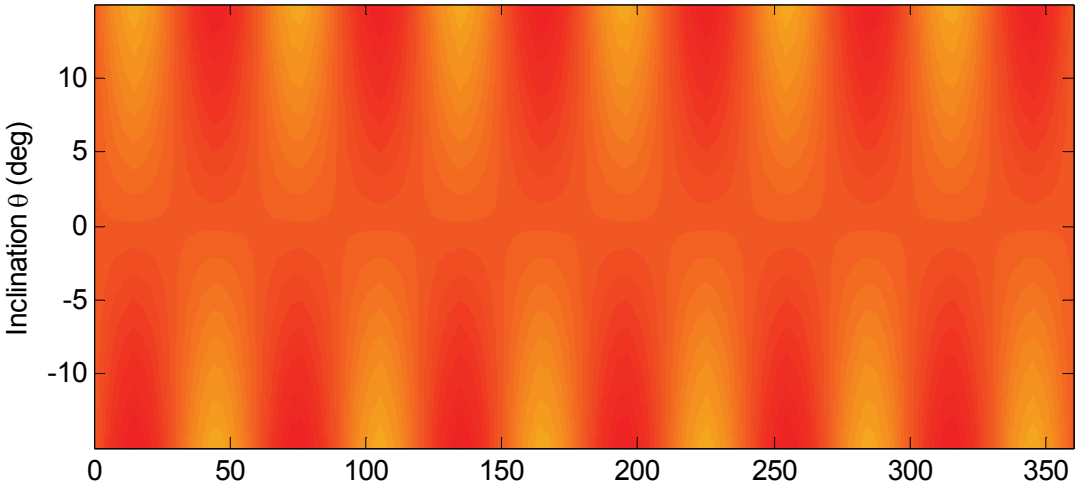

(b) *Y*-component

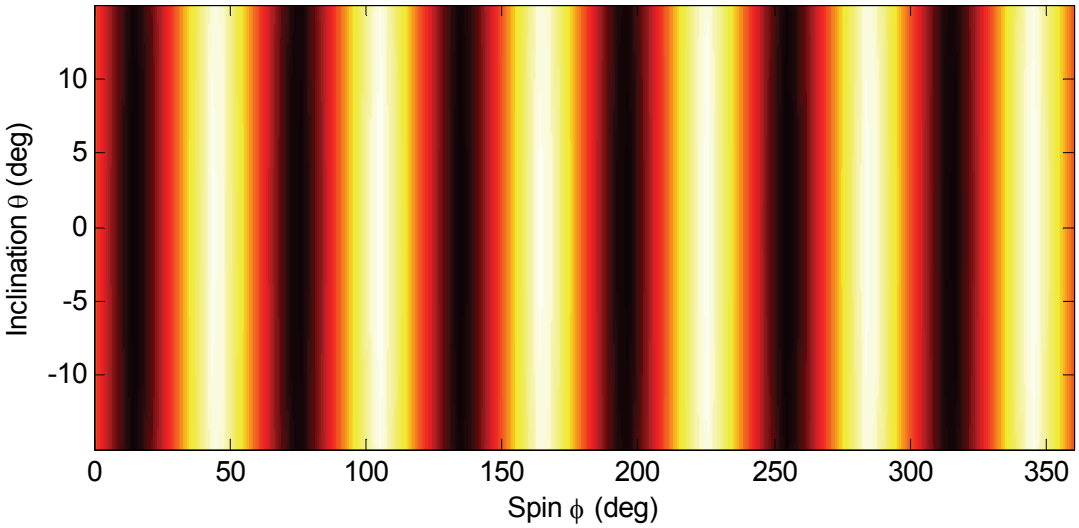

(c) *Z*-component

Figure 4-9 Contour field map of measurements by S_3 in parametric space (Units: Tesla)

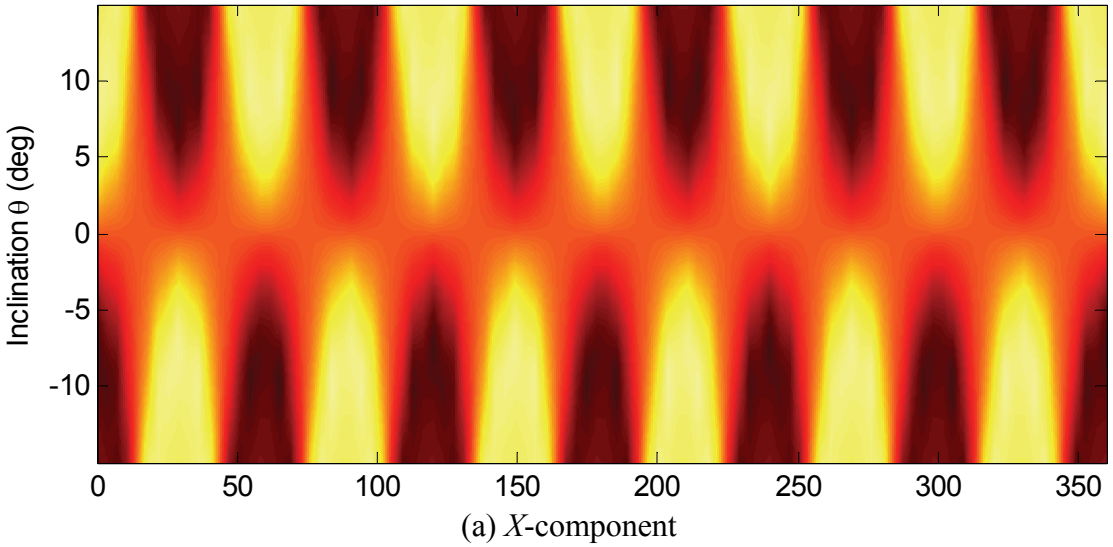

(a) *X*-component

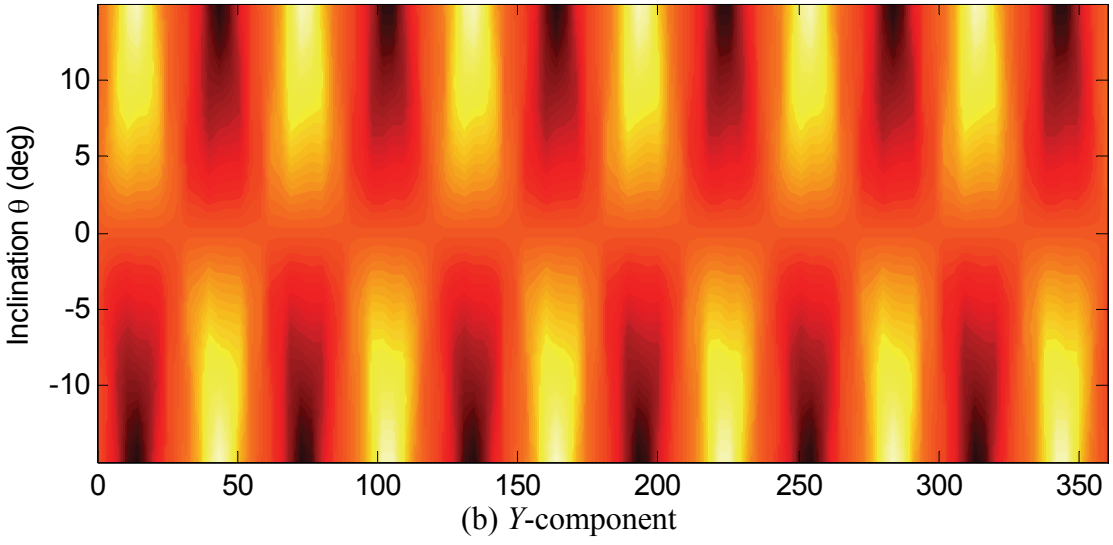

(b) *Y*-component

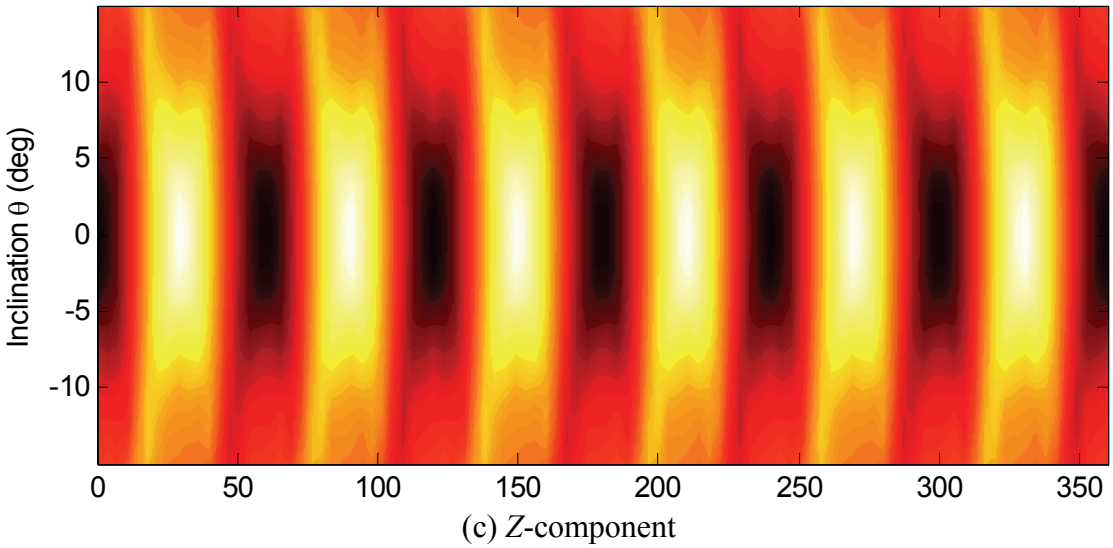

(c) *Z*-component

Figure 4-10 Contour field map of measurements by S_4 in parametric space (Units: Tesla)

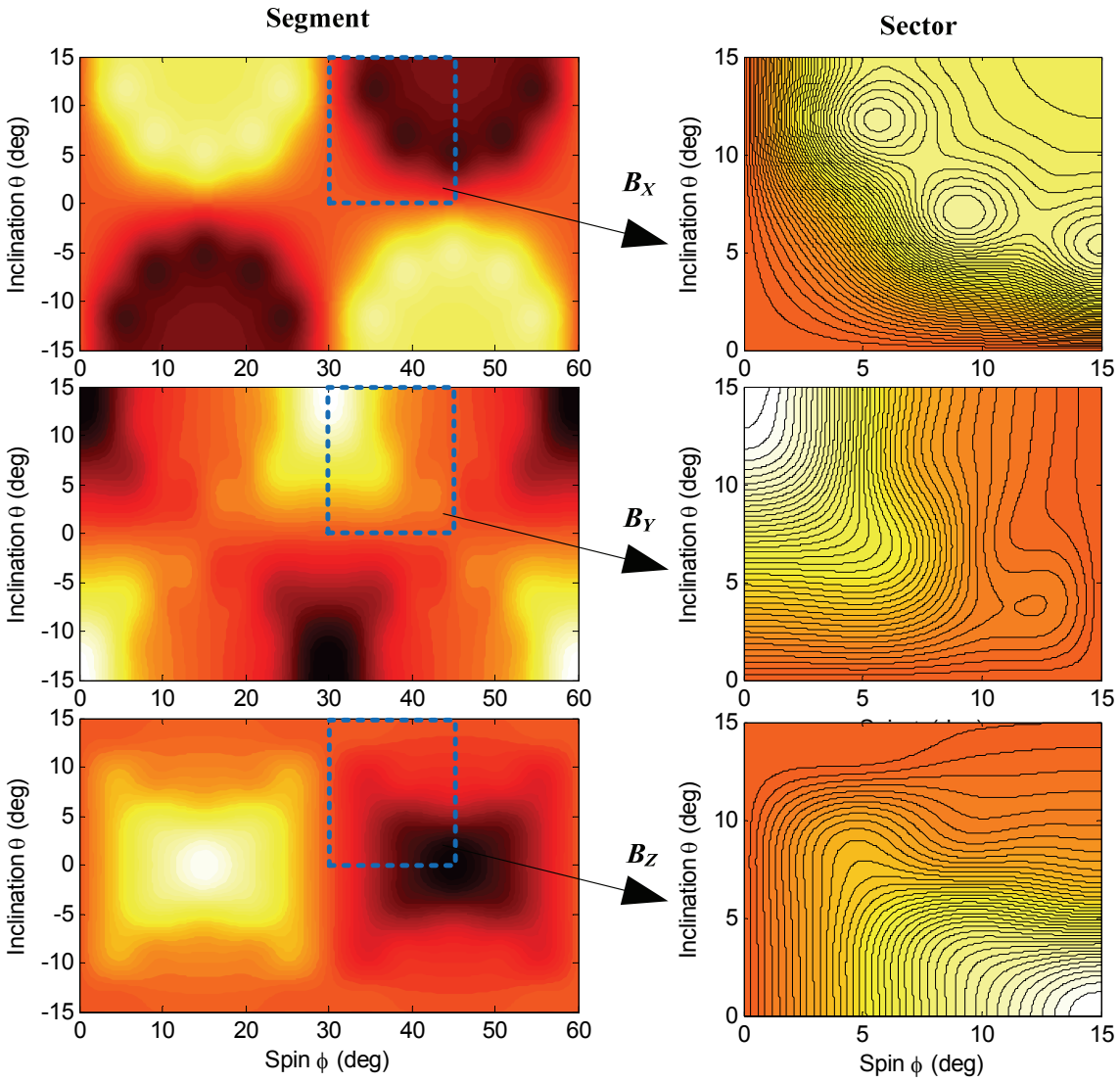

Figure 4-11 Segment and sector segregation for S_1

Sector Mapping Analysis

Using the map described by Figure 4-6 the 02th sector enclosed by the region $0 \le \theta \le \Phi / 4 = 15°$ and $0 \le \phi' \le \Phi / 4 = 15°$ is chosen to be characterized using the neural network. Back propagation artificial neural networks are used to characterize the mapping between magnetic flux density measurements by sensors to the angular positions of θ and ϕ. Each of the three sector surface (one for each axis) of S_1 in Figure 4-11 is discretized into a square 100×100 grid (resulting in 0.15° spatial resolution) to

produce 10000 pairs of training sets. Using these training sets, single hidden layer ANNs with varying number of hidden nodes are trained and the MSE and number of epochs required of the resulting network recorded. Training of the ANNs is halted once the gradient of the MSE is reduced below 0.0001. The MSE of the ANN angular estimates of θ and ϕ in logarithmic scale are shown as a function of the number of hidden nodes in Figure 4-12. Increasing the number of nodes generally reduces the MSE and for 10000 training sets, the MSE converges to 10^{-2} deg^2 when h=100. The number of epochs required to reach the stopping training criteria remains fairly constant throughout.

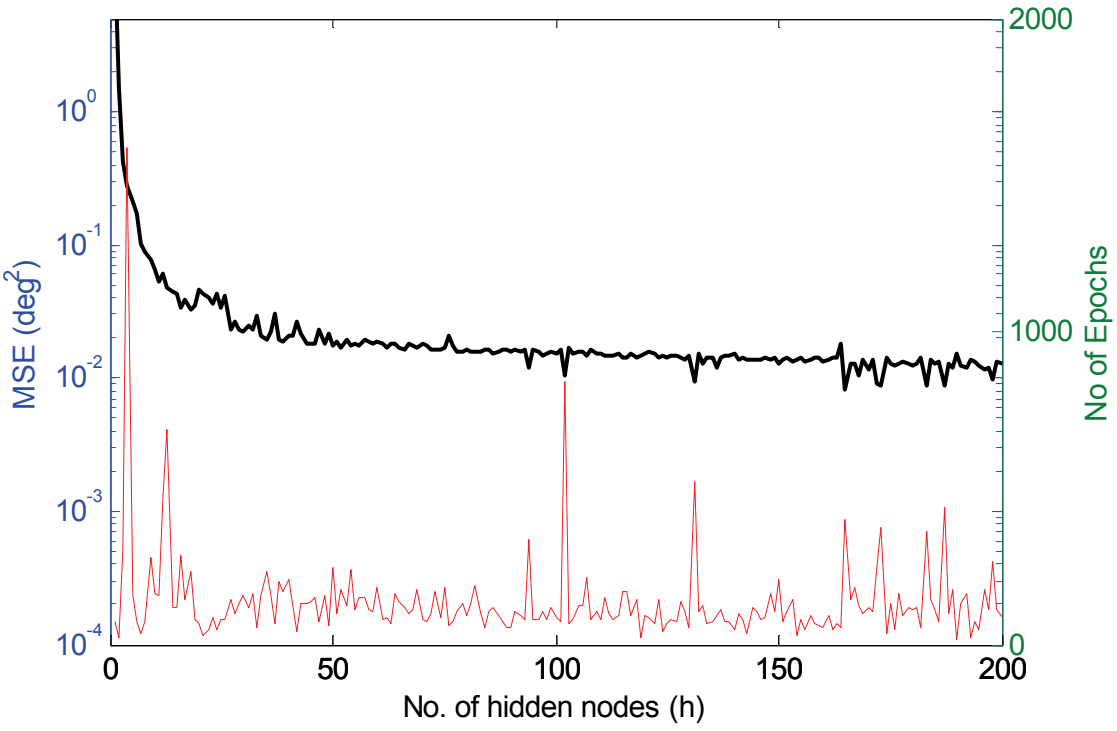

Figure 4-12 MSE and required epochs as a function of hidden nodes

The angular error of the estimates of θ and ϕ' of the neural networks at each training set is compiled in Figure 4-13(a) and (b) respectively for h=5, 20 and 70. As suggested by the plots, increasing the number of hidden nodes reduces the angular error

across the entire sample set. A spatial distribution of the absolute angular error across the sector surface is shown in a 3-D plot in Figure 4-13(c). For the network with 70 hidden nodes, the absolute errors for both angle estimates throughout the surfaces are less than 1.5° and over 90% of the surface has an absolute error less than 0.5°.

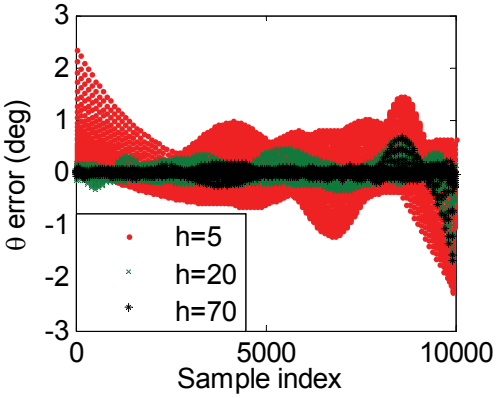

(a) Error of $\hat{\theta}$ at each sample.

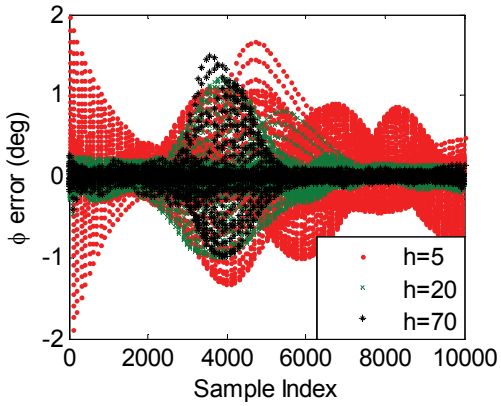

(b) Error of $\hat{\phi}'$ at each sample.

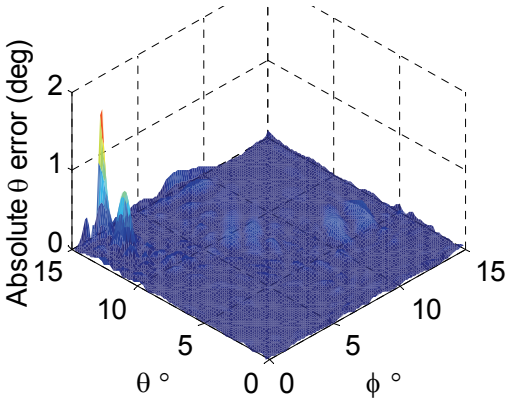

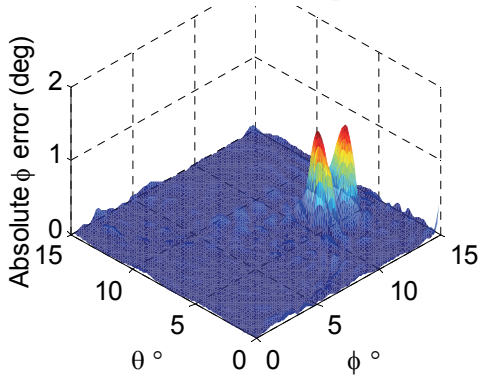

(c) Spatial distribution of $\left|\hat{\theta}-\theta\right|$ (left) and $\left|\hat{\phi}'-\phi'\right|$ (right). (h=70)

Figure 4-13 Error analysis of different neural networks

Another method of adjusting the order of the ANN is the number of hidden layers in the ANN. By maintaining the total number of hidden nodes in the ANN constant (100), the number of hidden layers was incrementally adjusted from 1 to 4. Using the segment training sets, each ANN is trained until the stopping criteria is met. Training is halted once the gradient of the MSE is reduced below 0.0001. The MSE and number of epochs

required for each ANN is tabulated in Table 4-3. Although the total number of hidden nodes in all layers might be equal, the total number of weights will not. Among the neural networks, the two hidden layer ANN had the most weights. However, as the data suggest, despite having fewer weights, the 3 layer neural network possesses the lowest MSE of 2.08×10^{-4} deg^2 as well as requiring the fewest epochs (175) to achieve it. In addition, a two hidden layer ANN with 50 hidden nodes in each layer outperforms a similar a single hidden layer ANN possessing the same number of weights. Although the former requires more epochs, the difference in MSE clearly suggests that the MSE is more sensitive to the number of layers and hidden nodes in the layer than the number of weights in the ANN.

Table 4-3 Effects of ANN architecture on MSE

N_1,N_2=100 No of hidden layers, g	Nodes per hidden layer, h	Total nodes	Total weights	Epochs	MSE (deg^2)
1	100	100	500	253	0.0152
2	50	100	2750	328	0.00104
3	33	99	2343	175	2.08×10^{-4}
4	25	100	2000	185	0.00159
1	550	550	2750	259	0.00695

The mapping performance is also dependent on the density of the training sets in the sector. To investigate this sensitivity, a single hidden layer ANN with 100 hidden nodes is used to train six different training sets. The difference between all six training sets is the various degree of discretization of the sector. For N_1=N_2=10, the spatial resolution is 1.5° and produces a total 100 training sets. The same gradient stopping criteria is applied to halt further training of the ANN in each case. To provide a fair comparison across all ANNs, a randomized set is used to test the ANN performance at

non training set data points. The results of these simulations are shown in Table 4-4. The results depicts a trend of increased required number of epochs and reduced training MSE (MSE resulting from training sets) with decreasing spatial resolution. The MSE obtained from applying the randomized set is higher for high spatial resolutions and this can be attributed to the poor spatial interpolation of the ANN between training data points. For spatial resolution lower than and equal to 0.15°, the randomized MSE are comparable to the training MSE.

Table 4-4 Effects of training set resolution on MSE

$g = 1$ N_1,N_2	$h = 100$ Training sets	Spatial resolution (deg)	Epochs	Training MSE (deg^2)	Randomized MSE (deg^2)
10	100	1.5	6	0.0114	2.9394
25	625	0.6	49	0.0152	0.0444
50	2500	0.3	220	0.0144	0.0223
100	10000	0.15	128	0.0154	0.0149
200	40000	0.075	492	0.0109	0.0104
400	160000	0.0375	2404	0.0085	0.0079

With 4 independently located sensors (S_1, S_2, S_3 and S_4), the mapping performance and accuracy can be improved by utilizing measurements from a combination of all available sensing measurements. With four sensors, up to a total of 12 independent sensing measurements are available. Table 4-5 summarizes the resulting MSE from pertinent combinations of sensors and sensing axes. From the data, for a single hidden layer ANN with 50 hidden nodes, the MSE drastically decreases as the number of inputs is increased. For better comparison, the absolute θ and ϕ error as a function of training sample index for different number of inputs is shown in Figure 4-14. This figure clearly shows the lower mapping error with increased number of sensors used.

Another point of interest is that for the same number of inputs, the mapping accuracy is sensitive to both the selection of the sensors and sensing axis. Among the cases with 4 inputs, the specific selection of *Y* and *Z* axes produced the lowest MSE (comparable to 6 input case using sensors 1, 2 and 3). In addition, for the mapping involving 2 sensors, selecting S_1 and S_4 had lower MSE than the other cases of S_1 and S_2 and S_1 and S_3. The lowest MSE is obtained by training the ANN using all 4 sensors (12 inputs) and the error distribution illustrated spatially is shown in Figure 4-15. For both plots, the maximum error does not exceed 0.0004°.

Table 4-5 MSE resulting from various combination of sensors and sensing axes

g=1, h=50	Epochs=5000	N_1,N_2=100	
No. of Inputs	Sensors	Axes	MSE (deg^2)
3	1	*X,Y,Z*	0.0166
4	1,2	*X,Y*	0.0958
4	1,2	*X,Z*	0.00147
4	1,2	*Y,Z*	5.81×10^{-5}
6	1,2	*X,Y,Z*	1.48×10^{-6}
6	1,3	*X,Y,Z*	4.14×10^{-5}
6	1,4	*X,Y,Z*	9.84×10^{-7}
9	1,2,3	*X,Y,Z*	2.62×10^{-7}
12	1,2,3,4	*X,Y,Z*	3.55×10^{-9}

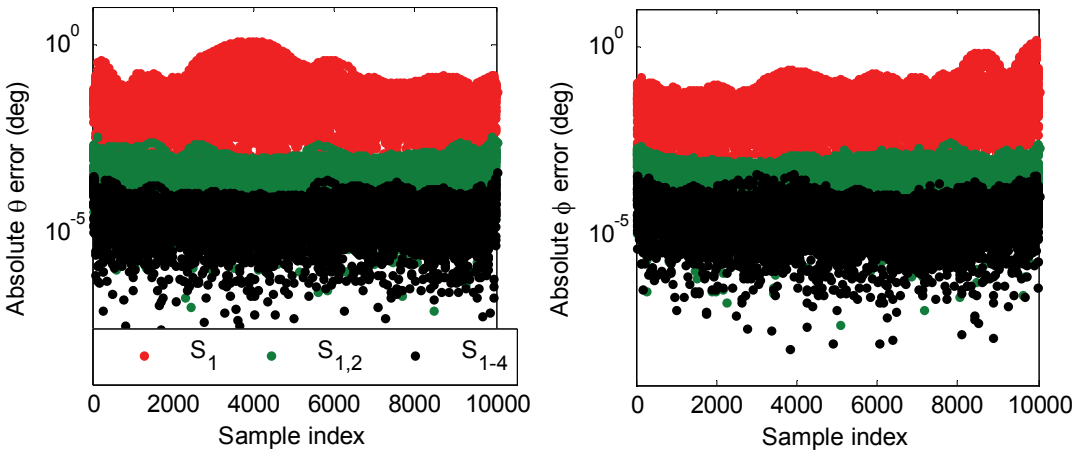

Figure 4-14 Absolute mapping error resulting from using multiple sensors

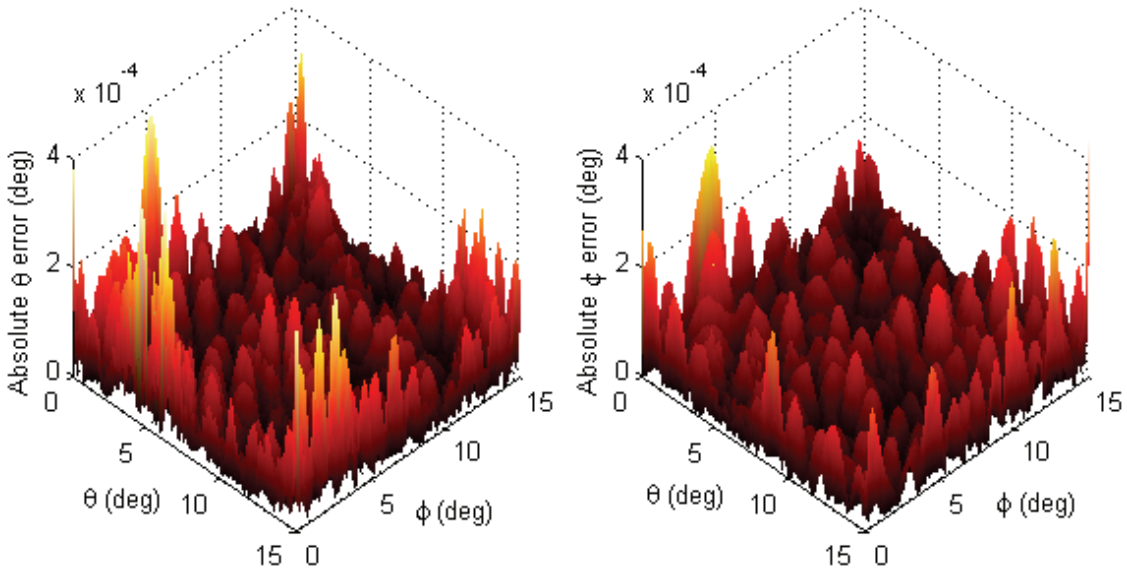

Figure 4-15 Spatial distribution of $\left|\hat{\theta}-\theta\right|$ and $\left|\hat{\phi}'-\phi'\right|$ for ANN using 4 sensors

4.3.2 3 DOF Characterization

In the 3 DOF case, the total range of motion is the unrestricted spin of the rotor about the z-axis $(-\infty \le \phi \le \infty)$, inclination of the rotor about the y-axis ($-15° = -\theta_{\max} \le \theta \le \theta_{\max} = 15°$) and direction of the inclination axis $(0 \le \psi \le \pi)$. As with the 2 DOF case, only the segment and/or sector mapping is required. However unlike the 2 DOF case, the 3 DOF forward parametric space is no longer in 2-D but in 3-D and this increase in dimension reduces the number of sectors in a segment from 8 to 2. The volumetric field plot of the segment in parametric space is produced in Figure 4-16 using a conic plot. The direction and size of the arrow represent the direction and magnitude of the field at that point respectively. The MSE of the ANN mapping using all 4 sensors and every sensing axis (12 inputs in total) are tabulated in Table 4-6. Results are consistent with the 2-D case.

Table 4-6 MSE of 3-DOF mapping

Spatial Grid	No of hidden layers, g	Nodes per hidden layer, h	MSE (deg^2)
$N_1 = N_2 = 31$	3	33	0.8668
$N_3 = 46$	3	55	0.7105

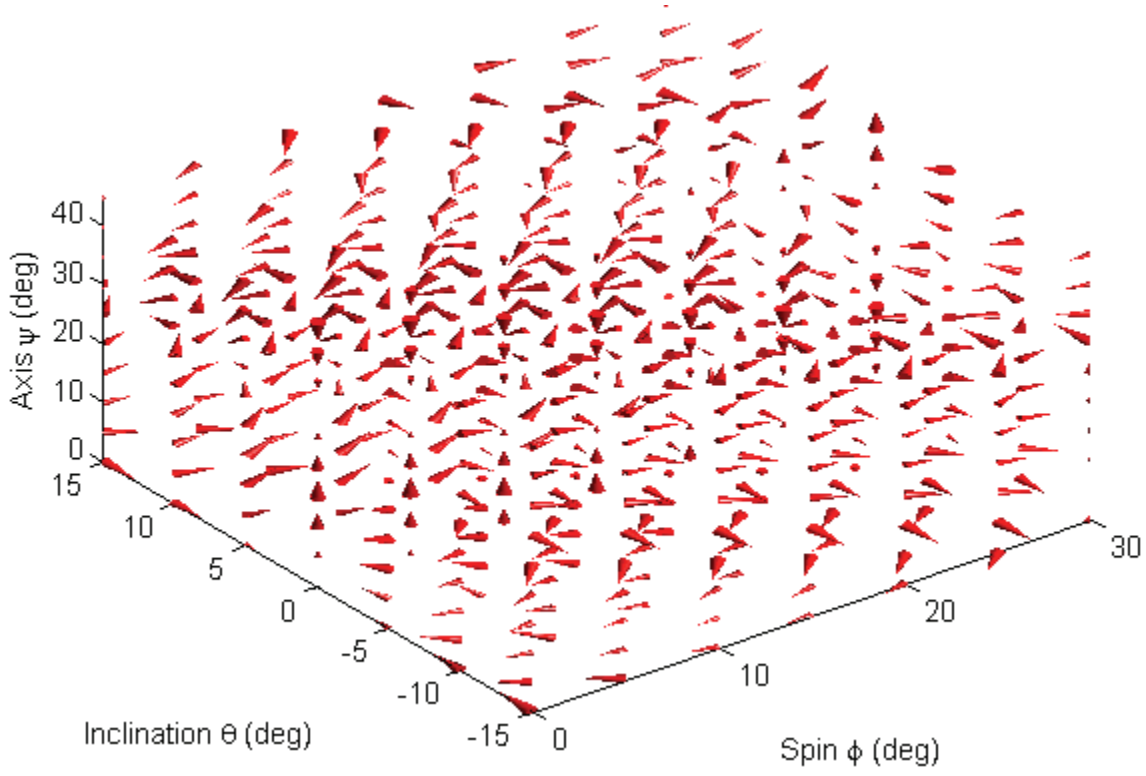

Figure 4-16 3-D sector volumetric parametric space by S_1 in forward parametric space

4.4 EXPERIMENTAL INVESTIGATION

This section provides the experimental investigation of the field-based sensing system using industrial magnetic sensors. From simulations in the preceding section, due to the close proximity of the PMs, the multi-axis sensors were required to measure fields up to 0.5 T. Although high-field magnetic sensors measuring up to 2 T are available, they are only available in single-axis packages (Asahi HG-362A). The multi-axis magnetic

sensor available commercially with the largest measuring range of 7.3 mT is the Ametes MFS-3A. In this study, the performance of using both types (high and low field) of sensors will be examined. Due to the limited range of the multi-axis low field sensors, they have to be positioned further away from the PMs to avoid saturation which necessitate the adjustment of the sensor plane (H_s).

4.4.1 Using Low Field Sensors

In order to obtain a correspondence between orientation and measured rotor field, the rotor is rigidly attached to a rotary track of radius R by means of a mechanical strut as shown in Figure 4-17. The center of the rotary track is positioned such that it coincides with the spherical bearing of the rotor. The arc length of the track contains measurement markings that allow correspondence between the curvature distance, ρ and inclination, θ. An optical incremental encoder (Kübler T8.A02H) with a resolution of 1000 counts per revolution is affixed onto the strut to measure the spin position of the rotor. The sensing network, comprised of two 3-axis Hall-effect magnetic field sensor (Ametes MFS-3A), are fixed to the top of the stator base at a vertical offset of $-H_s$ from the bearing center. A photo illustration of the rotor attached to the rotary track is shown in Figure 4-18. The parameters used in the experiment are tabulated in Table 4-7.

Table 4-7 Experimental parameters

Sensor:	$2s_T = 2$, $H_S = 3.04$ cm
Setup:	$R = 31.34$ cm, $\theta_{max}=22.5°$, $\Phi=60°$

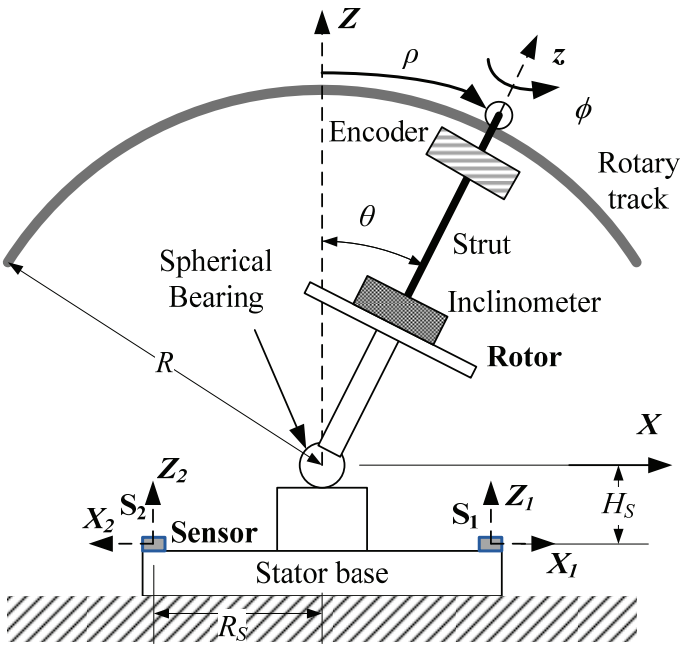

Figure 4-17 Schematic of experimental setup using multi-axis weak-field sensors

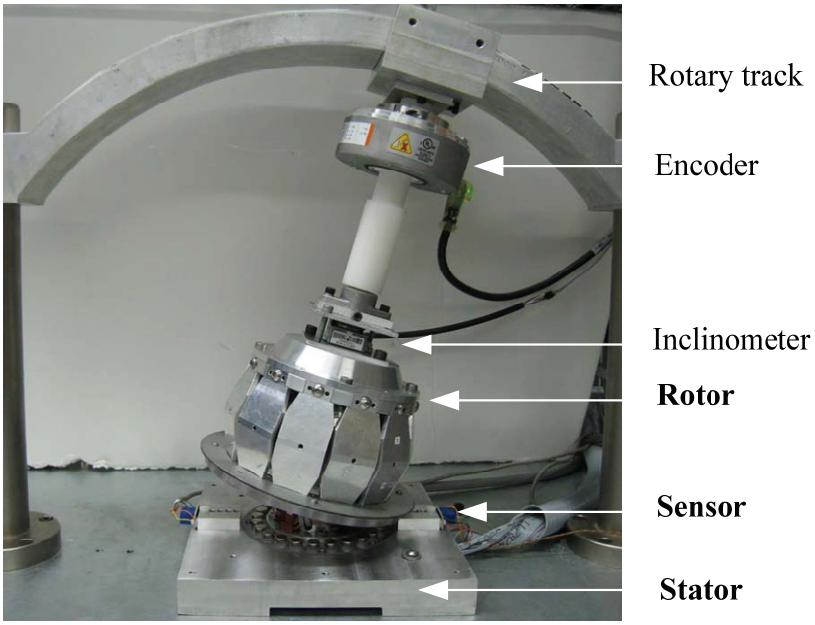

Figure 4-18 Experimental setup

The electrical and communication schematics of the setup are presented in Figure 4-19. It is largely similar to the setup in Figure 3-3 with the exceptions of the 3-axis Hall-Effect sensors powered by 5V DC power supply and the optical encoder replacing the

stepper motor. The quadrature outputs of the encoder are captured using a high-speed counter module attached to the SAG and relayed to the computer/HMI for data capture and display respectively.

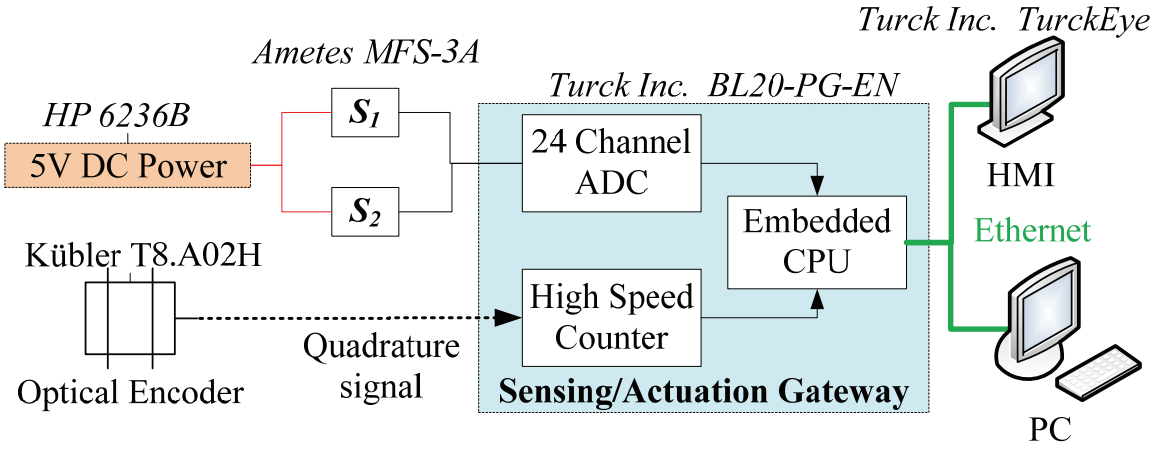

Figure 4-19 Electrical and communication schematics

4.4.1.1 2-DOF Characterization

The simultaneous measurement of all three sensing axis of both sensors along with the two independent orientation angles (θ, ϕ) allow construction of a 2-D surface field map for each sensing axis of each sensor as depicted in Figure 4-20. As a result of the spatial periodicity of the rotor PM configuration, there will be a total of 6 segments. As there are two 3-axis sensors, each segment contains six 2-D surface field maps. Each segment can be further divided into sectors through magnetic field symmetry. Due to the displacement of the sensor plane, the segment loses some symmetry and instead of the 8 sectors in the simulations, only 2 sectors exist.

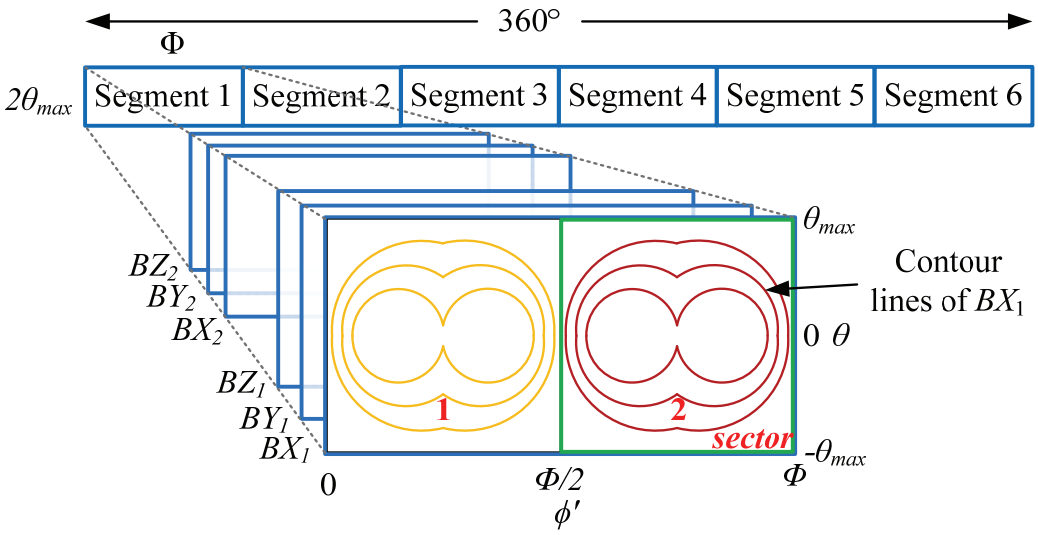

Figure 4-20 Segmentation and sectorization of 2-D surface map

To experimentally construct these surface maps, the rotor was preset to known inclinations ($-22.5° < \theta < 22.5°$) using the rotary track (at 5 mm increments measured on the track or 0.914° measured angularly) and the field measurements **B** of the 3-axis magnetic Hall-Effect sensors were recorded as the spin of the rotor is rotated at 0.36° increments (1000 data points per inclination set point). A complete contour field map (2-D image with 47×1001 pixels) for each sensing axis of sensors S_1 and S_2 are reproduced in Figure 4-21 and Figure 4-22 respectively. Through visual inspection of both figures, 6 distinct segments (demarcated by $(n-1)\Phi \le \phi \le n\Phi$, for n=1,…,6) can be easily detected. As this pair of sensors is located directly across from each other, their 2-D field maps are mirror images of each other about the ϕ-axis.

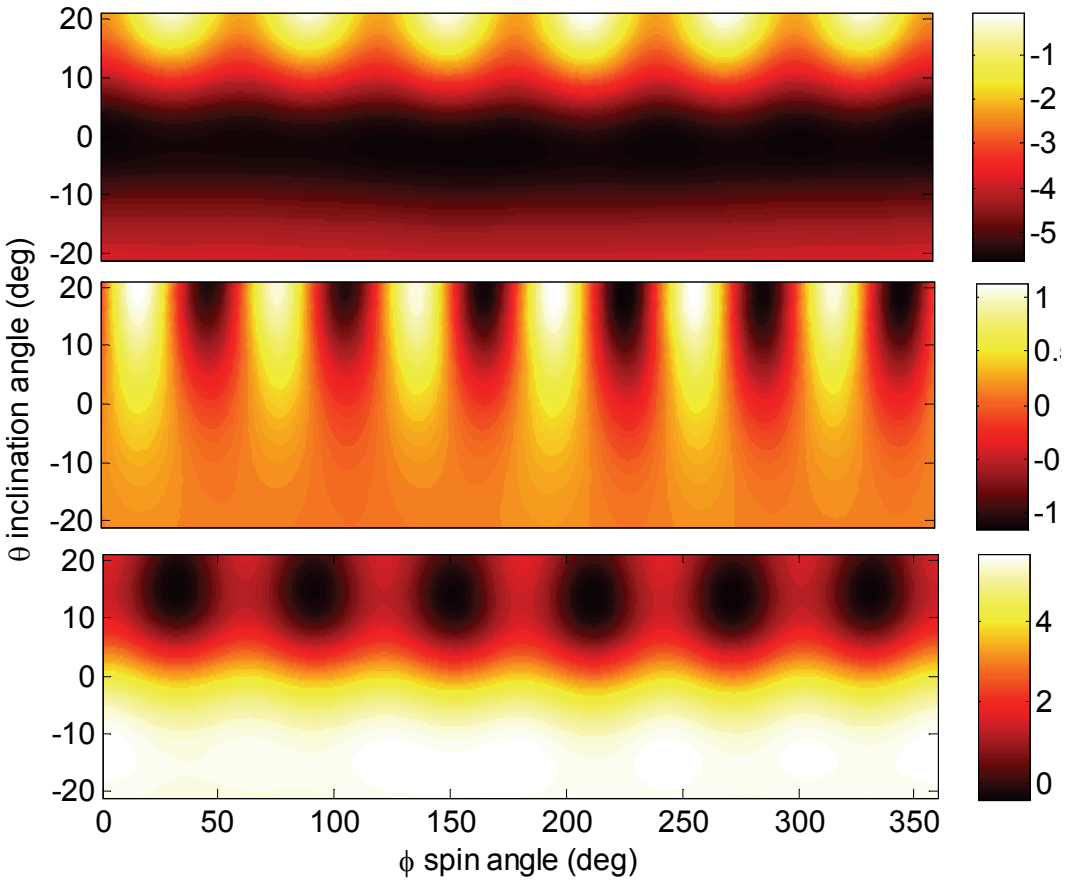

Figure 4-21 Contour field map for S_1 (Top: B_X, middle: B_Y, bottom: B_Z, units: mT)

The contour map of a single segment is presented in Figure 4-23 to offer a closer view to the intricate non-linear magnetic field map. Unlike the segment field maps of B_X and B_Z, the segment field map of B_Y is particularly unique as it allows discerning and identification of sectors via the direction of the field measurement in B_Y.

By only considering the magnitude ($|B_X|$, $|B_Y|$ and $|B_Z|$) and sensitivity analysis is performed. This analysis measures the rate of change of field magnitude per unit change in orientation and allows identification of areas of large field changes which corresponds to higher SNR. The sensitivity is computed from

$$\text{Sensitivity} = \left| dB_\eta / d\chi \right| \tag{4.10}$$

where η=X,Y or Z and χ=ϕ or θ.

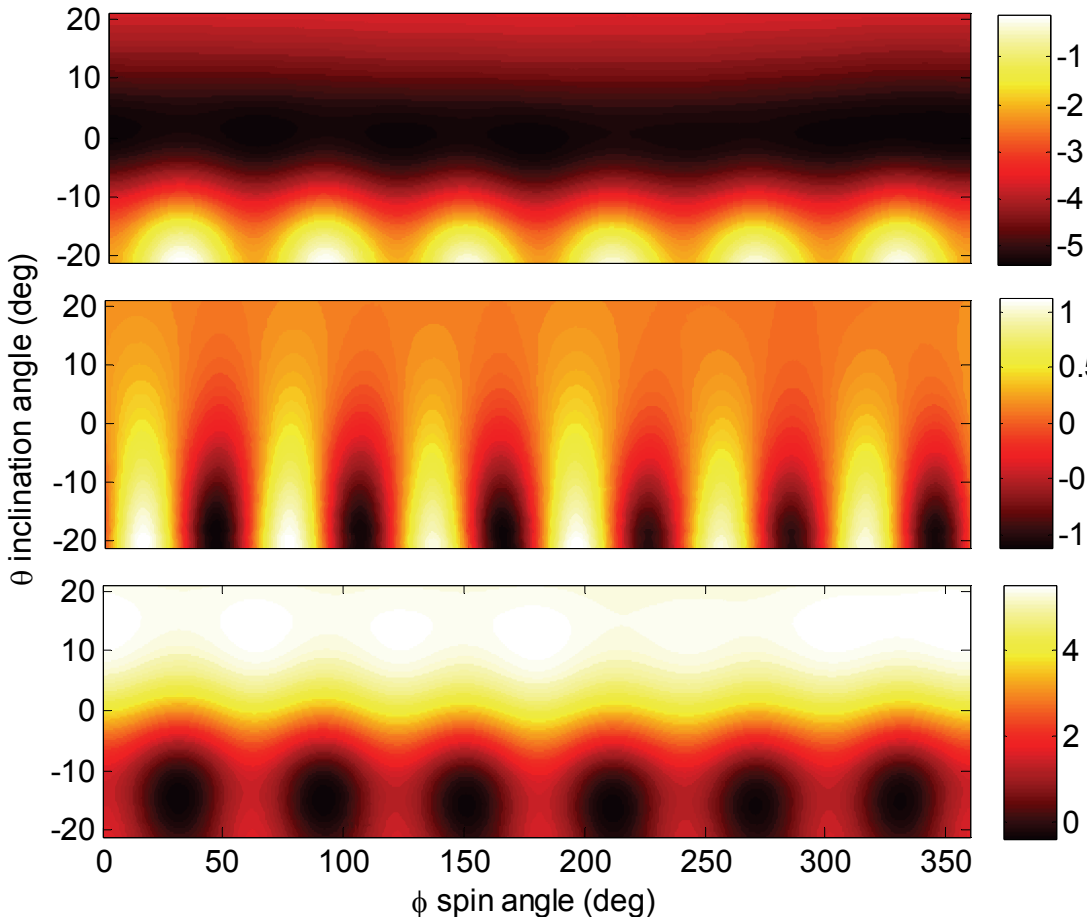

Figure 4-22 Contour field map for S_2 (Top: B_X, middle: B_Y, bottom: B_Z, units: mT)

The spatial distribution of field sensitivity of S_1 is compiled in Figure 4-24 where the columns represent three different sensing axis and the two rows signify the two independent rotor orientations. The sensing sensitivity of S_2 is similar to that of S_1 with the exception that they are mirrored about ϕ-axis. From Figure 4-24, it is observed that the sensitivity for positive θ inclination is significantly higher than the sensitivity in the negative θ inclination. Noting that the field measurements of S_2 are mirrored about ϕ-axis, the sensitivity for S_2 will be more pronounced for negative θ inclination.

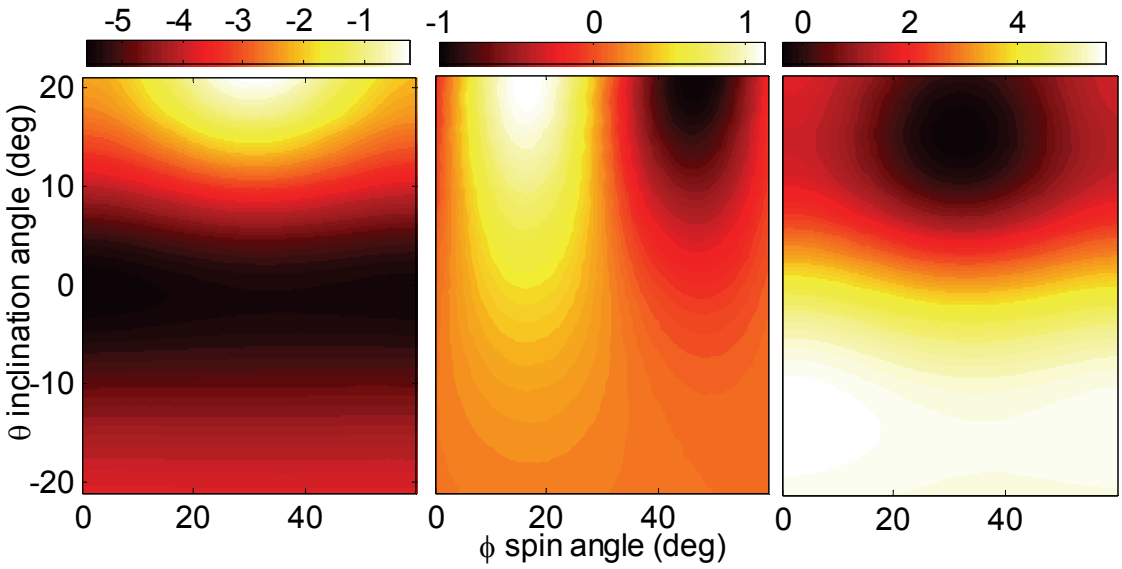

Figure 4-23 Segment field map for S_1 (Left: B_X, middle: B_Y, right: B_Z, units: mT)

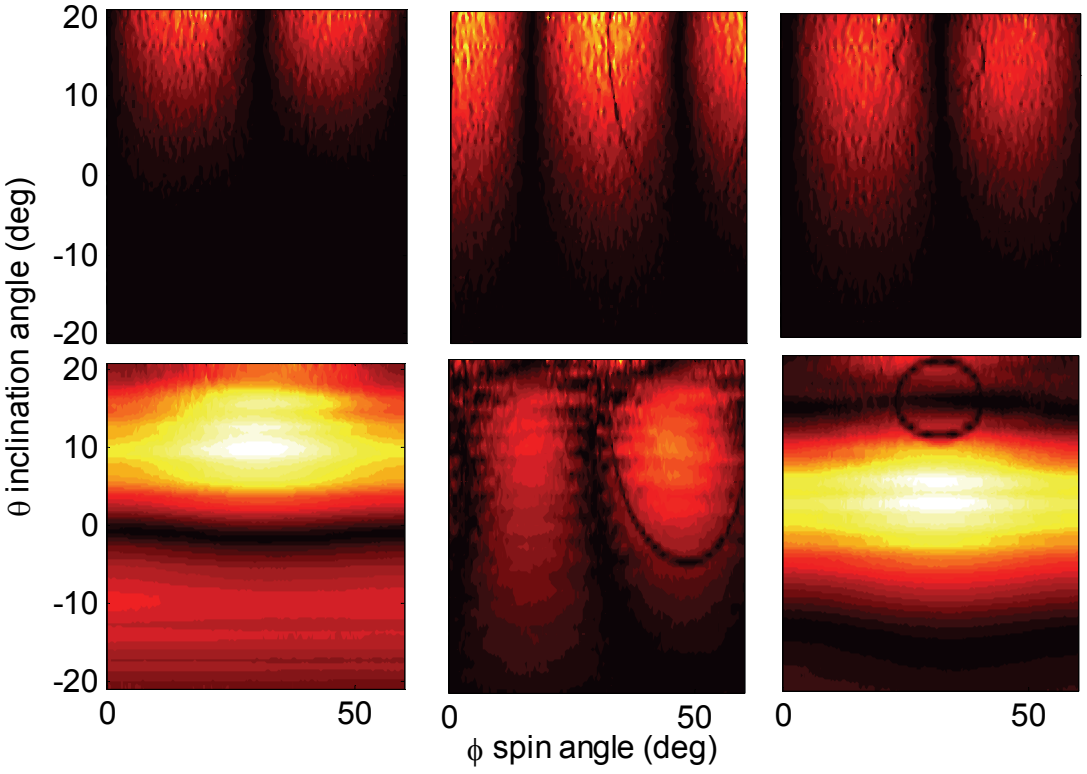

Figure 4-24 Sensitivity analysis for S_1 (Left: B_X, middle: B_Y, right: B_Z) (Top: w.r.t to ϕ)

4.4.1.2 Singular Segment Mapping

It is desired to obtain the rotor orientation from isolated field measurements Λ from the magnetic sensors. Within each segment, the mapping between orientation and magnetic field measurements of any single axis is not bijective (encompassing one-to-one correspondence) as evident in the presence on field contours (multiple positions share the field measurement). Hence, it is not possible to derive a mathematical expression that describes the inclination of the rotor from measurements of a single axis from any sensor. However, bijectivity can be obtained by considering simultaneous multiple axis measurements, multiple sensor measurements or combination of both. The segment map in Figure 4-23 is mapped rotor orientation using various combinations of B_X, B_Y and B_Z measurements from the two 3-axis Hall sensors and the MSE of the resulting map are compiled in Table 4-8. These mappings were achieved using an ANN with 25 hidden nodes.

Table 4-8 MSE resulting from multi-axis and multi-sensor segment mapping

ANN h=25				
Multi-axis		Multi-sensor/ Multi-axis		
S_1	MSE (deg^2)	S_1	S_2	MSE (deg^2)
X	54.3	*X*	*X*	4.91
Y	72.0	*Y*	*Y*	40.2
Z	31.2	*Z*	*Z*	5.87
XY	36.7	*XY*	*XY*	1.04
YZ	22.8	*YZ*	*YZ*	0.302
XZ	11.1	*XZ*	*XZ*	0.133
XYZ	**0.641**	***XYZ***	***XYZ***	**0.00737**
S_2	MSE (deg^2)	*XZ*	*Y*	4.74
X	51.9	*YZ*	*X*	2.87
Y	71.0	*XY*	*Z*	1.87
Z	29.1	*XY*	*YZ*	0.953
XY	34.8	*XZ*	*YZ*	0.0572
YZ	22.4	*XYZ*	*XY*	0.0418
XZ	3.97	*XYZ*	*XZ*	0.0330
XYZ	1.74	*XYZ*	*YZ*	0.0224

For mapping pertaining to multi-axis measurements, as expected, the MSE is high when using only single axis measurements (X,Y or Z only) for both S_1 and S_2. Using any two combinations of sensing axis from one sensor reduces the MSE of the resulting map and using all three sensing axes reduces the MSE an order of magnitude for both sensors. The spatial distribution of the absolute inclination and spin angle errors resulting from the ANN mapping which uses all three sensing axes of S_1 are shown in Figure 4-25 and Figure 4-26 respectively. These plots also illustrate the clustering of high errors near zero inclination. The lowest MSE (0.00815 deg^2) is obtained when using all sensing axes of both sensors (S_1 and S_2) and a spatial distribution of the absolute errors of both angles are shown in Figure 4-27 and Figure 4-28. These plots visually demonstrate that the absolute errors in the segment mapping never exceeds 0.6° and 0.15° for the θ and ϕ angles respectively. In addition, these errors are distributed evenly throughout the segment domain. MSE resulting from other combinations of multi-axis and multi-sensor mapping suggests that increasing the number of independent sensing measurements into the ANN generally reduces the MSE.

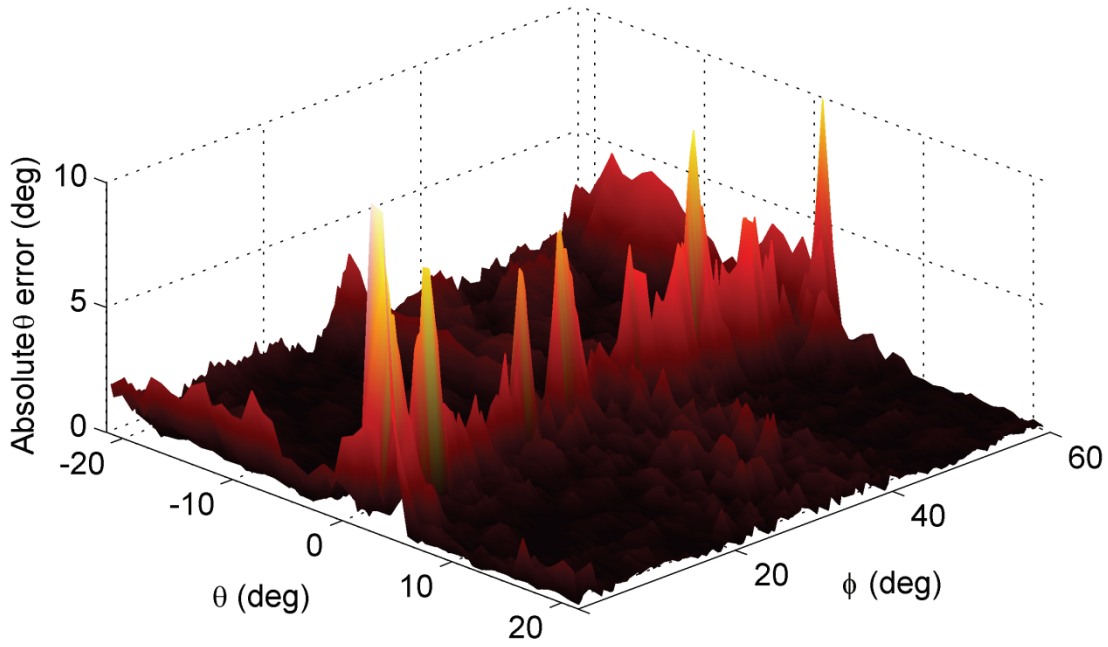

Figure 4-25 Spatial distribution of absolute inclination θ error for mapping using S_1 only

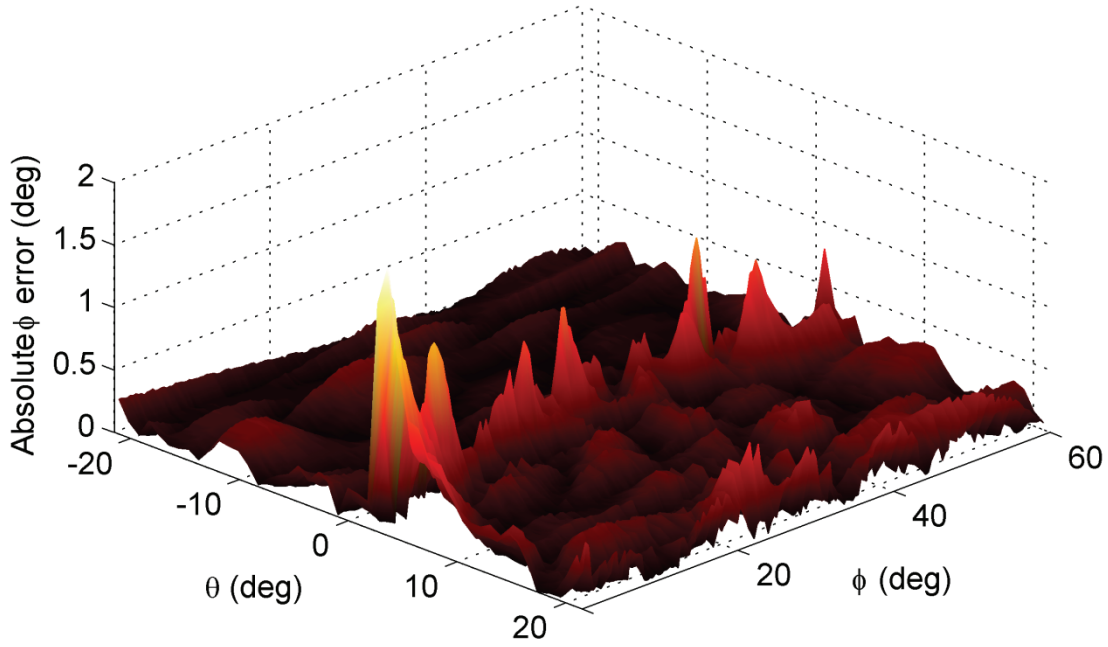

Figure 4-26 Spatial distribution of absolute spin ϕ error for mapping using S_1 only

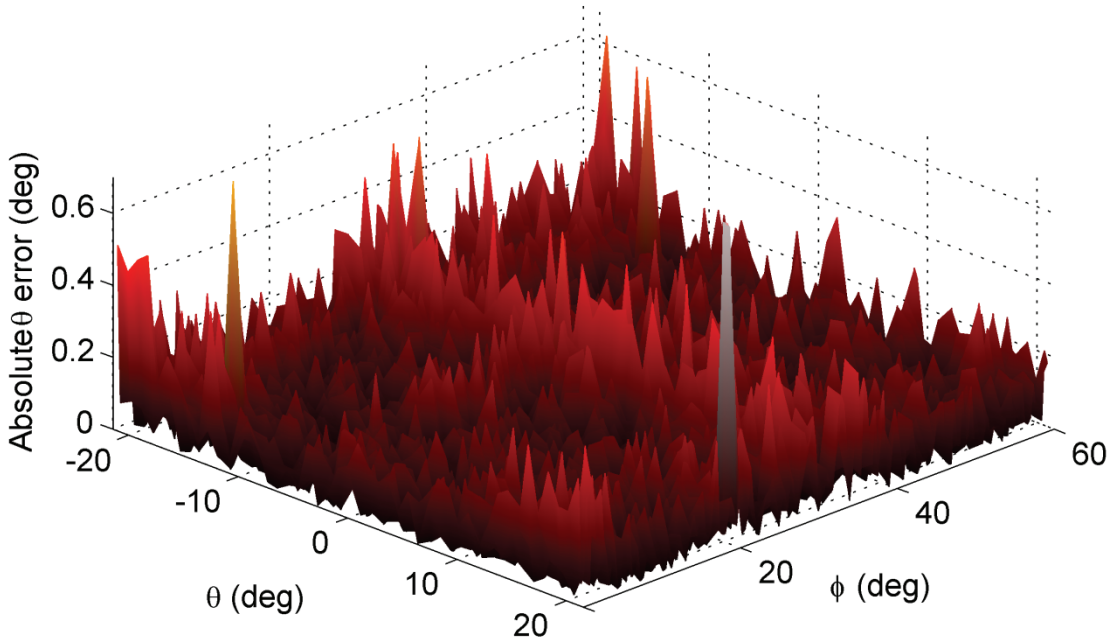

Figure 4-27 Spatial distribution of absolute inclination θ error using S_1 and S_2

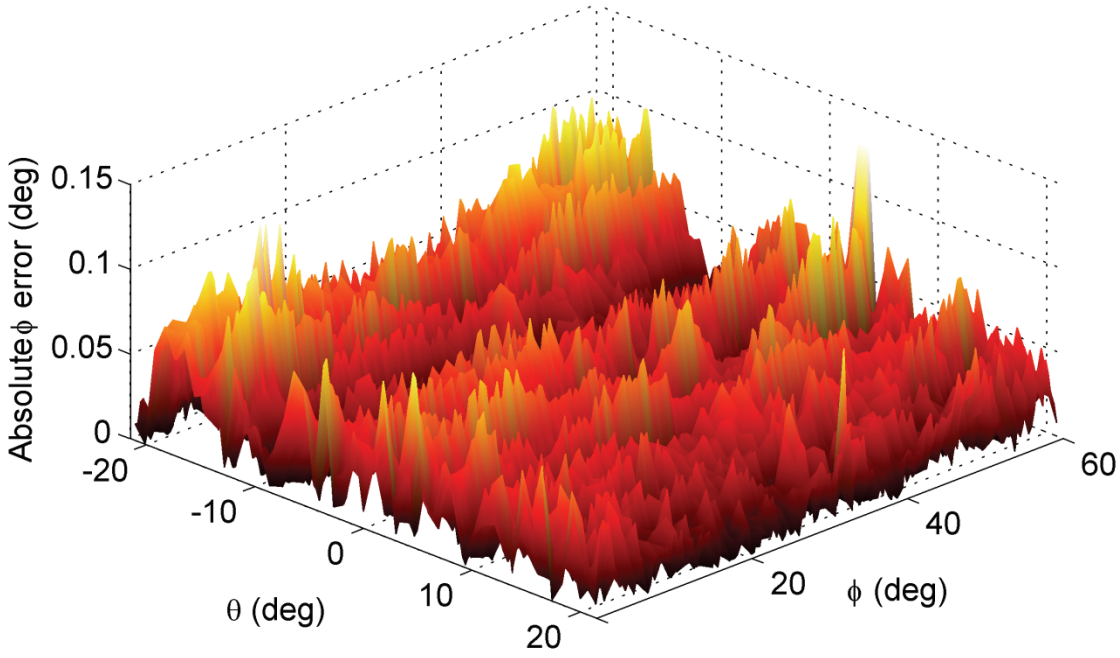

Figure 4-28 Spatial distribution of absolute spin ϕ error for mapping using S_1 and S_2

4.4.1.3 Multiple Segment/Sector Mapping

Using the two sectors in segment 1 as the reference segment and constructing fitting models in each sector, the field measurements in the remaining segments can be 'statistically standardized' using affine transformation. Using a joint 5th order polynomial surface fitting model (5th order in both ϕ and θ) to characterize both sectors of segment 1, the affine transformation coefficients for each of the remaining sectors in each segments can be computed for both sensors. As a single field measurement by a single sensor possesses 3 independent values (one for each sensing axis), the AT coefficients are no longer scalar quantities but matrix valued quantities: $\mathbf{a} \in \Re^{3\times3}, \mathbf{b} \in \Re^{3}$. Hence there are a total of 12 coefficients for each sector/segment AT transformation. The computed optimal values are tabulated in Table 4-9. Statistical visualization of the variation in field measurements in each segments for all three sensing axes without AT and with AT for both sectors in S_1 are shown in Figure 4-29 to Figure 4-32. From these plots, it is clear that statistically, the variation between segments are reduced after AT as shown by agreement of the means.

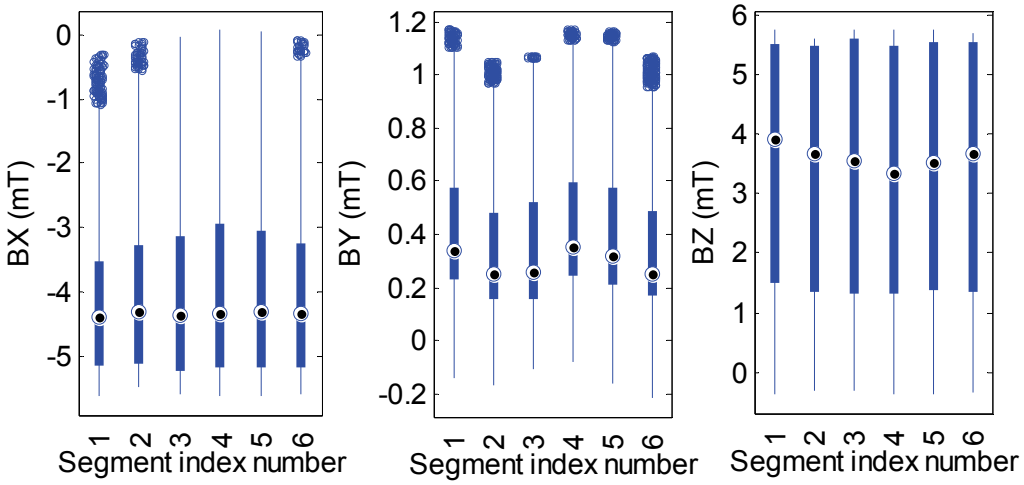

Figure 4-29 Sector 1 box plot of field measurements by S_1 in all segments

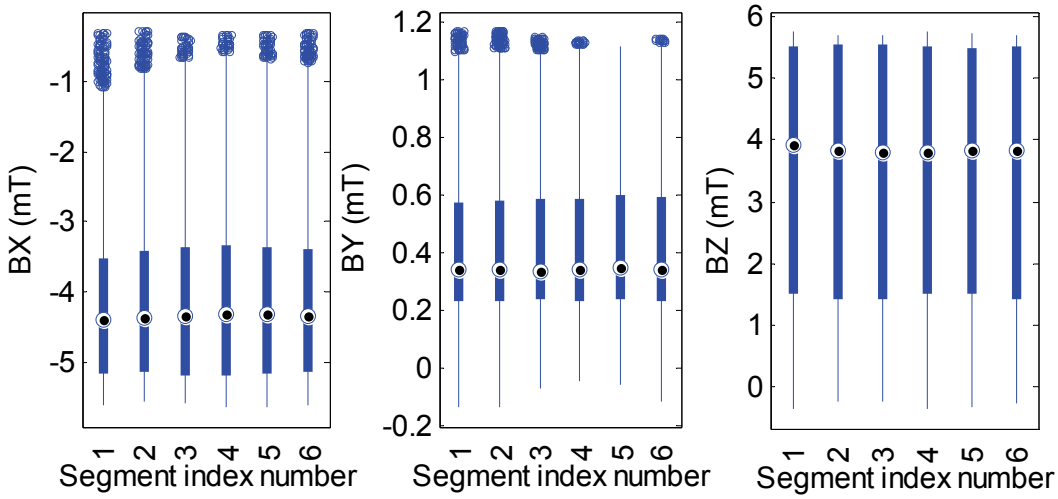

Figure 4-30 Sector 1 box plot of field measurements by S_1 in all segments after AT

Table 4-9 Sector affine transform coefficients for each segment in S_1 and S_2

	a_{11}	a_{12}	a_{13}	a_{21}	a_{22}	a_{23}	a_{31}	a_{32}	a_{33}	b_1	b_2	b_3
					S_1 (Sector 1)							
Seg 1	1	0	0	0	1	0	0	0	1	0	0	0
Seg 2	1.0079	-0.0893	-0.0409	0.0105	1.0897	-0.0005	0.0406	-0.0821	0.9736	0.1928	0.0212	0.0540
Seg 3	0.9925	-0.1184	-0.0901	0.0031	1.0432	0.0077	0.1182	-0.0727	0.9100	0.4031	0.0208	-0.0591
Seg 4	1.0165	-0.0540	-0.1335	-0.0035	0.9383	-0.0061	0.1976	0.0223	0.8889	0.5053	0.0500	-0.2573
Seg 5	0.9950	-0.0989	-0.1006	0.0046	0.9022	-0.0092	0.1448	-0.0433	0.9125	0.4662	0.0764	-0.1563
Seg 6	0.9877	-0.0546	-0.0433	0.0130	0.9931	-0.0160	0.0644	-0.0535	0.9510	0.2525	0.0874	0.0008
					S_1 (Sector 2)							
Seg 1	1	0	0	0	1	0	0	0	1	0	0	0
Seg 2	0.9950	-0.0523	-0.0312	-0.0112	0.9758	0.0168	0.0309	-0.1555	0.9625	0.1106	0.0178	0.0127
Seg 3	0.9808	-0.0974	-0.0751	-0.0054	0.8488	0.0006	0.1075	-0.2159	0.9079	0.3145	0.0375	-0.0995
Seg 4	0.9878	-0.1421	-0.1059	-0.0397	0.7590	0.0293	0.1477	-0.2075	0.8933	0.4791	0.0772	-0.1047
Seg 5	0.9661	-0.1424	-0.0605	-0.0334	0.8063	0.0239	0.0855	-0.1212	0.9317	0.4010	0.0620	-0.0453
Seg 6	0.9492	-0.1567	0.0110	-0.0220	0.7972	0.0181	-0.0272	-0.1613	0.9823	0.1385	0.0442	0.1015
					S_2 (Sector 1)							
	a_{11}	a_{12}	a_{13}	a_{21}	a_{22}	a_{23}	a_{31}	a_{32}	a_{33}	b_1	b_2	b_3
Seg 1	1	0	0	0	1	0	0	0	1	0	0	0
Seg 2	0.9705	-0.0522	0.0368	0.0091	0.9150	-0.0081	-0.0561	-0.1152	1.0149	-0.0277	0.0620	0.1544
Seg 3	0.9497	0.0002	0.0980	0.0168	1.0314	-0.0139	-0.1481	-0.1280	1.0478	-0.2047	0.0652	0.3586
Seg 4	0.9512	0.0841	0.1434	-0.0016	1.0235	0.0037	-0.2113	-0.0634	-1.0874	-0.4351	-0.0050	0.3890
Seg 5	0.9704	0.0034	0.1020	0.0124	1.1308	0.0024	-0.1722	-0.1333	1.0694	-0.2748	0.0043	0.4104
Seg 6	0.9616	-0.0557	0.0494	0.0059	1.0791	0.0094	-0.0877	-0.1130	1.0113	-0.0818	0.0046	0.2599
					S_2 (Sector 2)							
Seg 1	1	0	0	0	1	0	0	0	1	0	0	0
Seg 2	0.9667	-0.0092	0.0480	0.0063	1.0227	-0.0083	-0.0669	0.0799	1.0307	-0.0451	0.0022	0.0942
Seg 3	0.9355	-0.0560	0.1242	0.0250	1.0111	-0.0148	-0.1932	0.0084	1.0762	-0.2751	-0.0352	0.3015
Seg 4	1.0005	0.1583	0.1084	0.0410	1.1442	-0.0433	-0.1561	0.1811	1.0873	-0.4440	0.0071	0.1863
Seg 5	0.9949	0.0946	0.0791	0.0328	1.2094	-0.0178	-0.1324	0.0038	1.0563	-0.3371	-0.0355	0.2221
Seg 6	0.9864	0.0057	0.0287	0.0348	1.0353	-0.0387	-0.0496	-0.0776	1.0027	-0.1335	0.0144	0.0974

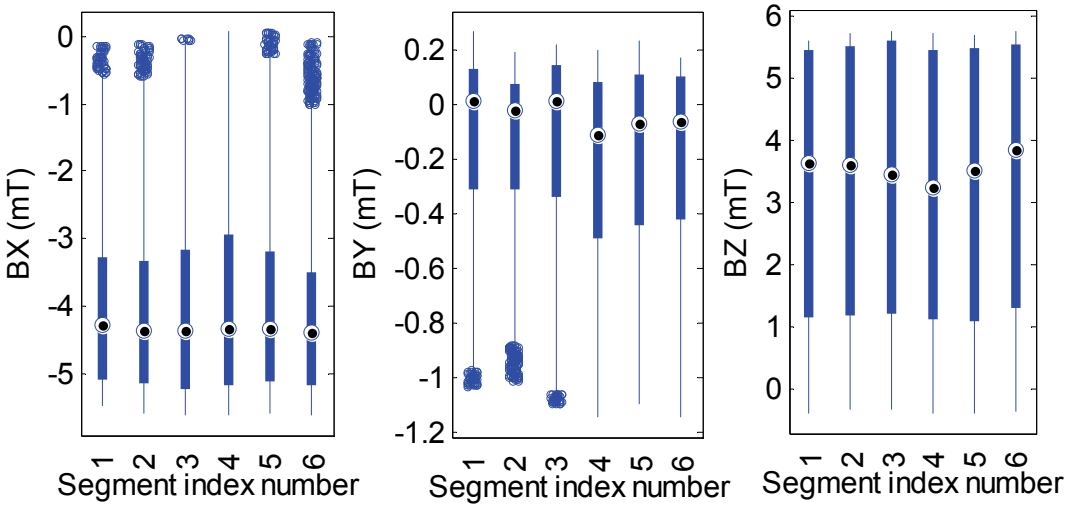

Figure 4-31 Sector 2 box plot of field measurements by S_1 in all segments

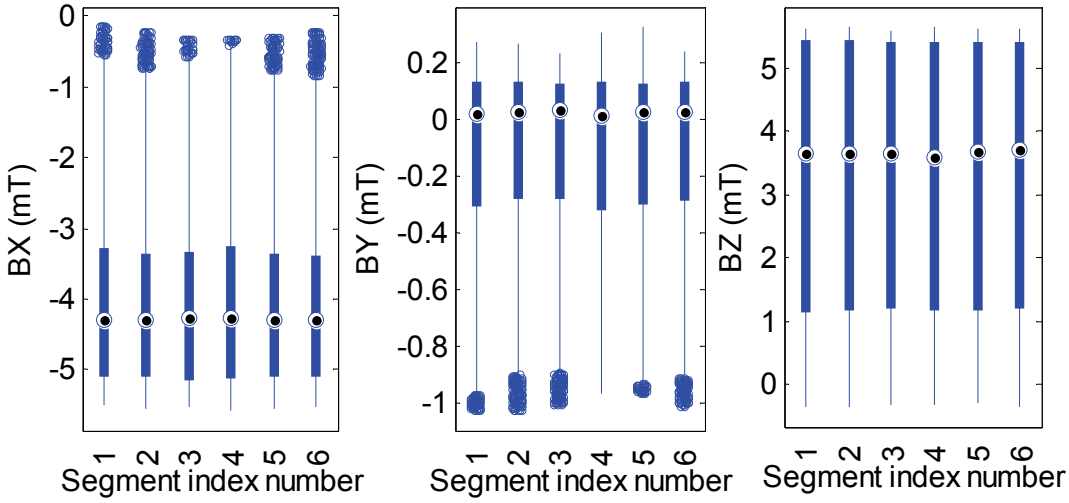

Figure 4-32 Sector 2 box plot of field measurements by S_1 in all segments after AT

Using sector 1 and 2 of the reference segment (segment 1), two independent ANNs (with 25 hidden nodes) are used to map field measurements to instantaneous orientation. Using all three field measurements of S_1 as input to the ANN, the resulting MSE of the mapping is 0.120 deg^2. As observed earlier in singular segment mapping, using all field measurements of S_1 and S_2 resulted in a significantly lower MSE of 0.00566 deg^2. Each of these reference maps can be applied on the other 5 segments and

the MSE computed in each segment. Table 4-10 summarizes the computed error of using trained reference ANN on the remaining 5 segments. When applied to the field measurements of other segments after AT, the errors are much lower than when applied to segments without AT. For both sectors 1 and 2, and using the ANN trained using all 6 sensing axes, the MSE on all non-reference segments are less or equal to 1 deg^2 with AT as compared to without AT which reaches up to 6 deg^2. For comparison, the absolute error distributions of the reference trained ANN on sector 1 of segment 4 without and with AT are shown in Figure 4-33 and Figure 4-34 respectively. Figure 4-35 and Figure 4-36 shows the corresponding comparison for sector 2 of segment 6. These surface plots clearly show the reduced error across the entire sector domains with the implementation of AT.

Table 4-10 Resulting MSE obtained from using trained reference ANN on other segments

ANN *g=1,h*=25		Mean Squared Error (deg^2)					
		Segment					
Sector 1		1 (Ref)	2	3	4	5	6
S_1	No AT	0.120	2.9919	5.5705	2.9107	2.6760	2.5429
B_X,B_Y,B_Z	With AT		2.2086	2.9941	1.5423	2.2219	1.4723
S_1, S_2	No AT	0.00566	0.7887	1.5317	1.1377	1.4511	0.9747
B_X,B_Y,B_Z	With AT		0.7322	1.0530	0.7023	0.8894	0.9198
Sector 2							
S_1	No AT	0.457	1.4029	3.5290	6.0823	2.0121	5.2861
B_X,B_Y,B_Z	With AT		0.9402	2.7203	3.1583	1.9216	2.4430
S_1, S_2	No AT	0.00540	2.1436	2.9923	1.3858	1.1583	2.4805
B_X,B_Y,B_Z	With AT		1.0454	0.8194	0.9493	0.7463	0.7003

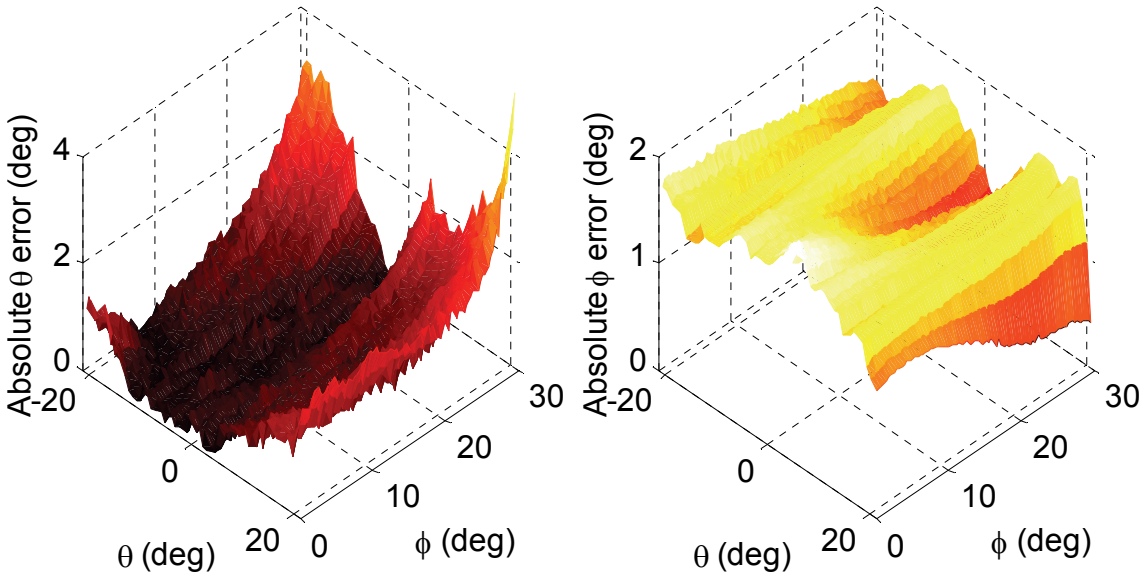

Figure 4-33 Absolute orientation error distribution on sector 1 of segment 4 without AT

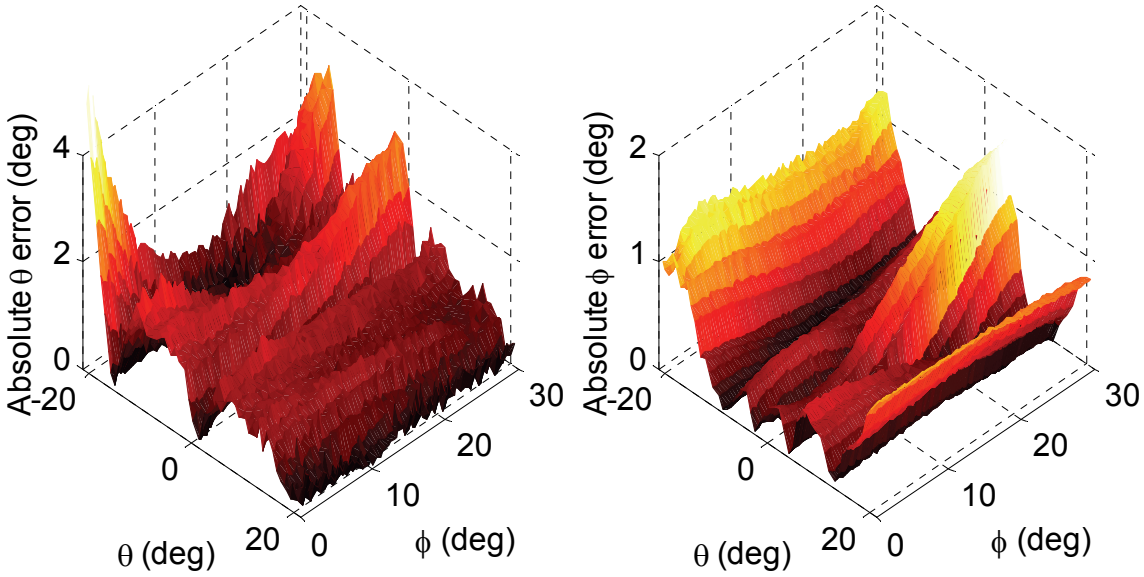

Figure 4-34 Absolute orientation error distribution on sector 1 of segment 4 with AT

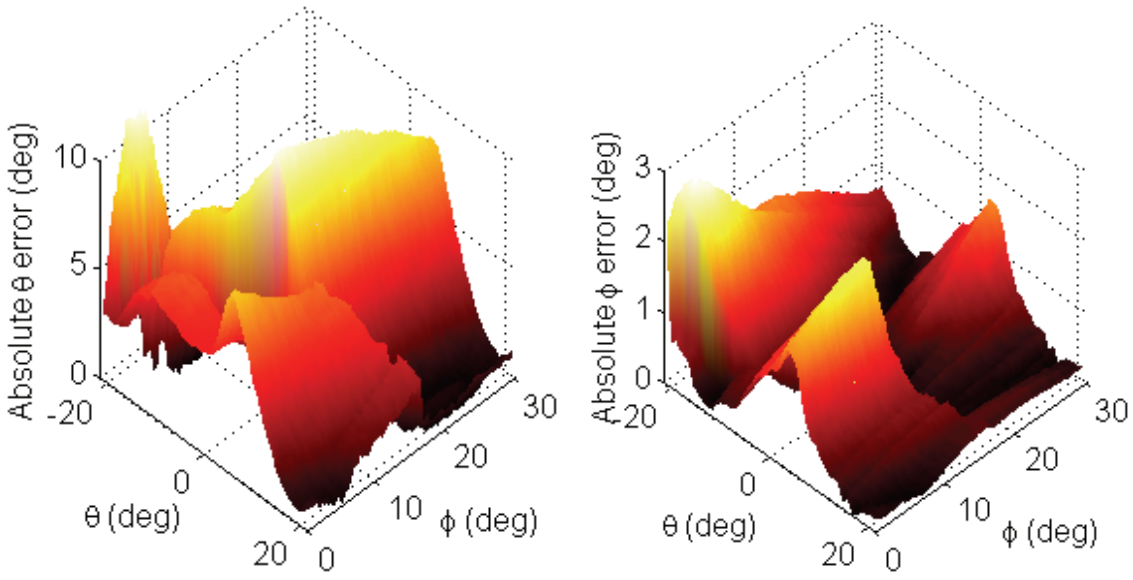

Figure 4-35 Absolute orientation error distribution on sector 2 of segment 6 without AT

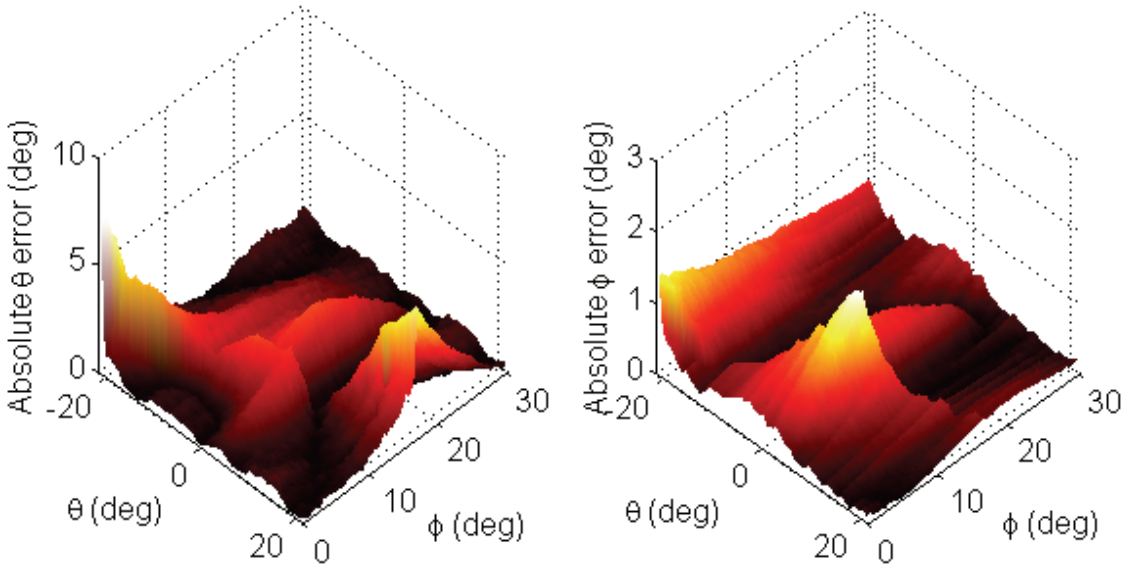

Figure 4-36 Absolute orientation error distribution on sector 2 of segment 6 with AT

To arrest these errors further, each sector in every segment can be individually trained. For this system with 6 segments and 2 sectors within each segment, a total of 12 individually trained ANNs are required. The MSE resulting from dedicated segment mapping are shown in Table 4-11. As seen from the data, the MSE are fairly consistent across segments and using more field measurements reduces MSE for both sectors.

Table 4-11 MSE across segments using dedicated segment mapping

ANN *g=1,h=25*		Mean Squared Error (deg^2) Segment					
Sector 1		1	2	3	4	5	6
S_1	B_X,B_Y,B_Z	0.120	0.114	0.110	0.125	0.139	0.133
S_1, S_2	B_X,B_Y,B_Z	0.00566	0.00553	0.00579	0.00481	0.00511	0.00479
Sector 2							
S_1	B_X,B_Y,B_Z	0.457	0.399	0.376	0.401	0.421	0.312
S_1, S_2	B_X,B_Y,B_Z	0.00540	0.00675	0.00690	0.00598	0.00440	0.00412

4.4.2 Using High Field Sensors

With high field sensors, saturation of sensor signals is a non-issue. To produce a sensor/EM pair, 24 magnetic sensors are placed at the center of all EMs. The resulting distribution of the 24 sensors can be visualized by Figure 4-37. This figure also shows the indexing of the 24 sensors. All sensors are installed such that the measuring axis is normal to the surface of the EM (inwards towards the rotor center). The 6 sensors demarcated by the red dashed line denote the basic group of sensors which is a representative set of all sensors in the system.

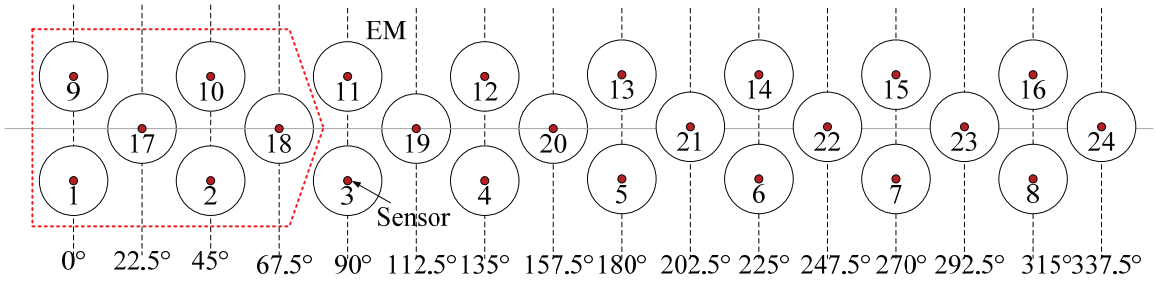

Figure 4-37 Distribution of high field sensors in spherical coordinates

Using the same approach as for low field sensors, the 2-D surface field map for each sensor can be constructed. The field maps of sensor 1, 2, 9, 10, 17 and 18 are shown in Figure 4-38 and Figure 4-39. With these figures, the segregation of the field map into 6

segments can be visually verified. Using segment 1 (47 by 67 pixels) of the field maps of all sensors, the ANN can be trained using combinations of the sensor field maps. In this ANN, the total number of training sets is 3149. The resulting MSE from different sensing groups are summarized in Table 4-12. These results suggest that increasing the number of sensors/ ANN inputs reduces the MSE; the ANN trained using the field measurements of all 24 sensors had the lowest MSE of 0.000339 deg^2. The spatial distributions of the resulting absolute errors for both angular estimates are shown in Figure 4-40 and Figure 4-41 respectively. As shown in the figures, the errors do not exceed 0.02° for the entire segment. An interesting observation is if only 8 sensors can be used, using the 8 equatorial sensors (17-24) had a significantly higher MSE than using the 8 top latitude sensors (9-16). This observation reinforces the finding that the mapping performance is highly sensitive to the choice of sensors.

Table 4-12 MSE due to different sensing groups

Group	**# of sensors**	**Locations**	**MSE (deg^2)**
Equatorial	1	17	**191**
	2	17, 21 (180° apart)	**108**
	4	17 to 20	**11.4**
	8	17 to 24	**0.127**
Group	6	1,2; 9,10;17,18	**0.1831**
Latitude	8 (Top)	9 to 16	**0.00999**
	16 (Top/bottom)	1 to 16	**0.000826**
All	24	1 to 24	**0.000339**

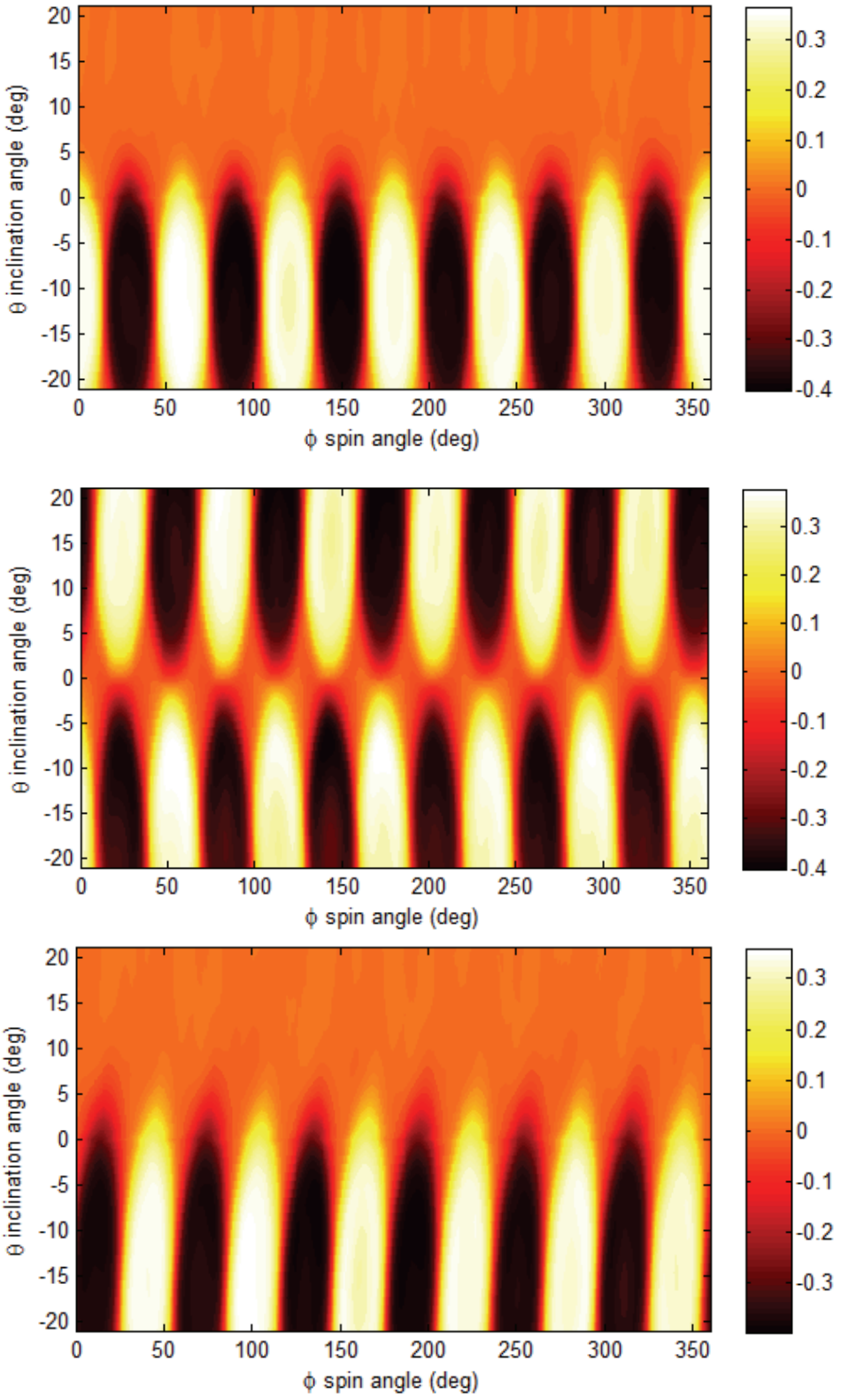

Figure 4-38 2-D field map of Sensor 1(top), 17 (middle) and 2 (bottom), Units: Tesla

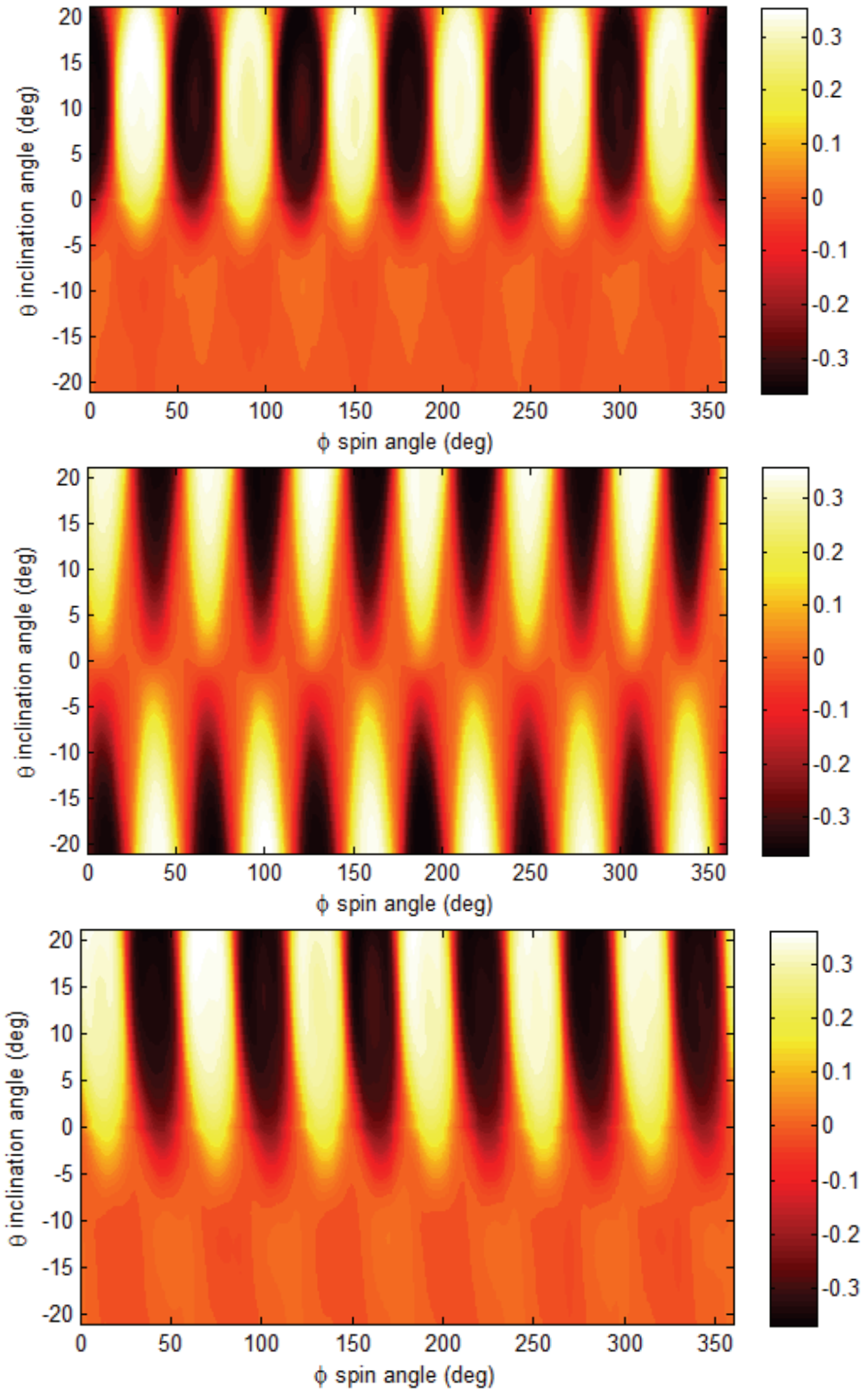

Figure 4-39 2-D field map of Sensor 9(top), 18 (middle) and 10 (bottom) , Units: Tesla

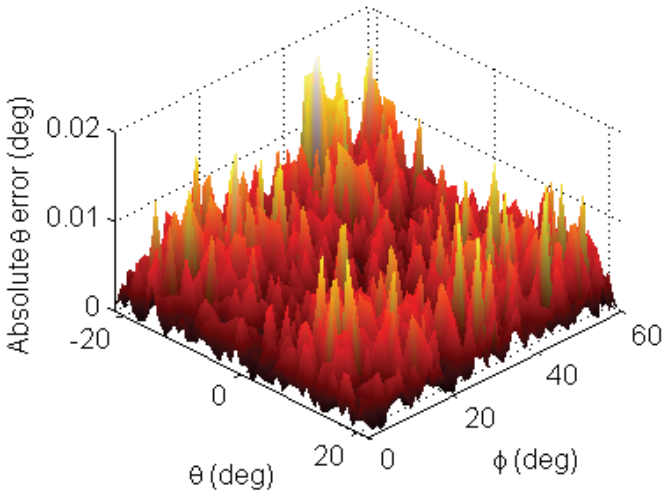

Figure 4-40 Distribution of absolute θ error for mapping using all high field sensors

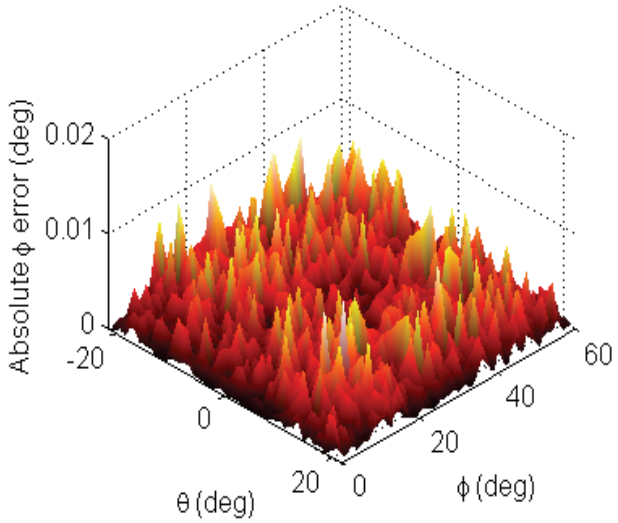

Figure 4-41 Distribution of absolute ϕ error for mapping using all high field sensors

4.5 SUMMARY

In summary, using a prototype multi-DOF electromagnetic actuator with an assembly of identical PMs on the rotor, a field-based sensing system comprising of a network of magnetic sensors placed in close proximity is evaluated. Using the magnetic DMP field model, the effects of the type of mapping function, spatial resolution and type of inputs used on the mapping performance of the sensing system for a prototype EM

actuator were investigated. Field simulation using DMP models illustrate that the absolute errors do not exceed 0.0004° using 4 multi-axis sensors. Subsequently, the mapping accuracy is experimentally verified and examined using an array of both single axis high and multi-axis low field sensors. Evaluation of the responsiveness and bandwidth of the sensing system is performed in tandem with a control implementation of an actuator in the following chapter.

CHAPTER 5

EMBEDDED FIELD CONTROL OF TWO-DOF ACTUATOR

5.1 OVERVIEW

The chapter presents the implementation of the magnetic field-based sensing system for direct system identification and control of an electromechanical actuator with an embedded field. This multi-DOF actuator uses the torques produced by electromagnetic interactions between stationary EMs and a moving PM for actuation as well as stationary PMs to provide restoring forces about an equilibrium position. Through diligent specifications of the input current into the actuating EMs, the sensing requirement of the actuator can be reduced to a single-DOF system. A field-based approach as outlined in the previous chapters is used to directly map field measurements to orientation of the system. Since energized EMs emit magnetic fields, they must be characterized so that active compensation of the field can be performed for accurate field-based sensing. As the sensing system is non-contact and non-invasive in nature, orientation measurement does not affect the dynamics of the system, facilitating accurate parameter identification. Precise knowledge of the system model allows synthesis of open loop controllers and aid in the design of closed loop controllers. In addition, an industrial inclinometer is used as a comparison to assess the performance of the field-based sensing in low and high frequency motion.

5.2 ACTUATOR SPECIFICATIONS AND MODELING

This electromagnetic actuator is composed of a moving rotor with an embedded magnetic field generated by a grade N45 ring magnet and a stationary stator containing actuating EM coils and stabilizing PMs as well as the field based sensing system. The rotor is supported mechanically via a spherical bearing and through magnetic interaction between the ring magnet and stator PMs, is kept at equilibrium position as shown in Figure 5-1. As the rotor obscures the underside of the rotor, Figure 5-2 provides better visualization of the underlying sensing system and EM configuration. The stator is made translucent to facilitate viewing of the stator PMs located underneath the stator. A total of 8 EMs are used to provide an applied torque via the attracting and repelling the rotor ring PM by adjusting the magnitude and polarity of the current inputs. 24 strong field Hall-Effect sensors, configured in a circular arrangement are positioned into the system using the sensor bracket. The disk shaped rotor, as shown in Figure 5-3, is comprised of a ring magnet held into position by a spacer. The rotor is attached to the stator mechanically using a spherical bearing. This torque applied about the bearing due to energized EMs causes subsequent inclination of the rotor. Due to the proximity of the sensor network to the rotor ring PM, the instantaneous orientation is determined using field measurements by the sensors.

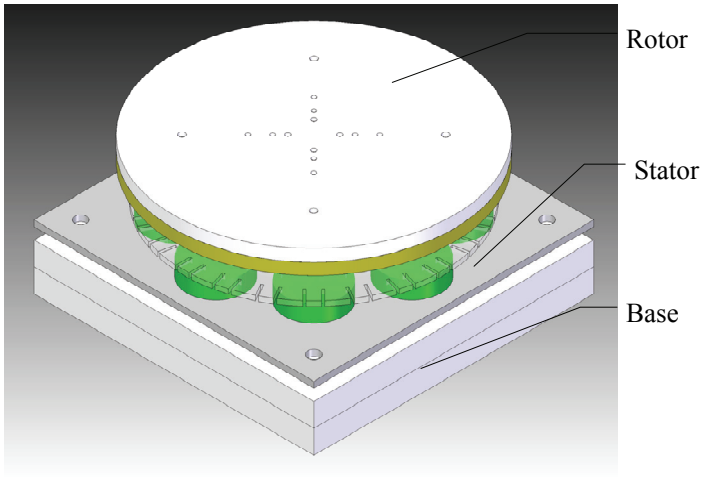

Figure 5-1 CAD rendition of multi-DOF actuator

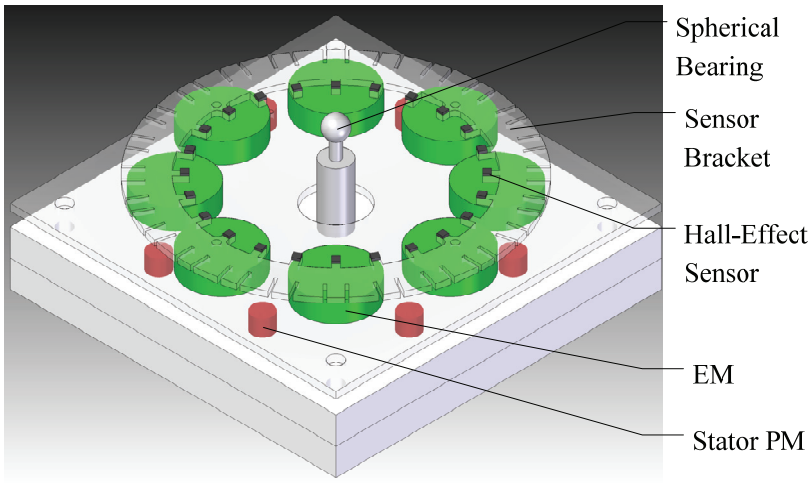

Figure 5-2 CAD Sensor and EM positioning and placement (stator translucent)

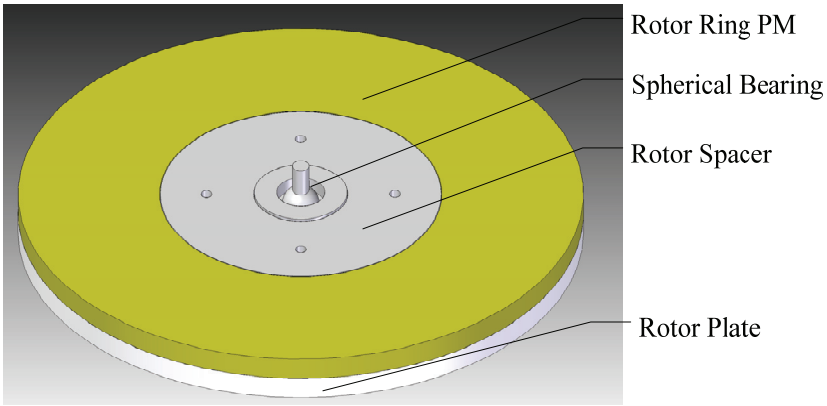

Figure 5-3 Underside of CAD rotor assembly

A schematic specifying the various system dimensions and coordinate systems is shown in Figure 5-4. The bearing center is the origin of the stator reference *XYZ* frame and the moving rotor *xyz* frame is described using two independent angles, α (about *X*-axis) and β (about *Y*-axis). Each sensor and EM are individually indexed; where the 1st sensor is located at the *X*-axis and the index increases in a counter-clockwise direction. The measuring axes of the sensors are along the *Z*-axis. The sensors, EMs and stator PMs are placed in the *XY* plane but displaced in the negative *Z*-axis by H_s, H_{EM} and H_{PM} respectively.

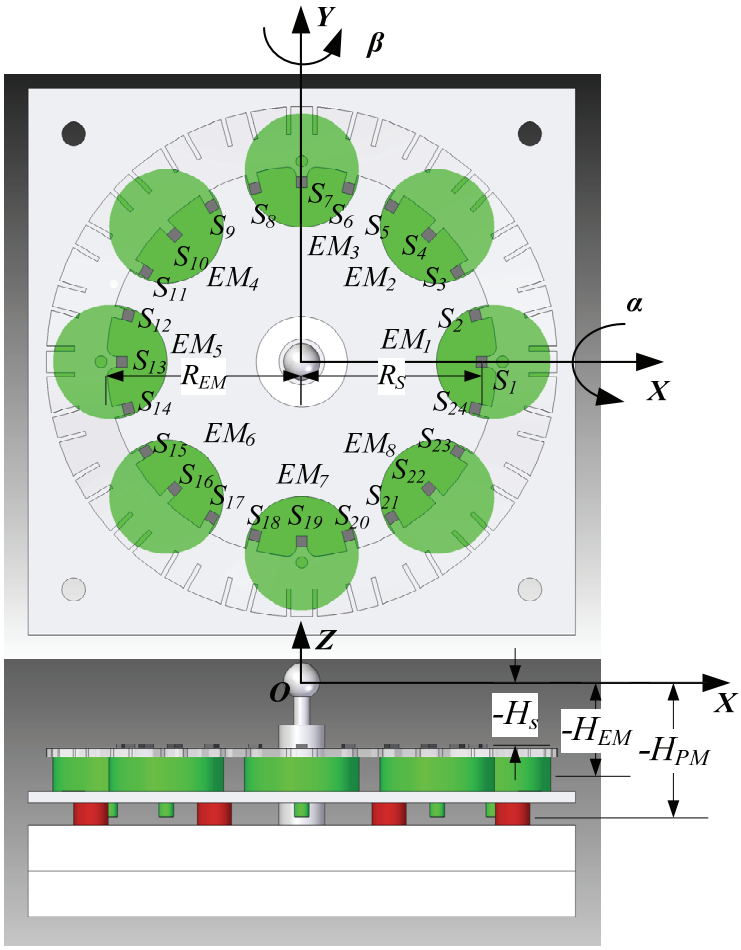

Figure 5-4 Coordinate systems, sensor and EM indices and physical parameters

A feedback control operation of the actuator is illustrated in the block diagram shown in Figure 5-5. Using the positional feedback from the sensing system, the error **E** computed from the difference between the desired $\mathbf{q_d}$ and estimated position $\hat{\mathbf{q}}$ is amplified by the controller to produce a input signal **U**. A saturator is enforced to prevent excessive currents from damaging the EM coils. This input signal (as an analog voltage) is converted to a current output **I** using current servo amplifiers. The current in each individual EM generates a resultant torque **T** about an axis of the rotor which translates into change in rotor orientation **q**. The subsequent change in the magnetic rotor orientation dynamically changes the rotor magnetic field $\mathbf{B}_{PM}$ and is measured by a distributed network of magnetic sensors. This measurement $\mathbf{\Lambda}$, also contains field effects due to the EMs as well but can be compensated with an EM field model which relates the current input **I** to the field effects at each sensor $\mathbf{\Lambda}_{EM}$. After compensation, the isolated signal $\mathbf{\Lambda}_{PM}$ contains only field measurements resulting from the moving rotor and utilized by the embedded sensing system to produce the estimated rotor position $\hat{\mathbf{q}}$.

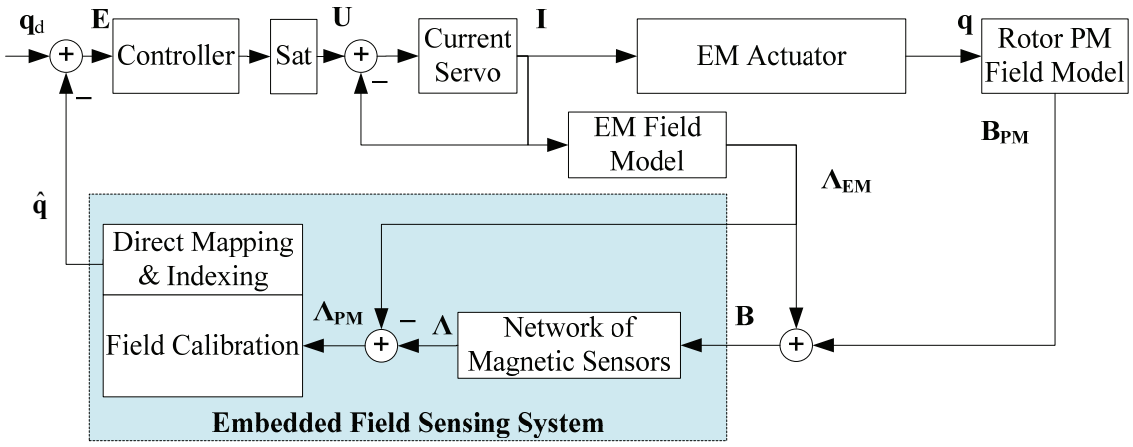

Figure 5-5 Control implementation for EM actuator

5.2.1 Mechanical and Sensing Equations of Motion

The generalized equation of motion of the rotor can be succinctly described by

$$\mathbf{J}\ddot{\mathbf{q}} + \mathbf{C}(\dot{\mathbf{q}},\mathbf{q})\dot{\mathbf{q}} + \mathbf{K}(\dot{\mathbf{q}},\mathbf{q})\mathbf{q} = \mathbf{T}(\mathbf{u},\mathbf{q}) \tag{5.1}$$

where **J** is the moment of inertia, **C** is the damping matrix, **K** is the stiffness matrix and **q** is the orientation of the rotor. The applied torque onto the system is denoted by **T** and is a function of the current inputs into the system **u** as well as the orientation of the system. The damping of the system is mainly due to the mechanical friction at the spherical bearing and the stiffness is a result of the rotor PM and stator PM nonlinear magnetic repulsive forces which provides an equilibrium point of the system when **q**=0.

Although the rotor has 3-DOF mechanically, the spin of the rotor is not detectable by the sensors because of the homogeneity of the ring PM field about the *z*-axis. Hence, the embedded field sensing system can only detect the relative inclination of the rotor (2-DOF) and not the spin motion of the rotor. From the sensing system point of view, the orientation of the rotor can be described by a series of body fixed rotations of α and β (Tait-Bryan angles) or ψ and θ (Euler angles).

If the axis of inclination is known (ψ), the system simplifies to a single DOF system (as a function of θ). For a small operating range of θ, the linearized EOM of the system can be expressed as follows if the axis of inclination is known,

$$J\ddot{\theta} + C\dot{\theta} + K\theta = T_a(\mathbf{u}) \tag{5.2}$$

where J,C and K are the inertia, damping and stiffness coefficients. T_a is the EM induced torque about the specified axis of inclination. As will be shown in the subsequent section, the meticulous specification of **u** allows the determination of the inclination axis. Consequently, for a desired rotor orientation in Tait-Bryan or Euler angles (they are

equivalent as introduced in Chapter 2), the corresponding desired axis of inclination is defined by the application of **u** and the instantaneous degree of inclination is measured by the field based sensing system.

Although the linearized model of the system is known, the exact values for J, C, K and T_a are not. While J can be computed analytically (function of the rotor geometry) and the quantities K and T_a estimated from various models, the damping of the system C, contributed from the friction in the spherical bearing, is significantly harder to model and estimate. However, with a non-invasive sensing system which does not affect the system's dynamics, a system identification approach is used to experimentally obtain all parameters of the system.

5.2.2 Controlling Input Specifications

The controlling input of the system is a 1×8 matrix $\mathbf{u}=[I_1\ I_2\ I_3\ I_4\ I_5\ I_6\ I_7\ I_8]$ where each column represents the desired specified current into the respective indexed EM. A larger current input to a single EM will increase the attractive and repulsive magnetic force between the EM and rotor PM and subsequently affect the degree inclination of the rotor. The polarity of the current input determines the direction of the applied torque. Due to the circular arrangement of EMs, it is possible to specify an arbitrary axis of inclination of the rotor through meticulous specification of individual EMs. Expressing the position of the EMs in terms of the polar angle as shown in Figure 5-6, a shifted periodic function with period equal to 2π (360°) and amplitude of I_{amp} is used to establish the required direction and magnitude of the input current into each EM to achieve positive inclination about the inclination axis defined by ψ_a. This periodic function can be mathematically expressed by

$$I = I_{amp} f_u(\psi - \psi_a) \tag{5.3}$$

where f_u is an odd periodic function with period 2π and unit amplitude. Possible functions include sinusodials $f_u(\psi)$=-sin(ψ) and triangle waveforms. Regulation of I_{amp} will adjust the applied torque about the desired inclination axis. The angular position of each EM can be described by

$$\psi_e = (e-1)\pi/4 \tag{5.4}$$

where e is the index of the EM. Hence the required current into each EM is simply

$$I_e = I_{amp} f_u(\psi_e - \psi_a) \tag{5.5}$$

Because of the periodicity, all current inputs are not independent and can be verified visually or analytically that the following relation holds:

$$I_1 = -I_5, I_2 = -I_6, I_3 = -I_7, I_4 = -I_8, \tag{5.6}$$

Hence for this configuration of EMs, only the specifications of four EM inputs are required to specify the desired inclination axis. The resulting controlling input can be expressed as

$$\mathbf{u} = I_{amp}\left[f_u(\psi_1 - \psi_a) \quad \cdots \quad f_u(\psi_e - \psi_a) \quad \cdots \quad f_u(\psi_8 - \psi_a)\right] \tag{5.7}$$

where the magnitude of **u** is solely a function of I_{amp} for a given constant inclination axis. Assuming the applied torque is a linear function of **u** and hence I_{amp}, the EOM in Equation (5.2) can be expressed as

$$J\ddot{\theta} + C\dot{\theta} + K\theta = T_a I_{amp} \tag{5.8}$$

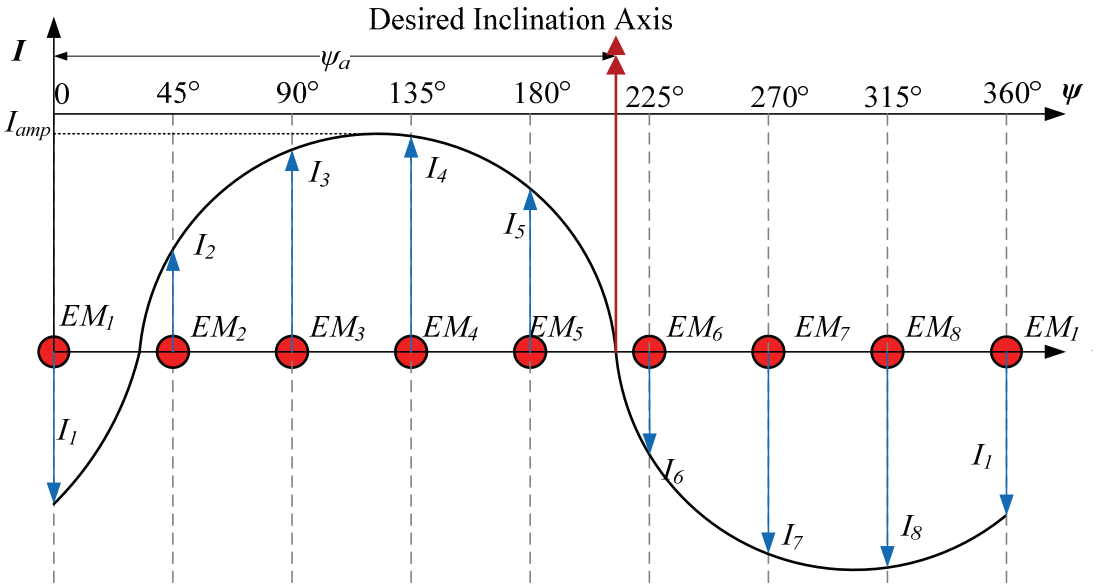

Figure 5-6 Determination of controlling input using shifted periodic function

Using a sinusoidal function for f_u, the input currents for unit I_{amp} can be computed as a function of the desired inclination axis. Only the first 4 current inputs are plotted since the remaining 4 are related through Equation (5.6). Due to the discrete placement of EMs, the average current magnitudes of these 4 inputs are not independent of the desired inclination axis as shown in Figure 5-7. If the inclination axis coincides with the angular position of an EM, the current input will be zero into that particular EM. For example, the current input in EM_3 (I_3) will be zero if the desired inclination axis is 90° (or 270°) from X-axis.

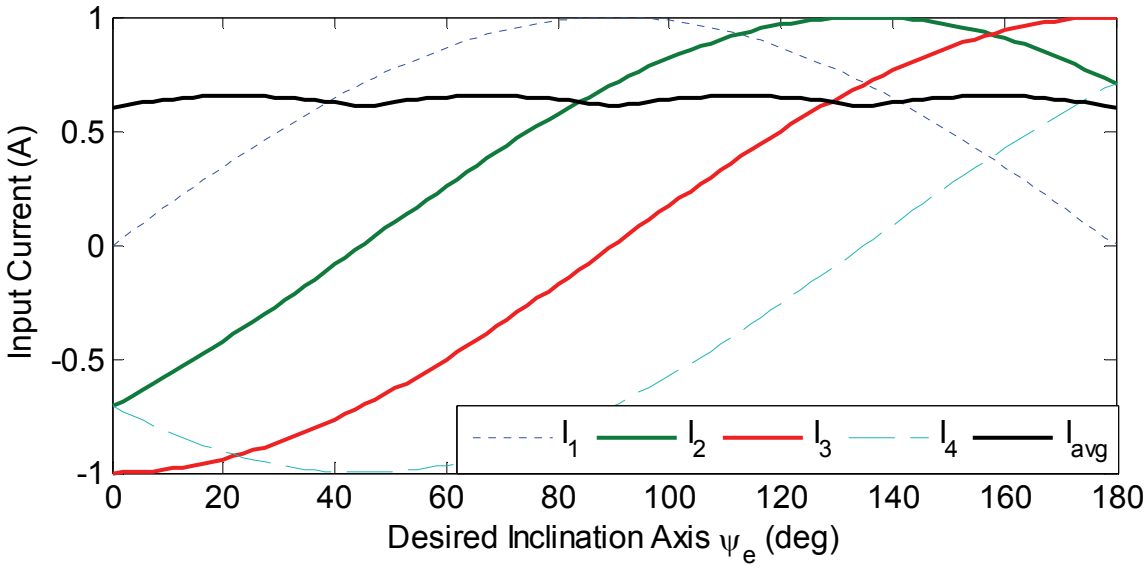

Figure 5-7 Current input into EMs as a function of desired inclination axis

5.2.3 Aggregate Field Sensing System

The sensing field map of this 2-DOF system is a surface demarcated by

$$0 \le \psi \le \pi, \quad -\theta_{\max} \le \theta \le \theta_{\max} \tag{5.9}$$

This system contains only one rotor PM and hence has only one segment. Using aggregate multi-sensing, this field map can be complementary characterized by the 24 sensors (12 pairs), each with the reduced domain of

$$(p-1)\pi / s_T \le \psi'_p \le p\pi / s_T \ , \ -\theta_{\max} \le \theta \le \theta_{\max} \tag{5.10}$$

where p is a positive integer that represents reduced sensor pair indexer (p=1,2,…, s_T=*12*). In polar coordinates, the domain of the entire map is the area within red circle and each pair of opposite wedges constitutes one possible reduced domain map as shown in Figure 5-8. Selection of wedges for sensing is determined by the location of the rotor x-axis (ψ) which is directly related to the desired inclination axis by π/2. Due to lack of

multiple segments, the combined field measurements of all single axis sensors for the p^{th} wedge is

$$\mathbf{\Lambda}_p = \begin{bmatrix} B_{Zp} & \cdots & B_{Z2s_T} & B_{Z1} & \cdots & B_{Zp-1} \end{bmatrix} \tag{5.11}$$

As discussed in earlier chapters, $\mathbf{\Lambda}$ can be completely characterized alternatively with only one pair of wedges $\mathbf{\Lambda}_p$ due to the similarity between wedges. Using ANNs or LS models, any of the $\mathbf{\Lambda}_p$ can be used to map measurements to instantaneous position for that particular reduced domain as well as the remaining domain.

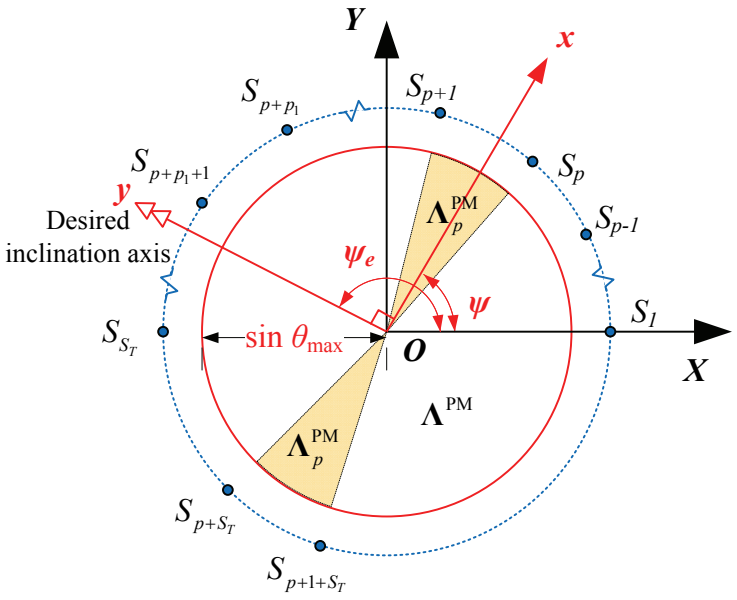

Figure 5-8 Aggregate sensing using multiple sensors and specified inclination axis

5.3 EXPERIMENTAL SETUP

The experimental setup consisting of the magnetic rotor, stator and base is shown in Figure 5-9. Due to balanced magnetic repulsive forces between the rotor ring PM and stator PM, the rotor has a level equilibrium position. With the rotor removed, Figure 5-10 reveals the view of the sensing and actuation assembly which is now unobscured. The 24

sensors are positioned in a circular path of radius R_S centered about the Z-axis. The angular spacing between sensors is ψ_s and this path is displaced by $-H_s$ from the XY plane. All sensors (Asahi HG-362A) are oriented such that their sensing axes are parallel to Z-axis. The sensing bracket, made of polycarbonate, is used for securing the sensing assembly to the stator. Each of the 8 EMs has 775 turns of 29 AWG wire and has a physical radius a_{EM} and length l_{EM}. The EMs are also configured in a circular path of radius R_{EM} centered about the Z-axis. The angular spacing between EMs is ψ_{EM} and all EMs are displaced by $-H_{EM}$ from the XY plane. Located below the aluminum stator plate are 8 PMs that provide repulsive magnetic forces to keep the rotor at equilibrium in absence of applied torque. These cylindrical PMs have radius of a_{PM} and length l_{PM} and are evenly distributed along a circular path of radius R_{PM} centered about the Z-axis. As a result, the angular spacing between PMs is ψ_{PM} and all PMs are displaced by $-H_{PM}$ from the XY plane. The underside of the rotor is shown in Figure 5-11 which clearly shows the spherical bearing and rotor ring magnet. The physical dimensions and parameters of the entire setup are summarized in Table 5-1.

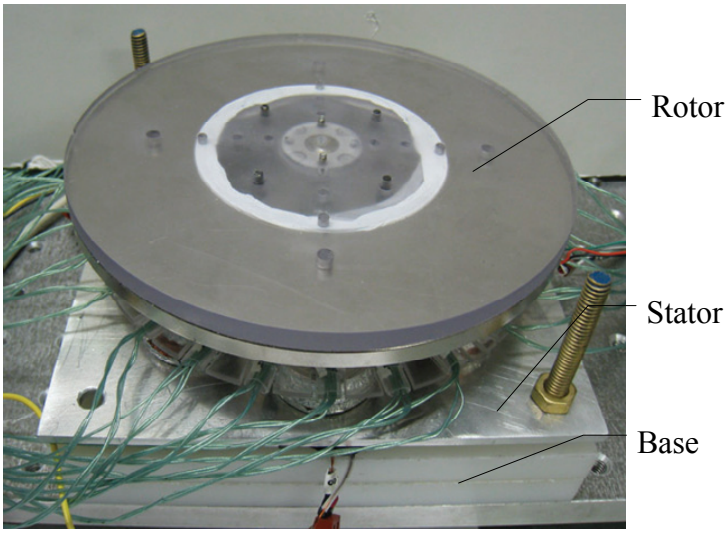

Figure 5-9 Experimental setup of multi-DOF actuator

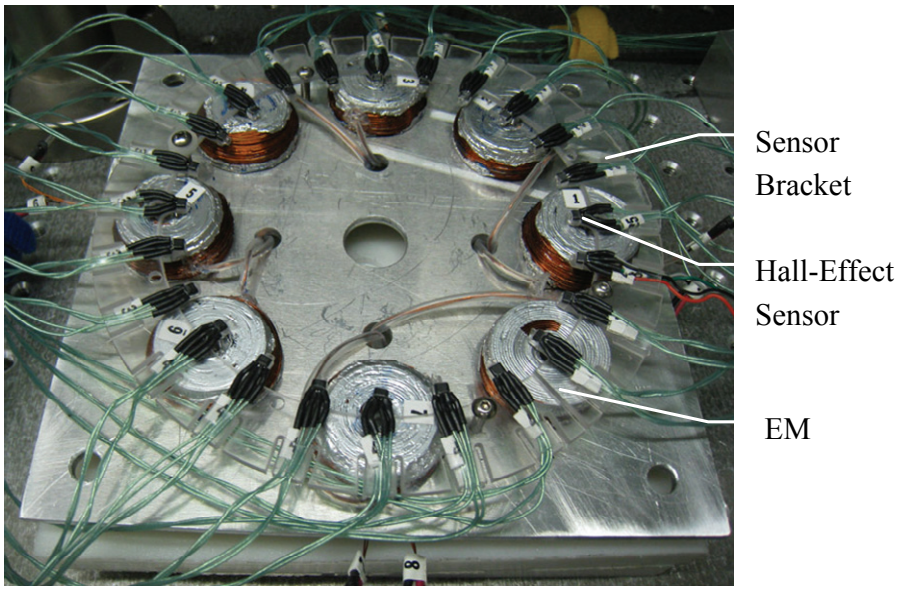

Figure 5-10 Sensor and EM placement (with rotor removed)

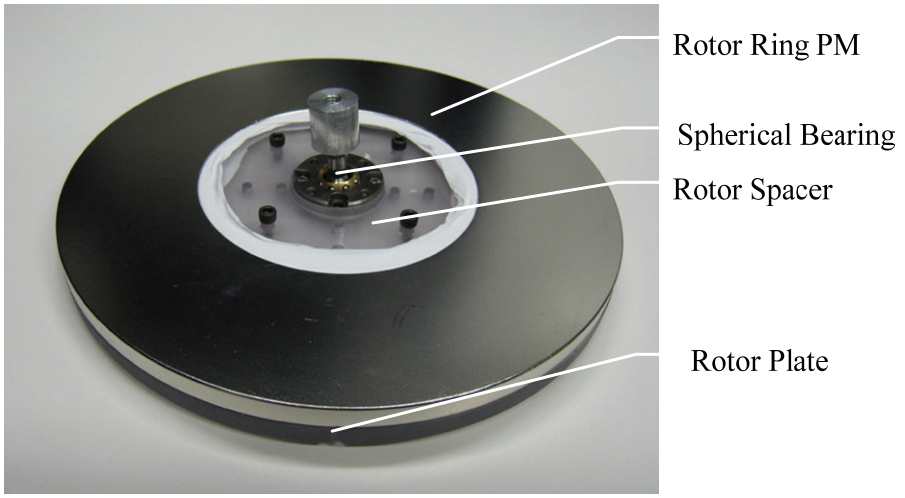

Figure 5-11 Underside of rotor

Table 5-1 Experimental physical dimensions and parameters

EM						**Sensors**			
No. of turns	a_{EM} (mm)	l_{EM} (mm)	R_{EM} (mm)	ψ_{EM} (deg)	H_{EM} (mm)	$2S_T$	R_S (mm)	ψ_s (deg)	H_s (mm)
775	15.87	9.65	53.34	45	26.99	24	49.53	15	19.63
Stator PMs						**Rotor Ring PM**			
	a_{PM} (mm)	l_{PM} (mm)	R_{PM} (mm)	ψ_{PM} (deg)	H_{PM} (mm)	R_1 (mm)	R_2 (mm)	l (mm)	
	4.76	12.7	63.5	45	40.17	38.1	76.2	6.35	

A diagram describing the electrical and communication connections is shown in Figure 5-12. The outputs of the magnetic sensors, which are powered by a 8V DC power supply (HP 6236B triple output power supply), are transmitted in analog format as voltages and digitally acquired using 24 independent and dedicated 16-bit (15-bit signed format) Delta Sigma analog to digital converter (ADC) banks (aggregated using four Turck Inc. BL20-4AI-U/I and two Turck Inc. BL20-2AI-U). Similar to setups of the previous chapters, the gateway is used to sample and record field measurements. However, due to the high sampling time of the gateway (15 ms), it is not suitable for real-time control implementation. Hence, a National Instruments real-time controller (NI-cRIO 9012) is used. This module consists of 4 16-bit Delta Sigma ADC and 4 digital to analog converters (DAC). The effective sampling time of the NI controller which includes data sampling and computation is 1 ms (1 kHz). Control signals to the EMs are transmitted to the current servos (Three Kepco BOP 50-2M and one Kepco BOP 50-4M) via the 4 DAC banks. These control signals and field measurements by the sensors are communicated to a Human Machine Interface (HMI) (Turck Inc. Turckeye) and a PC over Ethernet connection to provide instantaneous display and data logging capabilities.

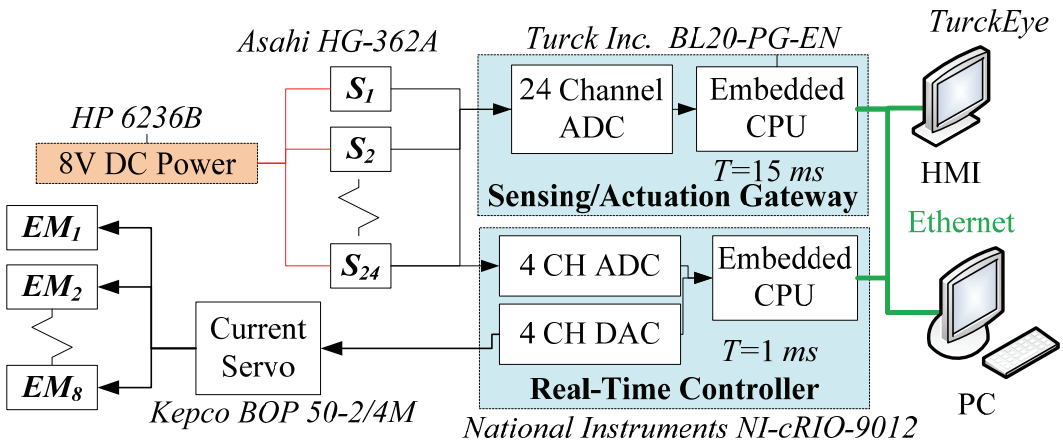

Figure 5-12 Electrical and communication schematics

5.3.1 Field Characterization and Sensor Calibration

In order to obtain a correspondence between orientation and measured rotor field, the rotor is rigidly attached to a rotary track of radius R by means of a mechanical strut as shown in Figure 5-13. The center of rotary track is positioned such that it coincides with the spherical bearing of the rotor. The arc length of the track contains measurement markings that allow correspondence between the curvature distance, w and inclination, β.

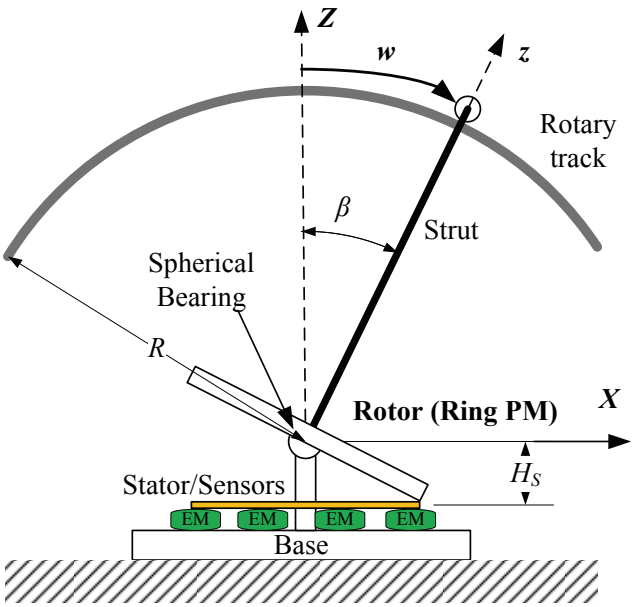

Figure 5-13 Schematic of measured field and position

Figure 5-14 shows the variation in measured field along the Z-axis by S_1 to S_7 with zero inclination as the reference field measurement. As S_1 is placed furthest from the inclination axis, it exhibits the largest field variation and hence superior SNR. Conversely, as S_7 is collinear with the inclination axis, its field variation is minimal. Sensitivity analysis presented in Figure 5-15 affirms that field sensitivity is higher for positive inclination (where the ring PM inclines towards the sensors). For completeness, the field variations of the remaining sensors are categorized in quadrants and presented in

Figure 5-16, Figure 5-17 Figure 5-18. As reinforced by the circular arrangement of sensors, the field measurements by S_7 to S_{13} (or S_{13} to S_{19}) are related to the measurements of S_1 to S_7 (or S_{19} to S_1) through reflection about the zero inclination. With this information, as seen from previous chapters, a direct mapping between measured field and instantaneous orientation of the rotor can be constructed using ANNs.

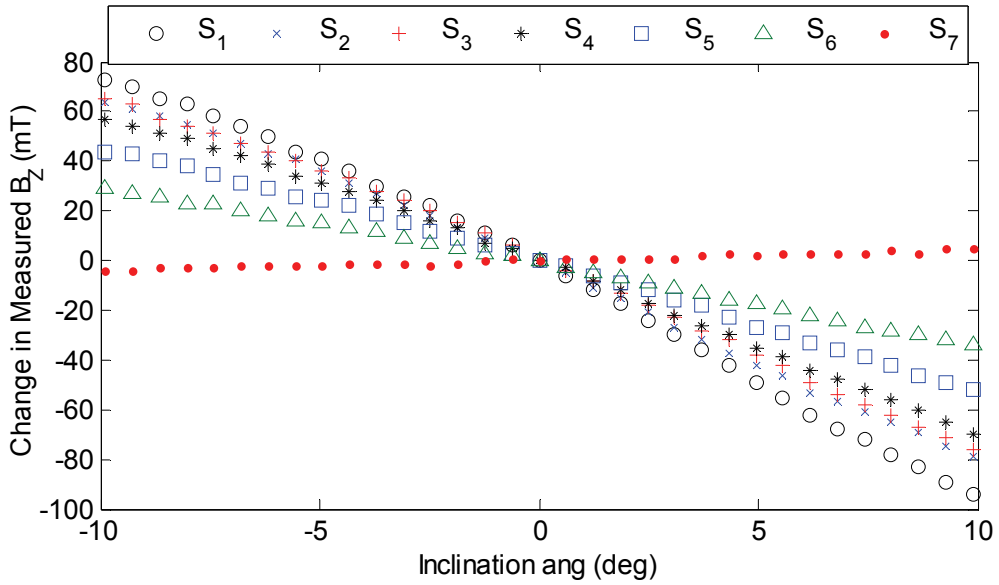

Figure 5-14 Field measurements by sensors (S_1 to S_7) as a function of inclination

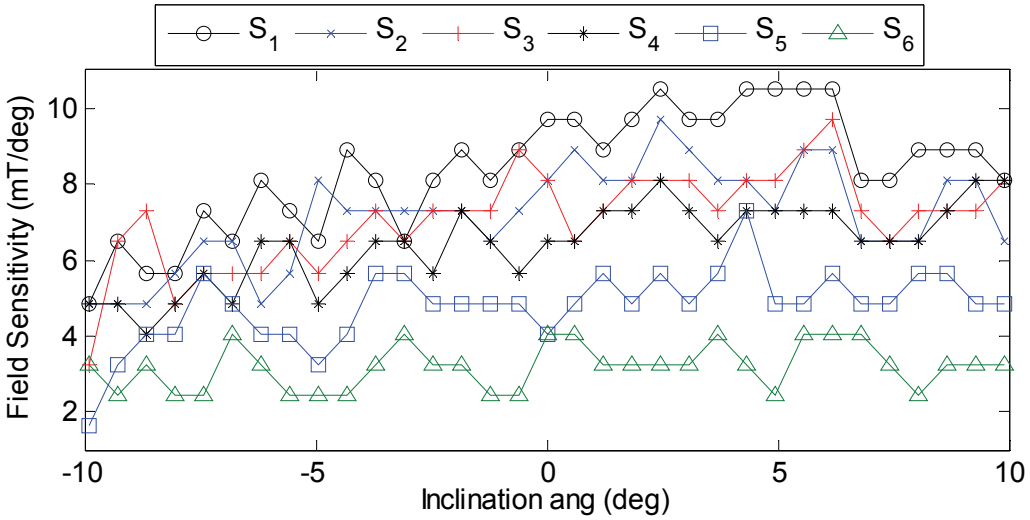

Figure 5-15 Field sensitivity analysis for sensors S_1 to S_6

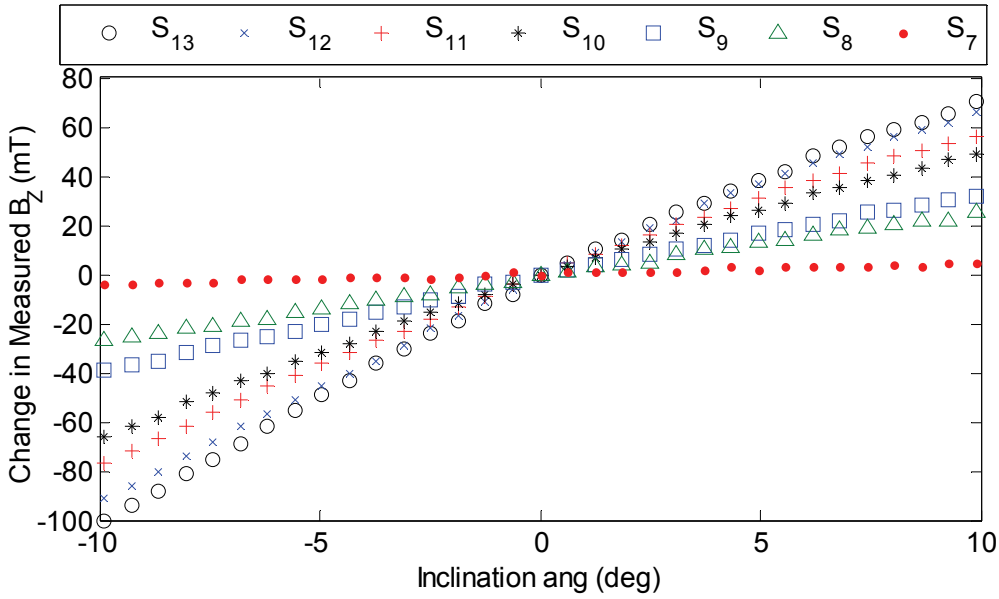

Figure 5-16 Field measurements by sensors (S_7 to S_{13}) as a function of inclination

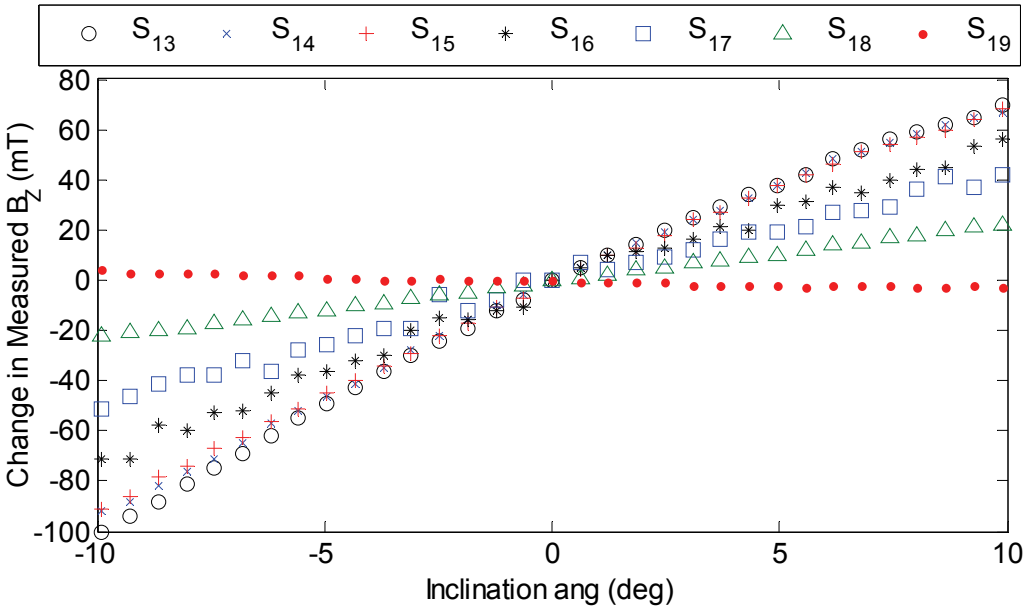

Figure 5-17 Field measurements by sensors (S_{13} to S_{19}) as a function of inclination

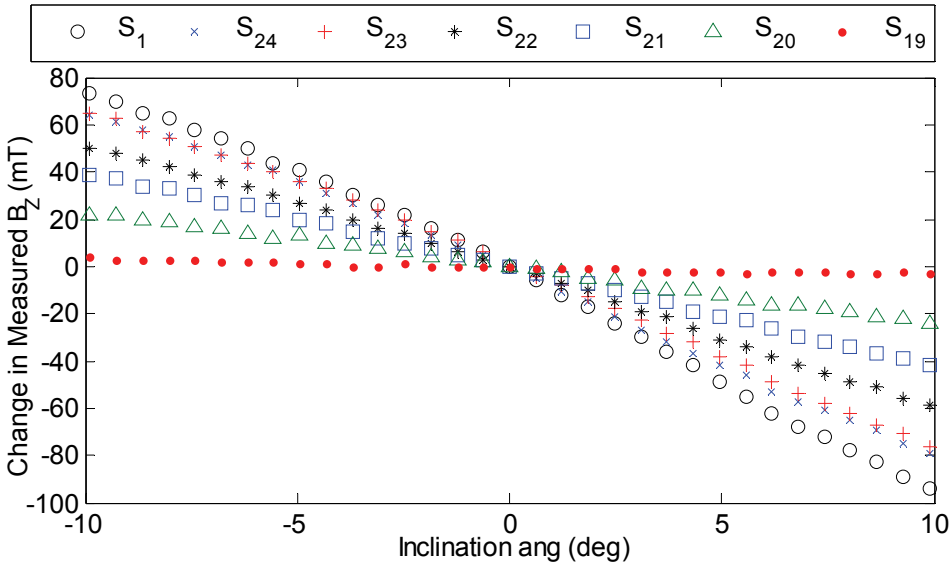

Figure 5-18 Field measurements by sensors (S_{19} to S_1) as a function of inclination

Due to the close proximity of EM coils and field sensors, the magnetic field produced by energized coils are inadvertently measured by the sensors. With the rotor removed, EM field calibration can be performed to compensate for these effects to isolate rotor field measurement. By individually adjusting the input current to each EM and measuring the field variation by all 24 sensors, the EM field model can be experimentally obtained. Figure 5-19(a) depicts the measured field by the three sensors (S_1, S_2 and S_{24}) with the closest proximity to EM_1 as the current flowing into EM_1 was regulated using the current servo. As S_1 is situated near the center of EM_1, it recorded the largest variation in measured field; about 25 mT when the input current was 1 A. The neighboring sensors of S_2 and S_{24} exhibited significantly less variation; less than 5 mT when the input current of EM_1 was 1A. The field measurements for all sensors however varied linearly with input current and a linear model ($y=C_1x$) can be used to fit the experimental measurements. The coefficients (C_1) of the fitted linear model for five sensors (S_1, S_2 , S_2 , S_{23} and S_{24}) closest to EM_1 are compiled in Table 5-2. The remaining sensors had no noticeable measured

field variation and are omitted. This procedure is repeated for the remaining 7 EMs to construct the complete EM field model. Sensing field calibration for EMs 1-4 are shown in Figure 5-19 along with the fitted model coefficients in Table 5-2. With these coefficients, given an arbitrary **u**, the field effects due to the EMs on any sensor can be actively compensated.

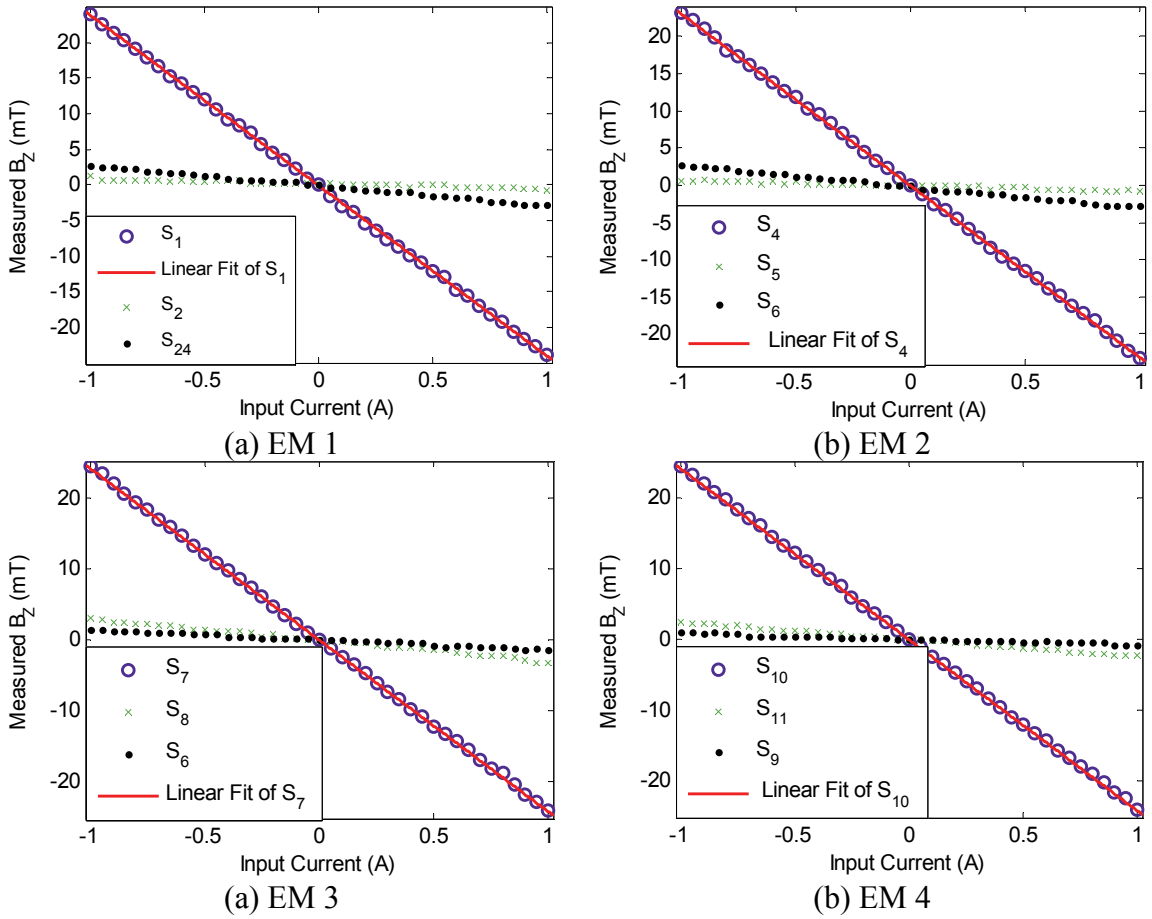

Figure 5-19 Sensor field calibration for EMs 1-4

5.3.2 Parameter and System Identification

With a calibrated sensing system, the stiffness of the system can be experimentally obtained through direct field measurements as shown in Figure 5-20. By adjusting the distance L and mass m_p, the applied torque about the Y-axis caused by the

mass can be computed. The degree of inclination of the rotor can be obtained from the sensor field measurements. The experimental relationship between the restoring torque of the system as a function of rotor inclination is shown in Figure 5-21. As observed in the diagram, the torque is a nonlinear function of the rotor inclination as shown by the quadratic fit of the experimental data in red. However, for inclinations less than 6°, the relationship is approximately linear as seen by the black linear fit. Assuming linearity, the stiffness of the system (K) is 0.006379 Nm/deg.

Table 5-2 Coefficients of fitted linear model for each sensors for all EMs.

EM₁	S_{23}	S_{24}	S_1	S_2	S_3
C_1 (mT/A)	0.9363	-2.819	-23.96	-0.7212	0.9687
EM₂	S_2	S_3	S_4	S_5	S_6
C_1 (mT/A)	0.8749	-2.877	-23.16	-0.6923	1.174
EM₃	S_5	S_6	S_7	S_8	S_9
C_1 (mT/A)	0.5378	-3.01	-24.25	-1.451	1.008
EM₄	S_8	S_9	S_{10}	S_{11}	S_{12}
C_1 (mT/A)	0.937	-2.438	-24.34	-0.8537	1.085
EM₅	S_{11}	S_{12}	S_{13}	S_{14}	S_{15}
C_1 (mT/A)	0.8134	-1.971	-24.38	-1.193	0.787
EM₆	S_{14}	S_{15}	S_{16}	S_{17}	S_{18}
C_1 (mT/A)	0.8124	-3.321	-22.68	-1.928	1.028
EM₇	S_{17}	S_{18}	S_{19}	S_{20}	S_{21}
C_1 (mT/A)	0.8894	-3.177	-24.78	-1.959	1.024
EM₈	S_{20}	S_{21}	S_{22}	S_{23}	S_{24}
C_1 (mT/A)	1.002	-0.7335	-25.43	-1.119	1.078

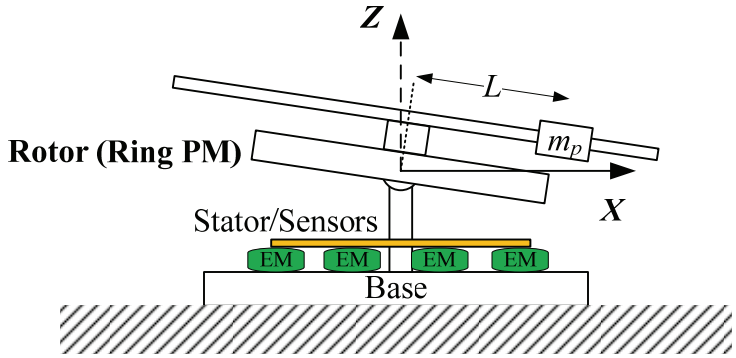

Figure 5-20 Schematic for determining restoring torque of system

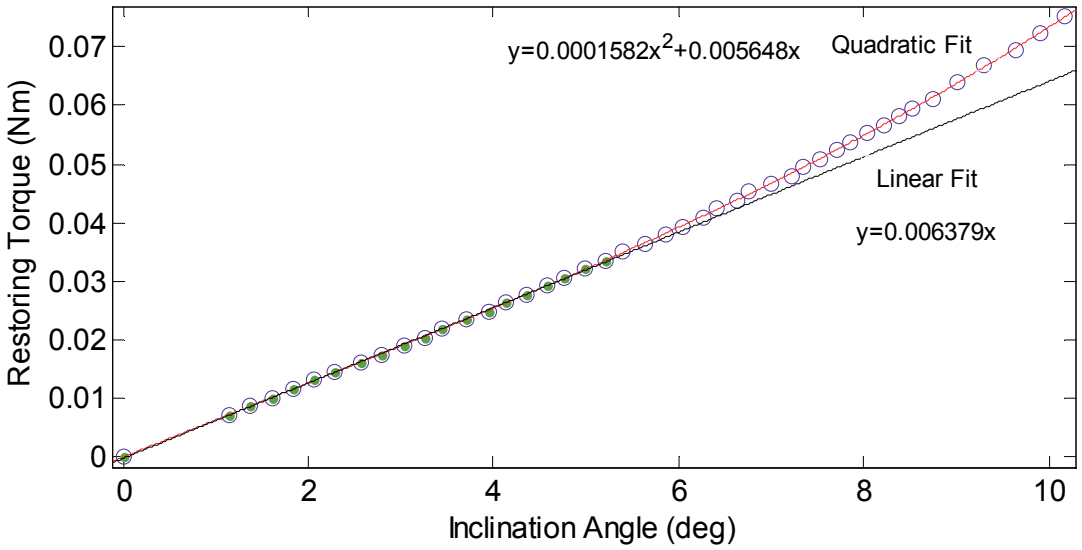

Figure 5-21 Restoring torque of the system as a function of inclination angle

The remaining parameters of the actuator can be determined experimentally by analyzing the step response of the system. The transfer function of the linearized system in Equation (5.8) can be written as

$$\frac{\Theta(s)}{I_{amp}(s)} = \frac{T_a}{Js^2 + Cs + K} = \frac{T_a / J}{s^2 + (C/J)s + K/J} \tag{5.12}$$

Alternatively, the state space representation is

$$\begin{bmatrix} \dot{x}_1 \\ \dot{x}_2 \end{bmatrix} = \mathbf{A}\mathbf{x} + \mathbf{B}I_{amp} = \begin{bmatrix} 0 & 1 \\ -K/J & -C/J \end{bmatrix} \begin{bmatrix} x_1 \\ x_2 \end{bmatrix} + \begin{bmatrix} 0 \\ T_a / J \end{bmatrix} I_{amp} \tag{5.13}$$

$$\theta = \begin{bmatrix} 1 & 0 \end{bmatrix} \begin{bmatrix} x_1 \\ x_2 \end{bmatrix} \tag{5.14}$$

where x_1 and x_2 are the states of the system (angular position and velocity respectively). Using the Identification Toolbox in MATLAB, the variables in Equation (5.12) can be estimated. The step response of the system with the inclination axis about the *Y*-axis is shown in Figure 5-22. In this case, the degree of inclination of the rotor can be described by β and the measurement of S_1 is used to infer rotor inclination. As EMs are energized to

induce inclination, the field measurements are actively compensated using EM field models in Table 5-2. The step response appears noisy and this is due to the active compensation of the EM field. The required current input into each EM to achieve this step response is shown in Figure 5-23. The parameters estimated by the toolbox are tabulated in Table 5-3. The damping coefficient and natural frequency of the system is 0.044 (underdamped system) and 19.7 Hz respectively.

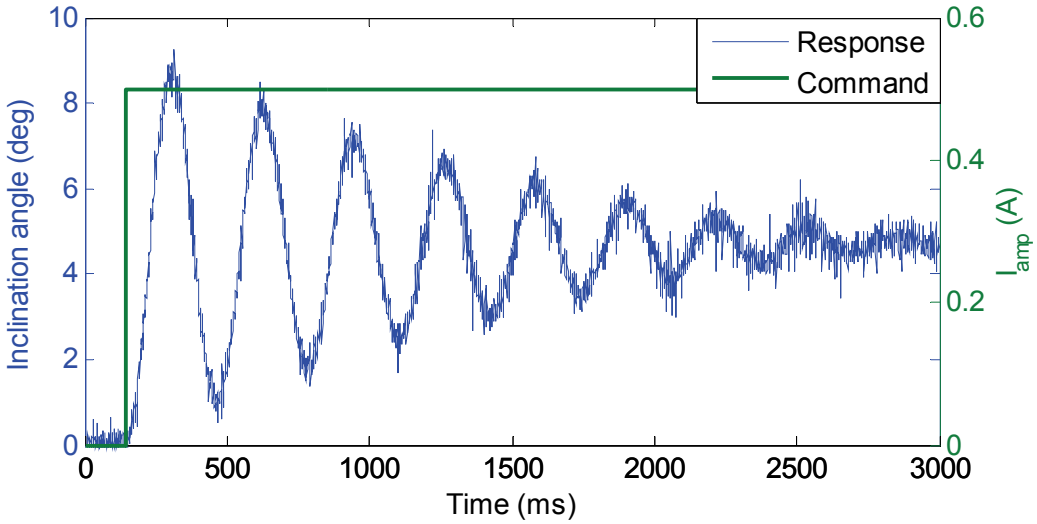

Figure 5-22 Step response of rotor

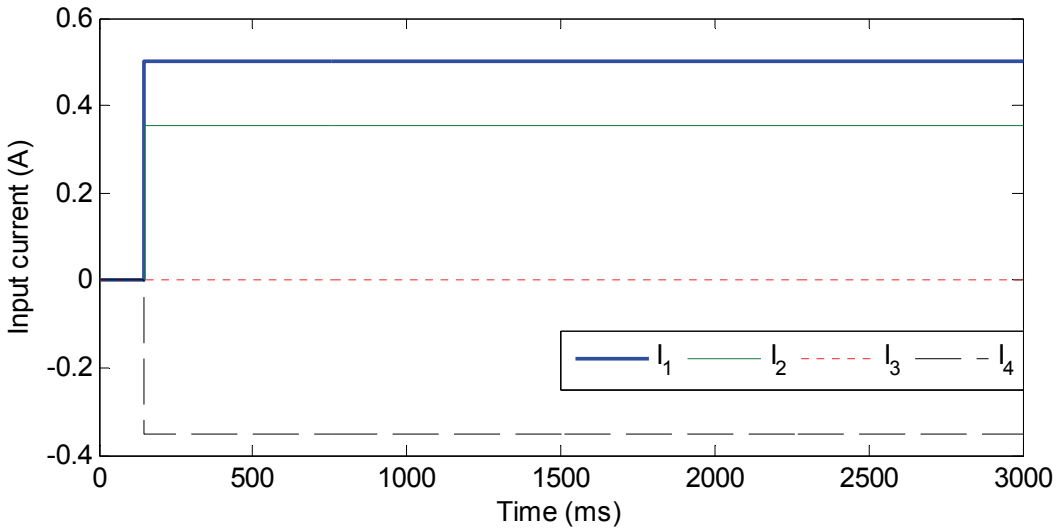

Figure 5-23 EMs individual inputs during step response

With an identified model of the system, the step and free response of the model can be compared with the corresponding experimental responses. The comparisons between a delayed step and free response due to an initial condition are shown in Figure 5-24 and Figure 5-25 respectively. As expected, there is a close correspondence between the identified model and experimental responses.

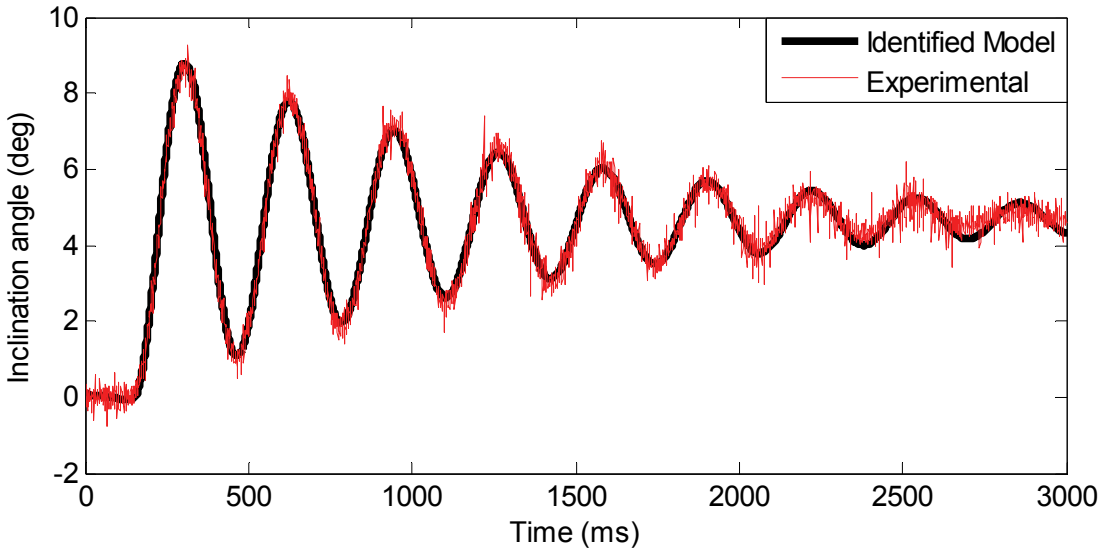

Figure 5-24 Comparison between step response of identified model and experiment

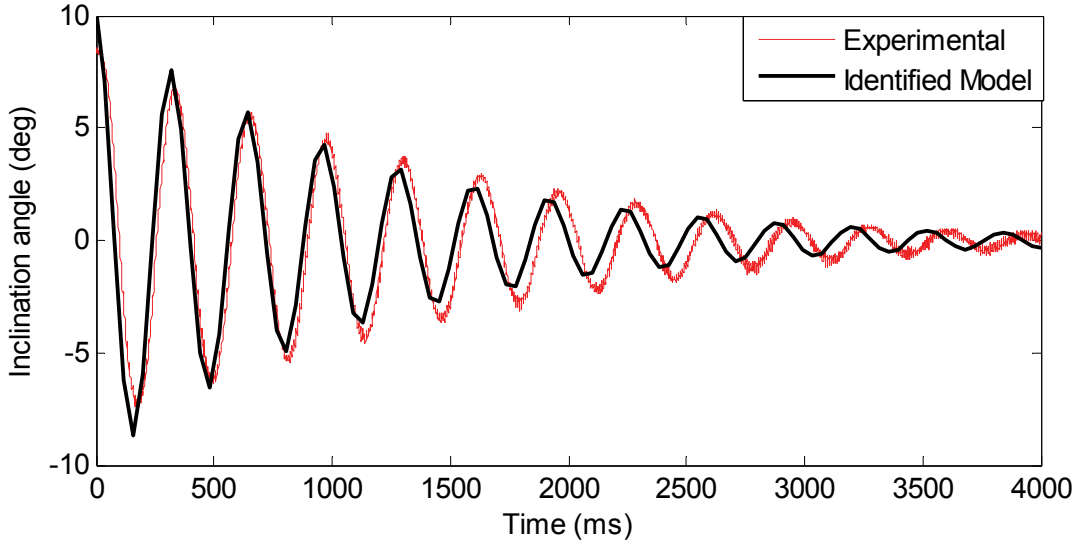

Figure 5-25 Comparison between free response of identified and experiment

Table 5-3 Experimentally identified system parameters

Parameter	T_a/J (deg/sec^{2}A^1)	C/J (1/sec)	K/J (1/sec^2)	ζ	ω_n (Hz)
Value	3620	1.75	387	0.044	19.7

5.4 EXPERIMENTAL RESULTS

From the step response of the system, it can be seen that the system is underdamped and vulnerable to vibratory motion. Using the data comprising of the system model as well as real-time feedback of position information obtained from the field sensing system, open and closed loop controllers can be designed. In addition, an industrial inclinometer, commonly used in various devices for tilt determination is used as a comparison for this field-based sensing system.

5.4.1 Comparison with Inclinometer

An industrial inclinometer (TURCK B2N10H-Q20L60-2LU3-H1151) is installed onto the rotor to provide a comparison to the field based sensing system. This inclinometer (with a measuring range of ±10°) incorporates a micro-electro-mechanical capacitive element into the sensor that utilizes two parallel plate electrodes, one stationary and one attached to a spring-mass system. Movement produces deflection in the non-stationary electrode. This results in a measurable change in the capacitance between the two plates that is proportional to the angle of deflection. These signals are conditioned to provide voltage output proportional to the degree of inclination.

By generating a sinusoidal input to the EMs at a frequency much lower than the natural frequency of the system of 0.3 Hz, the rotor's corresponding oscillation can be measuring by both sensors. The comparison between the signals measured by the magnetic and inclinometers are compiled in Figure 5-26. Both signals share the same

peak to peak amplitude and period, and the only difference is the phase shift between both signals. The inclinometer signal appears to have a phase delay of 150 ms.

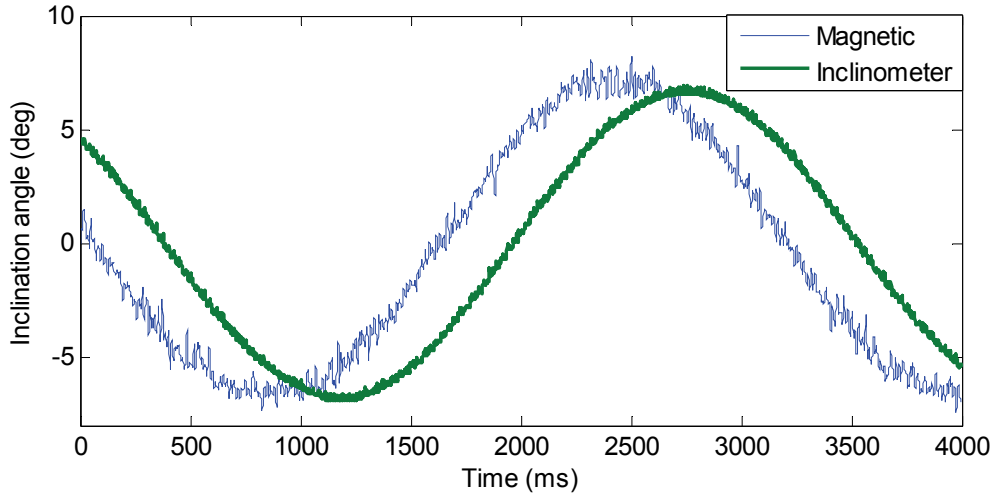

Figure 5-26 Comparison between field-based sensing and inclinometer at 0.3 Hz

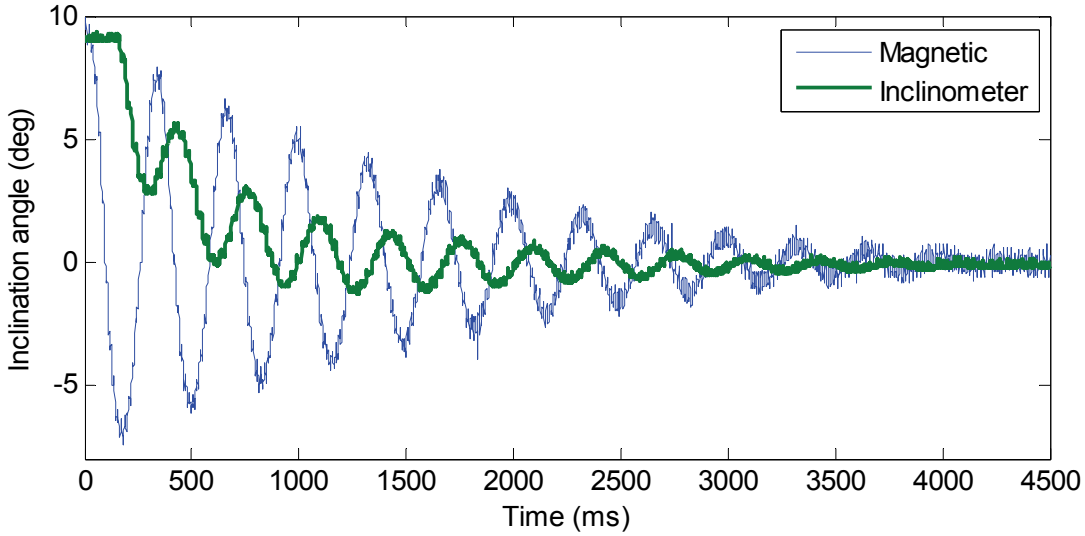

Figure 5-27 Comparison between field-based sensing and inclinometer at 3 Hz

To verify this phase delay, the free response of the system due to an initial displacement, which occurs at a much higher frequency of 3 Hz, is measured by both sensing system and shown in Figure 5-27. As depicted in the figure, initially the inclinometer output remains unchanged for 150 ms before registering a change in output

due to motion of the inclinometer. In addition, at this higher frequency, the inclinometer is unable to track the rapid motion of the rotor as illustrated by the large disparity between the signals in Figure 5-27. This is most likely due to the mechanics of the inclinometer which uses inertia for positional sensing. At these frequencies, the inertia load is unable respond quick enough for proper sensing.

5.4.2 Open-Loop Input Shaping Control

Using the experimentally obtained model of the system, an open-loop controller that actuates the rotor to a specified inclination with minimal overshoot and vibration residue can be designed. One approach is using input-shaping [51] where the command of the system is adjusted through careful analysis of the impulse response of the system. Two commonly used input shapers are used, the Zero-Vibration (ZV) shaper and Zero-Vibration-Derivative (ZVD) shaper. The synthesis of these open loop controllers are shown in Figure 5-28. The asterisks denote convolution and the Q_1, Q_2 and Q_3 denote the amplitude of the ZV and ZVD shapers and can be computed from the damping ratio of the system. T_1, T_2 and T_3 represent the time delay between the impulses and are obtained from the damped period of the system.

As described in [51], the sequences of the impulses for the ZV shaper can be written in matrix form as

$$\begin{bmatrix} Q_j \\ T_j \end{bmatrix} = \begin{bmatrix} \frac{1}{1+K_Z} & \frac{K_Z}{1+K_Z} \\ 0 & 0.5T_d \end{bmatrix} \tag{5.15}$$

$$K_Z = e^{\left(-\zeta\pi/\sqrt{1-\zeta^2}\right)} \tag{5.16}$$

for j=1,2 and T_d is the damped period of the vibration. Similarly, the ZVD shaper can be expressed as

$$\begin{bmatrix} Q_j \\ T_j \end{bmatrix} = \begin{bmatrix} \dfrac{1}{(1+K_Z)^2} & \dfrac{2K_Z}{(1+K_Z)^2} & \dfrac{K_Z^{\,2}}{(1+K_Z)^2} \\ 0 & 0.5T_d & T_d \end{bmatrix} \tag{5.17}$$

for j=1,2,3. For the system parameters identified, the amplitude and time delays for the ZV and ZVD shapers can be determined and summarized in Table 5-4. The input shaped step response of the system along with the specified input is shown in Figure 5-29 and Figure 5-31 respectively for the ZV and ZVD shaper. The associated EM input currents for both cases are shown in Figure 5-30 and Figure 5-32 respectively. For both the ZV and ZVD cases, the Signal to Noise Ratio (SNR) of the sensing signals after it has reached its targeted inclination is 33 dB. In other words, the sensor's signal is almost 45 times the average noise amplitude.

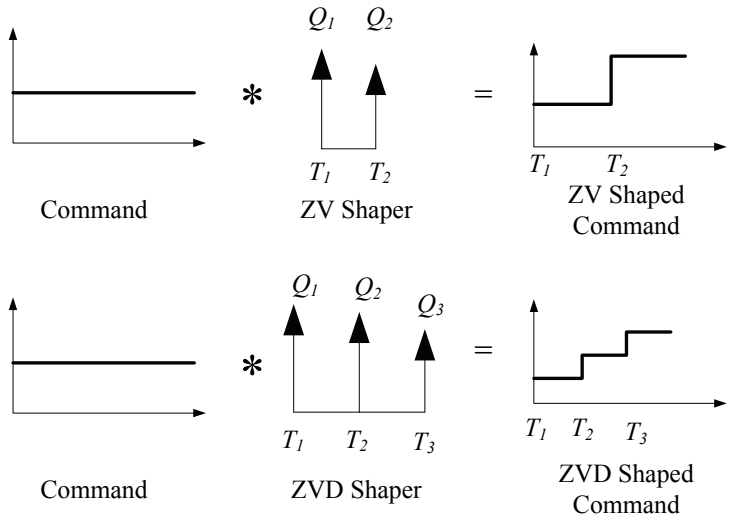

Figure 5-28 ZV and ZVD input shaping

Table 5-4 Input shapers parameters

ZV		ZVD		
Q_1	Q_2	Q_1	Q_2	Q_3
0.5348	0.4652	0.2860	0.4976	0.2164
T_1	T_2	T_1	T_2	T_3
0	0.1580	0	0.1580	0.3160

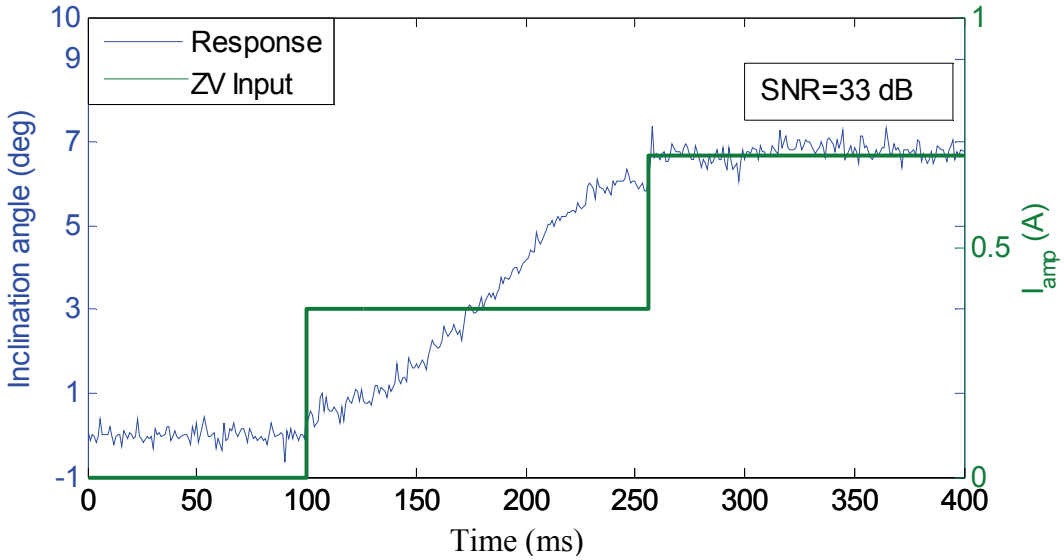

Figure 5-29 Response to ZV shaped command

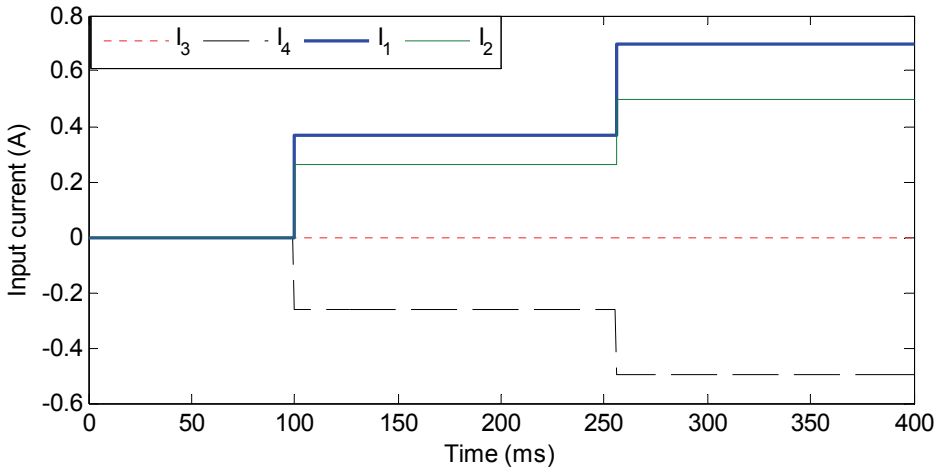

Figure 5-30 Current input into EMs due to ZV shaped command

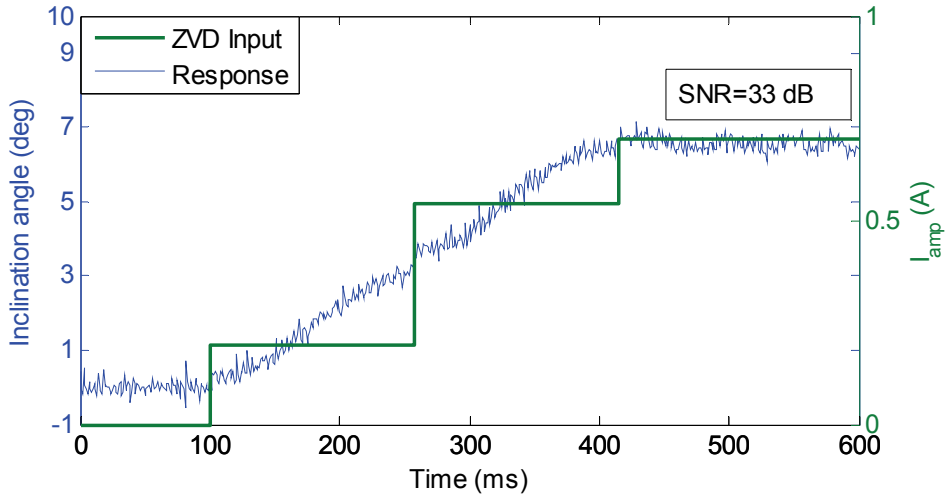

Figure 5-31 Response to ZVD shaped command

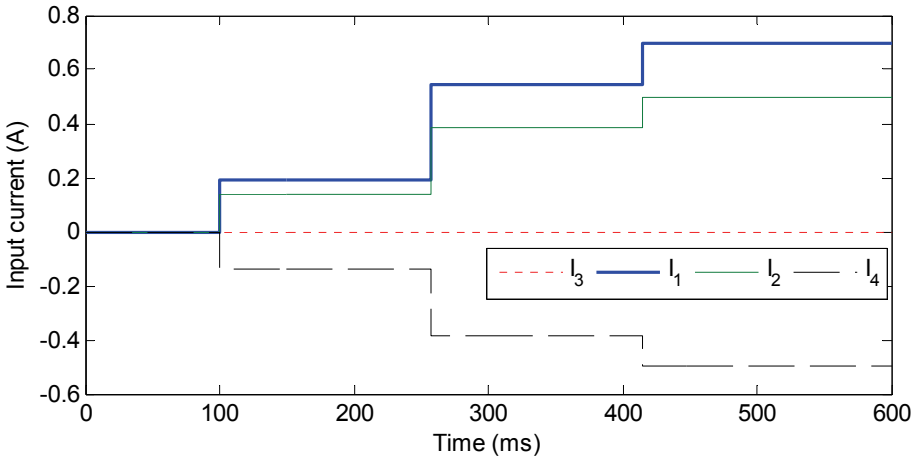

Figure 5-32 Current input into EMs due to ZVD shaped command

5.4.3 Full State Feedback with Minimum Order Observer

With real time measurement of the inclination of the rotor, the system can be stabilized using the field measurements for feedback control. Due to noise associated with taking derivatives of position measurement to obtain velocity, a reduced state observer is used to estimate the velocity of the rotor inclination using discrete measurements of rotor position. The discrete time representation of the system is

$$\begin{aligned}\mathbf{x}((k+1)T) &= \mathbf{G}(T)\mathbf{x}(kT) + \mathbf{H}(T)I_{amp}(kT) \\ &= \begin{bmatrix} G_{11} & G_{12} \\ G_{21} & G_{22} \end{bmatrix}\begin{bmatrix} x_1(kT) \\ x_2(kT) \end{bmatrix} + \begin{bmatrix} H_1 \\ H_2 \end{bmatrix} I_{amp}(kT)\end{aligned} \tag{5.18}$$

$$\theta(kT) = \begin{bmatrix} 1 & 0 \end{bmatrix}\begin{bmatrix} x_1(kT) \\ x_2(kT) \end{bmatrix} \tag{5.19}$$

Computation and determination of $\mathbf{G}(T)$ and $\mathbf{H}(T)$ are obtained using the following,

$$\mathbf{G}(T) = e^{\mathbf{A}T} \tag{5.20}$$

$$\mathbf{H}(T) = \left(\int_0^T e^{\mathbf{A}\lambda} d\lambda\right)\mathbf{B} \tag{5.21}$$

where the numerical values of **A** and **B** are experimentally obtained from direct system identification. From [53], the minimum-order observer, which assumes only the state x_1 (θ) is measurable, is defined by

$$\hat{x}_2(kT) = \eta(kT) + L_O\theta(kT) \tag{5.22}$$

$$\begin{aligned}\eta((k+1)T) &= \left(G_{22} - L_O G_{12}\right)\eta(kT) \\ &+ \left[(G_{22} - L_O G_{12})L_O + G_{21} - L_O G_{11}\right]\theta(kT) \\ &+ \left(H_2 - L_O H_1\right) I_{amp}(kT)\end{aligned} \tag{5.23}$$

where η is the observer state, L_O is the observer gain and $\hat{x}_2$ is the estimated state of the system (angular velocity). Full state feedback is achieved by defining the input as a function of the state and estimated state,

$$I_{amp}(kT) = -\mathbf{K_{SF}}\left[x_1(kT) \quad \hat{x}_2(kT)\right]^{\mathrm{T}} \tag{5.24}$$

Using the controller and observer gains listed in Table 5-5, the actuator was subjected to a step command of 4 degrees. Two sets of gains are used.

- The first set is an aggressive high gain controller designed to induce a rapid response (low rise time) to assess the bandwidth of the sensing system.
- The second set is a feedback controller optimized for low settling time for point to point motion.

The response of the system under the aggressive feedback gains is shown in Figure 5-33 and the corresponding EM inputs in Figure 5-34. For this motion, the rise time is 40 ms which is significantly quicker than the open-loop input shaped control. From the response, the highest angular velocity of the rotor occurs during the rise time and is approximately 100 deg/sec. At these speeds, the sensing system has no difficulty tracking the rotor position. For the second set of gains, the rotor response and EM inputs are appended in Figure 5-35 and Figure 5-36 respectively. At a penalty of doubling the rise time, the settling time of the system is 200 ms, which is still slower than the ZV shaped open loop response.

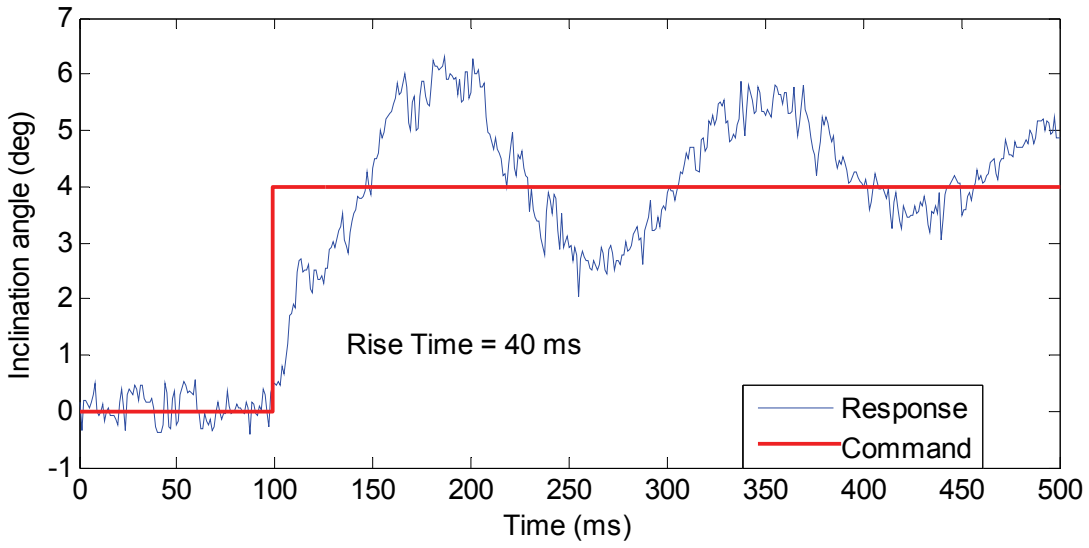

Figure 5-33 Step response of system to under aggressive gains

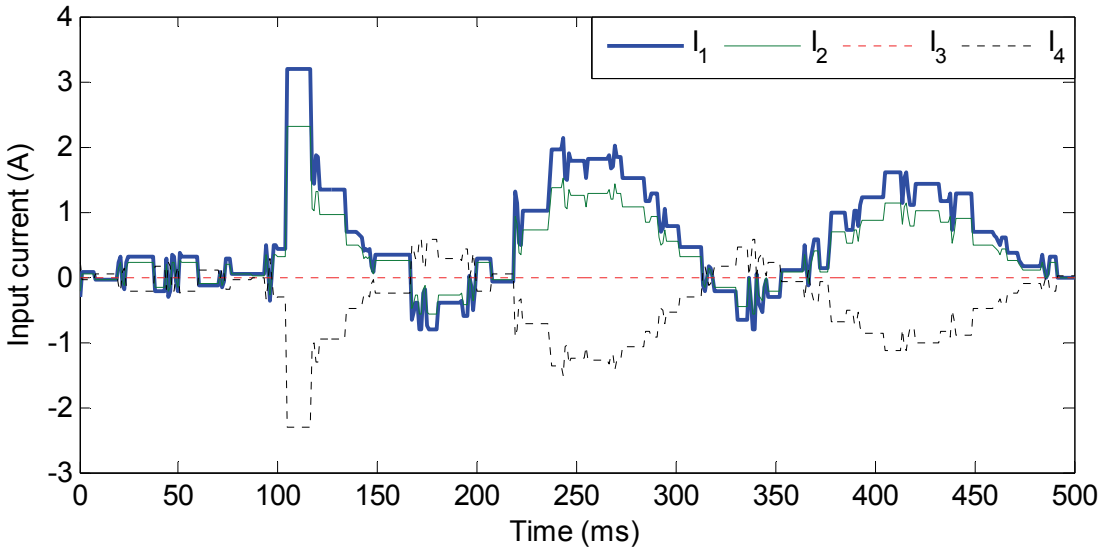

Figure 5-34 Current input into EM due to high gain aggressive controller

Table 5-5 Parameters for full state feedback and reduced order observer

G_{11}	G_{12}	G_{21}	G_{22}	H_1	H_2	L_O	$\mathbf{K_{SF}}$	
							Case 1	Case 2
0.9998	0.0009	-0.3867	0.9980	0.0018	3.6128	0.01	[0.55 0.01]	[0.2 0.03]

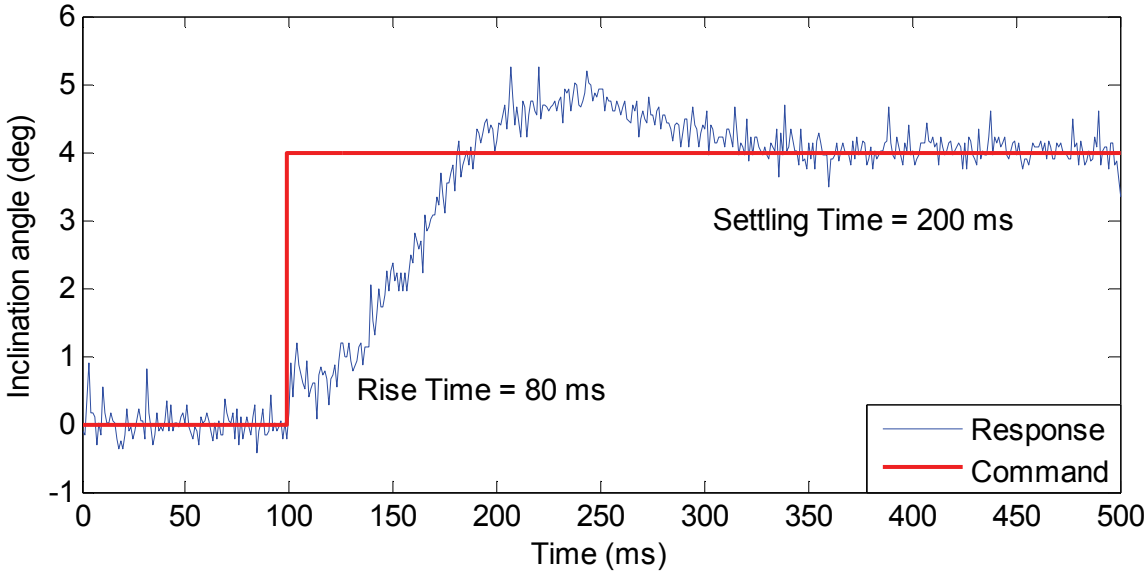

Figure 5-35 Step response of system to state feedback control with velocity observer

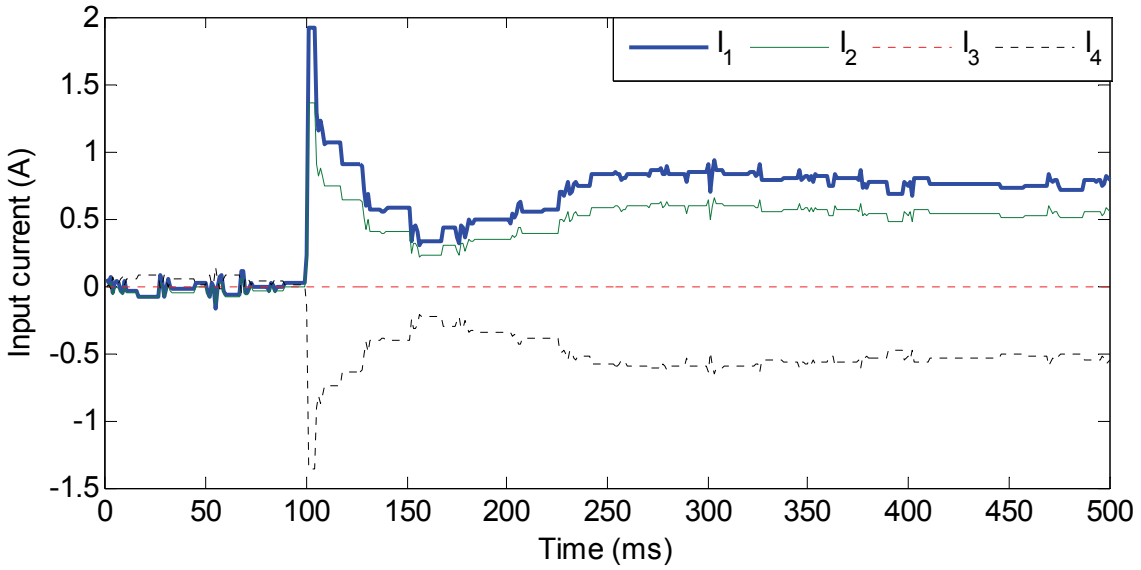

Figure 5-36 Current input into EM due to state feedback control with velocity observer

To investigate response of the system to point to point motion, a unit staircase reference command was utilized. Both this command and the corresponding response of the rotor are illustrated in Figure 5-37. The accompanying EM inputs are combined in Figure 5-38. As depicted in Figure 5-37, the full state feedback controlled system using a velocity state observer possesses good tracking performance for point to point motion.

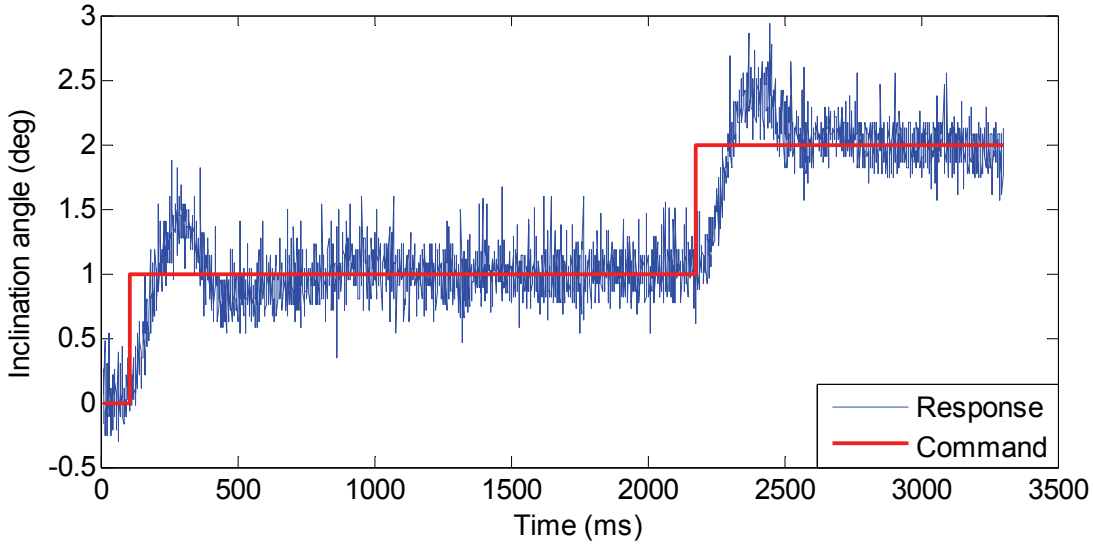

Figure 5-37 Multi-step response of system to feedback control with velocity observer

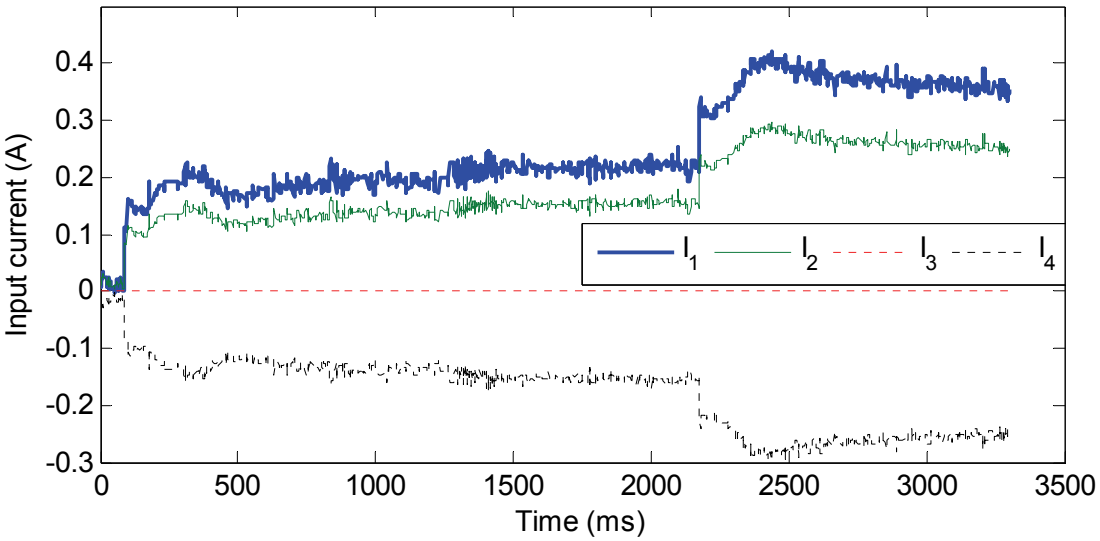

Figure 5-38 Current input into EM due to multi-step command

5.5 SUMMARY

In this chapter, the field-based sensing system was used for real-time control of an EM actuator. A direct approach, which exploits the non-invasive nature of the sensing system, was used to perform precise and accurate system identification for design of open and closed-loop controllers. The performance of the sensing system was evaluated against an industrial inclinometer and unlike such inertia-based sensors, did not suffer from poor tracking at high frequencies and delayed response. Exploiting the high bandwidth of the magnetic sensors and inertia-less nature of the magnetic field, the field-based sensing system is able to accurately track rapid motion of the rotor with no time delay for real-time feedback stabilization and control.

CHAPTER 6

CONCLUSIONS AND FUTURE WORKS

6.1 ACCOMPLISHMENT & CONTRIBUTIONS

This dissertation introduced an accurate and computationally swift distributed field-based positional sensing system for control of multi-DOF systems using high bandwidth and cost effective magnetic sensors. Of interest here is a class of dexterous multi-DOF systems with existing embedded magnetic field sources used for actuation. Using a field-based approach, these moving fields can be capitalized to provide non-invasive real-time concurrent positional and orientation sensing. The following contributions have been made:

1. *Development of a model independent embedded field-based sensing system*

This novel sensing method addresses the difficulties of magnetic inverse problems for multi source systems as well as the staunch requirement of fast computational speed for lag-free feedback control. The adopted approach is model independent and utilizes parametric spaces to spatially characterize the periodic field. Through this process, the entire field space can be divided in segments/sectors where bijection exists. With uniqueness, the mapping of only one segment/sector is required to completely characterize the whole field space. As the forward field models are highly non-linear with respect to the spatial coordinates, computation of the inverse field models is not tractable for real-time sensing. A non-linear function fitting approach of using highly scalable and robust ANNs is employed to efficiently approximate the inverse model (field

measurements to orientation of the moving system). As this technique assumes homogeneity between all magnetic field sources and sensing performance of all sensors, a requirement not realizable in actual implementation, statistical calibration is applied using affine transformation.

2. *Numerical and experimental performance evaluation of this sensing methodology on an existing electromechanical actuator*

Using the DMP model, the magnetic field as measured by a network of magnetic sensors can be simulated and subsequently used to create the inverse map between multiple field measurements and instantaneous orientation. This mapping performance is investigated with respect to spatial resolution, types of mapping functions and combinations of sensing inputs used. It was found that the choice of sensor as well as sensing axis has a profound impact on the sensing performance and this result is apparent during the experimental investigation on the electromechanical actuator.

Using a specially designed matching assembly of 24 identical PMs and magnetic sensors, the experimental field variation between identically graded and geometrically sized magnets as well as field measurement disparities between similar sensors were evaluated. The subsequent propagating effects of these field variations on the sensing performance using the inverse model free mapping approach were quantified. Using field calibration approach, which statistically standardizes field measurements across segments and sensors, these unavoidable field variations can be compensated in real time to minimize the detrimental effects on sensing accuracy.

3. *Field-based sensing system for controller design and real-time control implementation*

Electromagnetic actuators use the presence of magnetic fields for actuating as well as extraction of positional information via field-based sensing. As magnetic fields are linear and obey superposition, the measured fields in each sensor due to actuating fields from the EMs can be compensated in real-time with knowledge of the input current into each EM. The sensing performance of the field-based sensing system is evaluated against an industrial inclinometer. It was found that at high frequencies, the inclinometer is not able to track the rapid motion of the rotor during free response. At low frequencies, due to the inertia-based sensing system of the inclinometer, the output possesses a noticeable time delay of 150 ms which hinders real-time closed loop control performance. The field-based system, using high bandwidth magnetic sensors and using inertialess magnetic fields, has no such short comings and is able to unobtrusively perform accurate system identification on the system for design and implementation of open and closed loop controllers.

6.2 FUTURE WORKS

This research has provided a model-free approach in addressing the magnetic inverse problem of using distributed field measurements for real-time sensing and subsequent control. Further research and possible directions can be summarized as follows:

1. *Adapting the methodology to map other quantities*

While obtaining positional/orientation estimates from field measurements is the main focus of this study, other physical quantities of interest can be mapped directly to field measurements using ANNs. Some examples of these quantities are torques and

forces. In the case of electromagnetic actuators, the appliable torque is a function of the orientation of the rotor as well as the current input into the EMs. Hence a direct map between the field measurements and a baseline appliable torque will reduce the computational time required to compute the torque separately. Another possibility is mapping field measurements directly to the required controller output which are most commonly transmitted electrically using voltages and/or digital communications. Such an approach will avoid the computation of the orientation/position of the system for determination of the required controlling signal, thereby improving real-time performance.

2. *Considering heterogeneous sensor networks; combining high and low field sensors*

The sensor networks considered here are homogeneous. While high field sensors are proficient in detecting large changes in magnetic flux density, it is deficient in perceiving correspondingly small changes in magnetic field. In real world implementation, this issue is exacerbated by presence of sensing noise, further inhibiting discernment of small changes in magnetic fields. Low field sensors on the other hand possess higher SNR for small changes in magnetic field but encounter saturation effects in presence of strong magnetic fields. Therefore, a methodically designed network of both high and low field sensors can capitalize on the advantages of both types of sensors to generate a hybrid network that outperforms a homogeneous network of high or low field sensors.

3. *Effects of PM configuration on sensing performance*

The aim of this thesis is to develop a sensing system for pre-existing assemblies of PMs. The configurations of these PMs are usually optimized for actuation to maintain fairly constant torque at all orientation. As another avenue to improve sensing performance, the size, strength and configuration of PM assemblies can be further analyzed and optimized for systems primarily used for sensing such as haptic input devices.

Without the constraint of homogeneous PMs in actuating devices (to provide steady applied forces/torques), the use of heterogeneous PM assemblies is especially appealing due to the uniqueness of the resulting global field. Through meticulous selection and organization of the PM assembly, one possibility is the creation of a 'gray-coded' spatial field that is not only bijective for every point in space but has in-built error correction and noise suppression.

APPENDIX A

ORGANIZED SENSOR NETWORKS

Sensors in a network can be organized into s groups with each group containing r sensors that competitively and/or complementary sample some or all states of an n-order system. Graphically, the sensing states of the j^{th} sensor in the i^{th} group of the [s, r] network can be represented as shown in Figure 7-1. As each network sensor has individual characteristics, an organized sensor network is implemented for active management.

Figure 7-2 illustrates a control system using a network with [s, r] sequential and redundant sensors. It consists of a throttling controller, a weighting optimizer and a Kalman filter (DKF) working in tandem to produce a filtered estimate of the system states from noise corrupted individual sensor measurements. The throttling controller uses the desired controller output, sensor measurements and user defined performance specifications to determine the required [s, r] sensor configuration, and the optimal weighting distribution for each sensor group. Finally, the Kalman filter will utilize the weighted sensor measurements and system dynamics to generate a filtered estimate of the system states for subsequent control. A measurement model that characterizes the system state measurement by each sensor in the [s, r] network is developed in the temporal domain.

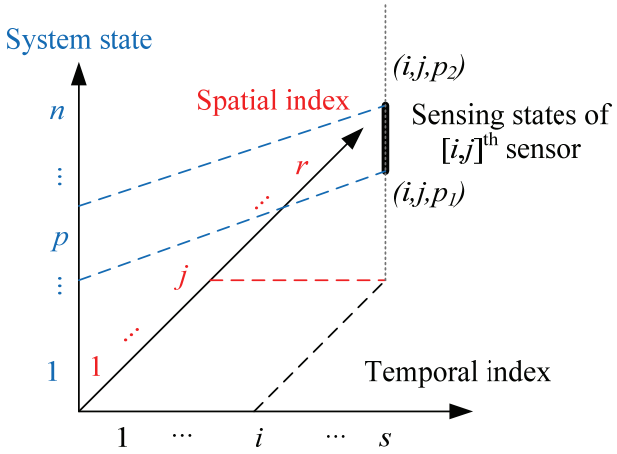

Figure 7-1 Graphical representation of network organization

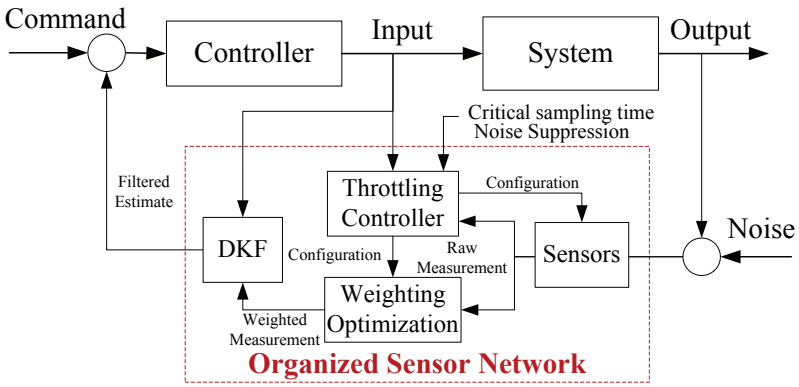

Figure 7-2 Block diagram of an organized sensor network

7.1 SENSOR TEMPORAL MEASUREMENT MODEL

The measurement of the state vector $\mathbf{x} \in \mathbb{R}^n$ by the j^{th} sensor of the i^{th} group in the sensor network at time t (with sampling period T_{ij}) is given by

$$\begin{cases} \mathbf{z}_{ij}(t) = \mathbf{L}_{ij}\left(\mathbf{x}(kT_{ij}) + \mathbf{v}_{ij}(kT_{ij}) + \mathbf{b}_{ij}\right) \\ \mathbf{v}_{ij}(kT_{ij}) = [\sigma_{ij1} \cdots \sigma_{ijp} \cdots \sigma_{ijn}]^T \sim \mathrm{N}\left(0, \mathbf{\Psi}_{ij}(kT_{ij})\right) \end{cases} \tag{7.1}$$

where $kT_{ij} \le t < (k+1)T_{ij}$; k is the time index integer, $\mathbf{b}_{ij}$ and $\mathbf{v}_{ij} \in \mathbb{R}^n$ are the bias and uncorrelated zero-mean Gaussian white measurement noise with covariance $\mathbf{\Psi}_{ij} \in \mathbb{R}^{n \times n}$; and the measurement matrix is

$$\mathbf{L}_{ij}\left(\in \mathbb{R}^{n\times n}\right) = \mathrm{diag}(\delta_{ij1}\cdots\delta_{ijp}\cdots\delta_{ijn}) \tag{7.2}$$

$$\delta_{ijp} = \begin{cases} 1 & \text{if } x_p \text{ is measurable} \\ 0 & \text{otherwise} \end{cases} \tag{7.3}$$

If all states are measurable, $\mathbf{L}_{ij}$ is an identity matrix. Similarly, if x_p is measurable,

$$\mathbf{\Psi}_{ij}\left(kT_{ij}\right) = \mathrm{diag}\left(\psi_{ij1}(kT_{ij})\cdots\psi_{ijp}(kT_{ij})\cdots\psi_{ijn}(kT_{ij})\right) \tag{7.4}$$

where ψ_{ijp} is the variance associated with σ_{ijp}.

7.2 WEIGHTING COEFFICIENTS OPTIMIZATION

The effective noise variance is minimized through constrained optimization. Without the loss of generality, we restrict our model to an [s, r] network with homogeneous sampling time T_{ij}=T_c as an illustration. In this network, the simultaneous sampling of r sensors by the i^{th} group provides a sequential weighed measurement $\bar{\mathbf{z}}_i$ at time t where $\left(kT+T_i\right) \le t < (k+1)T+T_i$:

$$\begin{cases} \bar{\mathbf{z}}_i\left(t\right) = \bar{\mathbf{L}}_i\left(\mathbf{x}(kT+T_i) + \bar{\mathbf{v}}_i(kT+T_i) + \bar{\mathbf{b}}_i\right) \\ \bar{\mathbf{v}}_i(kT+T_i) = \sum_{j=1}^{r} \boldsymbol{\alpha}_{ij}\mathbf{v}_{ij}(kT+T_i) \sim \mathrm{N}(0, \bar{\mathbf{\Psi}}_i(kT+T_i)) \end{cases} \tag{7.5}$$

and $T_i = (i-1)(T_c/s)$. In Equation (7.5), the over-bar "–" indicates that the quantity is weighted in the i^{th} sensor group and

$$\bar{\mathbf{L}}_i = \mathrm{diag}(\bar{\delta}_{i1}\cdots\bar{\delta}_{ip}\cdots\bar{\delta}_{in}) \tag{7.6}$$

where $\bar{\delta}_{ip} = \max(\delta_{i1p}\cdots\delta_{ijp}\cdots\delta_{irp})$. Similarly, the weighted bias and noise covariance matrix are given by:

$$\bar{\mathbf{b}}_i = \sum_{j=1}^{r} \boldsymbol{\alpha}_{ij}\mathbf{b}_{ij} \quad \text{where } \boldsymbol{\alpha}_{ij} \in \mathbb{R}^{n\times n} \tag{7.7}$$

$$\boldsymbol{\alpha}_{ij} = \text{diag}(a_{ij1} \cdots a_{ijp} \cdots a_{ijn}) \text{ and } \sum_{j=1}^{r} \boldsymbol{\alpha}_{ij} = \mathbf{I}_n \tag{7.8}$$

$$\bar{\boldsymbol{\Psi}}_i = \text{diag}(\bar{\psi}_{i1} \cdots \bar{\psi}_{ip} \cdots \bar{\psi}_{in}) \text{ where } \bar{\psi}_{ip} = \sum_{j=1}^{r} a_{ijp}^2 \psi_{ijp} \tag{7.9}$$

Hence, each sensor group contains r weighting coefficients to be selected for each of the n system states. One method to uniquely resolve for the $r \times n$ coefficients is by determining the coefficients that minimizes $\bar{\boldsymbol{\Psi}}$. For this, the first $(r-1)$ noise variance in (7b) is expressed as a multiple of the r^{th} variance, which yield

$$\bar{\psi}_{ip} = \left(a_{i1p}^2 m_{i1p} + \cdots + a_{i(r-1)p}^2 m_{i(r-1)p} + a_{irp}^2 \right) \psi_{irp} \tag{7.10}$$

where m_{ijp} is a known positive gain. Taking partial derivatives of (8) with respect to a_{ijp} (for j=1…r–1) and equating them to zero, (r–1) equations can then be obtained for computing the optimal weighting coefficients a_{ijp}:

$$\frac{\partial \bar{\psi}_{jp}}{\partial a_{ijp}} = m_{ijp} a_{ijp} + \sum_{j=1}^{r-1} a_{ijp} - 1 = 0 \tag{7.11}$$

Example:

Table 1 shows the computed optimal weighting coefficients where the subscripts (i, p) are omitted for readability for a network with 1, 2, 3 and 4 sensor redundancy.

Table 7-1 $\begin{pmatrix} a_1 & \cdots & a_r \end{pmatrix}$ for the [s, r] network configuration.

[s, 1]	$a_1 = 1$
[s, 2]	$\begin{pmatrix} a_1 & a_2 \end{pmatrix} = \dfrac{\begin{pmatrix} 1 & m_1 \end{pmatrix}}{m_1 + 1}$
[s, 3]	$\begin{pmatrix} a_1 & a_2 & a_3 \end{pmatrix} = \dfrac{\begin{pmatrix} m_2 & m_1 & m_1 m_2 \end{pmatrix}}{m_1 + m_2 + m_1 m_2}$
[s, 4]	$\begin{pmatrix} a_1 & a_2 & a_3 & a_4 \end{pmatrix} = \dfrac{\begin{pmatrix} m_2 m_3 & m_1 m_3 & m_1 m_2 & m_1 m_2 m_3 \end{pmatrix}}{m_1 m_2 + m_1 m_3 + m_2 m_3 + m_1 m_2 m_3}$

The normalized weighted variance for [s ,2] and [s ,3], which are computed using (7b) with unit covariance of the r^{th} variance and the coefficients in Table 7-1, are plotted as a function of the gains m_1 and m_2 in Figure 7-3(a) and (b). From both plots, the curve and surface approach unity asymptotically as m_1 and m_2 increase. Hence the inclusion of measurement from an additional sensor (no matter how noisy) will reduce the effective variance. It is noted that this weighting optimization is not restricted to the classical Gaussian noise distribution discussed here.

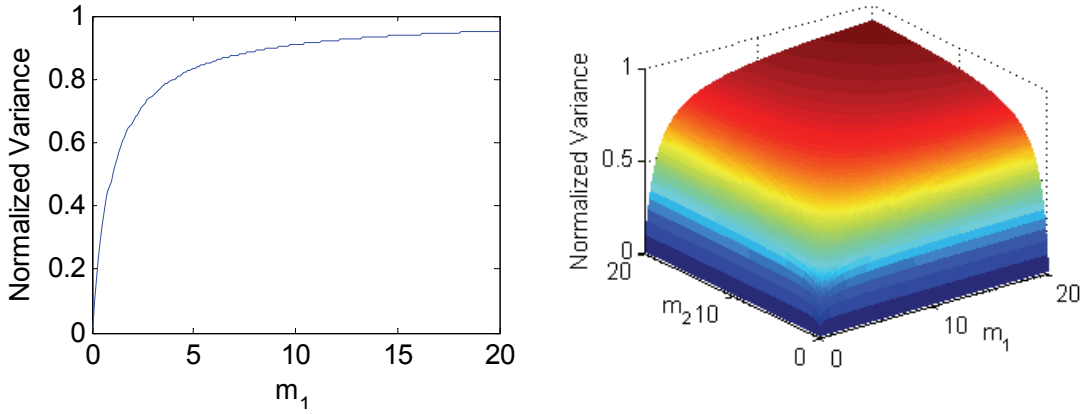

[s, 2] [s, 3]

Figure 7-3 Normalized effective variance for [s, 2] and [s, 3]

7.3 DISCRETE KALMAN FILTERING

As an illustration, we consider here a plant in continuous-time state-space representation with a controllable input **u**:

$$\begin{cases} \dot{\mathbf{x}}(t) = \mathbf{A}\mathbf{x}(t) + \mathbf{B}\mathbf{u}(t) \\ \mathbf{y}(t) = \mathbf{C}\mathbf{x}(t) + \mathbf{D}\mathbf{u}(t) \end{cases} \tag{7.12}$$

The corresponding discrete-time representation with process noise **ω** of covariance **Ω** is given by

$$\begin{cases} \mathbf{x}((k+1)T) = \mathbf{F}\mathbf{x}(kT) + \mathbf{G}\mathbf{u}(kT) + \boldsymbol{\omega}(kT) \\ \mathbf{y}(kT) = \mathbf{C}\mathbf{x}(kT) + \mathbf{D}\mathbf{u}(kT) \end{cases} \tag{7.13}$$

where $\mathbf{F}(T) = e^{\mathbf{A}T}$; $\mathbf{G}(T) = \int_0^T e^{\mathbf{A}\lambda} d\lambda \, \mathbf{B}$ and $T=T_c/s$. Without the loss of generality, the control law of the linear system using full state feedback (FSF) is

$$\mathbf{u}(kT \le t < (k+1)T) = -\mathbf{K}_F \hat{\mathbf{x}}\left(kT\right) \tag{7.14}$$

where $\mathbf{K}_F$ is the feedback matrix; and $\hat{\mathbf{x}}(kT)$ is the estimate of $\boldsymbol{x}$ at $t=kT$. The discrete Kalman filter [52] adapted for an [s, r] sensor-networked FSF system can be summarized by

$$\mathbf{K}(kT) = \mathbf{P}(kT)\left[\mathbf{I} + \bar{\mathbf{\Psi}}^{-1}(kT)\mathbf{P}(kT)\right]^{-1} \bar{\mathbf{\Psi}}^{-1}(kT) \tag{7.15}$$

$$\hat{\mathbf{x}}((k+1)T) = \mathbf{F}\hat{\mathbf{x}}(kT) - \mathbf{G}\mathbf{K}_F\hat{\mathbf{x}}(kT) + \mathbf{F}\mathbf{K}(kT)\left(\bar{\mathbf{z}}(kT) - \hat{\mathbf{x}}(kT)\right) \tag{7.16}$$

$$\mathbf{P}((k+1)T) = \mathbf{F}\mathbf{P}(kT)\left[\mathbf{I} + \bar{\mathbf{\Psi}}^{-1}(kT)\mathbf{P}(kT)\right]^{-1} \mathbf{F}^T + \mathbf{\Omega}(kT) \tag{7.17}$$

where **K** and **P** are the gain and estimate error covariance of the Kalman filter.

7.4 THROTTLING CONTROLLER

In an [s, r] network, a controller is required to select the desired sensor configuration out of a myriad of possible sensor configurations. For example, a three-sensor network contains five possible sensor configurations as illustrated in Figure 7-4, where each arrow in the acquisition timing diagram represents the measurement input from a solitary sensor.

A direct method that expresses the scalar integer quantities of r and s at a future time $t=(k+1)T$ as functions of all observable and measurable variables and parameters at the current time $t=kT$ can be expressed by:

$$r((k+1)T) = f\left(\hat{\mathbf{x}}(kT), c(kT), \mathbf{u}(kT)\right) \tag{7.18}$$

$$s((k+1)T) = g\left(\hat{\mathbf{x}}(kT), c(kT), \mathbf{u}(kT)\right) \tag{7.19}$$

where c is the desired command of the system.

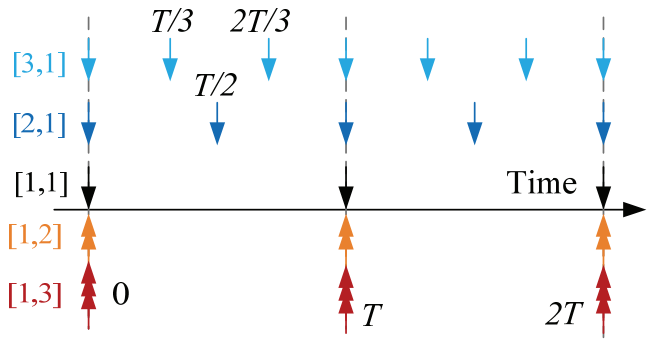

Figure 7-4 Acquisition schedule of different sensor configurations.

7.5 Simulation Results And Discussions

We investigate the effects of utilizing sensor networks on the controlled system performance under the influences of process and measurement noise. For numerical validation and performance evaluation, the inherently unstable inverted pendulum system (along with the parameter values in Table 7-2) where analytical solutions are available for validation, is chosen in this study. The system is under FSF control with optical cameras which has the advantage of measuring all state variables individually and simultaneously.

Table 7-2 Simulation parameters of inverted pendulum

System Parameters	l_p=0.5m; m_p=0.2kg; m_c=0.5kg; g=9.81ms^{-2}
Process Noise	$\mathbf{\Omega}$ = diag(0.015,0.002,0.15,0.15)
FSF Gains	$\mathbf{K}_F$ = [-26.9 -97.0 -23.9 -24.7]
Sensor Parameters	T_c = 0.1s; $\mathbf{L}_{ij} = \mathbf{I}$,, $\mathbf{b}_{ij} = 0$
Measurement Noise	$\mathbf{\Psi}_{ij}$ = diag(0.15^2,0.1^2,0.1^2,0.1^2)
DKF IC	$\mathbf{P}(0) = \mathbf{\Sigma}$, $\hat{\mathbf{x}}(0) = 0$

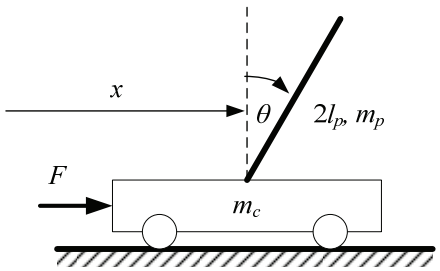

Figure 7-5 Schematic of inverted pendulum

The linearized equation of the pendulum motion is given by Equation (7.20)where $\mathbf{x} = \begin{bmatrix} x & \theta & \dot{x} & \dot{\theta} \end{bmatrix}^{\mathrm{T}}$:

$$\dot{\mathbf{x}}(t) = \begin{bmatrix} \mathbf{0}_{22} & \mathbf{I}_{22} \\ \mathbf{A}_{21} & \mathbf{0}_{22} \end{bmatrix} \mathbf{x}(t) + \begin{bmatrix} \mathbf{B}_1 \\ \mathbf{B}_2 \end{bmatrix} \mathbf{u}(t) \tag{7.20}$$

$$\mathbf{A}_{21} = \frac{1}{Ml_p} \begin{bmatrix} 0 & -3m_p g l_p \\ 0 & 3(m_p + m_c)g \end{bmatrix} \quad \mathbf{B}_2 = \frac{1}{Ml_p} \begin{bmatrix} 4l_p \\ -3 \end{bmatrix} \tag{7.21}$$

where $\mathbf{0}_{22}$ and $\mathbf{I}_{22}$ are the 2×2 null and identity matrixes respectively; $\mathbf{B}_1 = \begin{bmatrix} 0 & 0 \end{bmatrix}^{\mathrm{T}}$ and $M = \left(m_p + 4m_c \right)$.

The FSF gains are computed to place the desired closed-loop poles at −10, −8, −3 and −3. Modeled after an industrial network vision system [54], the optical camera, capable of sampling all four state variables at 10 frames per second (fps), has a sampling time $T_{ij}=T_c=0.1$s. To ensure asymptotic stability under FSF, the maximum sampling time of the discretized system is T_{crit} (or 0.0858 seconds for FSF gains in Table 7-2). The [s>1,r] ([1,r] would result in an unstable system) sensor network will possess an effective sampling rate of $T=T_c/s$.

Two performance criteria, command error (CE) and filtered measurement error (FE) are defined for the cart displacement over N measurements:

$$\mathrm{CE} = \int_0^{NT} \left(c(t) - x(t)\right)^2 dt \tag{7.22}$$

$$\mathrm{FE} = \sum_{k=0}^{N-1} \int_{kT}^{(k+1)T} \left(\hat{x}(kT) - x(t)\right)^2 dt \tag{7.23}$$

where c is the desired cart command. Since, in presence of noise, the time responses (and consequently the FE and CE) vary from simulation to simulation, the convergence of the mean and standard deviation (SD) of FE and CE as a function of number of simulation runs are statistically studied. From Figure 7-6, it can be seen that at least 200 runs are required for sufficient convergence of FE and CE.

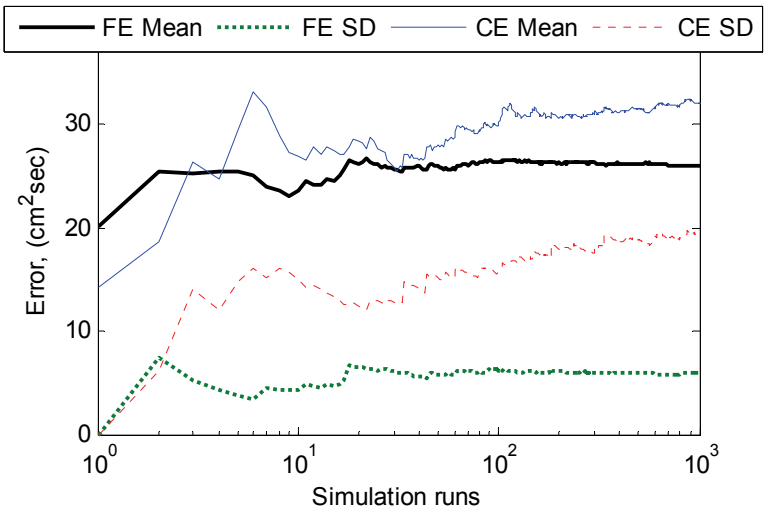

Figure 7-6 Convergence rate of FE and CE

7.6 EFFECTS OF NETWORK CONFIGURATIONS

The following cases were simulated:

[s>1, 1]: in the noise-free environment and zero sensor bias: This is equivalent to investigating the effect of the different sampling period T_c/s on the system. The special case [∞, 1] is analogous to a continuous-time system (T→0 as s→∞) which serves as a basis for comparison. The transient and steady-state results (compared against [∞, 1]) are

plotted in Figure 7-7, where only the first 0.5 second of the unit step response is shown in Figure 7-7(a) to magnify the differences during transient.

[2,1]: The interest here is to investigate the effect of sensor network on the stable system (with zero mean Gaussian white process and measurement noise as specified in Table 2) by comparing with/without Filter for the same sampling period of $T=T_c/s$:

- No measurement noise: $\mathbf{u}(t) = -\mathbf{K}_F\mathbf{x}(kT)$
- No filter: $\mathbf{u}(t) = -\mathbf{K}_F\bar{\mathbf{z}}(kT)$
- With DKF: $\mathbf{u}(t) = -\mathbf{K}_F\hat{\mathbf{x}}(kT)$

Table 7-3 compares the effects of using the DKF on CE and FE. Snapshot comparisons of the time responses are given in Figure 7-8.

[s, r]: To provide insights into trade-offs between sensor redundancy and effective sampling time for a total number of sensors, additional sensor network configurations are compared statistically. Figure 7-8(b) and (c) shows the effect on the time responses of the cart due to alterations in r and s independently. With [2,2] as a basis for comparison, the data are tabulated in Table 4 along with a surface plot relating CE/FE to the number of sensors in redundancy and sequential configuration in Figure 7-9. For each case, 500 simulation runs were executed and in each independent simulation, the same Gaussian noise is applied to all cases (type of filtering in Table 7-3 and configuration in Table 7-4) being studied.

Table 7-3 Effects of DKF on CE/FE (Mean, SD) in [2,1] network

Response	**Unit step** (cm^2sec)		**Steady- state** (cm^2sec)	
500 runs	CE	FE	CE	FE
No noise	7301, 499.3		43.30, 31.22	
No filter	7549, 973.2	666.2, 116.0	345.1, 175.	660.3,116.4
DKF	7475, 1091	323.1, 79.04	308.9, 182.	254.3, 58.10

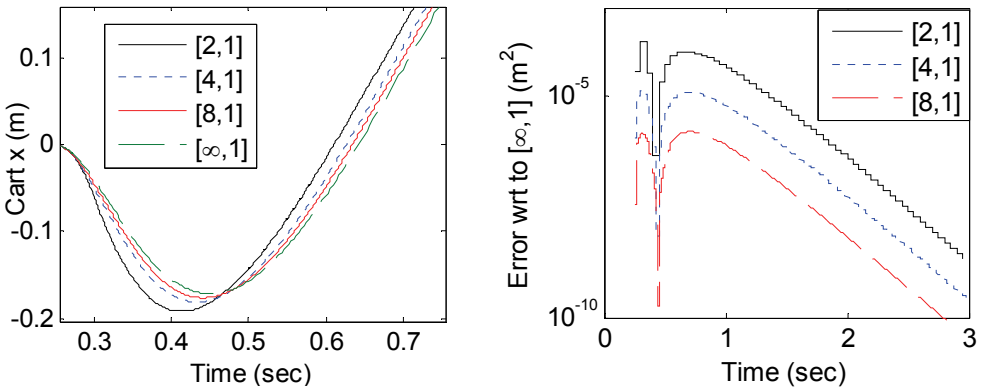

(a) Unit step response (b) Tracking error

Figure 7-7 In absence of process and measurement noise

Table 7-4 Effects of configuration on CE/FE (Mean,SD) with DKF

Response	**Unit step** (cm^2sec)		**Steady- state** (cm^2sec)	
500 runs	CE	FE	CE	FE
[2,2]	710.3, 33.57	7.276, 1.141	34.53, 22.76	70.7, 10.59
[4,2]	721.1, 27.15	7.049, 0.781	18.84, 11.17	70.42, 7.64
[8,2]	726.8, 23.19	7.008, 0.552	11.18, 6.69	70.09, 5.32
[2,4]	710.8, 21.63	2.400, 0.349	12.00, 7.91	22.29, 3.13
[2,8]	710.4, 17.97	0.841, 0.113	6.23, 4.17	6.66, 0.90

The observations from the results are briefly summarized:

Figure 7-7 shows that in a noise-free environment, the tracking error is reduced by 2 orders when the number of sensor groups is doubled (or increasing from $[2^1,1]$ to $[2^2,1]$, and to $[2^3,1]$).

Table 7-3 suggests that in an environment corrupted by Gaussian white noise, the filter lowers the CE and FE for both the unit step and steady-state response. In fact, the FE is halved when the DKF was used.

As Table 7-4 suggests, for the steady-state case, the CE decreases with increasing sensor usage. While increasing the number of sensor groups from 2 to 8 (s) reduces the CE by almost 60%, performing the identical change to the sensors in each group (r) is more effective and results in a reduction of almost 80%. However, the CE for the unit

step responses are unchanged with increasing redundancy and in fact higher at networks with higher *s*.

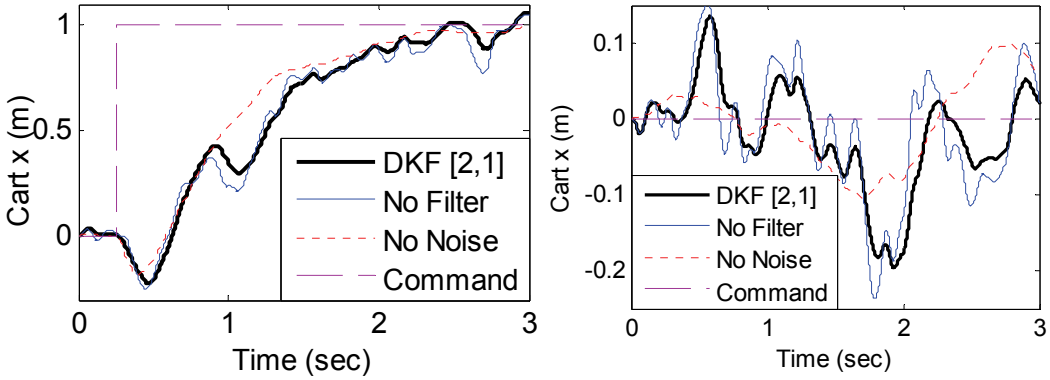

(a) Effects of DKF state estimates with [2, 1] configuration

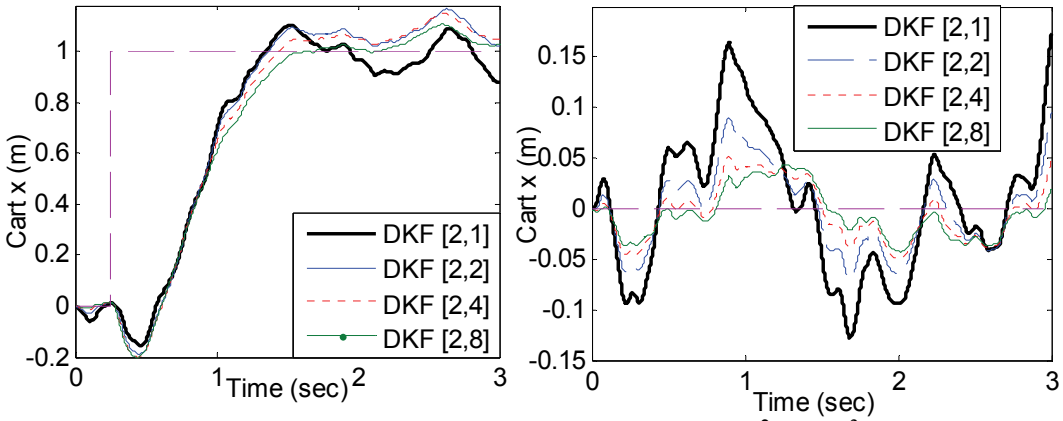

(b) Effects of redundancy [2, *r*], where r=1, 2, 2^2 and 2^3

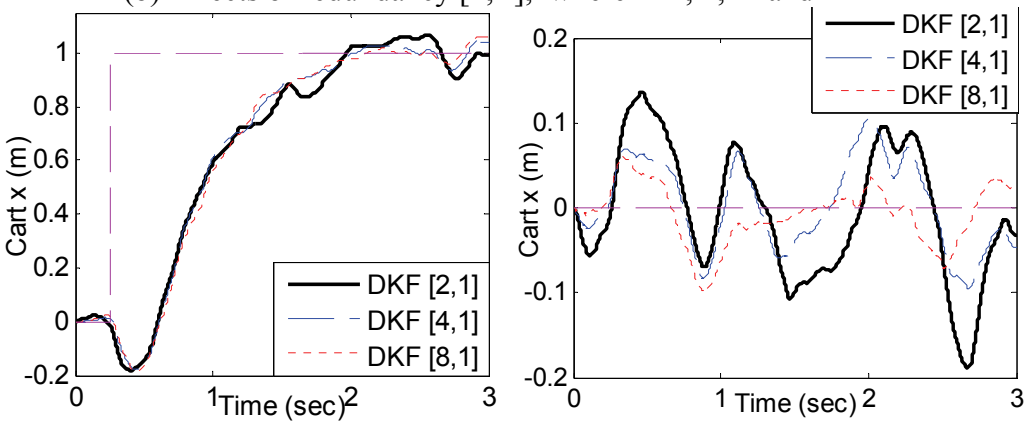

(c) Effects of sampling rate [*s*, 1] where s=2, 2^2 and 2^3

Figure 7-8 Effects of configurations on displacement (Left: step response, Right: steady-state)

The trend in the FE is similar to that of the CE. For both the unit step and steady-state cases, increasing the redundancy of the sensor network is more effective than increasing the network sampling rate in reducing the FE. Increasing the network redundancy from 2 to 8, reduces the FE reduced by 88% and 91% in the unit step and steady state case respectively. However, increasing the network sampling rate by the same factor could only muster an improvement in FE that is less than 5%.

As depicted in Figure 7-9, increasing the number of sensors in redundancy reduces the error in all cases except for the CE in the unit step case. On the other hand, the FE and CE for the unit step case is unaffected by the number of sensors in sequential mode. Increasing the number of sequential sensors is most effective in reducing the CE of the steady-state case.

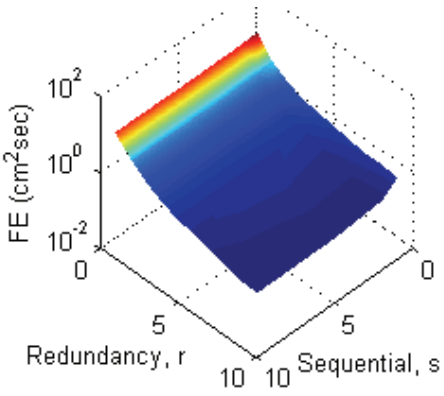

FE of unit step response

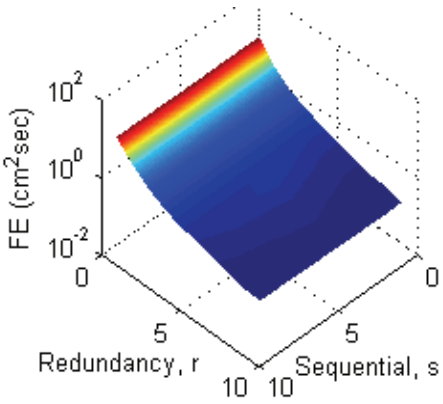

FE of steady-state response

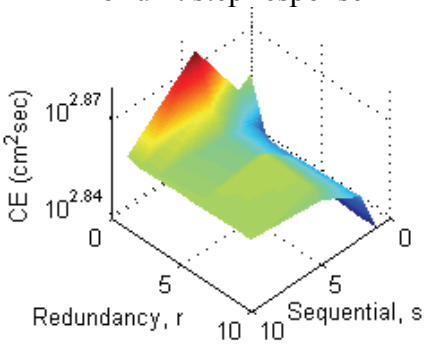

CE of unit step response

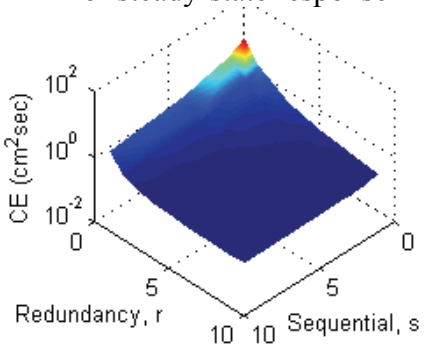

CE of steady-state response

Figure 7-9 Effects of *r* and *s* on CE and FE

7.7 THROTTLING CONTROLLER IMPLEMENTATION

From the results of the previous section, it can be seen that configurations with higher number of sensors in redundancy improve steady state tracking of the system. This is largely due to the presence of the DKF and accurate knowledge of the controlling input into the inverted pendulum system which allows accurate prediction of the state during transient motion. Assuming the following minimum and maximum configurations are available: [2,1] and [2,5], a throttling sensor configuration controller that employs variable configurations using feedback from the DKF state estimate and desired command is described as follows,

$$r((k+1)T) = \begin{cases} 1 & \text{if } V(kT) \geq q \\ 5 & \text{otherwise} \end{cases} \tag{7.24}$$

where $V(kT) = \left|c(kT) - \hat{x}(kT)\right| / \left|c(kT) - \hat{x}(0)\right|$ and q is the threshold transition between the network configurations. This threshold determines the specific crossover point where the network switches between the maximum and minimum configurations. As performance of the overall organized sensor network is sensitive to the value of q, and reusing the CE and FE as a means to critique performance, 500 simulations of a delayed step input of the system with the throttling controller utilizing different values of q are compiled in Table 7-5. The case where q=0.1 is omitted because at steady state the natural variation of $\hat{x}(kT)$ caused by the noise in the system will inadvertently trigger the transient mode of the network.

From the table, while employing the maximum configuration at all times, q=1, results in the lowest FE, it did not produce the lowest CE. Decreasing the value of q from 1 ([2,5]) towards 0 ([2,1]) results in increasing FE and decreasing sensor network

utilization. The corresponding trend in CE is however nonlinear and a minimum occurs between the two extreme values of q. The throttling networks that resulted in the lowest CE are: q=0.3, 0.4, 0.5 and 0.6. The best performing throttling network occurs at q=0.5; and it outperformed [2,5] in CE and maintained an average sensor utilization of 88.3% when compared to [2,5].

Table 7-5 Effects of q on CE/FE (Mean,SD) in throttling network

500 runs	q	CE (cm^2sec)	FE (cm^2sec)	Utilization (%)
[2,1]	0	777.5, 103.2	48.55, 9.618	20.0
Throttling	0.2	719.4, 54.82	18.69, 4.468	82.4, 3.55
	0.3	718.9, 54.67	17.57, 3.940	85.3, 2.19
	0.4	718.8, 54.59	16.87, 3.603	87.1, 1.67
	0.5	718.6, 54.58	16.29, 3.320	88.3, 1.41
	0.6	718.7, 54.87	15.80, 3.098	89.7, 1.23
	0.7	719.2, 55.03	15.33, 2.893	90.8, 1.08
	0.8	720.0, 55.13	14.89, 2.689	91.8, 1.01
	0.9	721.4, 54.88	14.46, 2.488	92.8, 0.97
[2,5]	1	730.8, 53.22	11.79, 1.360	100

The resulting response of the cart under a delayed unit step response using the throttling sensor controller (q=0.5) is shown in Figure 7-10.The corresponding responses of the cart using the static configurations [2,1] and [2,5] are added for comparison. It can be seen that the throttling controller has the characteristics of both extreme configurations: The transient performance of cart under throttling controller is similar to that of [2,1] and the steady state performance is similar to that of [2,5].

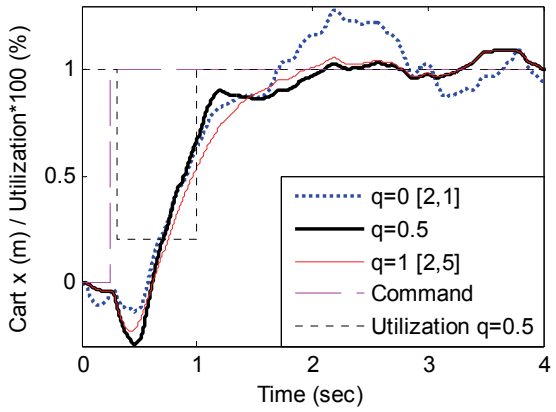

Figure 7-10 Cart response and utilization under throttling network

REFERENCES

[1] F. H. Raab, E. B. Blood, T. O. Steiner, and H. R. Jones, " Magnetic Position and Orientation Tracking System," *IEEE Transactions on Aerospace and Electronic Systems*, vol. AES-15, no. 5, pp. 709-718, 1979.

[2] J. Lenz and A. S. Edelstein, "Magnetic Sensors and Their Applications," *IEEE Sensors Journal*, vol. 6, no.3, pp. 631-649, Jun 2006.

[3] M. Caruso, T. Bratland, C. Smith, and R. Schneider, "A New Perspective on Magnetic Field Sensing," *SENSORS Mag*., pp. 34-45, Dec 1998.

[4] K.-M. Lee, K. Bai, J. Lim, "Dipole Models for Forward/Inverse Torque Computation of Spherical Motor," *IEEE/ASME Transactions on Mechatronics*, vol 14, no. 1, pp. 46-54, 2009.

[5] G. Krebs, A. Tounzi, B. Pauwels, D. Willemot, and F. Piriou, "Modeling of a Linear and Rotary Permanent Magnet Actuator," *IEEE Transactions on Magnetics*, vol. 44, no. 11, pp. 4357-4360, 2008.

[6] W. Wang, J. Wang, G. W. Jewell, and D. Howe, "Design and Control of a Novel Spherical Permanent Magnet Actuator with Three Degrees of Freedom," *IEEE/ASME Transactions on Mechatronics*, vol. 8. no. 4, pp 457-468, 2003

[7] K.-M. Lee, R. A. Sosseh, and Z. Wei, "Effects of Torque model on the Control of a VR Spherical Motor," *Control Engineering Practice*, vol. 12, pp. 1437-1449, 2004.

[8] L. Yan, I.-M. Chen, C. K. Lim, G. Yang, W. Lin, and K.-M. Lee, "Design and Analysis of a Permanent Magnet Spherical Actuator," *IEEE/ASME Transactions on Mechatronics*, vol. 13, no. 2, pp. 239-248, 2008.

[9] K.-M. Lee and D. Zhou, "A Real-Time Optical Sensor for Simultaneous Measurement of Three-DOF Motions," *IEEE/ASME Transactions on Mechatronics*, vol. 9, no. 3, pp. 499-507, 2004.

[10] H. Garner, M. Klement, and K.-M. Lee, "Design and Analysis of an Absolute Non-Contact Orientation Sensor for Wrist Motion Control," in *Proceedings of*

IEEE/ASME International Conference on Advanced Intelligent Mechatronics, Como, Italy, Jul 2001, pp. 69-74.

[11] I. F. Akyildiz, W. Su, Y. Sankarasubramaniam, and E. Cayirci, "A Survey on Sensor Networks," *IEEE Communications Magazine*, vol. 40, pp. 102-114, Aug 2002.

[12] R. C. Luo, C-C. Yih, and K. L. Su, "Multisensor Fusion and Integration: Approaches, Applications, and Future Research Directions," *IEEE Sensors Journal*, vol. 2, no. 2, pp. 107-119, 2002.

[13] C.-Y. Chong, and S. P. Kumar, "Sensor Networks: Evolution, Opportunities, and Challenges," in *Proceedings of IEEE*, vol. 91, no. 8, pp. 1247-1256, 2003.

[14] T. Arampatzis, J. Lygeros, and S. Manesis, "A Survey of Applications of Wireless Sensors and Wireless Sensor Networks," in *Proceedings of IEEE Mediterranean Conference on Control and Automation*, pp. 719-724, Jun 2005.

[15] I. Infantino, A. Chella, H. Dzindo, and I. Macaluso, "Visual Control of a Robotic Hand," in *Proceedings of the IEEE/RSJ International Conference on Intelligent Robots and Systems*, pp. 1266-1271, Las Vegas, Oct 2003.

[16] D. Willner, C. B. Chang, and K. P. Dunn, "Kalman Filter Algorithms for a Multi-Sensor System," in *Proceedings of IEEE Conference on Decision and Control*, vol. 15, pp. 570-574, Nov 1976.

[17] W. Saidani, Y. Morsly and M. S. Djouadi, "Sequential Versus Parallel Architecture for Multiple Sensors Multiple Target Tracking," in *Proceedings of Conference on Human System Interactions*, pp. 903-908, May 2008.

[18] S. Chroust, M. Vincze, R. Traxl, and P. Krautgartner, "Evaluation of Processing Architecture and Control Law on the Performance of Vision-Based Control Systems," *International Workshop on Advanced Motion Control*, 2000.

[19] E. M. Saad, M. H. Awadalla, M. A. Saleh, H. Keshk, and R. R. Darwish, "Adaptive and Energy Efficient Clustering Architecture for Dynamic Sensor Networks," *2nd International Workshop on Soft Computing Applications*, pp. 221-225, Aug 2007.

[20] K. Kaneko, I. Yamada, and K. Itao, "A Spherical DC Servo Motor with Three Degrees of Freedom," *ASME Publication of Dynamic Systems and Control Division*, vol. 11, pp. 433-443, 1988.

[21] K.-M. Lee, and J. Pei, "Kinematic Analysis of Three Degree-of-Freedom Spherical Wrist Actuator," *Fifth International Conference on Advanced Robotics*, vol. 1, pp. 72-77, 1991.

[22] H. H. Djambazian, C. Nerguizian, V. Nerguizian, and M. Saad, "3D Inclinometer and MEMS Acceleration Sensors," in *Proceedings of IEEE International Symposium on Industrial Electronics*, Montreal, Canada, Jul 2006, pp. 3338-3342.

[23] K.-M. Lee and H. Son, "Distributed Multipole Model for Design of Permanent-Magnet-based Actuators," *IEEE Transactions on Magnetics*, vol. 43, no. 10, pp. 3904-3913, 2007.

[24] H. Son and K.-M. Lee, "Distributed Multipole Models for Design and Control of PM Actuators and Sensors," *IEEE/ASME Transactions on Mechatronics*, vol. 13, no 2, pp. 228-238, 2008.

[25] C. K. Lim, and I. M. Chen, "A Novel 3-DOF Sensing Methodology for Spherical Actuator," in *Proceedings of IEEE/ASME Advanced Intelligent Mechatronics*, Zurich, Switzerland, Sep 2007, pp. 1-6.

[26] M.-C. Tsai, and C.-H. Yang, "A Flux-Density-Based Electromagnetic Servo System for Real-Time Magnetic Servoing/Tracking," *IEEE/ASME Transactions on Mechatronics*, vol. 13, no. 2, pp. 249-256, 2008.

[27] J. A. Baldoni, and B. B. Yellen, "Magnetic Tracking System: Monitoring Heart Valve Prostheses," *IEEE Transactions on Magnetics*, vol. 43, no. 6, pp. 2430-32, 2007.

[28] C. Hu, M. Q. Meng, and M. Mandal, "Efficient Magnetic Localization and Orientation Technique for Capsule Endoscopy," in *Proceedings of IEEE/RSJ International Conference on Intelligent Robots and Systems*, Edmonton, Canada, Aug 2005, pp. 628-633.

[29] C. Hu, M. Q. Meng, and M. Mandal, "Efficient Linear Algorithm for Magnetic Localization and Orientation in Capsule Endoscopy," in *Proceedings of IEEE*

Conference on Engineering in Medicine and Biology, Shanghai, China, Sep 2005, pp. 7143-7146.

[30] G. Li, and T.A. Kuiken, " Modeling of Prosthetic Limb Rotation Control by Sensing Rotation of Residual Arm Bone," *IEEE Transactions on Biomedical Engineering*, vol. 55, no. 9, pp. 2134-2142, 2008.

[31] G. Placidi, D. Franchi, and A. Sotgiu, "Design of a Magnetic Localisation System for *In-Vivo* Endovascular Interventions," in *Proceedings of the 29th Annual International Conference of the IEEE EMBS*, Lyon, France, Aug 2007, pp. 499-503.

[32] Y. Pang, A. L. De La Cruz, and G. Lodewijks, "Bipolar Magnetic Positioning System for Automated Guided Vehicles," in *Proceedings of IEEE Intelligent Vehicles Symposium*, Eindhoven, Netherlands, Jun 2008, pp. 883-888.

[33] D.-Y. Im, Y.-J. Ryoo, and Y.-Y. Jung, "Development of Steering Control System for Autonomous Vehicle Using Array Magnetic Sensors," in *Proceedings of International Conference on Control, Automation and Systems*, Seoul, Korea, Oct 2007, pp. 690-693.

[34] Y.-Y. Jung, D.-Y. Lim, Y.-J. Ryoo, Y.-H. Chang, and J. Lee, "Position Sensing System for Magnet Based Autonomous Vehicle and Robot Using 1-Dimensional Magnetic Field Sensor Array," in *Proceedings of SICE-ICASE International Joint Conference*, Busan, Korea, Oct 2006, pp. 187-192.

[35] U. Marschner, and W.-J. Fischer, "Indirect Measurement of a Bar Magnet Position Using a Hall Sensor Array," *IEEE Transactions on Magnetics*, vol. 43, no. 6, pp 2728-2730, 2007.

[36] V. Schlageter, P.-A. Besse, R. S. Popovic, and P. Kucera, "Tracking System with Five Degrees of Freedom Using a 2D-Array of Hall Sensors and a Permanent Magnet," *Sensors and Actuators, A: Physical*, vol. 92, no. 1-3, pp. 37-42, 2001.

[37] V. Schlageter, P. Drljaca, R. S. Popovic, and P. Kucera, "A Magnetic Tracking System Based on Highly Sensitive Integrated Hall Sensors," *JSME International Journal, Series C: Mechanical Systems, Machine Elements and Manufacturing*, vol. 45, no. 4, pp. 967-973, 2002.

[38] C. Hu, M. Q.-H. Meng, M. Mandal and X. Wang, "3-Axis Magnetic Sensor Array System for Tracking Magnet's Position and Orientation," in *Proceedings of 6th*

World Congress on Intelligent Control and Automation, Dalian, China, Jun 2006, pp. 5304-5308.

[39] C. Hu, M. Q.-H. Meng, M. Mandal, "A Linear Algorithm for Tracing Magnet Position and Orientation by Using Three-Axis Magnetic Sensors," *IEEE Transactions on Magnetics*, vol. 43, no.12, pp. 4096-4101, 2007.

[40] J. T. Sherman, J. K. Lubkert, R. S. Popovic, and M. R. DiSilvestro, "Characterization of a Novel Magnetic Tracking System," *IEEE Transactions on Magnetics*, vol. 43, no. 6, pp. 2725-2727, 2007.

[41] M. Akutagawa, Y. Kinouchi, and H. Nagashino, "Application of Neural Networks to a Magnetic Measurement System for Mandibular Movement," in *Proceedings of 20th Annual Conference of IEEE Engineering in Medicine and Biology Society*, Hong Kong, Oct 1998, pp. 1932-1935.

[42] S.-H. Jeong, S.-H. Rhyu, B.-I Kwon and B.-T Kim, "Design of the Rotary Magnetic Position Sensor with the Sinusodially Magnetized Permanent Magnet," *IEEE Transactions on Magnetics*, vol. 43, no. 4 pp. 1837-1840, 2007.

[43] J. J. H. Paulides, E. A. Lomonova, A. J. A. Vandenput and E.H. Zaaijer, "Sinusoidal Behavior of a Dipole Magnetization for Position Sensing Applications," *IEEE Transactions on Magnetics*, vol. 42, no. 10, pp 3294-3296, 2006.

[44] C. Schott, R. Racz, F. Betschart, and R. S. Popovic, "A New Two-Axis Magnetic Position Sensor," in *Proceedings of IEEE Sensors*, vol. 2, Orlando, FL, Jun 2002, pp. 911-915.

[45] A. Plotkin, and E. Paperno, "3-D Magnetic Tracking of a Single Subminiature Coil with a Large 2-D Array of Uniaxial Transmitters," *IEEE Transactions on Magnetics*, vol. 39, no. 5, pp. 3295-3297, 2003.

[46] A. Plotkin, V. Kucher, Y. Horen and E. Paperno, "A New Calibration Procedure for Magnetic Tracking Systems," *IEEE Transactions on Magnetics*, vol. 44, no. 11, pp. 4525-4528, 2008.

[47] J.T. Nenonen, "Solving the Inverse Problem in Magnetocardiography," *IEEE Engineering in Medicine and Biology Magazine*, vol. 13, no. 4, pp. 487-496, 1994.

[48] M. Xu and N. Ida, “Solution Of Magnetic Inverse Problems Using Artificial Neural Networks,” in *Proceedings of the 6th International Conference on Optimization of Electrical and Electronic Equipments*, vol. 1, 1998.

[49] W. S. Bennett, "Basic Sources of Electric and Magnetic Fields Newly Examined," *IEEE Antennas and Propagation Magazine*, vol. 43, pp. 31-5, 2001.

[50] D. K. Cheng, “Field and Wave Electromagnetics,” MA: Addison-Wesley, 1989

[51] W. Singhose and W. Seering, “Command Generation for Dynamics Systems, “ www.lulu.com , 2007

[52] A. Gelb, “Applied Optimal Estimation,” MIT Press, 1974.

[53] K. Ogata, “Discrete-Time Control Systems,” Second Edition, Prentice Hall, 1995.

[54] Banner Engineering, “Vision Presence PLUS® Series,” Banner Engineering Sensor Products Brochure, pp. 309-319

.

VITA

SHAOHUI FOONG

SHAOHUI FOONG was born in the island state of Singapore. After completing his pre-university education and national service in Singapore, he left for Atlanta, Georgia in the United States of America in 2002 to pursue his B.S. degree in Mechanical Engineering at the Georgia Institute of Technology. After receiving his undergraduate degree in 2005, He continued his graduate studies at the George W. Woodruff School of Mechanical Engineering where he obtained his M.S. degree in Mechanical Engineering in 2008 and actively pursuing his Ph.D. degree in Mechanical Engineering ever since.

His research interests include system dynamics and control, distributed sensing, sensor fusion and automation. He is also a recipient of Who's Who Award for best students in American Universities and Colleges in 2010 and a student member of *ASME* and *IEEE*.